UNIVERSIDAD AUTONOMA DE MADRID

Ph.D. Thesis

Biofouling and biofilm formation in engineered surfaces

Blanca Jalvo Sánchez

2017

UNIVERSIDAD AUTONOMA DE MADRID

Biofouling and biofilm formation in engineered surfaces

DOCTORAL PROGRAM IN MICROBIOLOGY

Blanca Jalvo Sánchez,

Madrid, 15 de junio de 2017

Doctoral Thesis supervised by:

Dr. Roberto Rosal García

Departamento de Química Analítica,
Química Física e Ingeniería Química
Universidad de Alcalá

Co-supervised by:

Dr. Marta Martín Basanta

Departamento de Biología
Universidad Autónoma de Madrid

Memoria presentada para optar al título de Doctor por la Universidad Autónoma de Madrid

Agradecimientos

En primer lugar, me gustaría agradecer a mi director de Tesis, Roberto Rosal García, y a mi tutora, Marta Martín Basanta, la confianza depositada en mí desde el principio así como sus consejos, paciencia y apoyo desde el primer día. Ha sido un honor aprender de y con vosotros.

Gracias también a la profesora Aji P. Mathew, de la Universidad de Estocolmo, quien me acogió con los brazos abiertos en Suecia e hizo que me sintiese como un miembro más de su grupo.

A todos mis compañeros de Fisiología Vegetal del Departamento de Biología de la UAM por hacer más llevaderos los comienzos, que nunca son fáciles. A Candela, por las horas y horas compartidas. A mis compañeros del Departamento de Ingeniería Química de la UAH, los días entre membranas hubiesen sido mucho más aburridos sin vosotros. A Sole y Jenni, gracias por vuestra ayuda infinita y amistad. A mis compañeros de la LTU y SU, en especial a Martha, Natalia, Adriana y Narges. Con vosotras todo fue mucho más fácil.

A mis amigos, especialmente a User, y mis Biolocas, todo lo que os pueda decir es poco. A Cristian, por compartir esta locura conmigo. A Minerva, más que una amiga una hermana, esta tesis también es tuya.

Y como no, a toda mi familia, a mi hermana, Alicia, y a mis padres, Carlos y Blanca. Sin ellos, sin su esfuerzo y apoyo durante todos estos años, nada de esto hubiese sido posible. Gracias por haberme enseñado a ser quien soy.

Acknowledgements

First of all, I would like to thank my supervisor, Roberto Rosal García, and my tutor, Marta Martín Basanta, for the trust deposited in me from the beginning, as well as their advice, patience and support from the first day. It has been an honor to learn from and with you.

Thanks also to Professor Aji P. Mathew, from the Stockholm University, who welcomed me with open arms in Sweden and made me feel like one more member of her group.

To all my colleagues from Biology Department, in UAM, to make more bearable the beginnings, which are never easy. To Candela, for the hours and hours shared. To my colleagues from Chemical Engineering Department, in UAH, the days between membranes would have been much more boring without you. To Sole and Jenni, thank you so much for your infinite help and friendship. To my colleagues from LTU and SU, especially Martha, Natalia, Adriana and Narges. With you everything was much easier.

To my friends, especially User, and my Biolocas, for all the patience they have had with me during this stage and all their support. To Cristian, for sharing this madness with me. To Minerva, more than a friend a sister, this thesis is also yours.

And of course, to my whole family, my sister, Alicia, and my parents, Carlos and Blanca. Without them, without their effort and support during all these years, none of this would have been possible. Thank you for teaching me how to be who I am.

Funding

This Thesis was supported by the European Union (7th Framework Programme FP7-ERA-Net Susfood, 2014/00153/001 No. 291766), by the Spanish Government (MINECO, Programa Estatal de Investigación, Desarrollo e Innovación Orientada a los Retos de la Sociedad, CTM2013-45775-C2-1-R) and the Dirección General de Universidades e Investigación de la Comunidad de Madrid, Research Network (REMTAVARES, Programas de I+D en tecnologías 2013, S2013/MAE-2716).

Contents

Resumen

El término ensuciamiento hace referencia a la deposición de cualquier material no deseado sobre superficies sólidas, pudiendo llevar a la pérdida de la función de las mismas. Estas impurezas pueden ser compuestos orgánicos, inorgánicos u organismos vivos. Este último caso se conoce como bioensuciamiento y consiste en la acumulación de microorganismos, plantas, algas o animales en superficies expuestas. Las biopelículas son comunidades de microorganismos adheridos a las superficies, embebidas en una matriz polimérica extracelular que tiene como objetivo facilitar su supervivencia en entornos adversos. Estas comunidades son omnipresentes, se producen en todo tipo de ambientes y plantean una serie de problemas que van desde la pérdida de la eficiencia de producción a problemas de salud pública.

Las biopelículas bacterianas suponen una gran preocupación en el desarrollo de biomateriales y en los campos de la biomedicina, industria alimentaria y sistemas de filtración, entre muchos otros. Probablemente, los más preocupantes son aquellos que afectan a las industrias biomédicas, ya que los organismos asociados en biopelículas son responsables de más del 60% de todas las infecciones microbianas en los seres humanos. La mayoría de los microorganismos tienen el potencial de adherirse y formar biopelículas en diferentes superficies y órganos, incluyendo implantes, catéteres urinarios, dientes o tejido pulmonar, siendo a menudo responsables de enfermedades crónicas e infecciones hospitalarias (nosocomiales). En la mayoría de los casos, las infecciones relacionadas con las biopelículas no responden a tratamientos antimicrobianos convencionales y, en consecuencia, conducen a enfermedades recurrentes y persistentes que suponen un riesgo importante para la vida. En la industria alimentaria existe una gran variedad de microorganismos capaces de colonizar y sobrevivir en los alimentos formando, en ocasiones, biopelículas multiespecíficas. Una vez desarrolladas, las biopelículas son una fuente importante de contaminación de otros productos. En las instalaciones de

tratamiento de agua y aguas residuales, las biopelículas, el ensuciamiento y la incrustación biológica son omnipresentes y causan corrosión, disminución de la calidad del agua tratada y menor eficacia de los sistemas de filtración. El ensuciamiento de las membranas provoca una disminución significativa en el flujo, lo que resulta en aumentos sustanciales en la demanda de energía y en los costos de operación y mantenimiento. En una planta de filtración típica, el mantenimiento, la sustitución de membranas y la limpieza de las mismas pueden representar hasta el 80% de los costes operativos totales. Debido al impacto negativo de las biopelículas, diversos métodos físicos y químicos para prevenir y eliminar su formación han sido investigados. Sin embargo, el éxito limitado de algunas de las estrategias seguidas para dicha prevención y la aparición de una plétora de recursos nuevos derivados de la ingeniería de materiales, hace necesario profundizar en los pasos iniciales de la colonización microbiana y en la forma de abolir la formación irreversible de biopelículas, particularmente, sobre nuevas superficies nanoestructuradas.

El objetivo de este trabajo fue estudiar las características de la colonización microbiana y la formación de biopelículas utilizando cepas de *Escherichia coli*, *Pseudomonas putida* y *Staphylococcus aureus* en diferentes sustratos, incluyendo materiales con hidrofilicidad variable y propiedades auto-limpiables fotocatalíticas. El objetivo principal fue determinar las condiciones requeridas para evitar la fijación de las biopelículas modificando ciertas propiedades superficiales, tales como la topografía y la química de la superficie. Para ello se utilizaron varias técnicas que incluyen tratamientos de irradiación con diferentes fuentes y espectros de radiación, conocidas como fuentes germicidas de ultravioleta, con y sin emisión en el vacío del ultravioleta, y radiación solar simulada con una lámpara de arco de Xe. Otras técnicas utilizadas en este trabajo incluyen los procesos electrohidrodinámicos de electrodisperisión y electrohilado, para producir nuevos materiales compuestos con comportamiento antimicrobiano y antibiótico específico. La electrodispersión es un método que produce gotas de tamaño micrométrico mediante la aplicación de un campo eléctrico. En esta técnica, una suspensión es forzada a dispersarse en forma de gotitas finas por una fuente de alta tensión. El tamaño de las gotitas electro pulverizadas oscila entre cientos de micrómetros y varias decenas de nanómetros, dependiendo de las propiedades físicas de la suspensión, del caudal de líquido y del voltaje aplicado entre la aguja y el colector. Mientras que la electrodeposición hace referencia a la formación de nanopartículas, el electrohilado describe la formación fibras poliméricas. El electrohilado es un procedimiento versátil

para producir fibras poliméricas por debajo de una escala micrométrica. La técnica ha sido ampliamente investigada debido a su potencial para generar materiales con una gran relación superficie-volumen funcionalizados con partículas nanométricas. Mediante el control de las condiciones de funcionamiento y los parámetros de la solución, el electrohilado puede emplearse para producir una variedad de nanofibras no tejidas, porosas o lisas, adecuadas para su uso en procesos de filtración. También existe la posibilidad de crear estructuras jerárquicas con núcleo y envoltura (electrohilado coaxial) así como fibras funcionalizadas en la superficie, que permiten el electrohilado de sustancias no hilables y funcionalizaciones superficiales complejas.

Los materiales elaborados a lo largo de esta tesis fueron caracterizados por microscopía electrónica de barrido (SEM), microscopía electrónica de transmisión (TEM) y microscopía de fuerza atómica (AFM). Las características fisicoquímicas de las superficies se determinaron mediante el potencial zeta de superficie (ζ) y la difracción de rayos X. También se determinaron las propiedades mecánicas de las membranas electrohiladas. El uso de técnicas de microscopía confocal y las medidas de la fluorescencia de ciertos fluorocromos, para establecer la viabilidad o integridad celular, permitieron determinar el efecto biocida de los materiales. Para ello, se utilizaron diacetato de fluoresceína (FDA), el marcador de ácidos nucleico SYTO 9 y yoduro de propidio (PI). Con el fin de visualizar la matriz polimérica extracelular, los biopelículas se tiñeron con FilmTracer SYPRO Ruby. Estos métodos se complementaron con el recuento de colonias y la medición de la biomasa celular.

Nuevos materiales compuestos fueron elaborados utilizando las técnicas descritas anteriormente. Los revestimientos resultaron, en general, como capas homogéneas de agregados de partículas agregadas, con superficies planas y completamente funcionales. Las membranas creadas presentaron fibras lisas, no tejidas y bien definidas, sin imperfecciones y con diámetros de unos pocos cientos de nanómetros. Los resultados mostraron que los tratamientos de irradiación aplicados a diferentes superficies funcionalizadas desencadenaron la transición de una superficie hidrófoba a una superficie hidrófila. Tales modificaciones, medidas a través de los ángulos de contacto, desempeñaron un papel determinante en la adhesión inicial de células bacterianas a las superficies manipuladas. Varios estudios realizados durante este trabajo revelaron que la colonización bacteriana fue favorecida en superficies con hidrofilicidad intermedia mientras que las superficies hidrofóbicas o superhidrófilas fueron menos propensas a la

adhesión bacteriana, independientemente de su carga superficial, medida como el potencial zeta. Por otro lado, la simulación de la radiación solar en las superficies funcionalizadas con nanopartículas fotocatalíticas mostró una fuerte actividad biocida en todos los casos. Las condiciones para las cuales es factible la eliminación de las biopelículas formadas durante períodos oscuros fueron estudiadas. Para una superficie dada el tratamiento de irradiación solar fue capaz de evitar completamente la acumulación de biopelículas, manteniendo la superficie libre de células y de matriz bacteriana exopolimérica. Los resultados obtenidos a lo largo de este trabajo son relevantes para aplicaciones que requieren una biocompatibilidad mejorada o suprimida de los materiales obtenidos o modificados a través de técnicas de ingeniería.

Abstract

The term *fouling* refers to the deposition of any undesired material on solid surfaces that leads to some kind of malfunction. The foulants materials can be either organic or inorganic compounds or living organisms. The latter is referred to as *biofouling* and consists of the accumulation of microorganisms, plants, algae, or animals on exposed surfaces. Biofilms are communities of microorganisms adhering to surfaces, which are embedded by a self-produced extra-polymeric matrix aimed at facilitating their survival in adverse environments. These communities are ubiquitous, occurring in all kinds of environments and pose a number of problems ranging from loss of production efficiency to product spoilage or safety problems.

Bacterial biofilms are a major concern in the development of biomaterials, biomedicine, food industry and filtration systems, among many other fields. Probably, the worst reputation belongs to those affecting the medical and healthcare industries because biofilm-associated organisms are responsible for more than 60% of all microbial infections in humans. Most of the microorganisms have the potential to adhere to and to form biofilms in different surfaces and organs including hospital settings, implants, urinary catheters, teeth or lung tissue, often being responsible for chronic illnesses and hospital-acquired (nosocomial) infections. In most cases, biofilm-related infections are not responsive to conventional antimicrobials and persistently reoccur occasionally leading to life-threatening diseases. In food processing environments, a variety of microorganisms colonize food and survive, grow, and sometimes form multispecies biofilm communities. Once developed, biofilms are a significant potential source of contamination of other products. In water and wastewater treatment facilities, biofilms, fouling and biofouling are ubiquitous and cause corrosion, decreased quality of treated water, and reduced efficacy of filtration systems. Membrane fouling causes a significant decrease in the permeation flux, which results in substantial increases in energy demand, and operational and maintenance costs. In a typical membrane filtration plant, the membrane replacement and membrane cleaning can account for up to 80% of the total operating costs. Due to the adverse impact of biofilms, different physical and chemical methods have been investigated to prevent and remove biofilms. However, the limited

success of the strategies followed to prevent biofouling and the emergence of a plethora of new engineered materials, makes it necessary to gain a deeper understanding on the initial steps of microbial colonization and the way of preventing the irreversible formation of biofilms, particularly in the case of new nanostructured surfaces.

The aim of this work was to study the steps of microbial colonization and biofilm formation using the strains *Escherichia coli*, *Pseudomonas putida* and *Staphylococcus aureus* on different engineered substrates, including materials with tunable hydrophilicity and self-cleaning photocatalytic properties. The goal pursued is to determine the conditions required to avoid biofilm attachment by modifying certain surface properties, such as topography and surface chemistry. Several techniques are used for this purpose, which include irradiation treatments with different sources and radiation spectra, namely germicidal ultraviolet sources, with and without emission in the vacuum ultraviolet, and solar radiation simulated with a Xe arc lamp. Other techniques used in this work include the electrohydrodynamic processes electrospray and electrospinning to produce new composite materials with specific antimicrobial and antibiofilm behavior. Electrospray is a method that produces micron sized droplets from a nozzle tip by applying an electric field. In this technique, a suspension flows out from a nozzle forced to disperse into fine droplets by a high voltage source. The size of electrosprayed droplets range from hundreds micrometers down to several tens of nanometer depending on the physical properties of the suspension, the liquid flow rate and the voltage applied between nozzle and collector. While electrospraying refers to the formation of nanoparticles, electrospinning describes the fabrication of fibrous polymer structures. Electrospinning is a versatile procedure for producing polymeric fibers below the micron scale. The technique has been recently investigated in view of its potential to generate high surface-to-volume ratio materials functionalized in the nanoscale. By controlling operating conditions and solution parameters, electrospinning can be used to produce a variety of non-woven porous or smooth nanofibrous structures suitable for their use in filtration processes. There is also the possibility of creating hierarchical structures such as core/shell (coaxial electrospinning) and surface decorated fibers, which allow the electrospinning of non-spinnable substances and complex surface functionalization as well as the improvement of certain properties of the electrospun membranes.

The materials were characterized by scanning electron microscopy (SEM), transmission electron microscopy (TEM) and atomic force microscopy (AFM). The physicochemical

characteristics of the engineered surfaces were determined by means of surface ζ-potential and X-ray diffraction. The mechanical properties of fibrous polymeric materials were also tested. Confocal microscopy and microplate readings with fluorochromes measuring cell viability or integrity allowed determining the biocidal effect of the materials. For it, the cell-permeant esterase substrate fluorescein diacetate (FDA), the nucleic acid stains SYTO 9 and propidium iodide (PI) were used. In order to visualize the extracellular polymeric matrix, the biofilms were stained with FilmTracer SYPRO Ruby. These methods were complemented by colony counting and the measurement of cell biomass.

New composite materials were successfully prepared using the previously described techniques. The coatings elaborated were, in general, homogeneous layers of tight aggregates of particles displaying planar and fully functional surfaces. The membranes created presented smooth, non-woven and well defined fibers without beading and with diameters of a few hundreds of nanometers. The results showed that the irradiation treatments applied to different functionalized surfaces triggered the transition from a hydrophobic to hydrophilic surface. Such modifications, measured from contact angles, played a determinant role on the initial attachment of bacterial cells to the engineered surfaces. Several studies carried out during this work revealed that bacterial colonization was favored in surfaces with intermediate hydrophilicity whereas hydrophobic or super-hydrophilic surfaces were less prone to bacterial adhesion, irrespective of the surface charge, measured as the zeta potential. On the other hand, the simulation of the solar radiation on the surfaces functionalized with photocatalytic nanoparticles displayed strong biocidal activity in all cases. The conditions for which the elimination of the biofilms formed during dark periods is feasible have been studied. For a certain surface a solar irradiation treatment was able to completely avoid biofilm accumulation keeping the surface free of cells and bacterial exopolymeric matrix. The results are relevant for applications that require enhanced or suppressed biocompatibility of engineered materials.

Chapter 1:

General introduction

1 General introduction

1.1 **Overview**

Bacteria inhabit nearly every type of environment and can be found in air, water, and, most notably, on surfaces. Once bacteria attach to a surface, a multi-step process starts, resulting in a complex adhering microbial community known as biofilm [1]. Surface attachment and subsequent biofilm formation are a type of "biofouling", which can be defined as the accumulation of biological matter on material surfaces. While bacterial biofouling can be beneficial under some circumstances, such as in biologically-based wastewater treatment systems [2], most biofouling can be detrimental and may be hazardous. Bacterial surface fouling is problematic for a wide range of applications and industries, including medical devices (implants, replacement joints, stents, pacemakers), municipal infrastructure (pipes, wastewater treatment), food production (food processing surfaces, processing equipment), and transportation (ship hulls, aircraft fuel tanks, among others) [3-6].

Preventing biofilm-associated infections has traditionally been accomplished using prophylactic antibacterial agents, whether delivered systemically or released directly from the biomaterial [7]. The pharmacokinetics and toxicity of the antibacterial agents incorporated in biomaterials limits the effectiveness of such approaches [7, 8] Antibiotics, antibodies, and phagocytes can clear planktonic cells released by the biofilm, but the sessile communities themselves are resistant to such agents [9]. Antibiotic therapy resulting in incomplete eradication of biofilm has been linked with the emergence of antibiotic-resistant bacteria, which may compromise their effectiveness even for non-biofilm-mediated infections [10].

New approaches for preventing the development of biofilms have been developed to modify the biomaterial surface properties, via surface chemistry and surface topography. It is also well-known fact that bacterial adhesion is influenced by properties of both the bacterial and the substratum surface [11]. Bacterial characteristics known to influence adhesion are hydrophobicity [12, 13], zeta potential [13], motility [14-16], and the release of extracellular substances, such as polysaccharides [17], proteins [18] and bio-surfactants [19]. Relevant properties of the substratum surface are hydrophobicity [12, 13] , surface charge [13] , and surface topography [20, 21] (Figure 1.1).

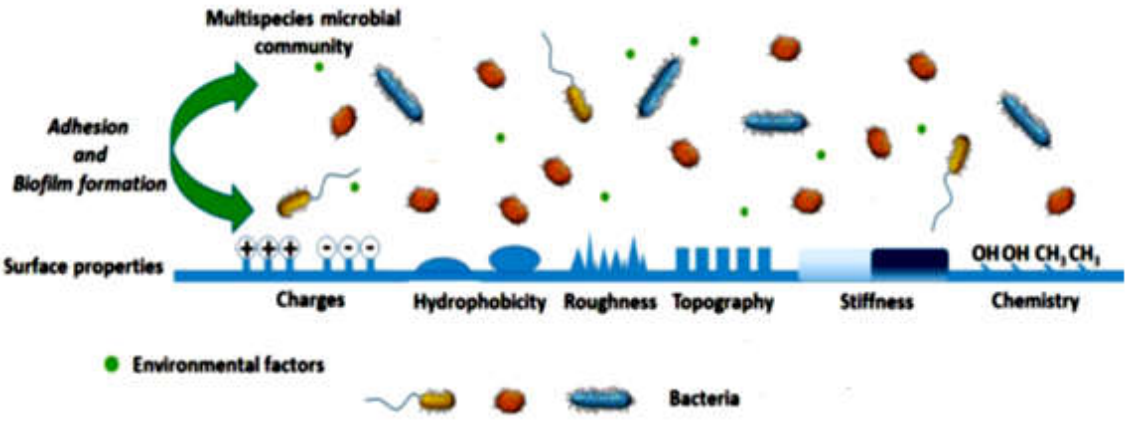

Figure 1.1. Schematic illustration of bacterial adhesion and the effects of material properties. Modified from [22].

The design of new surfaces is an emerging strategy to prevent biofilm formation in many industries requiring innovative techniques to create new surfaces via newly designed materials, surface modifications, new coatings, and paints.

The aim of the present thesis was to study microbial colonization and biofilm formation of three different bacterial strains on different engineered substrates, including materials with tunable hydrophilicity and self-cleaning photocatalytic properties. The goal pursued was to determine the conditions required to avoid biofilm attachment by modifying certain surface properties, such as topography and surface chemistry. Throughout this chapter, the principles and potential strategies about biofilm formation and engineered surface modifications will be discussed based on the currently available data, highlighting the advantages and difficulties of the different approaches.

1.2 Biofilm formation

Microorganisms can live and proliferate as individual cells swimming freely in the environment, or they can grow as highly organized, multicellular communities encased in a self-produced polymeric matrix in close association with surfaces and interfaces. This microbial lifestyle is referred to as biofilm [23]. A biofilm is an accumulation of microorganisms, with functional heterogeneity, embedded in a matrix of extracellular polymeric substances (EPS) produced by one or more of the attached bacteria. Biofilms constitute a protected mode of growth that allows survival in a hostile environment and are fundamental to the ecology and biology of bacteria [24, 25].

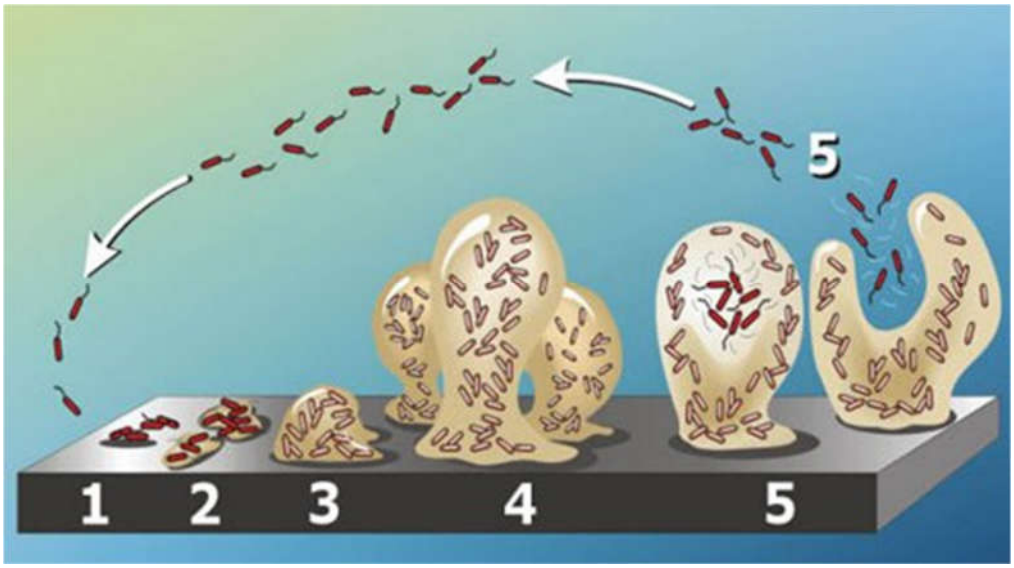

Figure 1.2. Representation of biofilm formation steps. 1) Initial attachment, 2) growth division 3) EPS production and quorum sensing, 4) Mature biofilm, and 5) dispersal. Adapted from [26].

Many bacterial species shown differences in biofilm formation steps, but in general, the phases comprise (1) an initial reversible adhesion to the surface to be colonized by the planktonic cell, (2) followed by irreversible coupling (3) which will lead to the formation of microcolonies; (4) the development of these small colonies encapsulated in EPS will eventually form a mature biofilm and finally, (5) once the matrix is developed, some bacteria are released, allowing the biofilm to expand more and more on the surface and to colonize new environments [23, 24, 27] (Figure 1.2).

In recent years, attempts have been made to elucidate how bacteria modify their gene expression at the time of forming the three-dimensional matrix. Although is not the only mechanism, most species use quorum sensing (QS) to modulate surface adhesion, mobility, EPS production and dispersion [28]. The QS is based on the existence of a complex communication systems, which let different members of the bacterial population know their density and, as a function of that, transcribe genes at specific moments to create an adaptive response to the environment [29].

1.3 **Bacterial adhesion**

Since adhesion is the first step of biofilm formation, understanding bacteria-surface interactions is essential for biofilm control. Bacterial cells approach surfaces by different means, including Brownian motion, sedimentation, movement with liquid flow, bacterial motility with cell surface appendages, and interaction with other cells to form aggregates

[11]. Once microorganisms reach the proximity of a surface, attachment is determined by physical and chemical interactions, which may be attractive or repulsive, depending upon the complex interplay of the chemistries of the bacterial and substratum surfaces, and the aqueous phase (Figure 1.3). To understand the forces that determine adhesion, a number of researchers have tried to determine whether bacterial attachment to surfaces is governed by the same physicochemical interactions that determine deposition of nonliving colloidal particles. Three theoretical approaches have been used: the Derjaguin, Landau, Verwey, and Overbeek DLVO model, the thermodynamic approach and the extended DLVO theory.

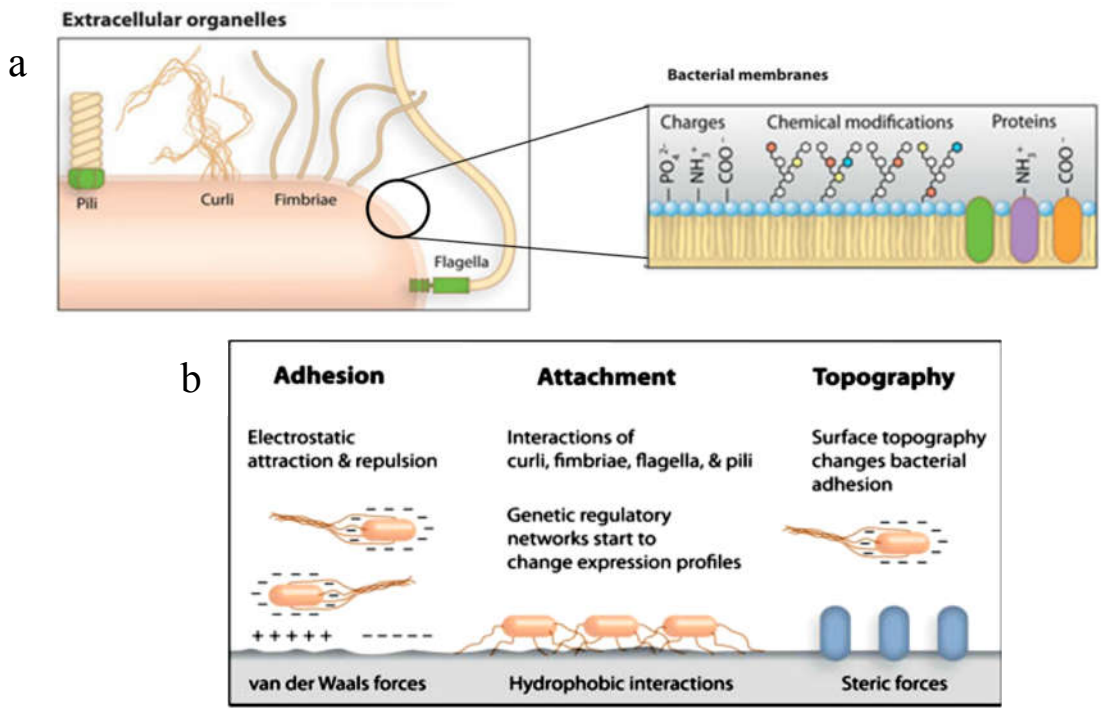

Figure 1.3. Interactions between substrate and bacterial cells. Modified from [30].

The DLVO theory has been used to describe the net interaction between a cell and a surface as a balance between two additive factors: van der Waals interactions, which are attractive, and repulsive interactions from the overlap between the electrical double layer of the cell and the substratum (Coulomb interactions, generally repulsive due to the negative charge of cells and substratum) [31-33]. This theory describes one of several components of the attachment process; that is the probability of an organism overcoming any electrostatic barrier. However, it does not describe the various molecular interactions that would come into play when polymers at the bacterial surface enter into contact with molecular groups on the substratum as well as any conditioning film [32]. Moreover, it

does not account for structures and molecules on bacterial surfaces that affect cell-surface distance and the exact type of interaction, for the substratum roughness and the fact that correlation between surface charge and adhesion is not straightforward: The effect of charge is more important for adhesion of hydrophilic than hydrophobic cells [34].

The Thermodynamic theory is the second physicochemical approach that has been used to describe bacterial attachment to surfaces [35]. It takes into account the various types of attractive and repulsive interactions, such as van der Waals, electrostatic or dipole but expresses them collectively in terms of free energy, a thermodynamic term. Adhesion is favored if the free energy per unit surface area is negative as a result of adhesion, which means that spontaneous attachment is accompanied by a decrease in free energy of the system, as required by the 2nd Law of Thermodynamics for spontaneous processes [34, 35]. Generally, it is very difficult to obtain accurate values for bacterial surface free energies because these surfaces possess complex chemistry and hydration *in vivo,* making the calculations of free energy changes during adhesion a very difficult task. Furthermore, the thermodynamic theory applies to closed systems where no energy is put into the system from outside. Bacteria, however, are living organisms that convert substrates into energy and adhesion, as well as the synthesis of adhesive polymers, may be driven by energy consuming physiological. Accordingly, the application of thermodynamic theory has not been entirely successful in explaining or predicting all the various attachment behaviors observed in bacterial systems [34]. However, this approach helped to explain a common observation: in numerous cases increased hydrophobicity of the solid surfaces or of the bacterial surfaces tended to result in increased numbers of attached cells [12, 36, 37].

The extended-DLVO theory accounts for Lifshitz–Van der Waals forces, electrostatic and short range acid–base interaction energies between the surface and the bacterium as a function of their separation distance [33, 38, 39]. In this theory, the distance dependence, which is important in the calculation of the total adhesion energy, is given from the classical DLVO theory for the van der Waals interactions. The double layer interactions and the distance dependence of the surface energy component decays exponentially from its value at close contact. Hence, the acid-base interactions at the first stage of adhesion are not involved. Therefore, the measured time dependent strengthening of the cell-substratum interaction is suggested to be due to the cell approaching to the surface [34, 38, 39]. The mechanistic knowledge of bacterial adhesion obtained from the extended-

DLVO theory provides guidelines for the development of surface coatings exhibiting minimal adhesion of bacteria, since the acid-base interaction also describes attractive hydrophobic interactions and repulsive hydration effects, which are 10-100 times stronger than the van der Waals interactions of surfaces in direct contact [34]. However, none of the theoretical models developed to date can accurately describe the adhesion of all bacteria on different surfaces. This is mostly due to the complexity of bacteria surface interactions and extracellular factors that cover the substratum surface [40], bacterial cell wall, adhesins and other membrane- associated structures (Figure 1.3).

1.4 Physical and chemical surface modifications

Zobell and Henrici described for the first time in the literature that bacteria could attach to and thrive on surfaces [41]. Physicochemical factors govern the initial attachment and adhesion of bacteria (Figure 1.1). As a general rule bacteria will preferentially colonize surfaces that are hydrophobic, have surface roughness on the nano and micro scale, and are exposed to a conditioning layer in contrast to smooth, hydrophilic surfaces [42]. Some authors affirm that the key challenge in this area is, actually, the prevention of the formation of a conditioning layer that exposes the surface chemistry and provides a site of attachment for bacteria [43]. However, how bacteria dynamically adjust physiology and cell surface properties in response to the local surface environment remains to be fully elucidated. The need for better understanding has led researchers to investigate the effects of material properties and their modifications on bacterial adhesion and several strategies have been used to create coatings with antimicrobial or anti-biofouling properties.

1.4.1 Roughness and topography

Among the surface properties, the role played by surface roughness has been one of the primary topics in biofilm research. Roughness refers to the intrinsic property of surface topography describing the degree of unevenness or irregularity exhibited by the surface and topography describes the degree of roughness that the surface exhibits [30]. In general, an increase in surface roughness promotes bacterial attachment due to the increase in contact area between the material surface and bacterial cells and protection from shear forces [11]. The interaction of bacteria with surface topography requires an understanding of their physical dimensions. Perera-Costa *et al.* observed that bacterial cells actively choose their position to settle differentiating upper and lower areas in all

the surface patterns that they evaluated. Such selective adhesion depends on the cell size and shape relative to the dimensions of the surface topographical features as well as surface hydrophobicity/hydrophilicity [44].

Whitehead *et al*. noted that the shape of the surface features is essential for understanding the effects of bacterial cell retention [45]. They pointed out three main cell retention characteristics: (1) when surface grooves are in close proximity to one another, with distances smaller than bacterium dimensions, cell-substratum interaction is minimal (Figure 1.4a); (2) as grooves become wider (on the size scale of individual cells) microorganisms are able to fit between grooves, benefiting from an enhanced cell-substratum contact. It is believed that this closer contact increases the binding energy and promotes the propensity of microorganism retention on the substratum surface (Figure 1.4b); (3) on wider spaced grooves (greater than the size of individual cells) there cell-substratum contact is insignificant. From the point of view of microorganisms in the latter situation, the cells do not experience roughness created from surface defects and, in this sense, the surface seems to be smooth for the bacterial cells (Figure 1.4c). Furthermore, due to low cell-substratum contact, cells may be washed out from the surface.

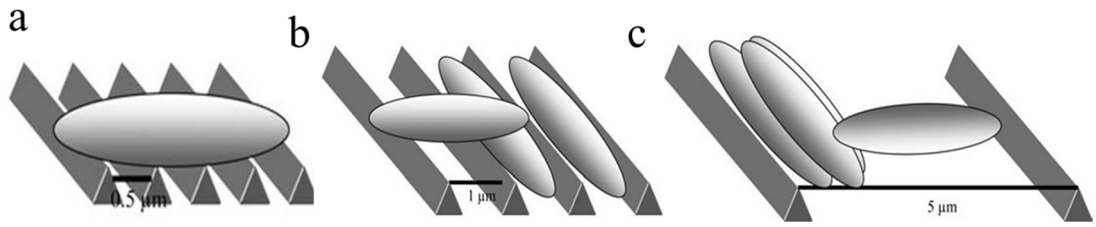

Figure 1.4. Effect of surface features on microbial retention. Modified from [45]

The hypothesis that surface roughness, including surface wearing, plays a pivotal role in cell retention has directed much recent work involving the use of engineered topography as a means of fabricating antifouling surfaces. A practical outcome is the connection between the size scale of an organism of interest, and the necessary size dimensions needed for the topographical features to reduce biofouling [45]. Furthermore, it has been established that the basic premise is that topography-based antifouling surfaces have greater efficacy when the size regime of the fouling organism of interest is taken into account [46]. Since microorganisms have a wide range of external dimensions, surface topographies that contain only one length scale would not be efficient as a universal antifouling coating [46]. In this sense, it becomes crucial to develop engineered

topographical patterns that can limit surface attachment by organisms with variable size and morphology.

1.4.2 Surface energy

The wettability of a solid surface with a liquid is governed by its chemical properties and surface microstructure. The role of hydrophobicity in bacterial adhesion has been extensively reported elsewhere [12, 30, 36, 47-49]. Generally, bacteria with hydrophobic properties prefer hydrophobic material surfaces (low surface energy) and the ones with hydrophilic characteristics prefer hydrophilic surfaces (high surface energy). The displacement of water molecules near surfaces enhances hydrophobic interactions and promotes close contact between cells and surfaces [30], but, bio-surface interactions are more complex due to cell appendages. The thermodynamic approach assumes direct contact between bacteria and surface, creating a new interface, but the presence of cell appendages hinders such direct interaction [42].

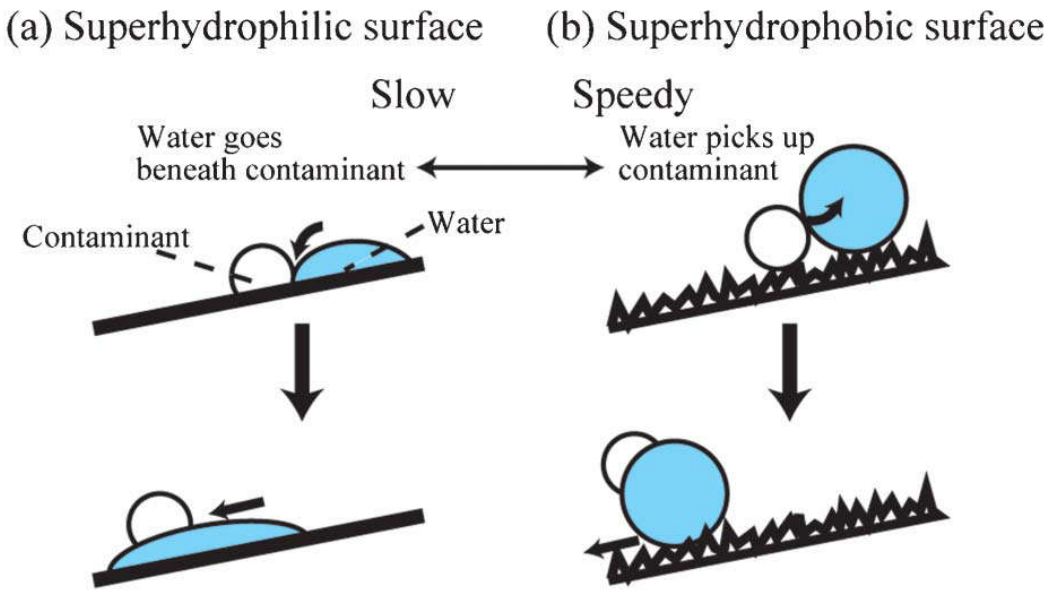

Figure 1.5. Schematic illustrations of self-cleaning processes on a superhydrophilic surface (a) and on a superhydrophobic surface (b). Modified from [49].

Attending to the wettability regimes and performing different surface modifications, it is possible to create self-cleaning surfaces and reduce biofilm formation as well as the accumulation of other kinds of contaminants (Figures 1.5 and 1.6). For example, on a superhydrophilic surface (Figure 1.5a), the water droplets go beneath the contaminant and wash it away. Water on such a surface spreads quickly, creating no streaks. The thin film

of water spread on the surface may evaporate rapidly. However, the surface may remain wet for a longer period as compared to superhydrophobic surfaces, which may be undesirable in some applications. On superhydrophobic surfaces (Figure 1.5b), water is repelled from and water droplets may roll off them, also taking contaminant particles with them [49]. In this case, unlike superhydrophilic/superhydrophobic surfaces, intermediate hydrophilic surfaces suffer more adhesion from contaminants and microorganisms.

The preferential alignment of hydrophobic functional groups on surfaces with the hydrophobic moieties on the bacterial cell wall, and extracellular organelles, stabilizes interfacial interactions (Figure 1.3a). The preference of different aquatic bacteria to attach to hydrophobic, low-energy surfaces demonstrates this phenomenon [50]. The bacterial attachment in nutrient-free media, which is a strategy to avoid the remodeling of surface by nutrients, allowed concluding that the physical (hydrophobic) interactions between cell surfaces and substrate were the main factor responsible for attachment [50]. Pringle and Fletcher's results uncovered a recurring theme in the description of cell-surface interactions: the physical interactions between hydrophobic surfaces and flagella, fimbriae, and pili facilitate the attachment of bacteria to non-polar, low-energy substrates [50]. During the initial approach and attachment, bacteria experience short-range repulsions in the close proximity to negatively charged surfaces (Figure 1.3). The displacement of water molecules near surfaces enhances hydrophobic interactions and promotes the contact between cells and surfaces [51]. Adhesion of bacteria to hydrophilic surfaces is enhanced if the surface tension of the bacterial cell wall is higher than the surface tension of the surrounding liquid [52]. Fluorinated materials exhibit large contact angles that are characteristic of low energy surfaces. The oxidation of fluorinated surfaces revealed that the initial hydrophilic properties of a substrate reduces the initial attachment of bacteria onto surfaces [53]. Unfortunately, a complication of engineered surfaces in real-life applications is that materials are exposed to environments with absorbed solutes at the interface. Consequently, the preliminary effects of surface energy on attachment disappear. Besides, the ability of bacteria to adhere to both hydrophilic and hydrophobic substrates suggests a strategy for biofilm formation (and survival) in diverse environmental conditions. The influence of surface energy on bacterial attachment is still not completely understood, and its extrapolation into a general principle and design rule for engineering and preventing adhesion is still pending.

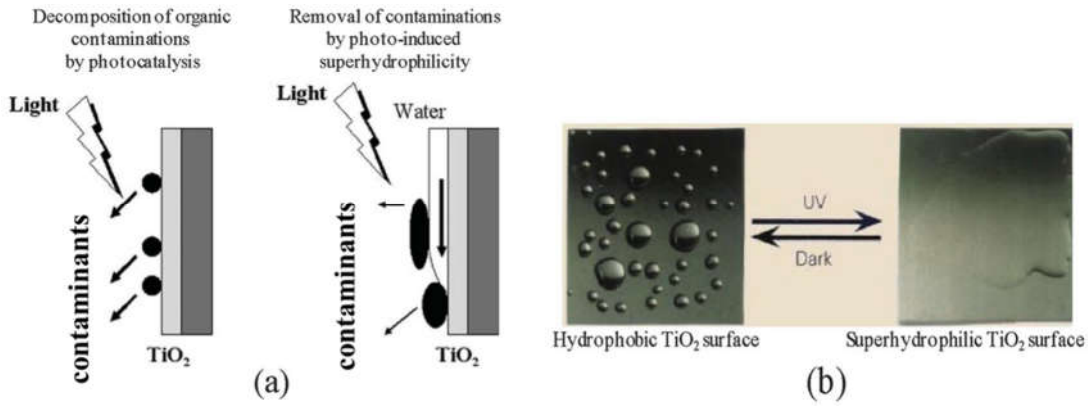

Figure 1.6. Schematic diagram of the self-cleaning process on the TiO_2 surface with photocatalytic organic decomposition properties (a). Photoinduced superhydrophilic properties photographs of the TiO_2 surface before and after ultraviolet irradiation (b). Modified from [49, 54].

1.4.3 Surface charge

Electrostatic forces are among the earliest interactions that influence the attachment of bacterial cells to surfaces (Figure 1.3b). Most bacterial genera have a net negative charge as determined by zeta-potential measurements [55, 56]. Bacteria attach rapidly and tightly to positively charged surfaces, and electrostatic repulsion destabilizes cell contact with negatively charged surfaces. Destabilizing interactions between cells and anionic surfaces during the initial stages of attachment can be overcome by extracellular organelles that promote adhesion, including fimbriae, flagella, curli, and pili (Figure 1.3a). The layer of the bacterial cell wall that is in contact with the extracellular environment is complex and exposes many different functional groups that may interact with substrates (Figure 1.3a). These functional groups include carboxylate, hydroxyl, phosphate, and amines [57]. In their native environments, bacterial cells are not in contact with "naked" surfaces. Diffusion and mass transport influence the adsorption of small molecules, ions, and proteins on surfaces and alter surface chemistry and charge. The layer of adsorbed molecules screens the intrinsic surface charge and promotes the adsorption of bacteria and their growth into biofilms. It has been described that surfaces presenting certain cationic groups, such as quaternary ammonium and polyethylenimines, have antimicrobial activities and thus can kill the attached cells [58]. In principle, controlling bacterial adhesion with surface charge may not work in static systems since the dead cells present a barrier that reduces the charge and facilitates the adhesion of other bacterial

cells. However, because shear forces producing by flow (rinsing and brushing) can facilitate the removal of dead cells from certain materials [22].

Rzhepishevska *et al*. showed that surface charge can also affect long-term biofilm structure. For example, *Pseudomonas aeruginosa* on negatively charged poly(3-sulphopropylmethacrylate) is able to form mature biofilms, with mushroom shape, which have a higher level of cyclic diguanylate monophosphate (c-di-GMP) than the relatively uniform biofilms formed on positively charged poly(2-(methacryloyloxy)-ethyl trimethyl ammonium chloride) surfaces [59]. Because the increase in c-di-GMP level is known to induce the production of extracellular matrix, it was suggested that *P. aeruginosa* may be able to modify cell surfaces to better attach on negatively charged substrates [59]. These findings emphasize that surface charge alone may not be sufficient to repel bacteria and prevent biofilm formation, at least, for some bacterial species.

1.4.4 Stifness

Among the material properties, the effect of stiffness is the least studied, and only a few reports are available in the literature. The first references date back to 2003, when Bakker *et al.* observed that surface stiffness may affect bacterial attachment. This study was carried out working with two different glass materials, which doubted this correlation [60]. Lichter *et al.* reported that the adhesion of *S. epidermidis* was positively correlated with the stiffness of their polyelectrolyte multilayer thin films composed of poly(allylamine hydrochloride) and poly(acrylic acid) as a model, independent of surface roughness and charge density [61]. In addition to adhesion, *E. coli* and *Lactococcus lactis* were found to grow faster on low Young's modulus than on high Young's modulus polyelectrolyte multilayer thin films [62]. Other studies reported that the elastic modulus of agarose hydrogels can affect cell cluster formation and protein synthesis in attached bacterial cells [63]. Song and Ren investigated the early biofilm formation on poly(dimethylsiloxane), (PDMS), with varying stiffness and found that an increase in PDMS stiffness reduced not only the adhesion and growth of *E. coli* and *P. aeruginosa* but also the size and antibiotic susceptibility of attached cells, indicating that bacteria are able to sense and respond to material stiffness during biofilm formation [64]. Although the underlying mechanism is still unknown, it is becoming clear that material stiffness does affect, somehow, bacterial adhesion and the physiology of attached cells to the surfaces.

1.5 New surface materials and surface modifications

The selection of materials that do not favor the surface attachment of microorganisms is a promising approach to the prevention of biofilms. Many studies have been conducted to search for materials that do not enhance or even suppress biofilm formation. Surface modification gives another potential way to prevent biofilms. Numerous studies have been conducted, especially in the medical fields, to prevent biofilm formation via incorporation of biocides into certain surface materials, or to coat surfaces with biocides and to further develop self-cleaning technologies including anti-smudge, anti-fouling, low adhesion, photocatalysis and self-sterilizing surface technologies as an environmentally friendly or green technology. The modifications include the use of coating and plasma [65, 66] techniques with a wide range of polymers [37, 49, 67], photocatalytic materials [54, 68-70] (Figure 1.6). The use of electrohydrodynamic processes, electrospray and electrospinning, is another way to add nanoparticles or nanocrystals that modify the absorption capacity of surfaces [36, 71-73]. Other possibility is the irradiation of certain surfaces light-responsive surfaces with different light sources and radiation spectra to achieve a transition between hydrophobicity and hydrophilicity [12, 74, 75].

Resistance of biofilms to biocides and antimicrobial agents is mainly achieved through a cell-to-cell communication (quorum sensing, QS) process. Thus, the blockage of cell–cell communication can be a novel approach to inhibition of biofilm formation. Recently, a peptide termed as “RNA III-inhibiting peptide” (RIP) was described that may prevent biofilm formation by *S. aureus*. The process by which RIP inhibits QS involves inhibition of the phosphorylation of a protein called “target of RNA III” activating protein (TRAP) [76]. These findings suggest that medical devices coated with RIP could be used to prevent biofilm formation. Another alternative method is to coat surfaces with nontoxic materials so that the adhesion of microbes is greatly reduced. This effect is mainly due to a combination of hydrophobicity, low surface free energy, and micro-roughness [77, 78].

1.6 Bacterial response to surface properties

The approaches discussed above suggest that bacteria have complex systems to sense and respond to environmental challenges. However, the genetic basis of surface sensing is still poorly understood. For instance, for *Pseudomonas aeruginosa* two systems for surface sensing have been reported. In the first system, the sensing of surface contact by

SadC leads to an increase in the production of the second messenger c-di-GMP, which binds to the transcriptional regulator FleQ. This interaction releases the inhibition of *pel* by FleQ and thus activates polysaccharide synthesis to form a biofilm matrix [79]. In the second system for surface sensing, the Wsp regulatory pathway, a membrane-bound chemoreceptor homolog WspA senses unknown surface signals (postulated to be related to mechanical stress) and phosphorylates WspR, causing an increase in c-di-GMP production and thus biofilm formation [80]. A homolog system is also known in *Pseudomonas fluorescens* F113 [16, 81, 82] and *Pseudomonas putida* [83]. However, these studies are based on sensing of general surface contact. The mechanisms of bacterial response to specific material properties remain to be revealed.

1.7 **Conclusions and perspectives**

The effects of material/surface properties, such as surface charge, hydrophobicity, roughness, topography, and chemistry, on bacterial adhesion and biofilm formation have been investigated for many years. Generally, negatively charged surfaces, super hydrophobic surfaces, super hydrophilic surfaces, and nanometric-submicrometric scale surface roughness have all been shown to reduce bacterial adhesion. This trend is not absolute for all bacteria; however, it provides a general design principle for developing bacteria-resistant surfaces. Some positively charged surfaces exhibit antimicrobial properties, which can be obtained by coating appropriate materials on a substrate. However, bacteria have remarkable strategies to overcome these barriers and develop biofilms. Other limitation of antimicrobial materials is that substrates designed to control bacterial attachment may have effects on one strain of bacteria that may not work for other strains. Besides, the design of surfaces has to accommodate the variety of shapes and sizes of bacteria, which will respond differently to the physical characteristics of surfaces. Considering the remarkable diversity of bacteria in the biosphere, it is difficult to imagine a universal set of guidelines for controlling biofilms, but a combination of these novel techniques with conventional methods (antibiotics, disinfectants, and physical methods) is expected to solve the “biofilm problem” in the near future. The applied technology that emerges in this area of materials science and engineering will open new doors in microbiology for this purpose.

1.8 References

[1] W.G. Characklis, M.H. Turakhia, N. Zelver, Transport and interfacial transfer phenomena, Biofilms, (1990) 265-340.

[2] C. Nicolella, M. Van Loosdrecht, J. Heijnen, Wastewater treatment with particulate biofilm reactors, Journal of biotechnology, 80 (2000) 1-33.

[3] V. Sihorkar, S. Vyas, Biofilm consortia on biomedical and biological surfaces: delivery and targeting strategies, Pharmaceutical research, 18 (2001) 1247-1254.

[4] S. Flint, P. Bremer, J. Brooks, Biofilms in dairy manufacturing plant-description, current concerns and methods of control, Biofouling, 11 (1997) 81-97.

[5] S. Srey, I.K. Jahid, S.-D. Ha, Biofilm formation in food industries: a food safety concern, Food Control, 31 (2013) 572-585.

[6] S. Dobretsov, R.M. Abed, M. Teplitski, Mini-review: Inhibition of biofouling by marine microorganisms, Biofouling, 29 (2013) 423-441.

[7] C.J. W, C. G, S. M, S. P, P. M, *Biomaterials Science*, Elsevier, San Diego, 2004.

[8] L.G. Harris, R.G. Richards, Staphylococci and implant surfaces: a review, Injury, 37 (2006) S3-S14.

[9] R.M. Donlan, J.W. Costerton, Biofilms: survival mechanisms of clinically relevant microorganisms, Clinical microbiology reviews, 15 (2002) 167-193.

[10] M.E. Cortés, J.C. Bonilla, R.D. Sinisterra, Biofilm formation, control and novel strategies for eradication, Sci Against Microbial Pathog Commun Curr Res Technol Adv, 2 (2011) 896-905.

[11] W. Teughels, N. Van Assche, I. Sliepen, M. Quirynen, Effect of material characteristics and/or surface topography on biofilm development, Clinical oral implants research, 17 (2006) 68-81.

[12] B. Jalvo, J. Santiago-Morales, P. Romero, R.G. de Villoria, R. Rosal, Microbial colonisation of transparent glass-like carbon films triggered by a reversible radiation-induced hydrophobic to hydrophilic transition, Rsc Advances, 6 (2016) 50278-50287.

[13] R. Bos, H.C. Van der Mei, H.J. Busscher, Physico-chemistry of initial microbial adhesive interactions–its mechanisms and methods for study, FEMS microbiology reviews, 23 (1999) 179-230.

[14] K. Kogure, E. Ikemoto, H. Morisaki, Attachment of Vibrio alginolyticus to glass surfaces is dependent on swimming speed, Journal of bacteriology, 180 (1998) 932-937.

[15] E. Barahona, A. Navazo, F. Yousef-Coronado, D. Aguirre de Cárcer, F. Martínez-Granero, M. Espinosa-Urgel, M. Martín, R. Rivilla, Efficient rhizosphere colonization by Pseudomonas fluorescens F113 mutants unable to form biofilms on abiotic surfaces, Environmental microbiology, 12 (2010) 3185-3195.

[16] F. Martínez-Granero, A. Navazo, E. Barahona, M. Redondo-Nieto, E.G. De Heredia, I. Baena, I. Martín-Martín, R. Rivilla, M. Martín, Identification of flgZ as a flagellar gene encoding a PilZ domain protein that regulates swimming motility and biofilm formation in Pseudomonas, PloS one, 9 (2014) e87608.

[17] J. Azeredo, J. Visser, R. Oliveira, Exopolymers in bacterial adhesion: interpretation in terms of DLVO and XDLVO theories, Colloids and Surfaces B: Biointerfaces, 14 (1999) 141-148.

[18] Y.F. Dufrêne, H. Vermeiren, J. Vanderleyden, P.G. Rouxhet, Direct evidence for the involvement of extracellular proteins in the adhesion of Azospirillum brasilense, Microbiology, 142 (1996) 855-865.
[19] C. Van Hoogmoed, M. van Der Kuijl-Booij, H. Van der Mei, H. Busscher, Inhibition of Streptococcus mutans NS Adhesion to Glass with and without a Salivary Conditioning Film by Biosurfactant-Releasing Streptococcus mitisStrains, Applied and environmental microbiology, 66 (2000) 659-663.
[20] N.P. Desai, S.F. Hossainy, J.A. Hubbell, Surface-immobilized polyethylene oxide for bacterial repellence, Biomaterials, 13 (1992) 417-420.
[21] N.B. Holland, Y. Qiu, M. Ruegsegger, R.E. Marchant, Biomimetic engineering of non-adhesive glycocalyx-like surfaces using oligosaccharide surfactant polymers, Nature, 392 (1998) 799-801.
[22] F. Song, H. Koo, D. Ren, Effects of material properties on bacterial adhesion and biofilm formation, Journal of dental research, 94 (2015) 1027-1034.
[23] I. Lasa, Towards the identification of the common features of bacterial biofilm development, International Microbiology, 9 (2010) 21-28.
[24] G. O'Toole, H.B. Kaplan, R. Kolter, Biofilm formation as microbial development, Annual Reviews in Microbiology, 54 (2000) 49-79.
[25] J.W. Costerton, P.S. Stewart, E.P. Greenberg, Bacterial biofilms: a common cause of persistent infections, Science, 284 (1999) 1318-1322.
[26] P. Stoodley, P. Dirckx, Biofilm formation in 3 steps, 2003.
[27] L. Hall-Stoodley, P. Stoodley, Developmental regulation of microbial biofilms, Current opinion in biotechnology, 13 (2002) 228-233.
[28] C.D. Nadell, J.B. Xavier, K.R. Foster, The sociobiology of biofilms, FEMS microbiology reviews, 33 (2009) 206-224.
[29] B.L. Bassler, R. Losick, Bacterially speaking, Cell, 125 (2006) 237-246.
[30] L.D. Renner, D.B. Weibel, Physicochemical regulation of biofilm formation, MRS bulletin, 36 (2011) 347-355.
[31] J.T.G. Overbeek, Recent developments in the understanding of colloid stability, Journal of Colloid and Interface Science, 58 (1977) 408-422.
[32] E.J.W. Verwey, J.T.G. Overbeek, J.T.G. Overbeek, Theory of the stability of lyophobic colloids, Courier Corporation1999.
[33] C. Van Oss, R. Good, M. Chaudhury, The role of van der Waals forces and hydrogen bonds in "hydrophobic interactions" between biopolymers and low energy surfaces, Journal of colloid and Interface Science, 111 (1986) 378-390.
[34] M. Katsikogianni, Y. Missirlis, Concise review of mechanisms of bacterial adhesion to biomaterials and of techniques used in estimating bacteria-material interactions, Eur Cell Mater, 8 (2004).
[35] M. Morra, C. Cassinelli, Bacterial adhesion to polymer surfaces: a critical review of surface thermodynamic approaches, Journal of Biomaterials Science, Polymer Edition, 9 (1998) 55-74.
[36] L.A. Goetz, B. Jalvo, R. Rosal, A.P. Mathew, Superhydrophilic anti-fouling electrospun cellulose acetate membranes coated with chitin nanocrystals for water filtration, Journal of Membrane Science, 510 (2016) 238-248.
[37] Y.-F. Zhao, L.-P. Zhu, Z. Yi, B.-K. Zhu, Y.-Y. Xu, Improving the hydrophilicity and fouling-resistance of polysulfone ultrafiltration membranes via surface zwitterionicalization mediated by polysulfone-based triblock copolymer additive, Journal of membrane science, 440 (2013) 40-47.
[38] B.A. Jucker, A.J. Zehnder, H. Harms, Quantification of polymer interactions in bacterial adhesion, Environmental science & technology, 32 (1998) 2909-2915.

[39] M. Hermansson, The DLVO theory in microbial adhesion, Colloids and Surfaces B: Biointerfaces, 14 (1999) 105-119.
[40] A.H. Nobbs, R.J. Lamont, H.F. Jenkinson, Streptococcus adherence and colonization, Microbiology and Molecular Biology Reviews, 73 (2009) 407-450.
[41] C.E. Zobell, D.Q. Anderson, W.W. Smith, The bacteriostatic and bactericidal action of Great Salt Lake water, Journal of bacteriology, 33 (1937) 253.
[42] K. Hori, S. Matsumoto, Bacterial adhesion: from mechanism to control, Biochemical Engineering Journal, 48 (2010) 424-434.
[43] G.C. Wong, G.A. O'Toole, All together now: Integrating biofilm research across disciplines, MRS bulletin/Materials Research Society, 36 (2011) 339.
[44] D. Perera-Costa, J.M. Bruque, M.L. González-Martín, A.C. Gómez-García, V. Vadillo-Rodríguez, Studying the influence of surface topography on bacterial adhesion using spatially organized microtopographic surface patterns, Langmuir, 30 (2014) 4633-4641.
[45] K.A. Whitehead, J. Verran, The effect of surface topography on the retention of microorganisms, Food and bioproducts processing, 84 (2006) 253-259.
[46] J.F. Schumacher, M.L. Carman, T.G. Estes, A.W. Feinberg, L.H. Wilson, M.E. Callow, J.A. Callow, J.A. Finlay, A.B. Brennan, Engineered antifouling microtopographies–effect of feature size, geometry, and roughness on settlement of zoospores of the green alga Ulva, Biofouling, 23 (2007) 55-62.
[47] H.J. Busscher, W. Norde, H.C. Van Der Mei, Specific molecular recognition and nonspecific contributions to bacterial interaction forces, Applied and environmental microbiology, 74 (2008) 2559-2564.
[48] G. Bruinsma, H. Van der Mei, H. Busscher, Bacterial adhesion to surface hydrophilic and hydrophobic contact lenses, Biomaterials, 22 (2001) 3217-3224.
[49] S. Nishimoto, B. Bhushan, Bioinspired self-cleaning surfaces with superhydrophobicity, superoleophobicity, and superhydrophilicity, Rsc Advances, 3 (2013) 671-690.
[50] J.H. Pringle, M. Fletcher, Influence of substratum wettability on attachment of freshwater bacteria to solid surfaces, Applied and Environmental Microbiology, 45 (1983) 811-817.
[51] W. Norde, My voyage of discovery to proteins in flatland… and beyond, Colloids and Surfaces B: Biointerfaces, 61 (2008) 1-9.
[52] D.R. Absolom, F.V. Lamberti, Z. Policova, W. Zingg, C.J. van Oss, A.W. Neumann, Surface thermodynamics of bacterial adhesion, Applied and environmental microbiology, 46 (1983) 90-97.
[53] C.A. Davidson, C.R. Lowe, Optimisation of polymeric surface pre-treatment to prevent bacterial biofilm formation for use in microfluidics, Journal of Molecular Recognition, 17 (2004) 180-185.
[54] A. Fujishima, X. Zhang, Titanium dioxide photocatalysis: present situation and future approaches, Comptes Rendus Chimie, 9 (2006) 750-760.
[55] K.A. Soni, A.K. Balasubramanian, A. Beskok, S.D. Pillai, Zeta potential of selected bacteria in drinking water when dead, starved, or exposed to minimal and rich culture media, Current microbiology, 56 (2008) 93-97.
[56] M. Katsikogianni, Y. Missirlis, Interactions of bacteria with specific biomaterial surface chemistries under flow conditions, Acta biomaterialia, 6 (2010) 1107-1118.
[57] Y. Hong, D.G. Brown, Electrostatic behavior of the charge-regulated bacterial cell surface, Langmuir, 24 (2008) 5003-5009.
[58] D. Campoccia, L. Montanaro, C.R. Arciola, A review of the biomaterials technologies for infection-resistant surfaces, Biomaterials, 34 (2013) 8533-8554.

[59] O. Rzhepishevska, S. Hakobyan, R. Ruhal, J. Gautrot, D. Barbero, M. Ramstedt, The surface charge of anti-bacterial coatings alters motility and biofilm architecture, Biomaterials Science, 1 (2013) 589-602.
[60] D.P. Bakker, F.M. Huijs, J. de Vries, J.W. Klijnstra, H.J. Busscher, H.C. van der Mei, Bacterial deposition to fluoridated and non-fluoridated polyurethane coatings with different elastic modulus and surface tension in a parallel plate and a stagnation point flow chamber, Colloids and Surfaces B: Biointerfaces, 32 (2003) 179-190.
[61] J.A. Lichter, M.T. Thompson, M. Delgadillo, T. Nishikawa, M.F. Rubner, K.J. Van Vliet, Substrata mechanical stiffness can regulate adhesion of viable bacteria, Biomacromolecules, 9 (2008) 1571-1578.
[62] N. Saha, C. Monge, V. Dulong, C. Picart, K. Glinel, Influence of polyelectrolyte film stiffness on bacterial growth, Biomacromolecules, 14 (2013) 520-528.
[63] C. Guegan, J. Garderes, G. Le Pennec, F. Gaillard, F. Fay, I. Linossier, J.-M. Herry, M.-N.B. Fontaine, K.V. Réhel, Alteration of bacterial adhesion induced by the substrate stiffness, Colloids and Surfaces B: Biointerfaces, 114 (2014) 193-200.
[64] F. Song, D. Ren, Stiffness of cross-linked poly (dimethylsiloxane) affects bacterial adhesion and antibiotic susceptibility of attached cells, Langmuir, 30 (2014) 10354-10362.
[65] C. Chaiwong, P. Rachtanapun, P. Wongchaiya, R. Auras, D. Boonyawan, Effect of plasma treatment on hydrophobicity and barrier property of polylactic acid, Surface and Coatings Technology, 204 (2010) 2933-2939.
[66] C.H. Park, S.Y. Lee, D.S. Hwang, D.W. Shin, D.H. Cho, K.H. Lee, T.-W. Kim, T.-W. Kim, M. Lee, D.-S. Kim, Nanocrack-regulated self-humidifying membranes, Nature, 532 (2016) 480-483.
[67] B. Bhushan, Y.C. Jung, Natural and biomimetic artificial surfaces for superhydrophobicity, self-cleaning, low adhesion, and drag reduction, Progress in Materials Science, 56 (2011) 1-108.
[68] S. Banerjee, J. Gopal, P. Muraleedharan, A. Tyagi, B. Raj, Physics and chemistry of photocatalytic titanium dioxide: visualization of bactericidal activity using atomic force microscopy, Current Science, 90 (2006) 1378-1383.
[69] Y. Cai, M. Strømme, Å. Melhus, H. Engqvist, K. Welch, Photocatalytic inactivation of biofilms on bioactive dental adhesives, Journal of Biomedical Materials Research Part B: Applied Biomaterials, 102 (2014) 62-67.
[70] P. Dunlop, C. Sheeran, J. Byrne, M. McMahon, M. Boyle, K. McGuigan, Inactivation of clinically relevant pathogens by photocatalytic coatings, Journal of Photochemistry and Photobiology A: Chemistry, 216 (2010) 303-310.
[71] A. Dasari, J. Quirós, B. Herrero, K. Boltes, E. García-Calvo, R. Rosal, Antifouling membranes prepared by electrospinning polylactic acid containing biocidal nanoparticles, Journal of Membrane Science, 405 (2012) 134-140.
[72] J. Quiros, K. Boltes, S. Aguado, R.G. de Villoria, J.J. Vilatela, R. Rosal, Antimicrobial metal-organic frameworks incorporated into electrospun fibers, Chemical Engineering Journal, 262 (2015) 189-197.
[73] M. Benhabiles, R. Salah, H. Lounici, N. Drouiche, M. Goosen, N. Mameri, Antibacterial activity of chitin, chitosan and its oligomers prepared from shrimp shell waste, Food hydrocolloids, 29 (2012) 48-56.
[74] X. Zhang, S. Wan, J. Pu, L. Wang, X. Liu, Highly hydrophobic and adhesive performance of graphene films, Journal of Materials Chemistry, 21 (2011) 12251-12258.

[75] Z. Xu, Z. Ao, D. Chu, A. Younis, C.M. Li, S. Li, Reversible hydrophobic to hydrophilic transition in graphene via water splitting induced by UV irradiation, Scientific reports, 4 (2014).
[76] N. Balaban, T. Goldkorn, Y. Gov, M. Hirshberg, N. Koyfman, H.R. Matthews, R.T. Nhan, B. Singh, O. Uziel, Regulation of *Staphylococcus aureus* pathogenesis via target of RNAIII-activating protein (TRAP), Journal of Biological Chemistry, 276 (2001) 2658-2667.
[77] D.M. Yebra, S. Kiil, K. Dam-Johansen, Antifouling technology—past, present and future steps towards efficient and environmentally friendly antifouling coatings, Progress in organic Coatings, 50 (2004) 75-104.
[78] A. Roosjen, W. Norde, H.C. van der Mei, H.J. Busscher, The use of positively charged or low surface free energy coatings versus polymer brushes in controlling biofilm formation, Characterization of polymer surfaces and thin films, Springer2006, pp. 138-144.
[79] J.W. Hickman, C.S. Harwood, Identification of FleQ from Pseudomonas aeruginosa as ac-di-GMP-responsive transcription factor, Molecular microbiology, 69 (2008) 376-389.
[80] R. Belas, Biofilms, flagella, and mechanosensing of surfaces by bacteria, Trends in microbiology, 22 (2014) 517-527.
[81] A. Navazo, E. Barahona, M. Redondo-Nieto, F. Martínez-Granero, R. Rivilla, M. Martín, Three independent signalling pathways repress motility in Pseudomonas fluorescens F113, Microbial biotechnology, 2 (2009) 489-498.
[82] F. Martínez-Granero, A. Navazo, E. Barahona, M. Redondo-Nieto, R. Rivilla, M. Martín, The Gac-Rsm and SadB signal transduction pathways converge on AlgU to downregulate motility in Pseudomonas fluorescens, PLoS One, 7 (2012) e31765.
[83] M. Martínez-Gil, M.I. Ramos-González, M. Espinosa-Urgel, Roles of cyclic di-GMP and the Gac system in transcriptional control of the genes coding for the *Pseudomonas putida* adhesins LapA and LapF, Journal of bacteriology, 196 (2014) 1484-1495.

Objectives

The objective of the work proposed for this Doctoral Thesis is the understanding and manipulation, in a molecular scale, of the hydrophilic / hydrophobic behavior of surfaces of different materials and their influence on microbial colonization and biofilm formation. Carbon surfaces, titanium dioxide and electrospun polymers are investigated to determine the influence of UV and solar radiation on the surfaces, and the role they play in bacterial colonization using strains of opportunistic bacteria such as *Escherichia coli*, *Pseudomonas putida* and *Staphylococcus aureus*. The biocompatibility of the surface and the extent of biofilm formation will be evaluated for this purpose.

Attention will be given to self-cleaning materials based on nanostructured titanium dioxide, which will be exposed to simulated solar radiation in order to determine how surface characteristics influence the formation of biofilms and, in particular, it is possible to achieve an efficient self-cleaning capacity and not only an inhibition of the initial stage of bacterial colonization. To do this, conventional coating techniques and a coating type based on the electrospray technique to produce TiO_2 coated surfaces from suspensions prepared by the sol-gel process will be used. TiO_2 will be used for different coverage densities, different base materials and dark-light cycles representative of various environmental conditions.

As regards the preparation of membranes resistant to biological soiling, electrospun materials coated with cellulose and chitin nanocrystals will be prepared either by electrospinning plus impregnation or by coaxial spinning. The approach consists of combining membranes based on renewable materials in order to produce high efficiency filters provided with a specific surface coating. The location of cellulose and chitin nanocrystals in the outer layer of the fibers that make up the membrane aims to modify the surface properties of the membrane to improve water permeability and resistance to fouling and biofilm formation.

Chapter 2:

Microbial colonization of transparent glass-like carbon films

2 Microbial colonization of transparent glass-like carbon films triggered by a reversible radiation-induced hydrophobic to hydrophilic transition

2.1 **Introduction**

Controlling cell-material interactions is essential in many expanding applications such as the production of antimicrobial surfaces or biocompatible materials. It has been shown that surface topography and physicochemical properties determine cell adhesion and proliferation [1,2]. The adhesion of microorganisms on natural or synthetic surfaces is a critical issue in many important fields, such as the fight against human infections and pathogen control during food processing and storage [3,4]. Microbial adhesion is detrimental when associated with the dissemination of pathogens, but can be also beneficial, for example for the production of wastewater treatment bioreactors or for biopolymer degradation [5]. Once attached to a surface, bacteria form biofilms consisting of cells immobilized cells embedded in a polymeric matrix of microbial origin. Biofilms are complex biological communities characterized by cells with an altered phenotype that create their own environment [6]. The prevention of biofilms and the enhancement of biocompatibility are closely interconnected goals that require a deep understanding of surface physicochemistry [7].

Tailoring hydrophilicity has been shown to be important in a range of biomedical uses, such as the creation of nano-bio interfaces for molecular medicine [8]. These applications usually require surface modifications that enhance hydrophilicity in order to allow cellular attachment and growth, and these are frequently accomplished by decoration with chemical functionalities such as hydroxyl or carboxylic acid groups [9]. Particular attention has been paid to systems in which a reversible hydrophobic-hydrophilic transition is triggered by external stimuli such as electrical potential or irradiation [10,11]. Several materials display reversible wettability upon ultraviolet (UV) irradiation. In particular, metal oxides switch between hydrophobicity and hydrophilicity due to the adsorption of water molecules that photo-dissociate to generate surface hydroxyl groups [12].

Several carbon-based materials also display reversible hydrophobic-hydrophilic transition. Graphene undergoes switching between hydrophobic and hydrophilic states upon application of an electric field, which reduces the energy barrier for dissociative adsorption of water [13]. The reversible wettability transition of carbon nanotube films upon UV exposure has been attributed to the formation of hydrophilic groups upon chemisorption of oxygen [11]. Graphene also becomes temporarily hydrophilic when irradiated [14,15]. These results suggest that hydrophilicity could be induced by the dissociative adsorption of oxygen or water molecules [14,15]. A similar behavior of graphene oxide has been attributed to reversible deoxygenation of the graphene oxide surface [16]. This phenomenon is largely, but not entirely superficial, as it has been shown that surface modification of graphene is only independent on substrate properties in films of more than about six layers [17].

Molecular-scale understanding and manipulation of the wetting behavior of carbon-based surfaces is still unclear and poses fundamental and practical challenges [18,19]. In this study, we investigated the influence of a radiation-induced wetting transition on the bacterial colonization of a carbonaceous surface using a strain of the opportunistic bacteria *E. coli* and assessing irradiation-triggered surface biocompatibility and biofilm formation. Furthermore, we examined an aspect that has received insufficient research attention to date, namely the spectral distribution of ultraviolet radiation using well-defined sources. Although it is well known that conventional low-pressure mercury-vapor 254 nm lamps emit a significant fraction of their power in the vacuum ultraviolet, this fact is generally overlooked in the literature. We used glass-like carbon films, which belong to a family of disordered carbons such as diamond-like or glassy carbon films, for which no data have been reported to date. In this regard, disordered carbons are easier to produce and manipulate than monolayer graphene, and consequently their use in real applications would be more feasible.

2.2 **Materials and methods**

2.2.1.1 Synthesis of the carbon films

A commercial copper foil was used as catalyst for chemical vapor deposition (CVD) of carbon films (100µm-thick copper foil, 99.8 % purity, Sigma Aldrich) following a process similar to that used to produce CVD graphene [20]. Pristine copper foils were cut into pieces measuring 22 x 50 mm^2 and cleaned in a pure ethanol ultrasound bath for 10

minutes. The foils were then air-dried. We used a custom-made CVD reactor consisting of a longitudinal mobile tubular furnace that allowed fast heating/cooling rates [21], and three gas lines (Ar, H_2 and C_2H_4) connected to a 22 mm diameter quartz tube. First, the lines were flushed with Ar to displace the air inside the tube, maintaining the copper foil outside the furnace heating zone. Then, the furnace was heated to the synthesis temperature (850 °C) with a flow of 1000/20 sccm Ar/H_2, maintaining the sample outside the heating zone. Once the temperature had stabilized, the furnace was rapidly moved (*ca*. 3s) to situate the center of the heating zone exactly in the copper foil position. Annealing was performed for 10 min with 1000/20 sccm of Ar/H_2. A gas mixture of 500/20/20 sccm of Ar/H_2/C_2H_4 was used in the next step for carbon film synthesis, which took 5 min. Finally, the furnace was moved back away from the sample to enable rapid cooling under an argon flow. Further details on the experimental procedure for producing carbon films can be found elsewhere [22].

During the CVD process, a carbon film of ca. 5 nm thick was deposited on top of the copper foil. Next, the carbon film was transferred to a thin polymer film following conventional PMMA-assisted transfer [23,24]. First, the carbon film/copper was gently flattened using two clean glass holders. Three drops of a PMMA solution (495PMMA A Resists, Microchem) were homogeneously distributed on top of the carbon film/copper using a laboratory weighing paper to level the liquid PMMA solution. We waited for two hours to allow the solvent to evaporate and then repeated the process two more times. Once the PMMA had dried under ambient conditions, the PMMA/carbon film/copper sandwich structure was placed in a $FeCl_3$–HCl copper etching solution (Sigma Aldrich 667528) with the PMMA face-down. After 2 h, the copper etchant was replaced with a fresh one, and etching continued for a further 24 h. Copper etchant was cleaned 5 times with deionised water and the sample was maintained in a deionized water bath for 24 h. After the cleaning process, PMMA/films were recovered with glass holders. We did not remove the PMMA, but used it as a support for the carbon films to perform the experiments described below. The 22 x 50 mm^2 sample was cut into slices with a stainless steel blade (approximately 10 x 15 mm), and these were submerged in new deionized water and placed on cover glasses (0.13-0.16 mm thickness, Labbox) with the carbon film facing up and the PMMA in contact with the cover glass. The samples were dried in a vacuum oven at 50 °C for 2 h.

2.2.1.2 Characterization of the carbon films

As synthesized carbon film on copper foil was dipped in $FeCl_3$–HCl copper etching solution (Sigma Aldrich, 667528) and detached in the form of flakes, which were cleaned several times with deionized water. The carbon flakes were then transferred onto a thermal oxide wafer (300 nm SiO_2 on Si) for both atomic force microscopy (AFM) and Raman measurements. AFM characterization and details of surface topography details are described in the Supplementary Information. Raman spectra of the carbon film were collected from the top of the wafers (Jasco, NRS-5100). At least three measurements per synthesis condition were taken, using a Nd:YAG green laser (532 nm, aperture: 4000 μm, grating: 1800 l/mm, slit: 200×1000 μm, resolution: 7.42 cm^{-1}), with two accumulations of 20 s exposure in a range of 1000–3250 cm^{-1} (laser power 5.3 mW). We compared the Raman spectra of our carbon films with monolayer graphene on a silicon wafer (Graphenea). Lastly, several carbon flakes were transferred onto a copper grid for analysis under a transmission electron microscope (JEOL JEM 3000F).

Carbon films wettability was tested as soon as possible before and after irradiation employing an optical contact angle meter (Krüss DSA25 Drop Shape Analysis System) at room temperature using the sessile drop technique. To measure bacterial hydrophobicity, bacterial surfaces for measuring contact angles were prepared by collecting bacterial cells on a cellulose acetate filter (pore diameter, 0.45 μm, MicronSep Cellulosic, Thomas Scientific) to a density of 10^8 cells per mm^2. Filters with a continuous bacterial layer were mounted on glass slides and dried for 15 to 60 min. Then, we measured the contact angle of drops of purified water on the bacterial surface. No change in contact angle occurred between 15 and 60 min. Samples were placed on the test cell and drops of purified water, glycerol and diiodomethane were gently deposited on the surfaces using a built-in delivery syringe. Contact angle measurements for each surface were taken at 20 °C in at least three different positions for each solvent.

The Lifshitz–van der Waals (LW), electron donor (−) and electron acceptor (+) components of the surface tension were estimated from CA values for water, glycerol and diiodomethane according to the following expression in which the free energy of interaction between a solid, S, and a liquid, L, can be obtained from pure liquid contact angles, θ [30]:

$$\Delta G_{SL} = -(1+\cos\theta)\,\gamma_L = -2\left(\sqrt{\gamma_S^{LW}\gamma_L^{LW}} + \sqrt{\gamma_S^{+}\gamma_L^{-}} + \sqrt{\gamma_S^{-}\gamma_L^{+}}\right) \quad (1)$$

In this approach, the total surface free energy (γ) is the sum of the non-polar Lifshitz-van der Waals component (γ^{LW}) and the acid-base component (γ^{AB}), which in turn comprises two non-additive parameters: the electron-acceptor (γ^{+}) and the electron-donor (γ^{-}) surface tension parameters. Eq. (1) contains the three components of the solid surface free energy, γ_S^{LW}, γ_S^{+} and γ_S^{-}, as unknowns, which can be solved by measuring the CA with three liquids. The components of the liquid surface free energy, γ_L^{LW}, γ_L^{+} and γ_L^{-}, for the probe liquids are available in the literature for a number of pure substances [26].

According to Van Oss, the total interfacial tension between the solid film and water, γ_{SL}, can be expressed as follows [32]:

$$\gamma_{SL} = \left(\sqrt{\gamma_S^{LW}} - \sqrt{\gamma_L^{LW}}\right)^2 + 2\left(\sqrt{\gamma_S^{+}\gamma_S^{-}} + \sqrt{\gamma_L^{+}\gamma_L^{-}} - \sqrt{\gamma_S^{+}\gamma_L^{-}} - \sqrt{\gamma_L^{+}\gamma_S^{-}}\right) \quad (2)$$

In addition, the free energy of interaction between two identical surfaces, S, immersed in a liquid, L, is:

$$\Delta G_{SLS} = -2\gamma_{SL} \quad (3)$$

The energy of interaction, ΔG_{SLS}, gives a direct measure of the hydrophobicity or hydrophilicity of the surface. When $\Delta G_{SLS} > 0$, the surface is hydrophilic, and when $\Delta G_{SLS} < 0$, it is hydrophobic.

Surface zeta potential (ζ potential) was measured via electrophoretic light scattering (DLS, Malvern Zetasizer Nano ZS) and using the surface zeta potential cell (ZEN 1020) from Malvern. In brief, a rectangular section no larger than 7 mm x 4 mm was glued onto the sample holder using Araldite adhesive. The cell was inserted into a disposable plastic 10 mm square cuvette containing 1.2 mL of 10 mM KCl (pH 7.0) aqueous solution, with 0.5 % (w/w) polyacrylic acid (450 kDa) as a tracer (a negatively charged tracer is required for negatively charged surfaces). Measurements were performed, before and after irradiation, at 25 °C at six different displacements from the sample surface, which enabled the surface zeta potential to be calculated by Zetasizer software. The pH was adjusted using 1M KOH and 1 M HCl.

2.2.1.3 Irradiation

UV irradiation of glass-like carbon films was performed at 20 °C. Prior to irradiation, carbon films were heated at 50 °C for 2h under a vacuum of 10 kPa. The equipment used for irradiating carbon films was as follows. (1) A 15 W Heraeus Noblelight TNN 15/32 low-pressure mercury vapor lamp emitting at 254 nm with a secondary peak at 185 nm. This lamp uses synthetic quartz, which is transparent to the vacuum ultraviolet emission at 185 nm (5 % of the radiant power). Using hydrogen peroxide actinometry, we determined that lamp irradiance was 18.7 mW cm^{-2}. (2) A Vilber-Lourmat Bio-Link BLX-254 Crosslinker equipped with 5 x 8 W 254 nm T-8C lamps. These lamps are "ozone-free", meaning that the quartz they are made of absorbs most of the 185 nm emission line. Irradiance at 15 cm, in the lower part of the chamber, was 820 μW cm^{-2}. (3) An FQSS 266-200 diode pumped passively Q-switched solid-state laser (CryLas, Germany) emitting pulses (< 1.5 ns) at 266 nm > 200 μJ at 20 MHz. The irradiance for a given set of conditions was determined by means of a LOT-Oriel LSZ014 radiant power meter with a spectral range of 0.19 to 25 μm connected to a Gentec-EO Tuner monitor. To investigate the effects of humidity, a sufficient amount of distilled water at 85 °C was placed in the UV chamber or in a structure enclosing the irradiation space, which made it possible to maintain ~80 % RH throughout the experiment. In all cases, the temperature was maintained at 20 °C ± 2 °C. At least 5 min preconditioning was applied before irradiation.

2.2.1.4 Bacterial bioassays

Escherichia coli cells (CECT 516) were grown overnight at 37 °C in nutrient agar medium (for 1 L solution in distilled water: 5 g beef extract, 10 g peptone, 5 g NaCl and for solid media 15 g agar powder with pH adjusted to 7.2), while shaking. After reactivation, cell density was tracked by measuring optical density (OD) at 600 nm. Exponentially growing cultures on nutrient medium were diluted to an OD_{600} of 0.04, and 150 μL was placed on a carbon film inside 24-well polystyrene plates and incubated for 18 h at 30 °C without shaking. After incubation and liquid culture removal, films were carefully washed with distilled water.

The Live/Dead BacLight Bacterial Viability Kit (Molecular Probes, Invitrogen Detection Technologies, Carlsbad, CA, USA) was used to evaluate bacterial viability. Under live/dead staining all cells exhibit green fluorescence (SYTO 9), whereas nonviable

bacterial cells display red fluorescence (Propidium iodide, PI) with dye uptake depending upon cell membrane integrity. Films were stained with 10□□L BacLight stain (a mixture of SYTO 9 and PI in DMSO) according to the manufacturer's recommendations, and incubated in the dark for 15 min at room temperature. For matrix visualization, biofilms were also stained with 200 μL Film Tracer SYPRO Ruby Biofilm Matrix Stain (Molecular Probes, Invitrogen) per film, incubated in the dark for 30 min at room temperature, and then rinsed with distilled water. After incubation, films were transferred to a glass slide, covered with a glass cover slip and sealed. All images were acquired at 18 h after inoculation in the microdevice using a Leica Microsystems Confocal SP5 fluorescence microscope (Leica Microsystems, Germany). For green fluorescence (SYTO 9), excitation was performed at 488 nm (Ar) and emission was recorded at 500-575nm. For red fluorescence (PI, dead cells), the excitation/emission wavelengths were 561 nm (He-Ne) and 570-620 nm, respectively. For SYPRO Ruby Biofilm Matrix Stain the excitation/emission wavelengths were 450 nm and 610 nm respectively. A modification of Fletcher's method was used for biofilm quantification[33]. Approximately 200 μL of a crystal violet 0.1 % solution was extended over the washed film surface and incubated for 15 min in order to stain adhered cells. Excess stain was eliminated by rinsing with water. Plates were air-dried and 1 mL of 95 % ethanol was added to each well in order to extract crystal violet from cells. Distaining was performed overnight while gently shaking. Lastly, the dye was measured at OD_{590}. Measurements were taken three times for each experimental condition.

2.2.2 Results and discussion

2.2.2.1 Physical characterization of carbon films

The physical characterization results are presented in Figure 2.1. The carbon films were composed of semi-continuous curved crystallites of about 5 nm in an amorphous carbon matrix (Figure 2.1a), which resembled the curved graphene fragments that form glass-like carbons [25, 26]. The Raman spectra, which are compared to monolayer graphene in Figure 2.1b, revealed a certain degree of disorder due to the increase in D peak at 1350 cm-1, G band broadening, the presence of a D″ band (ca. 1100 cm–1) and additional peaks at about 1240 and 1480 cm-1 [27]. The combination of these modes produced the D+D″ band at 2450 cm^{-1} and D+D′ at 2950 cm^{-1}. D and D´ overtones at 2D 2700 cm^{-1} and 2D′ at 3250 cm^{-1} also broadened in disordered graphites [28,29].

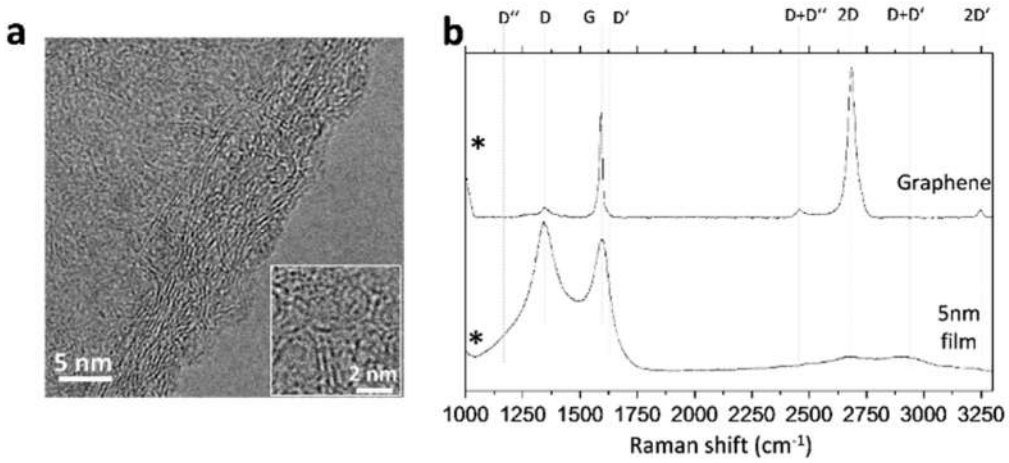

Figure 2.1. Transmission electron micrograph of a 5-nm-thick carbon film (a) and Raman spectra of CVD glass-like carbon films compared to monolayer graphene (b).

2.2.2.2 Wettability and the effect of radiation sources

Reversible hydrophobic-hydrophilic transition of transparent glass-like carbon films was achieved using UV irradiation from three different sources: (1) a low-pressure mercury lamp emitting at 254 nm with a secondary peak at 185 nm, representing about 5 % of the radiant power; (2) a crosslinker chamber equipped with "ozone-free" lamps, which have a tube that absorbs most of the 185 nm emission line and (3) a diode pumped solid-state laser emitting pulses at 266 nm. Low-pressure mercury vapor lamps emitting VUV light of 185 nm can photolyse water molecules into hydrogen atoms and hydroxyl radicals. Ozone-free lamps also have this capacity, although weaker. The reason for using multiple irradiating devices was to determine the effect of vacuum ultraviolet (VUV) water-splitting emission, which is usually overlooked. The laser emits pure 266 nm without any line in the vacuum ultraviolet (VUV), while sources (1) and (2) have high and residual 185 nm lines, respectively. Figure 2.2 shows the effect of irradiation at different UV doses on the water CA measured in transparent glass-like carbon films. Each sample was preconditioned under vacuum (10 kPa, 50 °C) for 2 h prior to irradiation. A set of samples were measured at 30 % ± 5 % RH, identified in what follows as "dry" conditions. A parallel set of films were irradiated under wet air (80 % ± 5 % RH), which was obtained by placing cups containing water at 85 °C into the irradiation space. In this case, carbon films were preconditioned under wet air for at least 10 min before irradiation. Water CA decreased upon irradiation from 99.0° ± 3.4° up to 22.8° ± 2.5°, which was the lowest CA obtained and corresponded to films irradiated with the 185+254 nm low-pressure mercury lamp. When using the 185-254 lamp, water CA initially decreased sharply from pre-

irradiation values until stabilizing after 4-5 min. The decrease in hydrophobicity was much slower when using the irradiation chamber, taking about 8 hours to reach a plateau. No significant effect was observed for irradiation using the 266 nm solid-state laser. The differences obtained for this device were essentially within the boundaries of experimental error. Water CA for the 185+254 lamp reached considerably lower values than those obtained using the irradiation chamber. The difference between the synthetic quartz VUV emitting lamp and the "ozone free" irradiation of the chamber amounted to ~23° in wet air. It is noteworthy that with UV doses of 5 or 25 J/m^2, the hydrophobic states changed to hydrophilic ones depending on whether the irradiation was performed with the low-pressure mercury lamp or the irradiation chamber.

After reaching maximum hydrophilicity, corresponding to the water CA plateau shown in Figure 2.2, glass-like carbon films were stored under laboratory conditions (1 atm, 20 °C) to investigate the recovery of hydrophobicity. The results are shown in Figure 2.3, where zero time represents the end of irradiation and the first measurement was performed after 1 h. During the first 24 h following irradiation, the samples recovered most of their hydrophobicity, with contact angle values increasing up to the 81°-89° range. After 24 h, all samples displayed a water CA > 90°, close to the values of non-irradiated carbon films. The water CA of irradiated samples completely restored to the initial level by storing samples for sufficient time under ambient conditions.

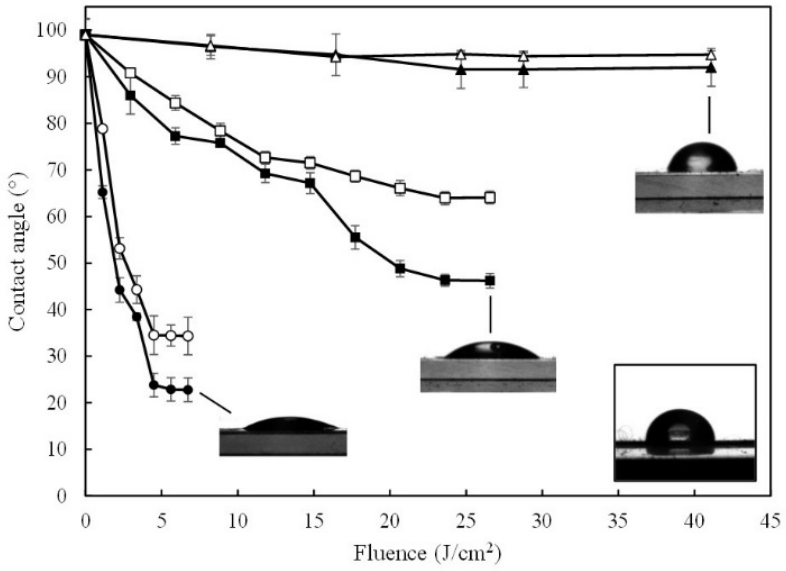

Figure 2.2. Water contact angles of transparent glass-like carbon films for different irradiation devices and UV doses. Low-pressure mercury lamp (○, ●), irradiation chamber (□, ■), laser (△, ▲). Empty symbols: dry air (~ 30 % RH), filled symbols: wet air (~ 80 % RH). Inset: glass-like carbon after vacuum treatment and before irradiation.

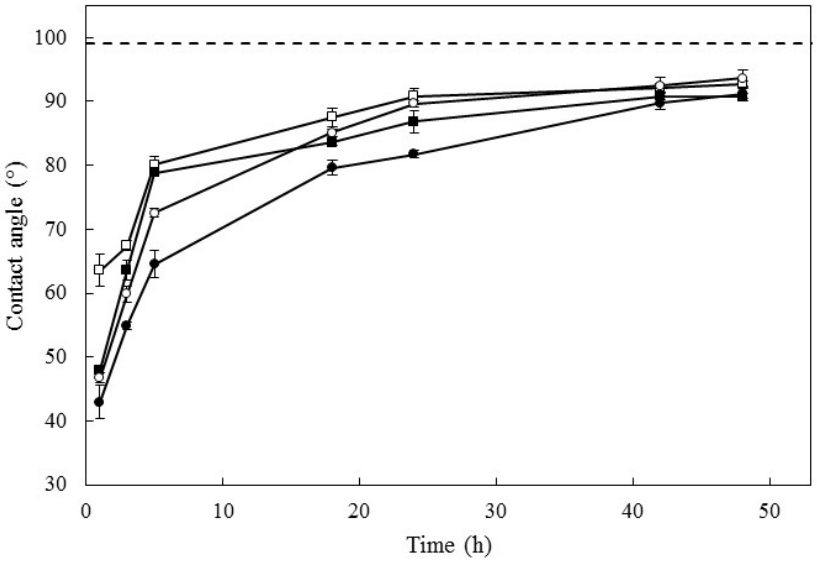

Figure 2.3. Evolution of water contact angles of irradiated carbon films for different times under ambient conditions. Low-pressure mercury lamp (○, ●), irradiation chamber (□, ■), laser (△, ▲). Empty symbols: dry air (~ 30 % RH), filled symbols: wet air (~ 80 % RH).

The CA values for water, glycerol and diiodomethane are shown in Table 2.1. In the case of bacteria, the measurements were performed on bacterial lawns deposited on cellulose acetate filters as described elsewhere [34]. The surface zeta potential was determined using the surface zeta potential cell described above and measuring the particle mobility of a tracer at several distances away from the surface. Figure 2.4 shows the surface zeta potential values for glass-like carbon films, vacuum preconditioned glass-like carbon, and samples irradiated in low and high RH air with the lamp and the irradiation chamber. In all cases, the surfaces were negatively charged, with the highest negative value corresponding to dry-irradiated samples (-54 mV) irrespective of the irradiation device. Samples irradiated in wet air reached a surface potential of -47 mV, whereas non-irradiated carbon films displayed a zeta potential of -41 mV. Although small, these differences were statistically significant, and could be due to the absorption of ultraviolet radiation by water molecules along the path.

Table 2.1. Surface characterization by means of contact angle measurements

Surface	θ_{water}	$\theta_{glycerol}$	$\theta_{diiodomethane}$
gC	82.3 ± 0.3	80.0 ± 3.3	44.4 ± 2.4
gC + vacuum*	97.7 ± 3.0	83.9 ± 3.7	36.3 ± 3.1
gC irradiated (dry)**	36.1 ± 0.5	68.6 ± 0.6	67.8 ± 1.3
gC irradiated (wet)**	23.6 ± 2.4	62.6 ± 3.2	68.0 ± 1.8
E. coli	16.7 ± 1.3	44.0 ± 3.5	58.7 ± 0.5

* 2 h, 50 °C, 10 kPa,
** Lamp 185+254 nm, 5 min.

Wettability transition in irradiated amorphous carbon materials has been considered a consequence of changes in surface topography. Carbon films have been shown to display important differences in wettability, switching from hydrophilicity to super-hydrophobicity, determined by a combination of morphology and carbon state features [18]. Work performed with carbon nanotube films suggests that oxygen chemisorption would lead to hydrophilic surface moieties, such as hydroxyl groups, which are mainly located at lattice defects [35]. Water molecules would physically adsorb at these sites, preferentially filling the apertures in rough surfaces, which results in a reduced water contact angle. The surface can even reach a superhydrophilic state. Reversibility can be explained by desorption of surface water, which is gradually replaced by oxygen molecules [11]. The induction of surface defects by irradiation or other treatments has been proposed as a starting point for dissociative adsorption of water and for inducing wettability transition in graphene films [14]. Carbon nanotube films reach superhydrophilicity, whereas graphene and amorphous carbon films, including those used in this study, give rise to moderately hydrophilic surfaces. The differing extent of hydrophilicity obtained during the treatment of different materials could be a consequence of the varying surface roughness of the irradiated materials. Carbon nanotube films, which exhibit multiscale surface roughness, can become superhydrophilic, whereas smoother surfaces such as graphene and amorphous carbon films yield moderately hydrophilic surfaces.

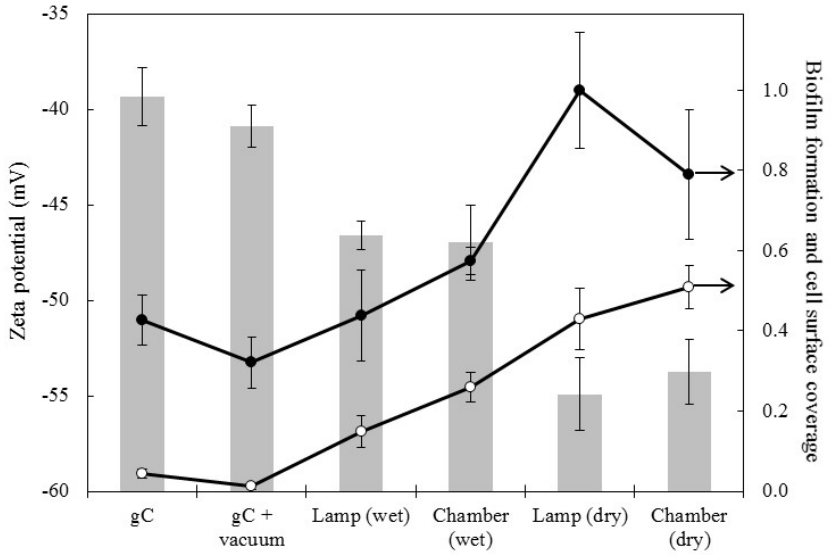

Figure 2.4. Surface zeta potential (bars, expressed in mV), bacterial colonization (lines) measured using the crystal violet method in units relative to their maximum value (lamp irradiation in dry air, •) and fractional surface coverage by metabolically active bacteria (from live/dead staining, ○).

The wettability transition for graphene has been simulated using Raman spectroscopy, suggesting that the dissociative adsorption of water could take place on a graphene surface under 254 nm irradiation [15]. However, the first gas-phase O-H bond scission, corresponding to the formation of the radicals HO and H, amounts to 497.1 kJ/mol or 5.15 eV [36]; consequently, the VUV line at 185 nm (6.70 eV) can split the water molecule, but the 254 nm UV-C radiation, equivalent to 4.88 eV, cannot dissociate it. On the other hand, the energy barrier for the dissociative adsorption of water on graphene is 3.455 eV, after which HO and H move to sites on top of carbon atoms, yielding a final structure that gives rise to an energy release of 0.921 eV. Because of this, the total energy balance for the dissociative adsorption of water on a graphene surface is 2.534 eV [13]. Therefore, it is energetically possible that interaction with a carbon sp2 surface will enable 254 nm radiation to split water, but it is not clear whether the transition could actually take place using monochromatic radiation because the experiments performed to date have used 185 nm emitting lamps [14, 15].

Our irradiation devices made it possible to determine the effect of 185 nm irradiation. The rapid increase in wettability under lamp (185+254 nm) irradiation and the complete lack of effect of the 266 nm solid-state laser setup (Figure 2.2) together suggest a determining role of VUV emission in creating hydroxyl radicals from water. These hydroxyl radicals would interact with the carbon film surface giving rise to the hydrophilic moieties responsible for the lower water CA of irradiated samples. Previous results have shown that an oxygen-rich environment does not enhance the hydrophilic transition, indicating that the oxidation of carbon atoms or vacancies by ozone produced upon VUV irradiation does not take place [15]. In addition, the reverse of the dissociative adsorption of water on carbon surface is energetically favoured, which is compatible with the reversible wettability transition observed in this study for glass-like carbon films (Figure 2.3) and in graphene by others [14,15].

CA values provided information about the hydrophobicity of surfaces. For non-irradiated glass-like carbon films, water CA was always > 80°, indicating a relatively hydrophobic surface. Upon irradiation, CA dropped to 20°-40° indicating a hydrophilic nature. In agreement with previously published data, the surface of *E. coli* cell lawns was clearly hydrophilic [37]. Table 2.2 gives the values of surface energy components for irradiated and non-irradiated films and bacterial lawns. The value observed for total solid-liquid interfacial energy, γ_S, was 39.7 mJ/m^2 for vacuum preconditioned glass-like carbon films.

This figure is relatively close to the surface energy reported for graphene, 46.7 mJ/cm^2, and lower than the 54.8 mJ/cm^2 and 62.1 mJ/m^2 reported for graphite and graphene oxide, respectively [38]. However, surface free energies for graphene are somewhat controversial. Kozbial *et al.* reported 53.0-63.8 mJ/m^2 (depending on the model used) with values fluctuating with the adsorption of airborne hydrocarbons and the wetting transparency effect [39].

Table 2.2. Surface energy components of glass-like carbon films and bacteria (mJ/m^2)

Surface	γ_S^{LW}	γ_S^+	γ_S^-	γ_S^{AB}	γ_S	ΔG_{SLS}
gC	35.4	0.02	5.8	0.7	36.2	-55.1
gC+vacuum*	39.6	0.02	0	0.1	39.7	-100.5
gC irradiated (dry)**	23.4	0	69.0	0	24.6	64.7
gC irradiated (wet)**	23.9	0.01	82.2	1.3	24.6	80.5
E. coli	29.4	1.5	63.2	19.1	48.5	43.4

* 2 h, 50 °C, 10 kPa
** Lamp 185+254 nm, 5 min.

2.2.2.3 Hydrophilicity and microbial growth on glass-like carbon surfaces

Figure 2.5 gives the results for live/dead bacterial viability staining. The images correspond to representative confocal micrographs of glass-like carbon films in contact with *E. coli* cultures for 18 h. The high growth rate of bacteria on irradiated surfaces was particularly clear for samples irradiated in dry air (Figures 2.5c and 2.5e). Conversely, non-irradiated carbon films were essentially free of bacteria (Figures 2.5a and 2.5b). It is interesting to note that some red-stained, nonviable bacteria appear on the lamp-irradiated film in wet air (Figure 2.5f).

Quantitative results were obtained by counting green pixels (viable bacteria) in digitally treated images with the aid of the public domain Java image processing software ImageJ. The percent surface colonized by bacteria (Figure 2.4) was 1.30 % ± 0.4 % in vacuum preconditioned carbon films, which increased to 51.0 % ± 2.7 % (chamber, dry air), 25.9% ± 1.8 % (chamber, wet air), 42.9 % ± 3.8 % (lamp, dry air) and 14.8 ± 2.0 % (lamp, wet air).

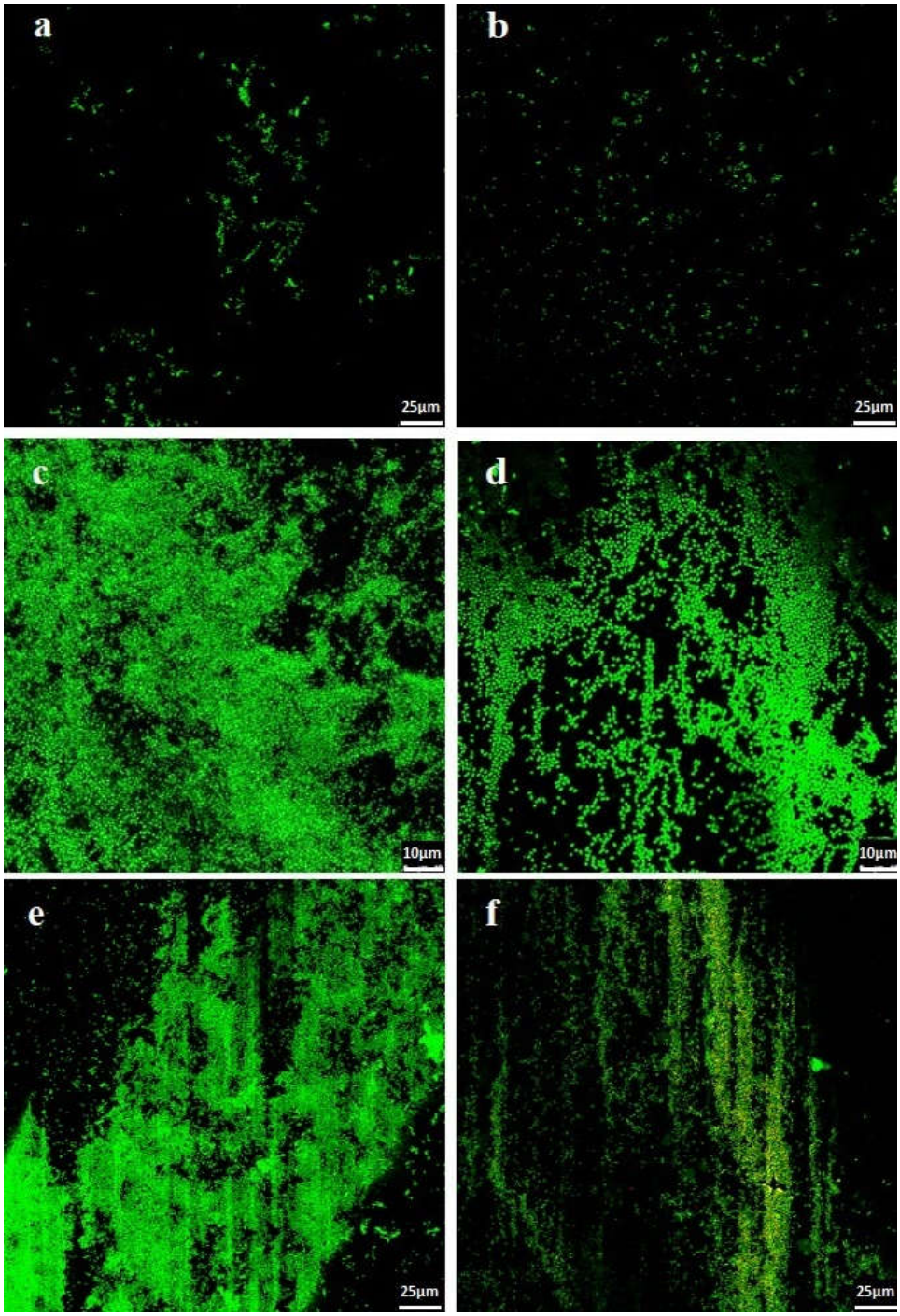

Figure 2.5. Live/dead confocal micrographs of *E. coli* cultured on (a) glass-like carbon film as produced, (b) vacuum preconditioned film, (c) chamber-irradiated films in dry air, (d) chamber-irradiated films in wet air, (e) lamp-irradiated films in dry air, (f) lamp-irradiated films in wet air.

Figure 2.6 shows SEM micrographs of *E. coli* cultured on different substrates, which essentially present the same behavior, with extensive colonization of glass-like carbon samples irradiated in dry air. Vacuum preconditioned film was almost free of bacterial growth (Figure 2.6a), but a high number of bacteria was clearly observed colonizing the

films irradiated in dry air (Figures 2.6c and 2.6d) and, to a lesser extent, on films irradiated in wet air (Figure 2.6b).

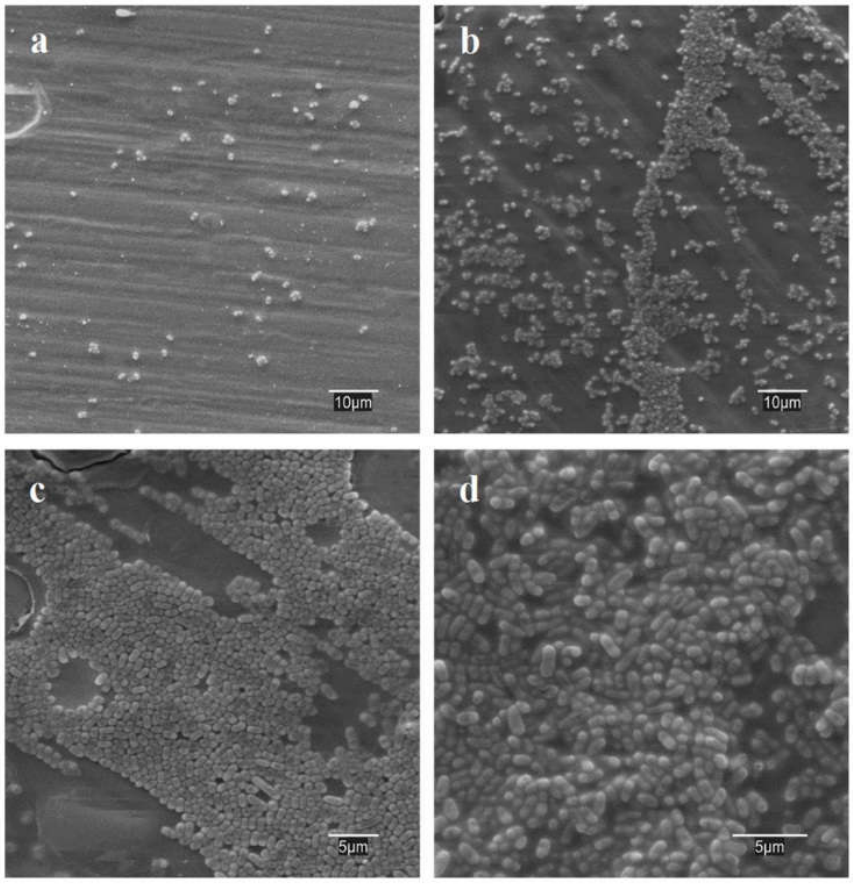

Figure 2.6. SEM images of *E. coli* cultured on (a) vacuum preconditioned film, (b) lamp-irradiated films in wet air, (c) chamber-irradiated films in dry air and (d) lamp-irradiated films in dry air.

The formation of an extracellular polymeric matrix was visualized using the FilmTracer SYPRO Ruby biofilm matrix stain. This stain labels most classes of proteins, including lipoproteins, porines and enzymes, which, among others, are found in the extracellular polymeric matrix of biofilms [40]. As with many other bacteria, *E. coli* tend to form biofilms consisting of cells immobilized at a substratum and embedded in an organic polymer matrix offering protection against hostile environments. The matrix also offers the possibility of intercellular communication, allowing rapid up- and down-regulation of gene expression and thus favoring adaptive strategies. The results of FilmTracer staining are shown in Figure S2.2 (Supplementary Information) as confocal micrographs. The extensive formation of biofilms is apparent in samples irradiated in dry air (Figures S2.2c

and 2.2e), whereas they are almost absent from non-irradiated films and scarce in those irradiated in wet air.

It has been shown that hydrophobic interactions play a dominant role in the adhesion of *E. coli* strains irrespective of lipopolysaccharide composition or cell charge [41]. They are responsible for the orientation of the water molecules adsorbed on the surfaces, which in turn determines the repulsion between surfaces [42]. If a surface is weakly polar, the most closely adsorbed water molecules are not rigidly oriented and another surface can approach under the influence of Lifshitz-van der Waals forces. It is interesting to note that rather than repelling water, a hydrophobic surface attracts water, although with less energy binding than hydrophilic surfaces [43]. Therefore, the hydrophobic interaction between two non-polar bodies in water is the result of the hydrogen-bonding energy of cohesion of the water molecules surrounding them. The consequence is that maximum interaction can be expected between two surfaces when the difference in hydrophilicity is not too great. Otherwise, adsorbed water molecules would lead to a net repulsion force.

Table 2.2 shows the ΔG_{SLS} values obtained by computing the hydrophilicity of bacteria and glass-like carbon films. Clearly, carbon films were hydrophobic as received and upon heating in vacuum their hydrophobicity increased to -100 mJ/m^2. Irradiation renders carbon films more hydrophilic, particularly when these are irradiated in wet air. The electron donor component of the surface energy corresponding to irradiated samples is clearly high, with the highest value corresponding to carbon films treated in wet air. This is consistent with the scenario depicted previously in which water molecules split into hydrogen and hydroxyl radicals, giving rise to oxygenated groups in surface carbon atoms. The data also show that the *E. coli* strain was highly hydrophilic and a predominantly electron donor (high value of γ_s^-). The bacterial strain and glass-like carbon irradiated in dry air displayed the closest ΔG_{SLS} values, whereas for wet air irradiation, the carbon surface became considerably more hydrophilic. The energy of interaction, ΔG_{SLS}, closely agrees with the extent of bacterial colonization as shown in Figures 2.4 to 2.6 and in Figure S2.2: the higher the similarity of ΔG_{SLS} with that of *E. coli*, the greater the bacterial growth observed.

As a rule, hydrophobic bacteria adhere on hydrophobic surfaces, whereas hydrophilic microorganisms attach to hydrophilic surfaces; however, bio-surface interactions are somewhat more complex. First, the thermodynamic approach assumes direct contact

between bacteria and surface, creating a new interface, but the presence of cell appendages, such as pili and flagella renders direct contact quite unrealistic [7]. On the other hand, solid surfaces exposed to culture media comprise complex interfaces with a number of adsorbed organic and inorganic compounds, which modify the way in which microorganisms adhere and complicate the use of simple physicochemical models [44]. In fact, the free energy of adhesion calculated from surface energy components is usually unsatisfactory because of the strong influence exerted by the growth medium used when culturing microorganisms, which has a significant impact on bacterial adhesion [45].

The other physicochemical factor affecting bacterial adhesion is surface charge, which we measured as surface zeta potential (Figure 2.4). All surfaces were negatively charged with a zeta potential ranging from -40.9 ± 1.1 mV for vacuum preconditioned films to -54.9 ± 1.9 mV for carbon irradiated in dry air. The negative charge of carbon films is due to the presence of oxygen-containing groups associated with sp3 hybridized carbon atoms at edges and defects. Such chemical functionalities, which include epoxy, hydroxyl and carboxylic groups, give rise to a negative charge in liquids with a high dielectric constant, such as water [46]. Irradiation increased the negative charge, as expected from the hydroxyl radical-driven formation of oxygenated functional surface groups explained previously. Moieties such as epoxide or carbonyl are responsible for polar surface properties, whereas carboxyl and hydroxyl groups are responsible for their negative charge [47,48]. Electrostatic repulsion could be expected to play a role in bacterial adhesion, given the negative surface charge of bacterial outer membranes: the zeta potential of *E. coli* is approximately -30 mV [41]. However, the data show that the more negatively charged surfaces were more prone to bacterial colonization as revealed by crystal violet (Figure 2.4) and live/dead staining (Figures2. 4 and 2.5) and SEM imaging (Figure 2.6). In all cases, dry-irradiated films were more easily colonized than the more hydrophilic ones irradiated in wet air. The more negative surface charge did not protect the surface from bacterial attachment. This is consistent with the secondary role played by electrostatic interactions during bacterial adhesion noted by other authors [49].

Bacterial colonization is a complex process which with bacterial adhesion to the substrate and continues with the formation of biofilms. Ruby FilmTracer images acquired after 18 h in contact with *E. coli* cultures (Figure S2.2) revealed a protein network of extracellular substances responsible for the mechanical stability of biofilms. They also showed extensive biofilm formation on irradiated surfaces of glass-like carbon film, indicating

that colonization proceeded easily on hydrophilic films, but an excessively hydrophilic surface, such as that obtained during irradiation in wet air, was relatively resistant to biofilm formation. Once formed, the biofilm constitutes a substrate in itself, and from then on, the characteristics of the underlying surface become less important for microbial growth. Reversibility of the hydrophilic-hydrophobic transition does not imply biofilm detachment because the polymeric matrix mediates between surface and cells forming a cohesive and three-dimensional network that is very difficult to remove [50].

2.2.3 Conclusions

In conclusion, we have shown that UV irradiation triggers the transition from a hydrophobic to hydrophilic surface in transparent glass-like carbon films. The effect took place with doses below 5 J/cm^2 using irradiation devices emitting at 185 nm, and was not observed in sources free from vacuum ultraviolet. The transition was reversible, and the water contact angle was essentially restored during the first 24 h under ambient conditions following irradiation. The hydrophilic transition is attributed to the dissociative adsorption of water molecules yielding oxygenated surface moieties. Carbon films were highly susceptible to bacterial colonisation and biofilm formation during the period in which they were hydrophilic. Up to 50 % of the surface of glass-like carbon films irradiated in dry air (~ 30 % RH) became covered by *E. coli* in the 18 h following inoculation. Irradiation in more humid air (~ 80 % RH) led to more hydrophilic surfaces, which were less prone to bacterial adhesion, indicating that bacterial colonisation took place preferentially on films with intermediate hydrophilicity values, whereas the higher energy of interaction associated with more hydrophilic surfaces resulted in a lower affinity for bacteria. Surface charge, always negative, did not play a significant role. These results are relevant for applications that require enhanced or suppressed biocompatibility of carbonaceous graphene-like materials.

2.2.4 References

[1] D. Aronov, R. Rosen, E.Z. Ron, G.Rosenman. Tunable hydroxyapatite wettability: effect on adhesion of biological molecules. *Process Biochem.* 2006, 41, 2367-2372.

[2] K. Anselme, P. Davidson, A.M. Popa, M. Giazzon, M. Liley, L. Ploux. The interaction of cells and bacteria with surfaces structured at the nanometre scale. *Acta Biomaterialia* 2010, 6, 3824-3846.

[3] R.J. Emerson, T.A. Camesano. Nanoscale investigation of pathogenic microbial adhesion to a biomaterial. *Appl. Environ. Microbiol.* 2004, 70, 6012-6022.

[4] E.A. Araújo, N.J. de Andrade, L.H.M. da Silva, A.F. de Carvalho, C.A. de Sá-Silva A.M. Ramos. Control of microbial adhesion as a strategy for food and bioprocess technology. *Food Bioprocess. Tech.* 2010, 3, 321-332.
[5] R. Bos, H.C. van der Mei, H.J. Busscher. Physico-chemistry of initial microbial adhesive interactions—its mechanisms and methods for study. *FEMS Microbiol. Rev.* 1999, 23, 179-230 (1999).
[6] M.E. Shirtliff, J.T. Mader, A.K. Camper. Molecular interactions in biofilms. *Chem. Biol.* 2000, 9, 859–871.
[7] K. Hori, S. Matsumoto. Bacterial adhesion: From mechanism to control. *Biochem. Eng. J.* 2010, 48, 424–434.
[8] D. Sahni, A. Jea, J.A. Mata, D.C. Marcano, A. Sivaganesan, J.M. Berlin, C.E. Tatsui, Z. Sun, T.G. Luerssen, S. Meng, T.A. Kent, J.M. Tour. Biocompatibility of pristine graphene for neuronal interface. J. *Neurosurg. Pediatr.* 2013, 11, 575-583.
[9] Y. Wang, Z. Li, J. Wang, J. Li, Y. Lin. Graphene and graphene oxide: biofunctionalization and applications in biotechnology. *Trends Biotechnol.* 2011, 29, 205–212.
[10] N. Verplanck, E. Galopin, J.C. Camart, V. Thomy, Y. Coffinier, R. Boukherroub. Reversible electrowetting on superhydrophobic silicon nanowires. *Nano Lett.* 2007, 7, 813-817.
[11] J. Yang, Z. Zhang, X. Men, X. Xu, X. Zhu. Reversible superhydrophobicity to superhydrophilicity switching of a carbon nanotube film via alternation of UV irradiation and dark storage. *Langmuir* 2010, 26, 10198-10202.
[12] S. Wang, X. Feng, J. Yao, L. Jiang. Controlling Wettability and Photochromism in a Dual-Responsive Tungsten Oxide Film. *Angew. Chem. Int. Ed.* 2006, 45, 1264-1267.
[13] Q.G. Jiang, Z.M. Ao, D.W. Chu, Q. Jiang. Reversible transition of graphene from hydrophobic to hydrophilic in the presence of an electric field. *J. Phys. Chem. C* 2016, 116, 19321-19326.
[14] X. Zhang, S. Wan, J. Pu, L. Wang, X. Liu, X. Highly hydrophobic and adhesive performance of graphene films. *J. Mater. Chem.* 2011, 21, 12251–12258.
[15] Z. Xu, Z. Ao, D. Chu, A. Younis, C.M. Li, S. Li. Reversible hydrophobic to hydrophilic transition in graphene via water splitting induced by UV irradiation. *Sci. Rep.* 2014, 4, 6450.
[16] J. Rafiee, X. Mi, H. Gullapalli, A.V. Thomas, F. Yavari, Y. Shi, P.M. Ajayan, N.A. Koratkar. Wetting transparency of graphene. *Nat. Mater.* 2012, 11, 217-222.
[17] S.B. Bon, M. Piccinini, A. Mariani, J.M. Kenny, L. Valentini. Wettability and switching of electrical conductivity in UV irradiated graphene oxide films. *Diam. Relat. Mat.* 2011, 20, 871–874.
[18] Y. Zhou, B. Wang. X. Song, E. Li, G. Li, S. Zhao, H. Yan. Control over the wettability of amorphous carbon films in a large range from hydrophilicity to super-hydrophobicity. *Appl. Surf. Sci.* 2006, 253, 2690–2694.
[19] Y. Zhou, B. Wang, X. Zhang, M. Zhao, E. Li, H. Yan. The modifications of the surface wettability of amorphous carbon films. *Colloid. Surf. A Physicochem. Eng. Asp.* 2009, 335, 128-132.
[20] X. Li, W. Cai, J. An, S. Kim, J. Nah, D. Yang, R. Piner, A. Velamakanni, I. Jung, E. Tutuc, S.K. Banerjee, L. Colombo, R.S. Ruoff. Large-Area Synthesis of High-Quality and Uniform Graphene Films on Copper Foils. *Science* 2009, 324, 1312-1314.

[21] P. Romero, R. Oro, M. Campos, J.M. Torralba, R. Guzman de Villoria. Simultaneous synthesis of vertically aligned carbon nanotubes and amorphous carbon thin films on stainless steel. *Carbon* 2015, 82, 31–38.22
[22] P. Romero, P. A. Postigo, E. Baquedano, J. Martinez, A. Bosca, R. Guzman de Villoria, Controlled synthesis of nanocrystalline glass-like carbon thin films with tuneable electrical and optical properties. *Chem. Eng. J.*, 2016, 299, 8-14.
[23] A. Reina, X. Jia, J. Ho, D. Nezich, H. Son, V. Bulovic, M.S. Dresselhaus, J. Kong. Large area, few-layer graphene films on arbitrary substrates by chemical vapor deposition. *Nano Lett.* 2009, 9, 30–35.
[24] W. Cai, Y. Zhu, X. Li, R.D. Piner, R.S. Ruoff. Large area few-layer graphene/graphite films as transparent thin conducting electrodes. *Appl. Phys. Lett.* 2009, 95, 123115.
[25] P.J.F. Harris. New Perspectives on the Structure of Graphitic Carbons. *Crit. Rev. Solid State Mater. Sci.* 2005, 30, 235–253.
[26] P.J.F. Harris. Fullerene-related structure of commercial glassy carbons. *Philos. Mag.*, 2004, 84, 3159–3167.
[27] A.C. Ferrari, J. Robertson. Interpretation of Raman spectra of disordered and amorphous carbon. *Phys. Rev. B* 2000, 61, 14095.
[28] P. May, M. Lazzeri, P. Venezuela, F. Herziger, G. Callsen, J.S. Reparaz, A. Hoffmann, F. Mauri, J. Maultzsch. Signature of the two-dimensional phonon dispersion in graphene probed by double-resonant Raman scattering. *Phys. Rev. B* 2013, 87, 075402.
[29] A.C. Ferrari, D.M. Basko. Raman spectroscopy as a versatile tool for studying the properties of graphene. *Nat. Nanotechnol.* 2013, 8, 235–246.
[30] C.J. Van Oss, M.K. Chaudhury, R.J. Good. Interfacial Lifshitz-van der Waals and Polar Interactions in Macroscopic Systems. *Chem. Rev.* 1988, 88, 927-941.
[31] A. Holländer, A. On the selection of test liquids for the evaluation of acid-base properties of solid surfaces by contact angle goniometry. *J. Colloid Interface Sci.* 1995, 169, 493-496.
[32] C.J. Van Oss. Development and applications of the interfacial tension between water and organic or biological surfaces. *Colloids Surf. B: Biointerfaces* 2007, 54, 2–9.
[33] M. Fletcher. The effects of culture concentration and age, time, and temperature on bacterial attachment to polystyrene. *Can. J. Microbiol.* 1977, 23, 1-6.
[34] H.J. Busscher, A.H. Weerkamp, H.C. van der Mei, A.W.J. van Pelt, H.P. de Jong, J. Arends. Measurement of the surface free energy of bacterial cell surfaces and its relevance for adhesion. *Appl. Environ. Microbiol.* 1984, 48, 980-983.
[35] T. Savage, S. Bhattacharya, B. Sadanadan, J. Gaillard, T.M. Tritt, Y.P. Sun, Y. Wu, S. Nayak, R. Car, N. Marzari, P.M. Ajayan, A.M. Rao. Photoinduced oxidation of carbon nanotubes. *J. Phys. Condens. Matter*, 2003, 15, 5915-5921.
[36] B. Ruscic, A.F. Wagner, L.B. Harding, R.L. Asher, D. Feller, D.A. Dixon, K.A. Peterson, Y. Song, X. Qian, C.Y. Ng, J. Liu, W. Chen, D.W. Schwenke. On the enthalpy of formation of hydroxyl radical and gas-phase bond dissociation energies of water and hydroxyl. *J. Phys. Chem. A* 2002, 106, 2727-2747.
[37] D. Aronov, R. Rosen, E.Z. Ron, G. Rosenman. Electron-induced surface modification of hydroxyapatite-coated implant. *Surf. Coat. Technol.* 2008, 202, 2093-2102.
[38] S. Wang, Y. Zhang, N. Abidi, L. Cabrales. Wettability and surface free energy of graphene films. *Langmuir* 2009, 25, 11078-11081.

[39] A. Kozbial, Z. Li, C. Conaway, R. McGinley, S. Dhingra, V. Vahdat, F. Zhou, B. D'Urso, H. Liu, L. Li. Study on the surface energy of graphene by contact angle measurements. *Langmuir* 2014, 30, 8598-8606.
[40] M.P. Nandakumar, A. Cheung, M.R Marten. Proteomic analysis of extracellular proteins from *Escherichia coli* W3110. *J. Proteome Res.* 2006, 5, 1155-1161.
[41] Y.L Ong, A. Razatos, G. Georgiou, M.M. Sharma. Adhesion forces between *E. coli* bacteria and biomaterial surfaces. *Langmuir* 1999, 15, 2719-2725.
[42] C.J. Van Oss. Hydrophobicity and hydrophilicity of biosurfaces. *Curr. Opin. Colloid Interface Sci.* 1997, 2, 503-512.
[43] C.J. Van Oss. Hydrophobicity of biosurfaces - origin, quantitative determination and interaction energies. *Colloids Surf. B Biointerfaces* 1995, 5, 91-110.
[44] M.G. Brading, J. Jass, H.M. Lappin-Scott. Dynamics of bacterial biofilm formation. In: *Microbial Biofilms*; Lappin-Scott, H.M., Costerton J.W., Eds.; Cambridge University Press, Cambridge, 1995, pp 46–63.
[45] Q. Zhao, Y. Liu, C. Wang, S. Wang. Evaluation of bacterial adhesion on Si-doped diamond-like carbon films. *Appl. Surf. Sci.* 2007, 253, 7254-7259.
[46] S.M. Notley, R.J. Crawford, E.P. Ivanova. Bacterial Interaction with Graphene Particles and Surfaces. In: *Advances in Graphene Science*, M. Aliofkhazraei, Ed.; InTech, 2013 (DOI: 10.5772/56172)
[47] I. Dékány, R. Krüger-Grasser, A. Weiss. Selective liquid sorption properties of hydrophobized graphite oxide nanostructures. *Colloid Polym. Sci.* 1998, 276, 570-576.
[48] K. Haubner, J. Murawski, P. Olk, L.M. Eng, C. Ziegler, B. Adolphi, E. Jaehne. The route to functional graphene oxide. *ChemPhysChem* 2010, 10, 2131-2139.
[49] J. Wang, N. Huang, P. Yang, Y.X. Leng, H. Sun, Z.Y. Liu, P.K. Chu. The effects of amorphous carbon films deposited on polyethylene terephthalate on bacterial adhesion. *Biomaterials* 2004, 25, 3163-3170.
[50] H.C. Flemming, J. Wingender. The biofilm matrix. *Nat. Rev. Microbiol.* 2010, 8, 623-633.

Chapter 3:

Photocatalytic materials: effect of titanium dioxide on biofilm formation

3 Photocatalytic materials: effect of titanium dioxide on biofilm formation

3.1

3.2 Part I: Biofilm formation on self-cleaning surfaces functionalized by photocatalytic nanoparticles

3.2.1 Introduction

The development of self-cleaning surfaces constitutes an active research domain in materials science [1]. Self-cleaning can arise from manipulating surface wettability behavior and different chemical processes can be used to produce highly hydrophilic and superhydrophobic surfaces with antifogging or water repellence properties [2, 3]. An active research is being undertaken to find new superhydrophilic or superhydrophobic surfaces to create materials with application in many technological and biomedical fields [4]. Since the early discovery of its photoinduced superhydrophilicity, titanium dioxide has been used to prepare inorganic self-cleaning surfaces [5]. It has been suggested that UV irradiation resulted in the weakening of Ti-O lattice bonds leading to photogenerated surface hydroxyl groups in the presence of water [6]. Titanium dioxide has also been widely studied as heterogeneous photocatalyst based on its capacity to produce surface reactive oxygen species (ROS) such as the radicals $HO^{\bullet}$, $O_2^{\bullet-}$ or $HO_2^{\bullet}$ in a very well documented process [7]. Photocatalysis and photoinduced superhydrophilicity can take place simultaneously on the same surface, and their combination has widened the potential application of TiO_2 coatings as self-cleaning materials [8].

The photocatalytic properties of TiO_2 have also been used for creating antimicrobial surfaces. Photocatalytic disinfection has been proposed for creating antimicrobial building materials, medical devices and packaging films among a wide variety of materials and applications [7]. The photocatalytic water disinfection has been explored to overcome the risk of the disinfection by-products generated by the use conventional disinfectants [9]. Photocatalysis has proved capable of killing many microorganisms including bacterial endospores [10]. There is a clear evidence that the mode of action of photoactivated TiO_2 against bacteria is due to oxidative damage [11]. The oxidation of

cell components can take place by direct contact with the catalyst surface or by the intermediation of ROS such as $HO^{\bullet}$ and H_2O_2 [12]. The production of $O_2^{\bullet-}$, the generation of bulk $HO^{\bullet}$ via Fenton mechanisms or the photodecomposition of H_2O_2 have also been proposed as sources of ROS in the process of bacterial inactivation [10]. The oxidative damage is more important when cells and TiO_2 photoactivated surface are in close contact, which is the reason why nanoparticle suspensions are more effective than immobilized particles [13]. As expected, the kinetics of microorganism inactivation is highly dependent on the presence of radical scavengers [14].

The adhesion of microorganisms on man-made surfaces is responsible for the spreading of infectious diseases, particularly in the case of medical devices or equipment [15]. Bacterial colonization is also associated to foodborne diseases and leads to high economic losses in the food processing industry [16]. Biofilms are of particularly concern due to their resistance to host defense mechanisms and to conventional disinfection processes [17]. The bacterial attachment and biofilm formation are complex processes still poorly understood that depend on several factors including the physicochemical properties of the surface, the temperature and pH, the availability of nutrients and the type of strain [18]. Once attached to a surface, bacteria form biofilms, which are structured aggregations of microorganisms consisting of cells immobilized and embedded within a polymeric matrix mainly made of exopolysaccharides. Significantly, bacteria in biofilms display altered phenotypes and create their own environment as an evolutionary adaptation to environmental challenges [19].

In this work, we prepared self-cleaning antimicrobial surfaces based on crystalline nanostructured TiO_2 exposed to simulated solar irradiation. The photooxidative damage produced to bacterial strains was studied using cultures of *Staphylococcus aureus* and *Pseudomonas putida*. The main goal of the article was to determine how surface characteristics influence the formation of biofilms on the TiO_2-functionalized material. The attention was focused on the antibacterial capacity against mature biofilms previously formed rather than on the inhibition of the initial colonization step, which is a topic extensively covered in the literature. Biofilm matrix visualization, bacterial viability and oxidative stress were monitored to assess the antimicrobial and antibiofouling activity of the self-cleaning material.

3.2.2 Material and methods

3.2.2.1 Synthesis and characterization of the Titanium dioxide nanoparticles

Suspensions of crystalline anatase TiO_2 nanoparticles were synthetized by sol-gel, typically adding 11.5 mL of titanium tetraisopropoxide to an acidic aqueous solution with a 140:1 water to nitric acid proportion, while stirring vigorously [20]. The suspension obtained was aged for three days and further dialyzed. 2 mL of this TiO_2 20 wt% preparation were extended over smooth glass slides 76 x 26 mm (VWR, Radnor, PA) and 47 mm, 1.6 μm pore size glass microfiber filters (Whatman International, Maidstone, UK). The material was spread by smearing in the case of the glass slides and by impregnation in the case of glass filters. Before and after the deposition, the coated substrates were dried at 110 °C and weighted to assess the amount of photocatalytic material deposited.

The synthetized TiO_2 nanoparticle suspension was characterized for dynamic particle size by Dynamic Light Scattering (Malvern, Nanosizer), zero charge potential (Zeta-meter Inc. Model 3.0), surface acidity, shape and size of TiO_2 particles by TEM (JEOL 2100F) and TiO_2 loading by formation of the corresponding xerogel. BET specific surface area and micro-mesoporosity were obtained from nitrogen the adsorption-desorption isotherms of the TiO_2 xerogel (Micromeritics, ASAP 2420) and from mercury porosimetry for the determination of meso-macropores and apparent density (Micromeritics, Poresizer 9520). Surface acidity was measured by ammonia chemisorption/physisorption isotherms (Micromeritics, ASAP 2010C). Band-gap was calculated from Tauc plots using UV-Vis Diffuse Reflectance Spectroscopy (Agilent Cary 5000). Powder X-ray Diffraction (PANalytical X'Pert Pro) offered information about crystalline phases of TiO_2 and allowed estimating crystallite size by means of Scherrer's equation [21]. Titanium content was measured by plasma emission (ICP-OES, Perkin-Elmer Optima 330DV) of samples previously digested in acidic media into a microwave oven.

The wettability and hydrophilicity of coated and uncoated surfaces was tested using an optical contact angle meter (Krüss DSA25 Drop Shape Analysis System) using the sessile drop technique. Samples were placed on the test cell and drops of the testing liquids were placed on the surfaces by delivering syringe. The Surface free energy was determined by measuring contact angles (CA) with water (Milli-Q), glycerol, and diiodomethane. The

components of the surface tension were estimated as described elsewhere [22] [23]. The procedure allowed calculating the free energy of interaction between two identical surfaces immersed in a liquid, ΔG_{SLS}, which gives a quantitative measurement of the hydrophobicity or hydrophilicity of the surface. If $\Delta G_{SLS} > 0$, the surface is hydrophilic, and if $\Delta G_{SLS} < 0$, it is hydrophobic. Details are included as Supplementary Material. Contact angle measurements for each surface were taken at room temperature on at least three different positions on each sample.

Scanning electron microscopy (SEM) images of the surface of materials were obtained using a Hitachi S-3000N microscope operating at 25 kV. The images of bacteria colonizing the surface of materials were taken in a ZEISS DSM-950 instrument. A process of dehydration and drying with ethanol at different concentrations was carried out before analyzing the samples in contact with microorganisms.

3.2.2.2 Photocatalytic activity studies

Two kinds of photodegradation test were used to assess the activity of TiO_2-functionalized surfaces. The anti-soiling chemical activity was studied using adsorbed organics under solid-solid conditions with methylene blue as probe compound. For the assessment of their effect on growth and viability of bacterial cells two biofilm-forming strains were used in a series of bioassays.

Dye photocatalytic degradation runs were performed in a closed and refrigerated camera (temperature was maintained at 25 ± 2 °C) equipped with six 15 W BBL fluorescent lamps, which emit in the UV-A range, centered at 365 nm. The procedure followed the procedure for adsorbed organics as described elsewhere [24]. The samples were located at 20 cm of distance from the lamps to ensure 20 W m^{-2} of irradiance, which was measured by a broadband UV CUV-4 Kipp & Zonen radiometer with UV range 306–383 nm. A spot of methylene blue (MB) was deposited on both substrates, slides and filters, by spraying with a nozzle regulated airbrush (Defynik 140 by Sagola) 5mL of MB solution 5 x 10^{-4} M in acetone. Previously the adequate amount of MB to provide enough color contrast was verified. A calibration with five points was carried out to correlate measured reflectance and surface concentration of MB. For that purpose, 1 mL of MB 5 x 10^{-4} M solution was consecutively sprayed on certain areas of both supports after adjusting the distance to the surface of the airbrush nozzle. The photodegradation of dye was followed in two ways: by taking micropictures (USB Microprobe Dino-Lite Edge AM4115ZT) to

visualize de photodegradation process and by measuring the diffuse reflectance spectra between 400-800 nm, where MB presents the maximum absorption, at different irradiation times between 0-750 minutes. Parallel reference photodegradation runs were carried out with slides and filters without photocatalytic coating, and in the absence of irradiation. All experiments were replicated until obtaining reliable results.

3.2.2.3 Photocatalytic bioassays

Irradiation experiments during bioassays were performed using a Heraeus TQ Xe 150 Xe-arc lamp with spectral emission mainly in the visible region with a minor contribution of UV-A (5.5 % output in the 320-400 nm region, 94.2 % > 400 nm). The lamp sleeve was equipped with a quartz cooling tube in which the lamps were fitted and was refrigerated by means of a thermostatic bath. The samples were irradiated at 15 cm from the lamp sleeve during 2 h after allowing 48 h for biofilm growth as indicated below. Fluence rate in the near UV was 11.2 W m^{-2} (measured in the 290–400 nm range), which was determined by chemical actinometry of 2-nitrobenzaldehyde [25]. The 290-400 nm range 5.8 % of the total radian power emitted by the lamp.

Staphylococcus aureus (CECT 240 equivalent to ATCC 6538P) and *Pseudomonas putida* (CECT 4584 equivalent to DSMZ 84) were used to test the antibacterial activity of TiO_2 photoactivated materials. *S. aureus* and *P. putida* were grown overnight in nutrient medium (beef extract 5 g/L, peptone 10 g/L, NaCl 5 g/L pH adjusted to 7.2), while shaking at 37 °C and 28 °C respectively. Exponentially growing cultures diluted to 10^8 cells/mL (optical density at 600 nm, OD_{600} = 0.0138) were placed on the studied TiO_2 substrates and their corresponding control samples and incubated without stirring for 48 h in the dark at 37 °C, in the case of *S. aureus*, and at 28 °C in the case of *P. putida*. This procedure allowed biofilm formation before irradiation. Afterwards, the materials were carefully washed with distilled water to remove planktonic and loosely attached cells before the irradiation treatment. Biofilm formation assays were performed with and without TiO_2 on the surface of 96-well polystyrene plates following a modification of the method of Fletcher as a standard procedure [26]. For it, TiO_2 solution was deposited covering the surface of some wells to evaluate the biofilm formation ability of a surface completely covered with TiO_2. Polystyrene has been widely used as a reference plastic surface for cell adhesion and in this experiment, was considered as the control surface. After TiO_2 consolidation, bacterial incubation and irradiation treatment performed as

described, the biofilm mass was quantified by measuring optical density. 200 µL of a crystal violet 0.1% solution were extended over the washed surface of each polystyrene well and incubated for 15 min to allow the staining of adhered cells. Excess stain was eliminated by rinsing with water. Plates were air dried and 1 mL of 95% ethanol was added to each well to extract crystal violet from cells. Distaining was performed overnight while gently shaking. Finally, the dye was measured at OD_{590}. Every measurement was performed twelve times for each experimental condition. For the visualization of the extracellular polymeric matrix, the biofilms were stained with 200 µL FilmTracer SYPRO Ruby (Molecular Probes, Invitrogen) per sample, incubated in the dark for 30 min at room temperature, and rinsed with distilled water. Then, they were observed using confocal microscopy (Confocal SP5, Leica Microsystems, Germany) with excitation/emission wavelengths of 450 nm and 610 nm respectively.

Bacterial viability assays were performed using LIVE/DEAD BacLight Bacterial Viability Kit (Molecular Probes, Invitrogen Detection Technologies, Carlsbad, CA, USA). Under LIVE/DEAD staining, all cells exhibit green fluorescence (SYTO 9), whereas nonviable bacterial cells display red fluorescence (Propidium iodide, PI) with dye uptake depending upon cell membrane integrity. For the staining of films 10µL of BacLight stain (a mixture of SYTO 9 and PI in DMSO, following the manufacturer's recommendations) were used. The incubation was performed in the dark for 15-30 min at room temperature. For green fluorescence (SYTO 9) excitation was performed at 488 nm and emission at 500-575 nm. For red fluorescence (PI, dead cells), the excitation/emission wavelengths were 561 nm and 570-620 nm respectively.

The oxidative stress suffered by bacterial cells on coated and uncoated surfaces was measured after 48 h of biofilm formation using 2',7'-dichlorodihydrofluorescein diacetate (H_2DCFDA). 50µL of a 10 mM H_2DCFDA stock solution were added to each sample and incubated for 1 h at room temperature. This probe is cell-permeable and undergoes intracellular hydrolysis to yield the dichlorodihydrofluorescein (DCFH) carboxylate anion, which is retained in the cell. Two-electron oxidation of DCFH results in the formation of dichlorofluorescein (DCF), which is fluorescent compound that serves as an indicator for hydrogen peroxide and other ROS, such as hydroxyl and peroxyl radicals [27]. The intracellular generation of DCF was monitored by confocal fluorescence microscopy with excitation at 488 nm and emission at 655 nm.

3.2.3 Results and discussion

3.2.3.1 Characterization

The main physicochemical properties of TiO_2 nanoparticles suspension and the TiO_2 xerogel, prepared by solvent evaporation at room temperature, are presented in Table 3.1.1. The synthetized suspension presents 20% anatase-TiO_2 content and is stabilized after dialyzation at pH 3.0. The primary particle size is around 4-5 nm as verified by XRD, TEM and DLS analysis, that also showed the presence of secondary particles due to different aggregates sizes. The high surface area, porosity and acidity found in the formed xerogel confirmed the noteworthy physicochemical properties of the prepared nanostructured TiO_2 suspension to perform photocatalytic coatings. The X-ray diffractogram in Figure S3.1.1 (Supplementary Information), permitted to prove the only presence of anatase crystalline phase.

Table 3.1.1. Physicochemical properties of TiO_2 suspension and xerogel.

TiO_2 suspension		Coated TiO_2 xerogel	
TiO_2	20 ± 2 wt%	Ti	54 ± 5 wt%
pH	3.0 ± 0.5	Band-gap	3.14 ± 0.06 eV
PZC	5.1 ± 0.5	Crystalline phase	anatase
DLS particle size	4 ± 1, 16 ± 3, 65 ± 6 nm	$d_{crystallite}$	3.8 ± 0.2 nm
Primary particle size	5.6 ± 1.4 nm	S_{BET}	340 ± 15 m^2/g
ζ-potential (pH 7.0)	(TEM, 500 particles)	V_{pore}	0.22 ± 0.08 cm^3/g
	34.0 ± 0.5 mV	d_{pore}	3.4 ± 0.5 nm
		Density	2.7831 ± 0.008 g/cm^3
		Acidity	1.28 ± 0.04 meq H^+/g

The surface density of TiO_2 on glass microfiber filters was $1.98 \cdot 10^{-3} \pm 1.5 \cdot 10^{-4}$ $g \cdot cm^{-2}$, whereas the coverage layer deposited on glass slides amounted to $8.55 \cdot 10^{-3} \pm 3.0 \cdot 10^{-4}$ $g \cdot cm^{-2}$. The values for the glass slides were calculated considering the surface on which the TiO_2 gel was smeared, which was 55 x 26 cm, excluding the frosted end of the slide. Figure 3.1.1 (A and B) shows typical SEM micrographs of the TiO_2 material on glass slides and filters. When deposited on glass slides, TiO_2 forms homogeneous layers of tight aggregates of particles displaying planar surfaces with some irregularities as shown in Figure 3.1.1A. The primary size of particles corresponded to that of the TiO_2 material as noted before (close-up of Figure 3.1.1B). The material dispersed in glass filters displayed similar aggregates, spread in smaller plates adhered to filter fibers or occupying the pores defined by them (Figure 3.1.1C). Overall, the total amount of TiO_2 per unit

surface was considerably lower when deposited in filters, but the dispersion was better due to the role of glass fibers in creating a pattern of microsized sheets.

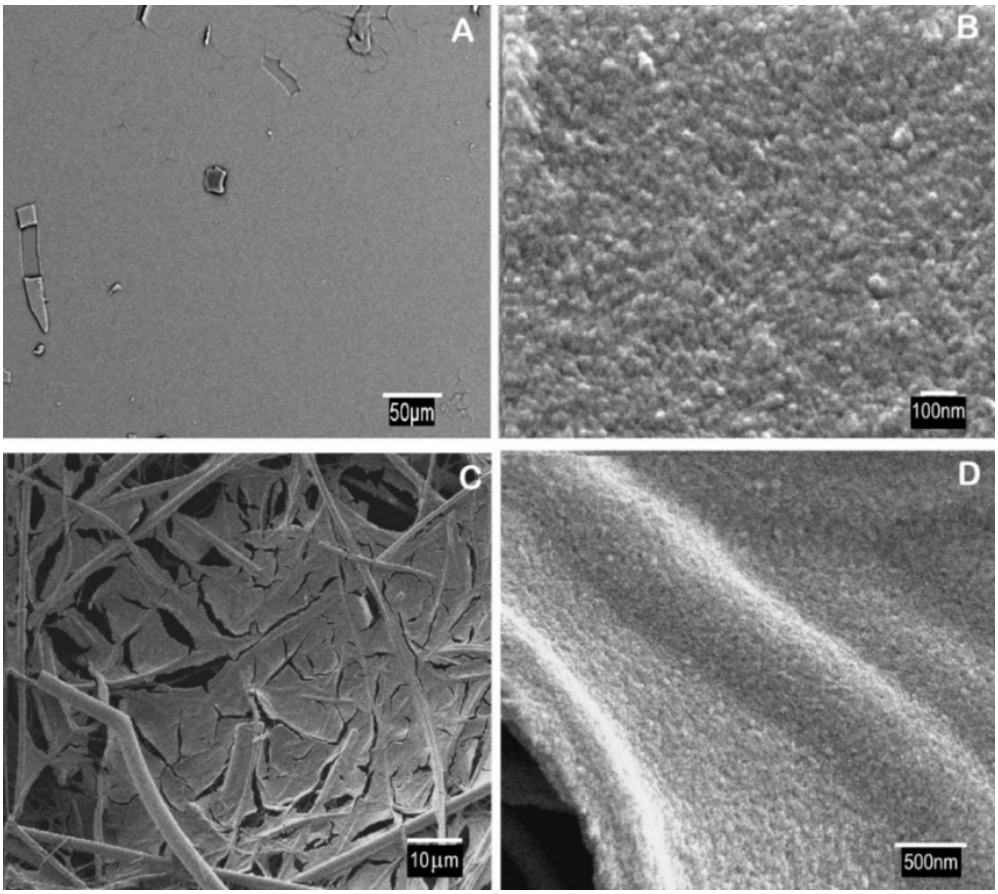

Figure 3.1.1. SEM images of TiO_2-coated glass slides (A, B), TiO_2-coated filters (C, D).

Table 3.1.2 gives the values of surface energy components for bare, irradiated and non-irradiated glass slides as well as for bacterial lawns. The value for the total solid-liquid interfacial energy, γ_S^{LW}, was 38.6 mJ m^{-2} for TiO_2 deposited on glass slides, which dropped to 23.2 mJ m^{-2} upon Xe-arc light irradiation. The figures were similar to the values reported elsewhere for comparable materials [28]. The surface of TiO_2/slides was hydrophobic, with considerably negative ΔG_{SLS} values. Upon irradiation, the surface turned hydrophilic with $\Delta G_{SLS} = +70 \pm 9$ mJ m^{-2}. It is a well-known fact that TiO_2 surfaces exhibit a photo-induced wettability transition, which leads to a decreased water contact angle following irradiation. This phenomenon has been attributed to the breaking of Ti-O lattice bonds by photogenerated holes. Water molecules would then coordinate the titanium site leading to an increase in the number of surface hydroxyl groups. As the newly formed hydroxyl groups are less stable than the initial doubly coordinated hydroxyl

groups, the material restores its initial hydrophobicity in the space of a few hours after irradiation [29].

Table 3.1.2. Surface characterization by means of contact angle measurements and derived surface energy components (mJ/m^2).

Material	θ_{water}	$\theta_{glycerol}$	$\theta_{diiodomethane}$	γ_S^{LW}	γ_S^+	γ_S^-	γ_S^{AB}	γ_S	ΔG_{SLS}
Glass slides	39.7 ± 3.5	42.5 ± 0.7	60.7 ± 0.4	28.2	0.02	5.90	0.75	28.9	-52 ± 8
TiO_2/slides	57.9 ± 3.9	71.9 ± 4.8	42.0 ± 2.6	38.6	0.02	0.05	0.06	38.6	-100 ± 11
TiO_2/slides*	34.3 ± 1.7	6.5 ± 2.4	1.3 ± 0.5	22.7	-	73.1	0.54	23.2	+70 ± 9
S. aureus	21.8 ± 4.6	76.4 ± 5.5	88.2 ± 5.3	13.6	0.01	106	1.69	15.3	+102 ± 15
P. putida	15.6 ± 2.8	63.2 ± 3.5	58.9 ± 3.7	29.2	1.44	62.3	18.9	48.2	+42 ± 8

* irradiated for 5 min, 25 °C

3.2.3.2 Self-cleaning photocatalytic activity

The efficiency of the photooxidative process upon irradiation of slides and filters in contact with MB is shown in form of a full series of micropictures in Figure S3.1.2 of Supplementary Information. Reference filters and slides without coating were used as blank (B) to discard MB photochemical degradation. As observed in Figure S3.1.2 the stain color was practically maintained along the 750 min irradiation period for blanks, while significant discoloration appeared in coated slides (slides 1 and 2) that exhibited only a residual heterogeneous speckled surface after irradiation. Samples of TiO_2-coated filters (filters 1 and 2) achieved complete photodegradation with negligible MB stain beyond 300 minutes. The photodegradation of MB, quantified by diffuse reflectance spectroscopy, is shown in Figure 3.1.2 for filters (A) and slides (B). Blanks are also shown to verify the absence of MB photochemical degradation. Filters presented complete photo-oxidation of MB, revealing remarkable self-cleaning performance, while slides were capable to photodegrade around 60% of MB without further reduction beyond 300 minutes of irradiation. The photocatalytic process progresses rapidly during the first 300 min, to slow down at longer irradiation times. The behavior on both supports was reproducible as observed with replicates.

The rate of photooxidative depletion of MB was one order of magnitude higher for filters both in terms of reaction rate and semi-reaction time. Table 3.1.3 shows the calculated values for MB depletion rate expressed per unit surface and per unit mass of TiO_2. The efficiency for MB removal was particularly high for TiO_2 deposited on glass filters, for

which MB depletion rate was 50-fold higher than that of glass slides when expressed per unit mass of TiO_2. The reason for the higher photocatalytic efficiency of TiO_2-loaded filters was the better dispersion obtained in them, with respect to the flat uniform surface of slides. As noted before, TiO_2 material deposited on glass slides formed a homogeneous layer in which the active surface was essentially coincident with that of the covered support. Accordingly, the half time of MB depletion was one order of magnitude lower for TiO_2 coated filters even when the amount of TiO_2 deposited on them was four times lower.

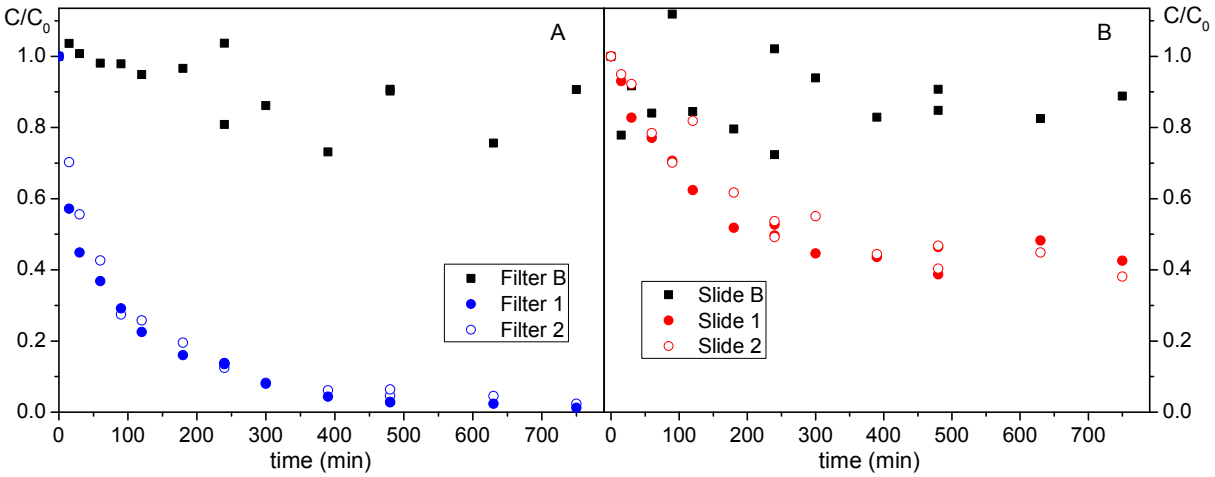

Figure 3.1.2. Photodegradation of MB with irradiation time for TiO_2-coated filters (A) and TiO_2-coated slides (B).

Table 3.1.3. Values of r_o and $t_{1/2}$ during the photocatalytic degradation of MB on slides and filters.

Kinetic Parameters	Slides		Filters	
	Blank	TiO_2-coated	Blank	TiO_2-coated
$t_{1/2}$ (min)	-	232 ± 11	-	27 ± 10
r_o ($mmol \cdot cm^{-2} \cdot min^{-1}$)	0.013 ± 0.009	0.078 ± 0.004	0.025 ± 0.009	0.97 ± 0.23
r_o ($\mu mol \cdot g^{-1} \cdot min^{-1}$)	-	0.0091±0.0005	-	0.49 ± 0.11

3.2.3.3 Antimicrobial performance

The effect on bacterial viability was studied using LIVE/DEAD staining and confocal microscopy. The confocal micrographs shown in Figure 3.1.3 correspond to slides and filters with, C(+), and without, C(-), TiO_2 coating and in irradiated, L(+), and non-

irradiated, L(-) samples. The growth of both strains, *P. putida* and *S. aureus*, was clear in control materials on which a considerable amount of viable green-labelled cells appeared. Xe-lamp irradiation did not induce bacterial damage in the absence of TiO_2, but cell impairment was apparent for TiO_2-irradiated materials. Cells on TiO_2-functionalized slides and filters showed extensive cell photo-impairment, with practically all cells red-marked because of membrane disruption. Certain cells appeared yellowish or orange. Yellow cells are generally considered viable, while orange cells can be considered damaged [30]. A certain amount of bacteria appeared yellow-to-orange in C(+) L(-) samples (samples with TiO_2 but kept in the dark). The effect may be associated to the irradiation suffered during confocal microscopy observations.

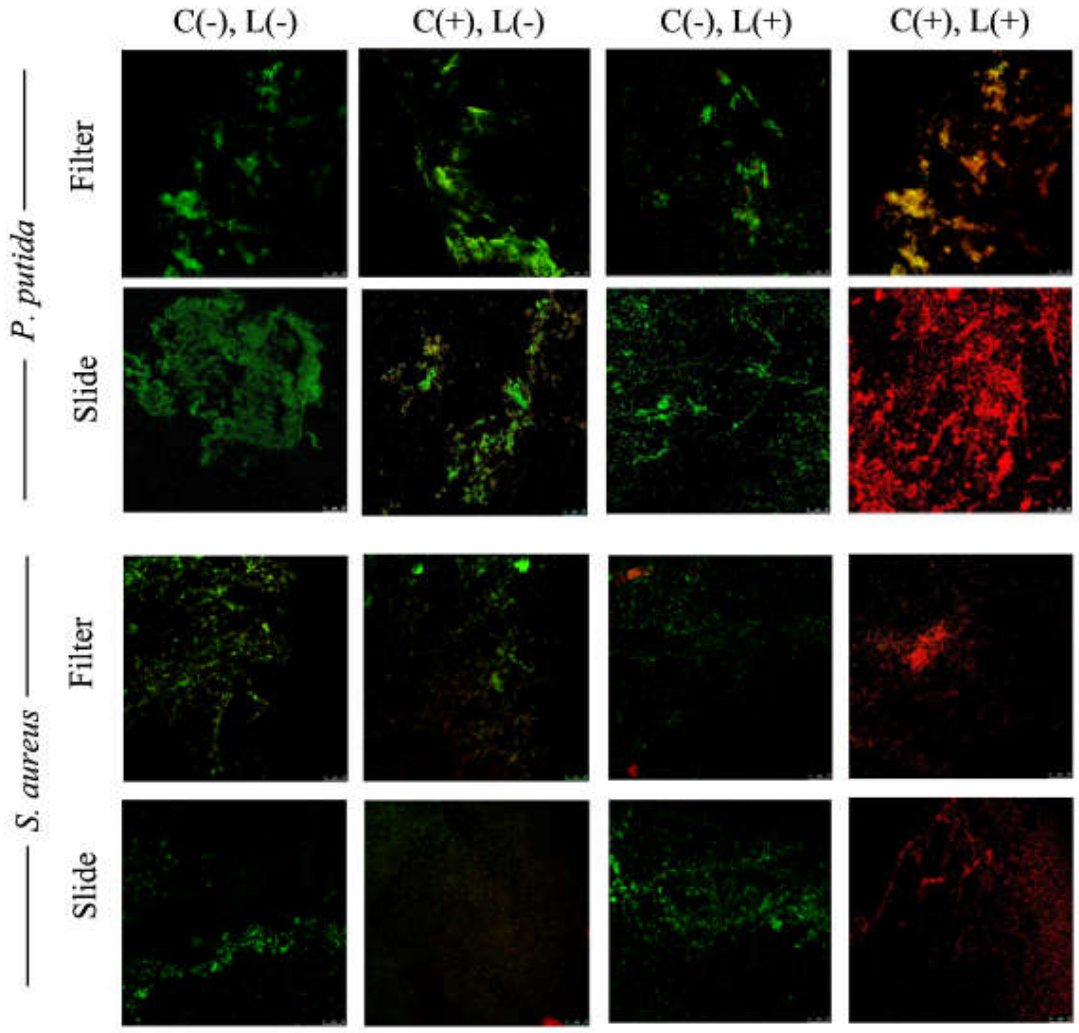

Figure 3.1.3. Live/Dead confocal micrographs of *P. putida* and *S. aureus* on TiO_2-coated glass filters and TiO_2-coated glass slides in irradiated, L(+), and no-irradiated, L(-), samples. Irradiation Conditions: 2 h under Xe arc lamp after 48 h in the dark at 28 °C (*P. putida*) or 37 °C (*S. aureus*). C(+): samples with TiO_2, C(-): control samples.

The cause for damage in bacterial cells exposed to photocatalytic irradiated material was the production of ROS as intermediates of oxygen-dependent photosensitized reactions. This was measured as DCF fluorescence intensity and recorded as confocal micrographs in Figure.3.1.4. The images on top are micrographs showing *P. putida* and *S. aureus* cultures kept for 48 h on TiO_2-functionalized slides and filters and subsequently irradiated for 2 h using Xe-arc lamp. All TiO_2-functionalized materials showed intense intracellular green DCF fluorescence because of ROS production. The confocal images on top correspond to filters and slides with TiO_2 but non-irradiated (A, E, C and G), and irradiated TiO_2-loaded filters (B and F) and slides (D and H). The quantification of ROS production was performed by digitally converting the images into pixels. Every image was treated to enhance contrast and pixels were transformed into percent surface using the public domain Java image processing software ImageJ. The results are also shown in Figure 3.1.4 for *P. pudida* (I) and *S. aureus* (J). Non-TiO_2 loaded specimens, C(-), and those kept in the dark, L(-), exhibited non-significant differences in DCF fluorescence intensity. Conversely, for TiO_2-functionalized and irradiated filters and slides, the increase in the intensity of the DCF signal was substantial, and higher in slides than in filters probably due to the greater load of photocatalytic material of the former.

The antimicrobial effect of TiO_2 materials has been linked to membrane integrity destabilization and oxidative toxicity due to the generation of hydroxyl radicals and other species that affects bacterial activity and growth rates [31] [32]. Figure 3.1.5 and Figure S3.1.3 (Figure 3.1.5 proofs cell damage while Fig. S3.1.3, with lower magnification, allows biofilm visualization) show SEM micrographs that detail the morphology changes of *P. putida* and *S. aureus* cells upon irradiation treatments in contact with TiO_2 nanomaterial. In non-irradiated samples, the morphology (rod shaped) of *P. putida* cells was retained (Figure 3.1.5A and 3.1.5E). However, after 2 h irradiation, the surface of *P. putida* cells appeared wrinkled and irregular with some cells clearly evidencing damaged membranes (arrows in Figure 3.1.5B and 3.1.5F). Also, for *S. aureus* cell irradiated on TiO_2-functionalizaed surface presented important morphology alterations, in contrast with the smooth cell contours of normal bacteria. Figures 3.1.5D and 3.1.5H show collapsed and lysed cells compared to normal cells in Figures 3.1.5C and 3.1.5G. Membrane integrity disruption leads to a reduced ability to control the movement of substances in and out of a bacterial cell, thereby causing homeostatic imbalance, cellular metabolic disturbance and death (as shown in Figure 3.1.3). The morphological

alterations agree with the rest of results presented before and confirmed the high antibacterial effect of TiO_2 nanomaterial.

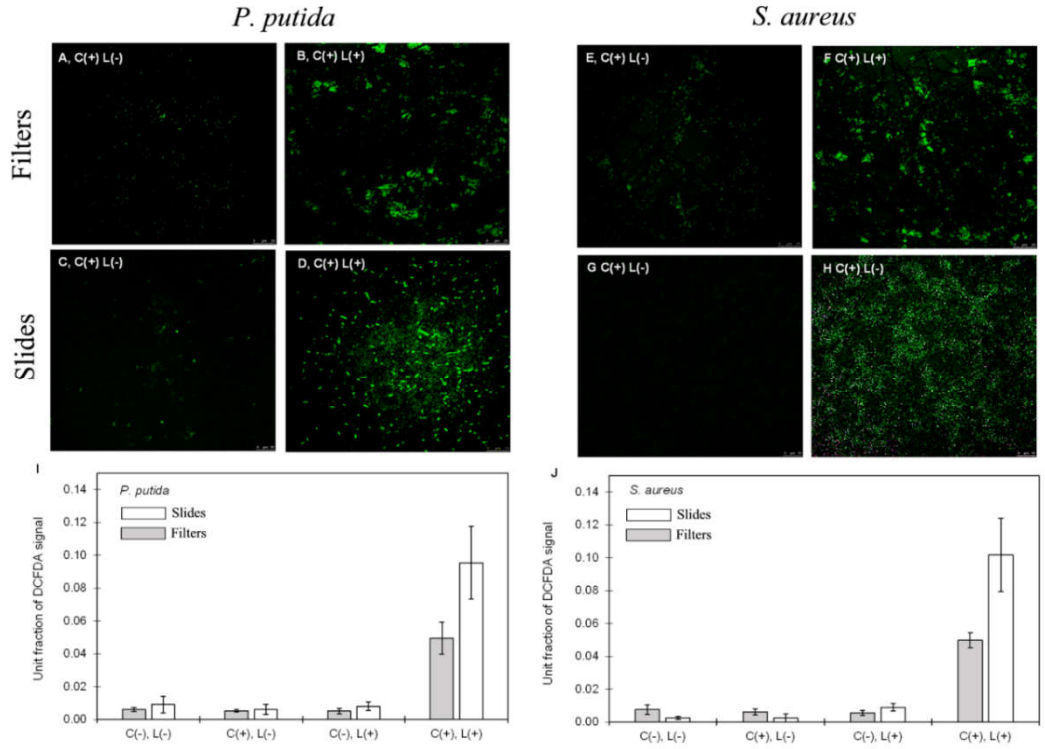

Figure 3.1.4. Confocal microscopy images of *P. putida* (A, B, C, D) and *S. aureus* (E, F, G, H) bacterial cultures on TiO_2 materials showing intracellular green DCF fluorescence because of ROS production. A, B, E and F: filters; C, D, G and H: slides. Figures I and J: grey bars: filters; white bars: slides. C(+): samples with TiO_2, C(-): controls, L(+): irradiated, L(-): non-irradiated. Irradiation conditions: 2 h under Xe arc lamp after 48 h in the dark.

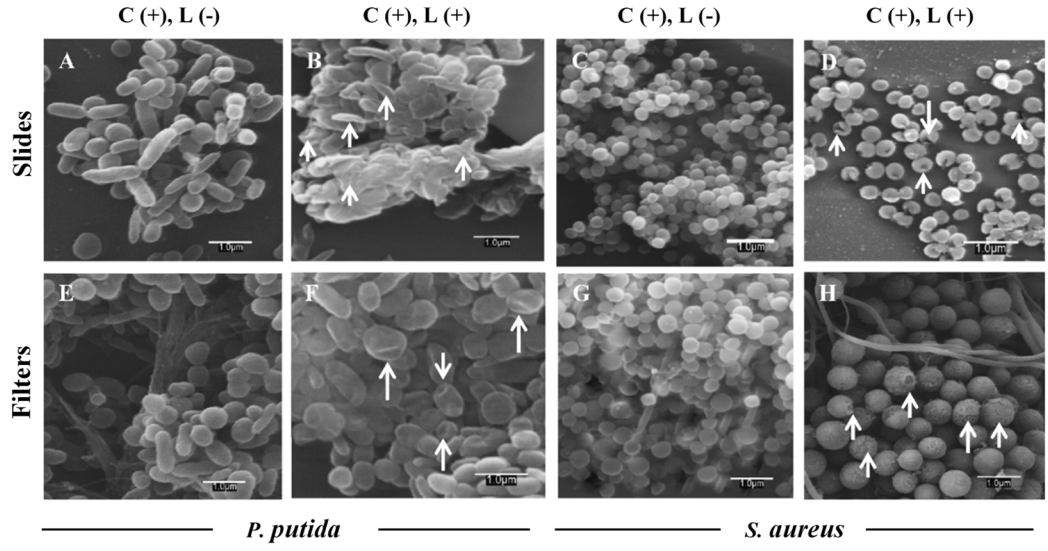

Figure 3.1.5. SEM images of *P. putida* (A, B, E and F) and *S. aureus* (C, D, G and H) biofilms on TiO_2-coated glass slides (A, B, C and D) and TiO_2-coated filters (E, F, G and H) before (A, C, E and G) and after irradiation (B, D, F and H).

ROS formation and cell photo-impairment were clearly cause-effect interconnected, but bacterial colonization not only refers to the attachment of free bacteria to a given surface, but mainly to the formation of structured aggregations of microorganisms and the extracellular polymeric matrix jointly referred to as biofilm. The extracellular polymeric substances (EPS) of microbial biofilms provide the structural stability as well as protection to the biofilm cells and, in fact, one of the main roles of extracellular proteins is to facilitate the initial colonization steps by planktonic cells. EPS is also composed by enzymes, which enable the digestion of exogenous macromolecules for nutrient acquisition and the degradation of structural biofilm macromolecules to release free cells for new colonization processes, among other functions [33]. Biofilm formation visualized using the FilmTracer SYPRO Ruby biofilm matrix stain, which labels most classes of EPS proteins, is shown in Figure 3.1.6. The results showed that biofilm formation took place in all samples. It was also observed (Figure S3.1.4, Supplementary information) that non-irradiated TiO_2-coated surfaces displayed higher amount of EPS for both strains than control filters and slides. The irradiation, either in the presence or absence of TiO_2 coatings did not modify the amount of biofilm revealed by the stain.

The quantification of biofilm formation was also performed by crystal violet staining on TiO_2 deposited on the bottom surface or polystyrene plates as described before. The experiment was designed to quantify the effect of TiO_2 and its Xe-arc light irradiation with the conventional method used to quantify biofilm density in bacterial cultures [34]. The results are shown in Figure 3.1.6A in which the bars correspond to relative biofilm formation (1 for non-irradiated control) together with their 95% confidence intervals. The amount of biofilm formed was higher for samples with TiO_2, which roughly doubled the amount measured by crystal violet staining with respect to controls without TiO_2 in agreement with the results provided by FilmTracer SYPRO Ruby micrographs. In fact, both methods offer complementary information on biofilm components. While crystal violet nonspecifically stains all cells attached to the surface, viable or not, and the EPS matrix, FilmTracer SYPRO Ruby preferentially binds proteins, which are the components providing structural stability to biofilms. Therefore, both using crystal violet and SYPRO Ruby staining it was demonstrated that the irradiation of TiO_2-functionalized slides or filters, did not suppose a reduction in the amount of biofilm and that TiO_2-coated surfaces were more easily colonized than the corresponding filters, slides or polystyrene pristine materials.

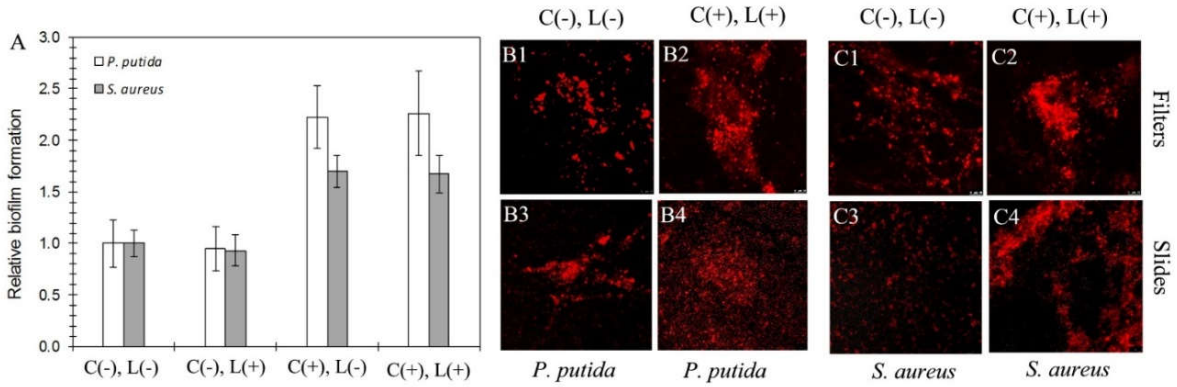

Figure 3.1.6. Left side (A): quantification of biofilms on polystyrene wells by means of the crystal violet method (A). C(-): control wells, C(+): wells with TiO_2, L(-): non-irradiated, L(+): irradiated. Right-side panel: FilmTracer SYPRO Ruby biofilm matrix staining of filters and slides comparing control samples (B1, B3, C1 and C3) and TiO_2-coated and irradiated filters (B2, C2) and slides (B4, C4).

TiO_2-functionalized surfaces can be more susceptible to bacterial colonization because the coating modifies the topography of the surface, offering more adhesion points for bacterial anchoring structures. Also, due to a more favorable energy of interaction. Table 3.1.2 displays the calculated values of ΔG_{SLS} for glass slides with and without TiO_2 and the latter after 5 min visible light irradiation and lawns of the two bacterial strains used in this work. The free energy of interaction, ΔG_{SLS}, gives a measure of the hydrophobicity or hydrophilicity of the surface. When $\Delta G_{SLS} > 0$, the surface is hydrophilic, and when $\Delta G_{SLS} < 0$, it is hydrophobic. No values were recorded for glass filters because probe liquids rapidly spread on their surface making it impossible to measure contact angles. Glass slides were initially hydrophobic and turned even more hydrophobic when covered with TiO_2, reaching ΔG_{SLS} = -100 mJ m^{-2}. Irradiation, however, renders TiO_2 films hydrophilic, with particularly high electron donor component, γ_s^-, of the surface energy. This is consistent with the data showing that the increase of the hydrophilicity of irradiated TiO_2 can be attributed to the increase of the surface hydroxyl groups formed from photogenerated surface holes [6]. The data shown in Table 3.1.2 indicated that both strains were highly hydrophilic, with ΔG_{SLS} values positive and close to those of irradiated TiO_2-covered slides. The preferred biofilm formation on TiO_2-covered slides must be analyzed in view of the forces governing the interactions between cells and surfaces. It has been shown that hydrophobic interactions are responsible for the orientation of adsorbed water molecules, which largely determines the repulsion between surfaces [35]. The maximum interaction expected between two surfaces takes place if the difference in hydrophilicity is not high. Otherwise, adsorbed water molecules would lead

to a net repulsion force [36]. However, bio-surface interactions are more complex. First, hydrophobic and steric interactions have been found to play a significant role in bacterial adhesion [37]. Second, the pure thermodynamic approach assumes direct contact between bacteria and surface, which is not true in the presence of cell appendages, such as pili and flagella as well as the EPS segregated by biofilm forming microorganisms [38]. Third, culture media exposes the surface to many adsorbable organic and inorganic compounds, which complicate the use of physicochemical models [35]. Fourth, the physiochemical characteristics of the surface itself can be modified by the irradiation potentially leading to drastic changes in the ability of microorganisms to colonize them [39]. And finally, there has been repeatedly noted a strong relationship between bacterial adhesion and surface roughness [40]. Surface irregularities are a key factor in promoting (or avoiding) bacterial adhesion and biofilm formation and smooth surfaces do not favor bacterial adhesion, which may explain why the more hydrophobic TiO_2-covered glass slides displayed more extended biofilms formation as shown in Figure 3.1.5.

Biofilms are the dominant lifestyle of microorganisms in all environments and remain a serious concern in the healthcare, food, and marine industries. The reduction of biofilm forming bacteria on photocatalytic surfaces containing TiO_2 nanoparticles has been described elsewhere. Wolfrum *et al*., studied the photocatalytic oxidation of bacteria, spores, and biofilms by measuring carbon dioxide evolution during the irradiation of quartz disks treated with TiO_2 nanoparticles (P25) and found high mineralization degrees in less than 24 h upon UV (365 nm) irradiation at a fluence rate of 104 W m^{-2} [41]. In another work, *Streptococcus mutans* was cultured on a TiO_2 photocatalytic surface for 16 h before irradiation with UV-A (371 nm) resulting in 5–6 orders of magnitude reduction in the number of viable bacteria for a dose of 43 J cm^{-2} (1 h, irradiance 120 W m^{-2}) [42]. For comparison, the near-UV (290-400 nm) solar irradiance monthly average at earth's surface is in the 2.0-13.8 W m^{-2} range [43], which is one order of magnitude lower and similar to the value used in this work. Our work showed that complete impairment of colonizing bacteria could be attained using the TiO_2 nanomaterial described here at realistic UV exposures, but the long-term formation of biofilms must be strictly avoided. The higher MB removal activity per unit mass of TiO_2 loading observed in filters emphasizes the need of proper photocatalyst dispersion. However, the quantification of cell damage by means of DCF fluorescence derived from ROS was higher in the case of slides. This result can be rationalized in terms of the surface structure of both materials

because the flat surface of slides offers fewer possibilities for bacterial colonization and less shadowed shelters. In fact, as it is shown in several images of Figure S3.1.3 and S3.1.4, bacteria tend to grow close to the glass fibers in filters, the lower part of which was relatively protected from the oxidative photo-impairment.

The results reported here showed that the irradiation had no effect on the amount of biofilm remaining after the exposure-treatment cycle with TiO_2-functionalized and irradiated surfaces displaying similar biofilm formation to non-irradiated surfaces. Biofilm formation, the process whereby microorganisms irreversibly attach to a surface in a mode of growth offering protection against antimicrobial agents, took place during the contact with microbial cultures prior to irradiation. The results show that even if bacterial cells could be completely impaired by ROS, the extracellular polymeric matrix could not be removed on TiO_2-functionalized surfaces once the formation of a mature biofilm took place. Some studies concluded that the resistance of bacterial populations towards antibacterial engineered nanomaterials depends on the initial cell density, dense cultures being more resistant than the less ones [44]. The rationale is that the population growth rate is immediately reduced when interacting with less dense populations due to, among other, a decrease in bacterial chemical communication, also stopping biofilm formation. In high density populations, the toxic effect is delayed offering them the possibility to recover. In fact, one major obstacle for biofilm treatment with photodynamic therapies is slime production and growth phases: both are properties of biofilms that reduce photodynamic inactivation of many pathogens such as *S. epidermidis* and *S. aureus*, turning the bacterial communities refractive to antimicrobial agents in oral bacterial biofilms [45]. In our study, despite the high density of bacterial populations used, most of the biofilm cells were damaged and render non-viable due to the photocatalytic effect of TiO_2, as shown in Figure 3.1.3, but the pre-existing biofilm architecture was not destroyed. Our results showed that the photocatalytic activity leading to complete cell impairment was unable to remove the extracellular structure of a mature biofilm, a result that has not been previously reported for self-cleaning surfaces and is important for practical applications, naturally subjected to light-darkness cycles.

3.2.4 Conclusions

TiO_2 nanoparticles consisting of anatase with a primary particle size of about 5 nm were used to functionalize glass microfiber filters and glass slides with a density of 1.98 x 10^{-}

^{3} ± 1.5 x 10^{-4} g cm^{-2} and 8.55 x 10^{-3} ± 3.0 x 10^{-4} g cm^{-2} respectively. TiO_2-functionalizaed surface was hydrophobic, turning hydrophilic upon simulated solar irradiation. The photocatalytic activity was assessed using the methylene blue photodegradation test upon UV-A irradiation at 365 nm. TiO_2-coated filters achieved total MB photo-oxidation with a photodegradation rate 50 times higher than coated slides, which was attributed to the better TiO_2 dispersion in glass fiber filters resulting in better and higher photoactive surface.

The biofilm-forming bacteria *Staphylococcus aureus* and *Pseudomonas putida* grew easily on TiO_2-functionalized filters and glass slides. After 2 h of visible/near UV light (11.2 W m^{-2} in the 290–400 nm range) irradiation practically all cells became non-viable evidencing clear membrane damage. Significant production of ROS was detected using an intracellular stain in all TiO2 irradiated specimens. The biofilm tracking assays performed in this work showed that the photooxidation induced by TiO2, although impairing essentially all bacterial cells, but was unable to remove the biofilm matrix formed during a period of darkness prior to irradiation.

3.2.5 References

[1] K. Liu, L. Jiang, Bio-inspired self-cleaning surfaces, Annual Review of Materials Research, 42 (2012) 231-263.

[2] K.T. Huang, S.B. Yeh, C.J. Huang, Surface modification for superhydrophilicity and underwater superoleophobicity: Applications in antifog, underwater self-cleaning, and oil–water separation, ACS Appl. Mater. Interfaces, 7 (2015) 21021-21029.

[3] S. Nishimoto, B. Bhushan, Bioinspired self-cleaning surfaces with superhydrophobicity, superoleophobicity, and superhydrophilicity, RSC Advances, 3 (2013) 671-690.

[4] B. Su, Y. Tian, L. Jiang, Bioinspired interfaces with superwettability: From materials to chemistry, J. Am. Chem. Soc., 138 (2016) 1727-1748.

[5] R. Wang, K. Hashimoto, A. Fujishima, M. Chikuni, E. Kojima, A. Kitamura, M. Shimohigoshi, T. Watanabe, Light-induced amphiphilic surfaces, Nature, 388 (1997) 431-432.

[6] N. Sakai, A. Fujishima, T. Watanabe, K. Hashimoto, Quantitative evaluation of the photoinduced hydrophilic conversion properties of TiO_2 thin film surfaces by the reciprocal of contact angle, The Journal of Physical Chemistry B, 107 (2003) 1028-1035.

[7] K. Nakata, A. Fujishima, TiO_2 photocatalysis: Design and applications, Journal of Photochemistry and Photobiology C: Photochemistry Reviews, 13 (2012) 169-189.

[8] C. Euvananont, C. Junin, K. Inpor, P. Limthongkul, C. Thanachayanont, TiO_2 optical coating layers for self-cleaning applications, Ceramics International, 34 (2008) 1067-1071.

[9] O.K. Dalrymple, E. Stefanakos, M.A. Trotz, D.Y. Goswami, A review of the mechanisms and modeling of photocatalytic disinfection, Applied Catalysis B: Environmental, 98 (2010) 27-38.
[10] H.A. Foster, I.B. Ditta, S. Varghese, A. Steele, Photocatalytic disinfection using titanium dioxide: spectrum and mechanism of antimicrobial activity, Appl. Microbiol. Biotechnol., 90 (2011) 1847-1868.
[11] Y. Cai, M. Strømme, K. Welch, Disinfection kinetics and contribution of reactive oxygen species when eliminating bacteria with TiO_2 induced photocatalysis, Journal of Biomaterials and Nanobiotechnology, 5 (2014) 200.
[12] T. Sato, M. Taya, Copper-aided photosterilization of microbial cells on TiO_2 film under irradiation from a white light fluorescent lamp, Biochemical Engineering Journal, 30 (2006) 199-204.
[13] V. Cohen-Yaniv, N. Narkis, R. Armon, Photocatalytic inactivation of *Flavobacterium* and *E. coli* in water by a continuous stirred tank reactor (CSTR) fed with suspended/immobilised TiO_2 medium, Water Sci. Technol., 58 (2008) 247-252.
[14] M. Cho, H. Chung, W. Choi, J. Yoon, Linear correlation between inactivation of *E. coli* and OH radical concentration in TiO_2 photocatalytic disinfection, Water Res., 38 (2004) 1069-1077.
[15] L. Hall-Stoodley, J.W. Costerton, P. Stoodley, Bacterial biofilms: from the natural environment to infectious diseases, Nature Reviews Microbiology, 2 (2004) 95-108.
[16] H.P. Blaschek, H.H. Wang, M.E. Agle, Biofilms in the Food Environment, 2007.
[17] C. de la Fuente-Núñez, F. Reffuveille, L. Fernández, R.E.W. Hancock, Bacterial biofilm development as a multicellular adaptation: antibiotic resistance and new therapeutic strategies, Current Opinion in Microbiology, 16 (2013) 580-589.
[18] R. Van Houdt, C.W. Michiels, Biofilm formation and the food industry, a focus on the bacterial outer surface, Journal of Applied Microbiology, 109 (2010) 1117-1131.
[19] M.E. Shirtliff, J.T. Mader, A.K. Camper, Molecular interactions in biofilms, Chemistry and Biology, 9 (2002) 859-871.
[20] D.H. Kim, M.A. Anderson, W.A. Zeltner, Effects of firing temperature on photocatalytic and photoelectrocatalytic properties of TiO_2, Journal of Environmental Engineering, 121 (1995) 590-594.
[21] R. Jenkins, R.L. Snyder, Index, Introduction to X-ray Powder Diffractometry, John Wiley & Sons, Inc.1996, pp. 397-403.
[22] C.J. van Oss, Development and applications of the interfacial tension between water and organic or biological surfaces, Colloids and surfaces B: Biointerfaces, 54 (2007) 2-9.
[23] C.J. Van Oss, M.K. Chaudhury, R.J. Good, Interfacial Lifshitz-van der Waals and polar interactions in macroscopic systems, Chem. Rev., 88 (1988) 927-941.
[24] DIN Standards Committee Materials Testing: Anti-soiling chemical activity using adsorbed organics under solid/solid conditions - Part 1: Dyes on porous surfaces, 2016.
[25] J.M. Allen, S.K. Allen, S.W. Baertschi, 2-Nitrobenzaldehyde: A convenient UV-A and UV-B chemical actinometer for drug photostability testing, Journal of Pharmaceutical and Biomedical Analysis, 24 (2000) 167-178.
[26] M. Fletcher, The effects of proteins on bacterial attachment to polystyrene, J. Gen. Microbiol., 94 (1976) 400-404.

[27] A. Gomes, E. Fernandes, J.L.F.C. Lima, Fluorescence probes used for detection of reactive oxygen species, Journal of Biochemical and Biophysical Methods, 65 (2005) 45-80.
[28] A. Almaguer-Flores, P. Silva-Bermúdez, R. Galicia, S.E. Rodil, Bacterial adhesion on amorphous and crystalline metal oxide coatings, Materials Science and Engineering: C, 57 (2015) 88-99.
[29] K. Hashimoto, H. Irie, A. Fujishima, TiO_2 photocatalysis: a historical overview and future prospects, Japanese Journal of Applied Physics, 44 (2005) 8269.
[30] L. Boulos, M. Prévost, B. Barbeau, J. Coallier, R. Desjardins, LIVE/DEAD® BacLight™: application of a new rapid staining method for direct enumeration of viable and total bacteria in drinking water, Journal of Microbiological Methods, 37 (1999) 77-86.
[31] O.N. Mileyeva-Biebesheimer, A. Zaky, C.L. Gruden, Assessing the impact of titanium dioxide and zinc oxide nanoparticles on bacteria using a fluorescent-based cell membrane integrity assay, Environmental Engineering Science, 27 (2010) 329-335.
[32] X. Lin, J. Li, S. Ma, G. Liu, K. Yang, M. Tong, D. Lin, Toxicity of TiO_2 nanoparticles to *Escherichia coli*: effects of particle size, crystal phase and water chemistry, PLOS ONE, 9 (2014) e110247.
[33] H.C. Flemming, J. Wingender, The biofilm matrix, Nature Reviews Microbiology, 8 (2010) 623-633.
[34] E. Burton, N. Yakandawala, K. LoVetri, M.S. Madhyastha, A microplate spectrofluorometric assay for bacterial biofilms, Journal of Industrial Microbiology & Biotechnology, 34 (2007) 1-4.
[35] C.J. van Oss, Hydrophobicity and hydrophilicity of biosurfaces, Current Opinion in Colloid & Interface Science, 2 (1997) 503-512.
[36] C.J. van Oss, Hydrophobicity of biosurfaces — Origin, quantitative determination and interaction energies, Colloids and Surfaces B: Biointerfaces, 5 (1995) 91-110.
[37] Y.L. Ong, A. Razatos, G. Georgiou, M.M. Sharma, Adhesion forces between *E. coli* bacteria and biomaterial surfaces, Langmuir, 15 (1999) 2719-2725.
[38] K. Hori, S. Matsumoto, Bacterial adhesion: From mechanism to control, Biochemical Engineering Journal, 48 (2010) 424-434.
[39] B. Jalvo, J. Santiago-Morales, P. Romero, R. Guzman de Villoria, R. Rosal, Microbial colonisation of transparent glass-like carbon films triggered by a reversible radiation-induced hydrophobic to hydrophilic transition, RSC Advances, 6 (2016) 50278-50287.
[40] M. Katsikogianni, Y.F. Missirlis, Concise review of mechanisms of bacterial adhesion to biomaterials and of techniques used in estimating bacteria-material interactions, Journal of European Cells and Materials, 8 (2004) 37-57.
[41] E.J. Wolfrum, J. Huang, D.M. Blake, P.C. Maness, Z. Huang, J. Fiest, W.A. Jacoby, Photocatalytic oxidation of bacteria, bacterial and fungal spores, and model biofilm components to carbon dioxide on titanium dioxide-coated surfaces, Environ. Sci. Technol., 36 (2002) 3412-3419.
[42] Y. Cai, M. Strømme, Å. Melhus, H. Engqvist, K. Welch, Photocatalytic inactivation of biofilms on bioactive dental adhesives, Journal of Biomedical Materials Research Part B: Applied Biomaterials, 102 (2014) 62-67.
[43] C.R.N. Rao, T. Takashima, W.A. Bradley, T.Y. Lee, Near ultraviolet radiation at the earth's surface: measurements and model comparisons, Tellus B, 36 (1984) 286-293.

[44] N. Musee, M. Thwala, N. Nota, The antibacterial effects of engineered nanomaterials: implications for wastewater treatment plants, Journal of Environmental Monitoring, 13 (2011) 1164-1183.
[45] J.F. O'Neill, C.K. Hope, M. Wilson, Oral bacteria in multi-species biofilms can be killed by red light in the presence of toluidine blue, Lasers in Surgery and Medicine, 31 (2002) 86-90.

3.3 Part II: Antibacterial surfaces prepared by electrospray coating of photocatalytic nanoparticles

3.3.1 Introduction

In the last 25 years, photocatalytic titanium dioxide (TiO_2) has been extensively studied for the removal of pollutants from water and air among other environmental applications [1, 2]. When TiO_2 surfaces are photoexcited by near-ultraviolet light (UV-A, wavelengths 320–400 nm) electrons from the valence band migrate to the conduction band, forming an e^-/h^+ pairs that generate, in the presence of water and oxygen, oxidants species like hydroxyl radical, hydrogen peroxide and superoxide anion, which, apart from removing many pollutants, convey biocidal activity [3, 4]. TiO_2 by itself is non-toxic for human beings, relatively inexpensive, environmentally friendly, chemically stable and effective under weak solar irradiation in atmospheric environments [5-7]. Indeed, the antimicrobial properties of photoactivated TiO_2 have been explored for a number of cell types, either in suspended form or supported on different substrates [8-11]. However, only a few publications addressed the specific subject of biofilm formation on photocatalytic TiO_2 [12-14].

Electrospray is a method that produces micron sized droplets from the nozzle tip by applying an electric field [15]. Together with electrospinning constitutes a field known as electrohydrodynamic techniques, which transform liquid droplets into nanomaterials using strong electric fields. While electrospraying refers to the formation of nanoparticles, electrospinning describes the fabrication of fibrous structures [16]. In electrospray, the suspension flowing out from a nozzle tip which is forced to disperse into fine droplets by the electric field created by a high voltage source. The size of electrosprayed droplets range from hundreds micrometers down to several tens of nanometer depending on the physical properties of the suspension, the liquid flow rate and the voltage applied between nozzle and collector [15, 17, 18]. Electrospray is easily scaled-up to industrial processes from laboratory data [19]. The interest in industrial or laboratory applications has recently prompted the search for new, more effective techniques which allow control of the processes in which the droplets are involved [15].

Staphylococcus aureus (*S. aureus*) is a prominent nosocomial pathogen and a major cause of biomaterial-associated infections. The success of *S. aureus* as a pathogen is due in part to its ability to adapt to stressful environments [20]. One adaptation strategy is biofilm

formation. Biofilms are complex communities of cells embedded in an extracellular polymeric matrix formed by polysaccharides, proteins, and nucleic acids, which protect cells from adverse conditions [21]. Biofilms are of particularly concern due to their resistance to host defense mechanisms and to conventional disinfection processes. Also because, once formed, they are difficult to remove [22].

In this work, the electrospray technique has been used to produce TiO_2-coated surfaces from suspensions of nanoparticles prepared by means of a sol-gel process. The main goal was to investigate its photocatalytic antimicrobial activity against *Staphylococcus aureus*. Specifically, the attention was focused on biofilms previously grown in the dark, in the dark using TiO_2-functionalized surfaces with different surface coverage which were subsequently irradiated for different periods to emulate solar irradiation conditions.

3.3.2 Materials and methods

3.3.2.1 Synthesis and characterization of the Titanium dioxide nanoparticles

Crystalline anatase nanoparticles were prepared by a sol-gel synthesis. Briefly, 1.43 mL of concentrated nitric acid (Panreac 65%) were mixed with 100 mL of deionized water by vigorous stirring. Then, 16.5 mL of titanium isopropoxide (Sigma-Aldrich 97%) were added dropwise. The mixture was kept closed and moderately stirred for at least three days or until complete peptization revealed because the white initial precipitate turns into a translucent suspension. Finally, the translucent sol was transferred to a glass bottle and stored in the dark and refrigerated before electrospray. No other conditioning was performed as the presence of organic volatile solvents do not interfere with electrospray and high conductivity is required for it. For other applications a dialysis (3500 MWCO) cleaning procedure is commonly carried out using deionized water until TOC < 1 mg L^{-1} and pH approx. 3. The fact that this post-conditioning step is not required is an important advantage of electrospray.

Two different TiO_2 nanoparticle suspensions (TiO_2 20 wt% and TiO_2 40 wt%) were characterized using Dynamic Light Scattering (DLS) and zeta potential (ζ-potential), measured via electrophoretic light scattering in a Zetasizer Nano ZS (Malvern Instruments, Malvern, UK) equipment. Surface ζ-potential was measured using the Capillary Zeta Cell DTS 1070 from Malvern. The pH and electrical conductivity of the suspensions were measured using a multimeter (Crison MM 40+, Spain). Surface tension was determined using the pendant drop method by means of an optical contact angle

meter (Krüss DSA25 Drop Shape Analysis System) and the Java open source ImageJ software [23].

3.3.2.2 Electrospray

Figure 3.2.1 presents a schematic illustration of the experimental setup used for the electrospray (ES) TiO_2 coating. Before the ES process, the TiO_2 nanoparticle suspension was sonicated using an ultrasonic probe VC505 (500W, Sonics and Materials Inc.) for 10 min carried out in short intervals at 20% amplitude followed by 10 min of magnetic stirring. The ES equipment consisted of a Heinzinger LNC 30000 high voltage power supply and a Harvard PHD PHD22/2000 syringe pump. The TiO_2 nanoparticle suspensions were deposited into a 5 mL syringe with a 23-gauge stainless steel blunt-tip needle at its end, which was connected to the high voltage power supply to create the required electric field. The voltage used was 19 kV and the flow rate was 0.1 mL/h. Electrosprayed drops were deposited on 13 mm diameter round glass coverslips (VWR, Germany), attached to a flat collector (16 cm x 16 cm aluminum grid) separated 10 cm from the needle tip. The flat collector and the needle were set horizontally in order to avoid gravity deposition. TiO_2 nanoparticles were sprayed for 2 and 4 h in order to obtain different surface coating densities. No polymer was added to the ES solution. Before and after ES coating, the cover supports were dried at 50° C for 1 h and accurately weighted to assess the amount of deposited photocatalytic material.

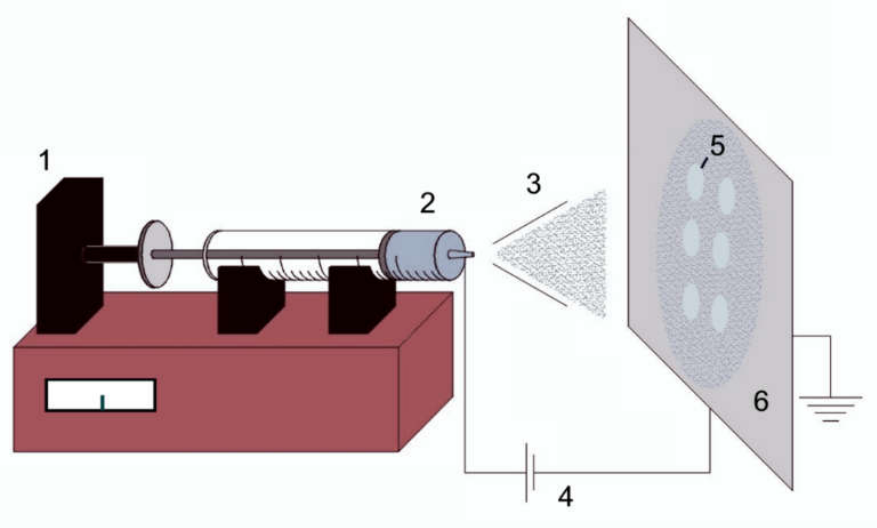

Figure 3.2.1. Schematic illustration of the electrospray setup for TiO_2 coating. (1) Syringe pump, (2) TiO_2 nanoparticle suspensions in a 5 mL syringe, (3) TiO_2 electrospray, (4) High voltage power supply, (5) Glass coverslips coated with electrosprayed TiO_2 electrospray, (6) Grounded collector.

3.3.2.3 Characterization of electrosprayed surfaces

Uncoated and electrosprayed TiO_2 coated surfaces were observed with scanning electron microscopy (SEM, ZEISS DSM- 950). Each sample was sputter-coated with gold prior to analysis. The wettability of the surfaces was characterized on the optical contact angle meter Krüss DSA25 Drop Shape Analysis System described in a previous section by means of the sessile drop technique. Samples were placed on the test cell and Mili-Q water drops were deposited on the coverslip surfaces by delivering syringe. Water contact angle (WCA) values were an average of at least three measurements on different positions of each surface. WCA measurements were taken at room temperature.

3.3.2.4 Photocatalytic bioassays

The bacterial strain used in this study to test the antibacterial activity of TiO_2 photoactivated materials was *Staphylocuccus aureus* (CECT 240 equivalent to ATCC 6538P). *S. aureus* was grown overnight in Nutrient Bacterial medium (NB, for 1 L solution in distilled water, beef extract 5 g, peptone 10 g, NaCl 5 g, pH was adjusted to 7.2) while shaking at 37 °C. The bioassays were performed using a flow-cell system as described previously with some modifications [24, 25]. Briefly, biofilm growth was allowed for 9 h or 18 h in darkness, on the surface of coated and uncoated coverslips kept in flow chambers 5 mm depth, 25 mm width and 50 mm length provided by Sigma-Aldrich. Three coated or uncoated circular coverslips were placed in each flow-cell and a total amount of six flow-cells were used at the same time (Figure 3.2.2). The entire flow system was connected by standard PVC tubing (1/16" ID x 1/8" OD, Sigma-Aldrich), except for the tubing going through the peristaltic pump, which was silicone 1/8" ID x 1/4" OD from Cole-Parmer. The circulating liquid was inoculated with exponentially growing cultures of *S. aureus* diluted in NB medium to an OD_{600} of 0.0138 (10^8 cells/mL). The feed bottle was maintained in a water bath incubator at 30 °C and the liquid culture it was pumped using a peristaltic pump (Watson-Marlow, 101 U/R) at a constant rate. The linear velocity of the liquid through the flow-cells was 0.5 mm s^{-1} kept constant along the experiments. Immediately after the dark period of biofilm formation, the samples were continuously irradiated for 15 h or 6 h (to complete a 24 h cycle in all cases) using a simulated solar irradiation provided by a Heraeus TQ Xe 150 Xe-arc lamp at a distance of 15 cm from the flow-cells. This lamp has a light spectral distribution comprising wavelengths shorter than 300 nm (UV-C range) and between 300 and 400 nm (UV-B, -A range). The 290-400 nm range was 5.8 % of the total output, while the visible part of

the spectrum (400-700 nm) supposed 94.2 % > 400 nm of the total radiant power emitted by the lamp. Fluence rate, measured in the 290-400 range, was 11.2 W m^{-2} as determined using 2-nitrobenzaldehyde as chemical actinometer [26].

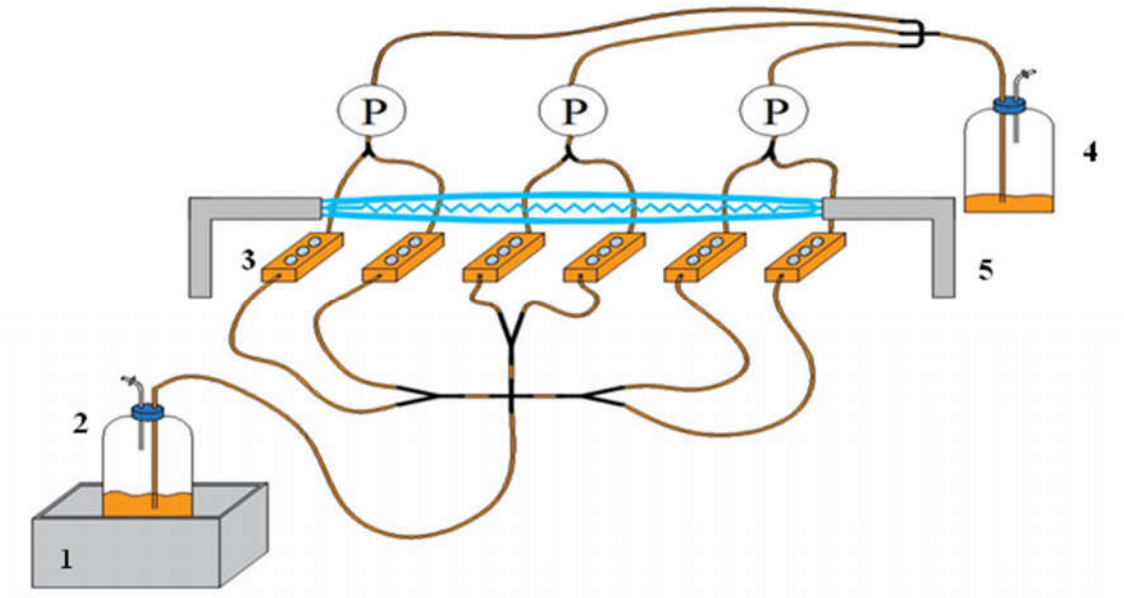

Figure 3.2.2. Schematic illustration of the flow-cell systems for photocatalytic bioassays. (1) Thermostatic water bath, (2) Feed tank with *S. aureus* culture, (3) TiO_2 coated/uncoated coverslips inside of the flow-cell chambers, (4) Effluent culture, (5) Xe-arc lamp. P: Peristaltic pump.

3.3.2.5 Bioanalytical procedures

After completing the photocatalytic assays consisting of biofilm formation and irradiation treatment as described before, the coverslips were transferred to 24-well polystyrene plates. The biofilm was quantified based on optical density measurements following a modification of the method of Fletcher as described elsewhere [27, 28]. For it, approximately 200 µL of a crystal violet 0.1% solution were extended over the washed surface of each coverslip and incubated for 15 min in order to allow the staining of adhered cells. Excess stain was eliminated by rinsing with distilled water. Plates were air dried and 1 mL of 95% ethanol was added to each well in order to extract crystal violet from cells. Distaining was performed overnight while gently shaking. Finally, the dye was measured at OD_{590}. Every measurement was performed at least three times for each experimental condition.

Bacterial viability assays were performed using LIVE/DEAD BacLight Bacterial Viability Kit (Molecular Probes, Invitrogen Detection Technologies, Carlsbad, CA, USA). Under LIVE/DEAD staining, all cells exhibit green fluorescence (SYTO 9), whereas nonviable bacterial cells display red fluorescence (Propidium iodide, PI) with dye uptake depending upon cell membrane integrity. For the staining of films 10μL of BacLight stain (a mixture of SYTO 9 and PI in DMSO, according to the manufacturer's recommendations) were used. The incubation was performed in the dark for 15-30 min at room temperature. For green fluorescence (SYTO 9) excitation was performed at 488 nm and emission at 500-575 nm. For red fluorescence (PI, dead cells), the excitation/emission wavelengths were 561 nm and 570-620 nm respectively.

In order to visualize the extracellular polymeric matrix, the biofilms were stained with 200 μL FilmTracer SYPRO Ruby (Molecular Probes, Invitrogen) per sample, incubated in the dark for 30 min at room temperature, and rinsed with distilled water. Then, the coverslips were observed using confocal microscopy (Confocal SP5, Leica Microsystems, Germany) with excitation/emission wavelengths of 450 nm and 610 nm respectively. For all bioassays, independent runs were performed together with their respective controls.

3.3.3 Results and discussion

3.3.3.1 Electrospray parameters

In a typical electrospray configuration, a conductive liquid is pumped at certain flow rate through a tube, forming a meniscus at its end. Due to the electrical field, the free charge in the conductive liquid meniscus generates an electric stress that opposes surface tension and forces the meniscus to adopt a conical shape [29]. The liquid jet eventually breaks into drops due to capillary instabilities, giving rise to an aerosol of charged droplets [30]. The droplet diameter is mainly depending on liquid conductivity, ranging from hundreds of micrometers to a few nanometers for the most conducting ones, with minor influence of the injected flow rate or voltage [31, 32]. In addition, it is known that electrospray is initiated when the coulomb repulsion in the solution is strong enough to overcome the surface tension [18]. Table 3.2.1 shows the effect of TiO_2 concentration on the properties of the electrospray suspension. The increase in TiO_2 concentration from 20 to 40 wt% in the electrospray suspension decreased surface tension 16% and increased electrical conductivity 60%. ζ-potential revealed a colloidal system with neutral particles at pH 7.

Table 3.2.1. Effect of TiO_2 concentration on the solution properties

Solution	Electrical conductivity ($\mu s\ cm^{-1}$)	Surface Tension ($mN\ m^{-1}$)	ζ-potential (pH 7.0, mV)	DLS (nm)
Water	0.046 ± 0.002	71.7 ± 0.2	–	–
TiO_2 (20 wt%)	$2.39 \cdot 10^4$ ± 0.003	45 ± 0.7	1.15 ± 0.7	574 ± 18.7
TiO_2 (40 wt%)	$3.47 \cdot 10^4$ ± 0.003	37.7 ± 0.4	0.66 ± 0.8	591 ± 17.4

It is a well-known fact that water solutions are not directly suitable for electrospraying due to their high surface tension [15, 29, 33]. In the case of the TiO_2 20 wt% suspension the surface tension decreased to 45 mN m^{-1}. The results showed that it was not possible to obtain a stable ES regime for the TiO_2 20 wt% suspension as prepared. The addition of polyethylene-oxide (PEO) at low concentration (< 1 wt%) allowed reducing the surface tension to 39 mN m^{-1}, which was low enough to allow electrospraying. Better results, however, were obtained for the TiO_2 40 wt% suspension, the surface tension of which was only 37.5 mN m^{-1}, low enough to obtain perform surfactant-free ES. The addition of PEO did not significantly modify the conductivity, showing that the control of surface tension was enough to obtain a good ES coating from TiO_2 nanoparticle suspensions used in this work.

3.3.3.2 TiO_2 nanoparticle electrospray coatings

The ES process was performed using two different spray time lengths, to get two different photocatalyst loads on the surface of glass coverslips. The nomenclature used for the electrosprayed samples and the values obtained for the surface density of TiO_2 and water contact angle (WCA) on the surface of the coverslips are shown in Table 3.2.2. The mean surface density of the samples with higher surface coverage, denoted as C(++), was 1/3 more than that of those with lower amount of electrosprayed TiO_2. The WCA on the surface of neat glass coverslips (without TiO_2 coating) was 75.2°± 2.8°, less hydrophilic that that of TiO_2 coated surfaces, for which WCA decreased to values in the 55-60° range. The wettability considerably increased leading to clearly hydrophilic surfaces upon irradiation. WCA dropped to values around 20-30°, after 6 h of irradiation treatment, and ~10° after 15 h under Xe-arc lamp. The WCA were lower for C(++) samples than for the surface with lower TiO_2 coverage, C(+), but the differences were minor. It has been previously reported that titanium dioxide surface experiences hydrophilic-hydrophobic transition induced by irradiating flat samples with light of specific wavelengths [34-36].

The contact angle of water on a clean TiO_2 surface can be repeatedly cycled between practically zero, after UV irradiation or 50-60° after exposure to visible light to their initial values, which recovered after dark storage [34-36]. This photo-induced wettability transition has been attributed to the breaking of Ti─O lattice bonds by photogenerated holes. Water molecules would then coordinate the titanium site leading to an increase in the number of surface hydroxyl groups. As the newly formed hydroxyl groups are less stable than the initial doubly coordinated hydroxyl groups, the material restores its initial hydrophobicity in the space of a few hours after irradiation [37].

Table 3.2.2. Surface characterization by surface density of TiO_2 and water contact angle measurements. (WCA = Water contact angle).

	Glass coverslip	Low coverage TiO_2 (40 wt%)	High coverage TiO_2 (40 wt%)
Identifier	C(-)	C(+)	C(++)
TiO_2 surface density (g cm^{-2})	-	$2.09 \cdot 10^{-3} \pm 1.2 \cdot 10^{-4}$	$2.78 \cdot 10^{-3} \pm 2.3 \cdot 10^{-4}$
WCA (°) Non-irradiated	75.2 ± 2.8	59.3 ± 2.7	56.4 ± 2.1
WCA (°) Irradiated for 6 h, 30°C	73.7 ± 2.1	28.5 ± 1.5	21.2 ± 3.3
WCA (°) Irradiated for 15 h, 30°C	75.4 ± 2.6	11.6 ± 2.2	9.6 ± 1.3

Different modes of electrospraying are distinguished in the literature depending on the form of the meniscus, the pattern of motion of the jet, and the way it disintegrates into droplets [15]. In our particular case, the liquid was ejected directly from the capillary nozzle as a combination of regular large drops (dripping mode) and fine droplets (micro-dripping mode), although cone-jet modes were obtained when PEO was added to the solution. Figure 3.2.3 shows SEM images of the electrospray coatings obtained from the polymer-free TiO_2 40 wt% solution. The electrosprayed surface consisted of a well dispersed pattern of solid TiO_2 spheres forming aggregates typically under 400 nm, which was consistent with the DLS size obtained for the electrosprayed suspension (Figure 3 a-c). The morphology of the drops was very similar in C(+) and C(++) samples. In some cases, the spherical shape of the dispersed particles appeared distorted with axial elongation as a result of the more stretching suffered by highly charged particles [38, 39].

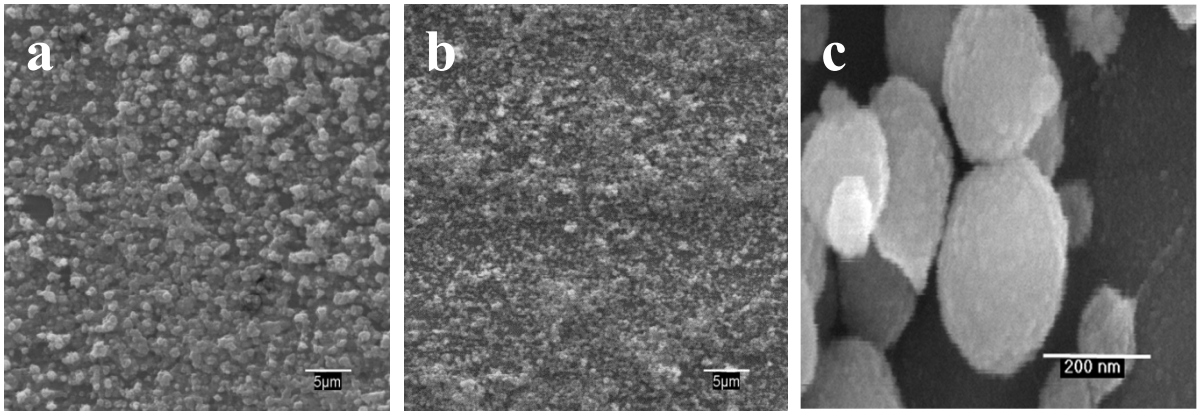

Figure 3.2.3. SEM images of TiO_2 40 wt% electrospray coating of low TiO_2 loading, C (+) (a), and high TiO_2 loading, C (+ +) (b and c) on glass coverslips.

3.3.3.3 Photocatalytic antibacterial effect

Two different sets of flow-cell photocatalytic assays were carried out, all of them lasting 24 h. In one set, the samples were incubated in the dark for 9 h, while the other was kept under the same conditions for 18 h. The samples, corresponding to the microbial colonization and biofilm growth, were taken then for some measurements while others were subsequently irradiated with the Xe-arc lamp mentioned before for 15 or 6 h, depending on the case, to complete an overall contact with the bacterial culture in flow regime of 24 h (9 + 15 or 18 + 6). These conditions were created to simulate the light-dark cycles that can be typically encountered in summer and winter conditions in average latitudes. In both assays cell viability and biofilm quantification was assessed by Live/Dead bacterial viability and crystal violet staining, respectively. Biofilm formation was visualized using the FilmTracer SYPRO Ruby biofilm matrix staining.

Figure 3.2.4 shows confocal images for Live/Dead bacterial viability staining on control coverslips without photocatalyst coating, C(-), and coverslips electrosprayed with low, C(+), and high, C(++), TiO_2 surface coverage either for non-irradiated, L(-), and irradiated, L(+), samples. During the 9 h or 18 h dark period, the growth of *S. aureus* took place without significant cell impairment both in C(-) and in C(+) or C(++) TiO_2 coated samples. This is clearly noted by the absence of red-marked (cell membrane-damaged) bacteria in Figure 3.2.4 a, b, c, g, h and i. Certain cells appeared yellowish in C(+) L(-) and C(++) L(-) samples (samples with TiO_2 but kept in the dark). Yellow cells are considered viable and the effect could be associated to the irradiation suffered during confocal microscopy observations [40]. Conversely, the presence of the photocatalytic material remarkably reduced the viability of the cells on TiO_2 coated coverslips under

Xe-arc irradiation, as noted by the reduction of the number of cells and by the fact that the few remaining were clearly PI-marked as non-viable ones (Figure 3.2.4 e, f, k and l). The highest cell impairment was observed in C(++) samples after 15 h of irradiation, while Xe-arc lamp irradiation did not induce significant bacterial damage in the absence of TiO_2 (Figure 3.2.4 d and g).

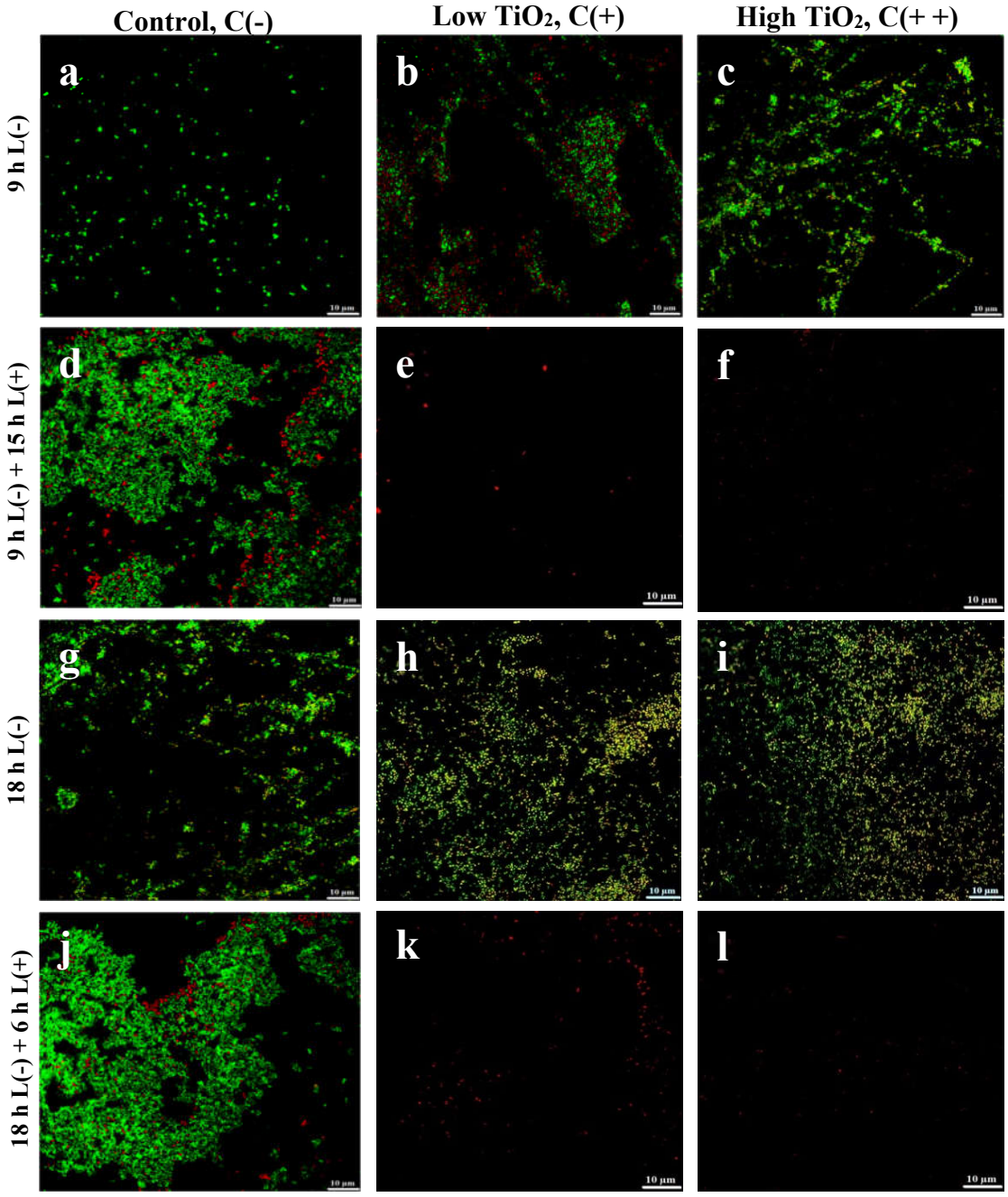

Figure 3.2.4. Live/Dead confocal micrographs of *S. aureus* on non-coated control coverslips C(-) (a, d, g and j) and TiO_2 electrosprayed coverslips with low, C(+), b, e, h and k, and high, C(++), c, f, I and l, surface coverage. Irradiated and non-irradiated samples are denoted by L(+) and L(-) respectively. Dark period: 9 h and 18 h. Irradiation time: 15 h and 6 h. Scale bar: 10 µm.

Many researches and previous studies carried out by our group (chapter 3.1) revealed that the cause for visible light damage in bacterial cells exposed to photocatalytic irradiated material was the production of reactive oxygen species (ROS) as intermediates of oxygen-dependent photosensitized reactions [41-45]. The photocatalytic action and the oxidative damage caused trigger the decreased expression of a large array of genes and proteins specific for regulatory, signaling and growth functions, in parallel with subsequent selective effects on coenzyme-independent respiration, cell wall structure and resistance ion homeostasis such us iron [41-45], which is an essential for cell growth and survival [20, 46]. Oxidative radicals disrupt the first cell defense barrier (the cell wall), which provides strength and rigidity. To compensate for these deficiencies, the cells react by activating a second defense barrier (the cell membrane), and detoxification and repair mechanisms [45]. However, after the irradiation periods performed in this study (6 h and 15 h) the cells were no able to survive even if they activated the mechanisms previously mentioned [39, 45].

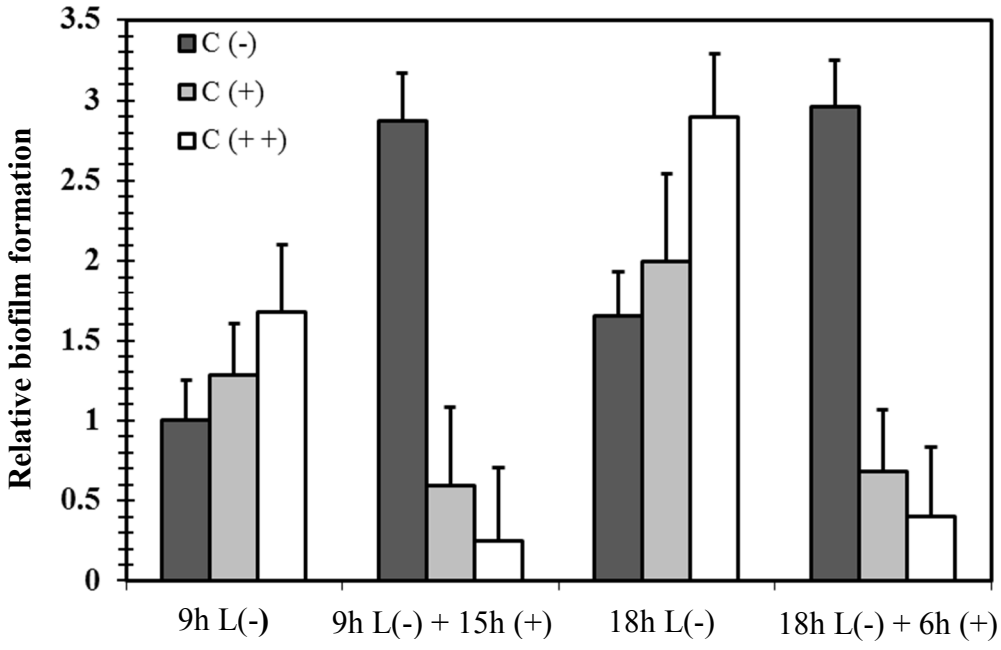

Figure 3.2.5. Quantification of biofilms by crystal violet method in control coverslips C (-) (dark grey bars); low C (+) (light grey bars) and high C (+ +) (white bars) TiO_2 electrosprayed coverslips, for non- irradiated L (-) and irradiated L (+) samples. Darkness period: 9 h. Irradiation time: 15 h.

The total amount of biomass on the surface of TiO_2 coated and uncoated coverslips was quantified by crystal violet staining before and after the dark incubation and after Xe-arc irradiation as described before. The results are shown in Figure 3.2.5, in which the bars

correspond to relative biofilm formation (1 for uncoated and non-irradiated control) together with their 95% confidence intervals. In both flow-cell biofilm assays the amount of biofilm formed, after the darkness period incubation (9 h or 18 h), was higher for samples with high TiO_2 load on the surface, specifically for the case of longer incubation time in the dark (18 h). However, after each illumination period the amount of biomass accumulated on the surface of the photocatalyst coated samples was reduced 2.2-fold, for C(+), and 8.5-fold for C(++), after 15 h of irradiation, and 2.8-fold for C(+), and 7.2-fold for C(+ +), after 6 h of irradiation compared to the same samples before irradiation. On the contrary, biofilm formation increased in uncoated controls due to the lack of harmful effect of irradiation without photocatalyst material on the surface.

As described previously, TiO_2 coated surfaces displayed moderate hydrophilicity. This fact could explain, together with the roughness offered by this material compared to the smooth surface of the uncoated samples, the greater bacterial adhesion found on the electrosprayed materials [47, 48]. In this case the more hydrophilic TiO_2 coated surfaces were more easily colonized during the dark exposure to bacterial cultures in agreement with the hydrophilic character of the strain, with a WCA of 21.8° ± 4.6°. The maximum interaction expected between two surfaces takes place if the difference in hydrophilicity is not high. Otherwise, adsorbed water molecules would lead to a net repulsion force [49]. This fact was also previously reflected in the crystal violet quantification (Figure 3.2.5) and in the higher amount of extracellular matrix formed in C(++) samples (Figure 3.2.6 c and i). However, the rationalization of bacterial attachment to surfaces exclusively in terms of hydrophilic-hydrophobic interactions has low predictive value at least due to two reasons. First, cell binding is affected by the culture media used due to differences in surface tension or the absorption of organic and inorganic compounds, which modify the way microorganisms adhere [50]. Second, bacterial morphology makes cell-surface interactions a complex issue due to the existence of cell appendages and adhesion structures avoiding direct contact (Figure 3.2.7 g, h and i) [51]. Besides, the physiochemical characteristics of the surface itself can be modified by the irradiation potentially leading to drastic changes in the ability of microorganisms to colonize them [47].

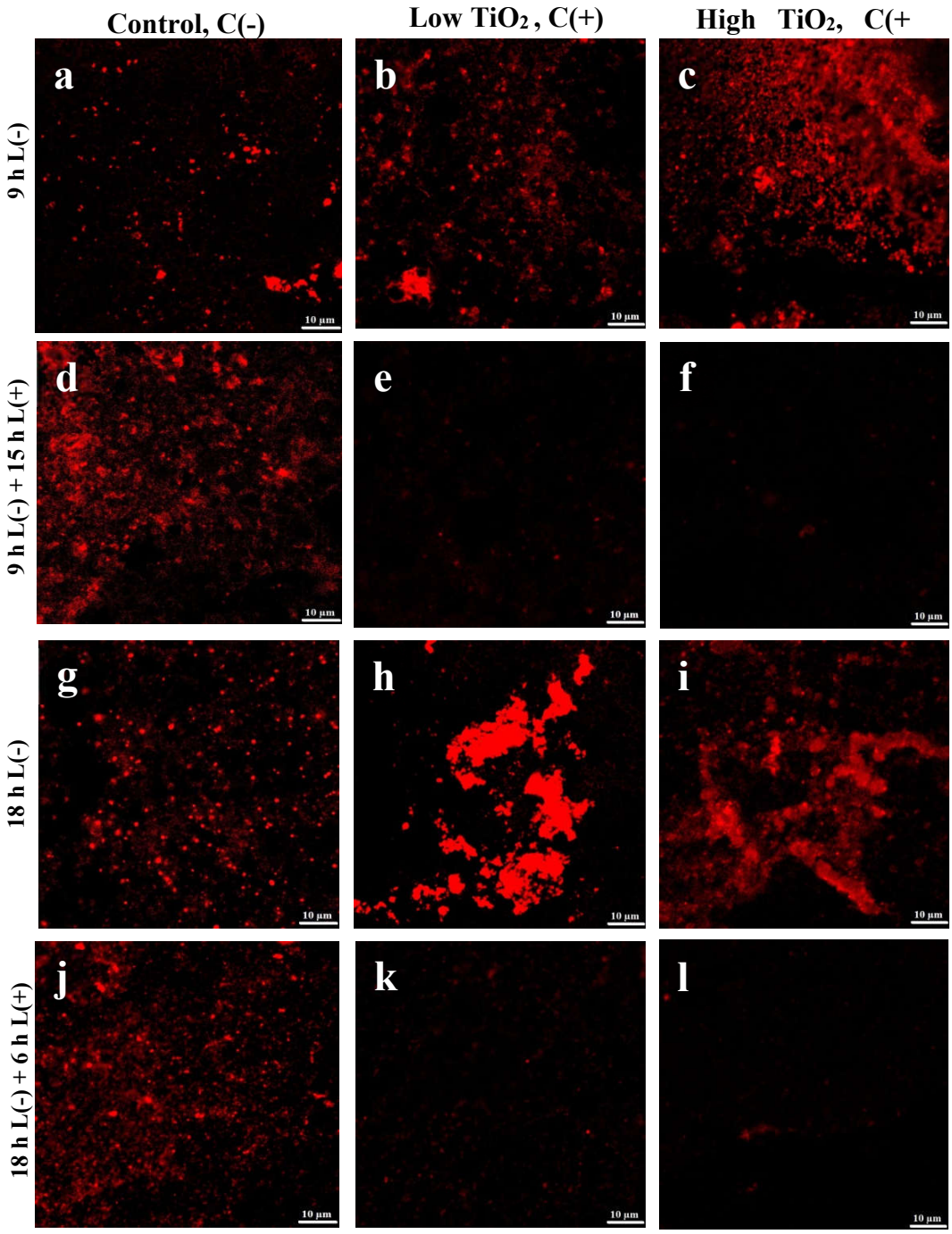

Figure 3.2.6. FilmTracer SYPRO Ruby biofilm matrix staining confocal micrographs of *S. aureus* on control coverslips C(-), (a, d, g and j); low C(+) (b, e, h and k) and high C(++) (c, f, I and l) surface coverage on TiO_2 electrosprayed coverslips. Irradiated and non-irradiated samples are denoted by L(+) and L(-) respectively. Dark period: 9 h and 18 h. Irradiation time: 15 h and 6 h. Scale bar: 10 µm.

The reduction of biofilm forming bacteria on TiO_2 photocatalytic surfaces was widely described [52-54]. Besides its effect in the cell wall and cell membrane composition and integrity, it is known that photocatalytic TiO_2 activity also has a negative effect in

appendage biosynthesis and protein insertion as well as in cell signaling and cell to cell communication, which have been shown to play a role in diverse functions such as pathogenesis, biofilm development, stress resistance and cell survival [45].

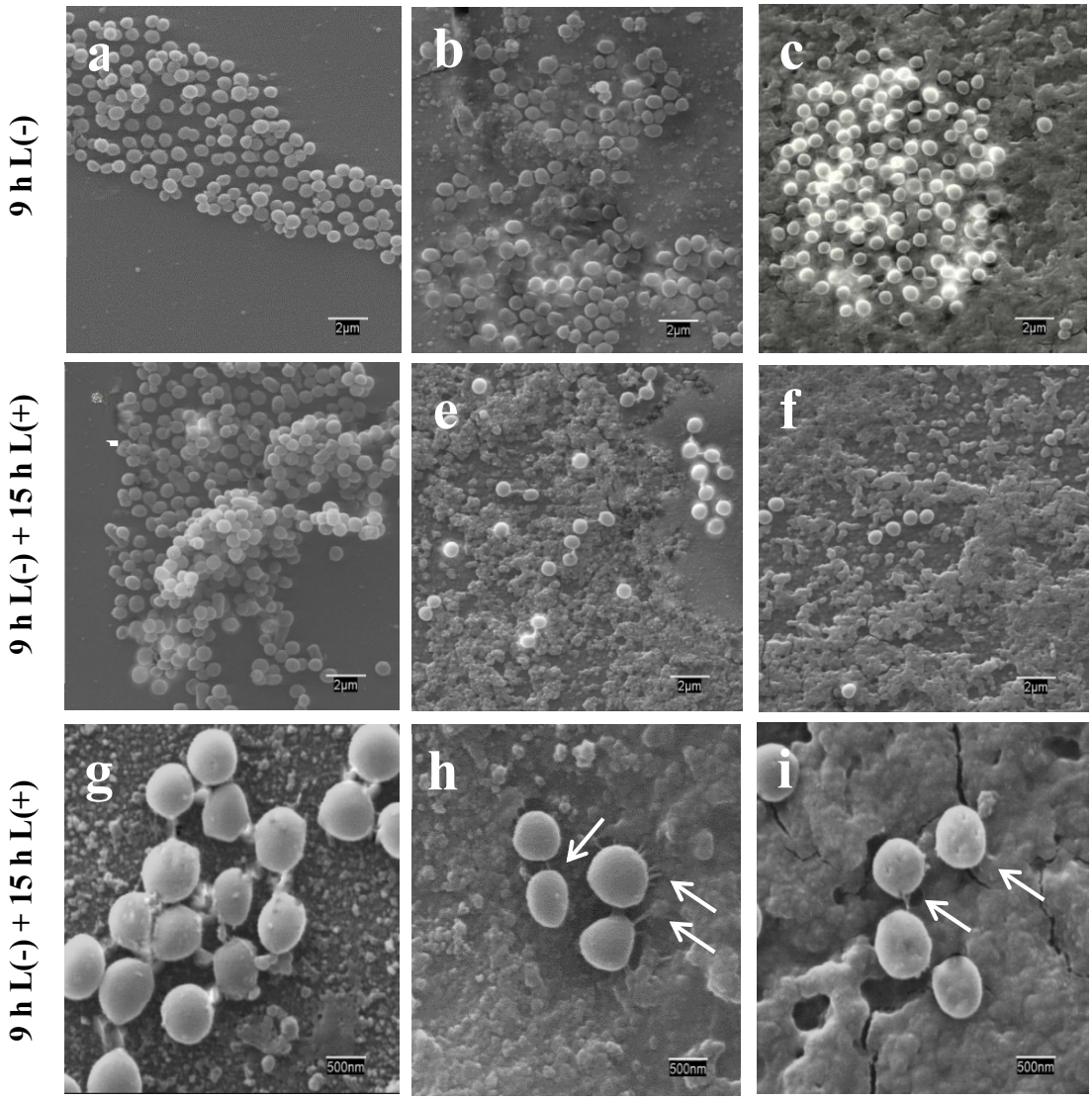

Figure 3.2.7. Representative SEM micrographs of *S. aureus* on control coverslips C (-) (a and d); low C (+) (b and e) and high C (+ +) (c and f) TiO_2 electrosprayed coverslips, for non- irradiated L (-) (a, b and c) and irradiated L (+) (d-i) samples. Images g, h and I show bacterial adhesion structures involved in biofilm formation in C(+) (g and h) and in C(+ +) samples (i). Darkness period: 9 h. Irradiation time: 15 h.

In the case of biofilm removal, the most important parameters for cleaning efficiency are total biomass and living bacterial cells [55]. The presence of viable cells enables fast recolonization if enough nutrients are available. In case inefficient cleaning procedures, nutrients could come from dead bacterial cells and the remaining exopolysaccharides can

be further used for bacterial adhesion and proliferation [56]. Our work showed that photocatalytic TiO_2 electrosprayed with low surface densities led to a complete removal of *S. aureus* cells with no viable colonization according to Live/Dead staining results (Figure 3.2.4). In our previous work we showed that mature biofilms of *Pseudomonas putida* and *Staphylococcus aureus*, formed for 48 h in static conditions and darkness on TiO_2-functionalize glass microfiber filters and glass slides, were not able to survive after an irradiation period of 2 h (chapter 3.1). However, because the biofilm was a mature formation, the exposure to irradiated TiO_2 for 2 h was not enough in this case to remove the dense matrix formed on the surface of the functionalized materials. For the TiO_2-covered electrosprayed surfaces used in this work, we showed that 15 h of irradiation after 9 h of contact with *S. aureus* cultures in the dark were enough to essentially eliminate the presence of biofilm structures, at least for the highest surface coverage assayed, C(++), while for C(+) some red-stained polymeric matrix could be observed after both irradiation periods (Figure 3.2.6 e and k). The results of crystal violet staining showed that the relative biofilm formation was significantly different from zero only in C(++) specimens, revealing that only the surface coverage of $2.78 \cdot 10^{-3}$ g/cm^2 could effectively avoid the accumulation of biofilms in the flow-cell arrangement used in this work. Consistent with these observations, SEM images of C(++) assays after irradiation show only some dispersed cells with few remaining adhesion structures (Figure 3.2.7 i), while for C(+) there are more cells attached to the surface and these structures are more apparent (Figure 3.2.7 g and h) after 15 h of irradiation. The results showed that the TiO_2 nanoparticles dispersed using ES and irradiated by simulated sunlight provide well-dispersed antimicrobial coatings and an efficient method for avoiding biofilm formation. ES allowed producing homogeneous photocatalytic surfaces with the precise surface coverage required to cope with the bacterial growth that could take place during dark periods under environmental exposure. The target value established in this work, > 2 mg/cm^2, was somewhat larger than the usual values for aqueous and gas phase TiO_2 photocatalytic surfaces, which are at or below the mg/cm^2 [57, 58]. It has to be considered that this value was the minimum required for ensuring the absence of biofilm accumulation under favorable conditions, namely long dark periods and warm conditions with nutrient availability for bacterial growth. This work showed that ES technique can be efficient for creating active self-cleaning surfaces with a precise and even dispersion of photocatalytic particles.

3.3.4 Conclusions

TiO_2 40 wt% suspension of crystalline anatase prepared using a sol-gel synthesis was used to prepare electrosprayed coating on the surface a glass surface. The surface density was tuned by using two different electrospray times to $2.09 \cdot 10^{-3} \pm 1.2 \cdot 10^{-4}$ and $2.78 \cdot 10^{-3} \pm 2.3 \cdot 10^{-4}$ g/cm^2. The electrosprayed surface resulted in a homogeneous dispersion of aggregates of solid and rough TiO_2 spherical particles with diameters generally below 400 nm. TiO_2-functionalized surfaces turned considerably more hydrophilic upon irradiation using a visible light Xe-arc source with a fluence rate 11.2 W m^{-2} (measured in the 290-400 range).

The antibacterial activity of TiO_2-covered surfaces was tested using flow-cell assays with *S. aureus* in NB at 37 °C. The experiments were carried out following two different dark-light cycles in order to simulate different environmental conditions. The electrosprayed surfaces were first put in contact with bacterial cultures in the dark to be exposed thereafter to Xe-arc lamp irradiation. The results showed that only samples with the highest surface coverage were capable of eliminate the biofilm once formed after irradiation treatments, although all irradiated surfaces could be considered free of viable bacteria after the dark-light cycles.

The results showed that even essentially clean surfaces can retain the polymeric structure of the extracellular material forming biofilms. Photocatalytic TiO_2 led to extensive membrane damage and cell impairment for bacteria in contact with functionalized coatings in spite of the inherently easier colonization of TiO_2-covered surfaces in comparison with more hydrophobic materials. Self-cleaning surfaces that avoid the proliferation of biofilms require surface coverage over the values commonly used for photocatalytic coatings.

3.3.5 References

[1] T. Nonami, H. Hase, K. Funakoshi, Apatite-coated titanium dioxide photocatalyst for air purification, Catalysis Today, 96 (2004) 113-118.

[2] S. Malato, P. Fernández-Ibáñez, M.I. Maldonado, J. Blanco, W. Gernjak, Decontamination and disinfection of water by solar photocatalysis: recent overview and trends, Catalysis Today, 147 (2009) 1-59.

[3] G.-J. Wang, S.-W. Chou, Electrophoretic deposition of uniformly distributedTiO_2 nanoparticles using an anodic aluminum oxide template for efficient photolysis, Nanotechnology, 21 (2010) 115206.

[4] S. Banerjee, J. Gopal, P. Muraleedharan, A. Tyagi, B. Raj, Physics and chemistry of photocatalytic titanium dioxide: visualization of bactericidal activity using atomic force microscopy, Current Science, 90 (2006) 1378-1383.
[5] Y. Oka, W.C. Kim, T. Yoshida, T. Hirashima, H. Mouri, H. Urade, Y. Itoh, T. Kubo, Efficacy of titanium dioxide photocatalyst for inhibition of bacterial colonization on percutaneous implants, Journal of Biomedical Materials Research Part B: Applied Biomaterials, 86 (2008) 530-540.
[6] J. Chen, C.-s. Poon, Photocatalytic construction and building materials: from fundamentals to applications, Building and Environment, 44 (2009) 1899-1906.
[7] D.B. Hamal, J.A. Haggstrom, G.L. Marchin, M.A. Ikenberry, K. Hohn, K.J. Klabunde, A multifunctional biocide/sporocide and photocatalyst based on titanium dioxide (TiO_2) codoped with silver, carbon, and sulfur, Langmuir, 26 (2009) 2805-2810.
[8] S. Swetha, S. Santhosh, R. Geetha Balakrishna, Synthesis and Comparative Study of Nano-TiO_2 Over Degussa P-25 in Disinfection of Water, Photochemistry and photobiology, 86 (2010) 628-632.
[9] A. Rincón, C. Pulgarin, Photocatalytical inactivation of *E. coli*: effect of (continuous–intermittent) light intensity and of (suspended–fixed) TiO_2 concentration, Applied Catalysis B: Environmental, 44 (2003) 263-284.
[10] B. Kim, D. Kim, D. Cho, S. Cho, Bactericidal effect of TiO_2 photocatalyst on selected food-borne pathogenic bacteria, Chemosphere, 52 (2003) 277-281.
[11] L. Rizzo, Inactivation and injury of total coliform bacteria after primary disinfection of drinking water by TiO_2 photocatalysis, Journal of hazardous materials, 165 (2009) 48-51.
[12] J. Gage, T. Roberts, J. Duffy, Susceptibility of Pseudomonas aeruginosa biofilm to UV-A illumination over photocatalytic and non-photocatalytic surfaces, Biofilms, 2 (2005) 155-163.
[13] B. Li, B.E. Logan, The impact of ultraviolet light on bacterial adhesion to glass and metal oxide-coated surface, Colloids and Surfaces B: Biointerfaces, 41 (2005) 153-161.
[14] S. Ciston, R.M. Lueptow, K.A. Gray, Controlling biofilm growth using reactive ceramic ultrafiltration membranes, Journal of Membrane Science, 342 (2009) 263-268.
[15] A. Jaworek, A. Sobczyk, Electrospraying route to nanotechnology: an overview, Journal of electrostatics, 66 (2008) 197-219.
[16] C.J. Hogan, K.M. Yun, D.-R. Chen, I.W. Lenggoro, P. Biswas, K. Okuyama, Controlled size polymer particle production via electrohydrodynamic atomization, Colloids and Surfaces A: Physicochemical and Engineering Aspects, 311 (2007) 67-76.
[17] S.U. Halimi, N.F.A. Bakar, S.N. Ismail, S.A. Hashib, M.N. Naim, H. Setyawan, W. Widiyastuti, S. Machmudah, Electrospray deposition of titanium dioxide (TiO_2) nanoparticles, AIP Conference Proceedings, AIP, 2014, pp. 57-62.
[18] S. Zhang, K. Kawakami, One-step preparation of chitosan solid nanoparticles by electrospray deposition, International journal of pharmaceutics, 397 (2010) 211-217.
[19] F. Huijing, H.R. A., Electrospray:Scaling-Up, in: S.E. Lyshevski (Ed.) Dekker Encyclopediaof Nanoscience and Nanotechnology, CRC Press2014, pp. 1-11.
[20] N. Ledala, B. Zhang, J. Seravalli, R. Powers, G.A. Somerville, Influence of iron and aeration on *Staphylococcus aureus* growth, metabolism, and transcription, Journal of bacteriology, 196 (2014) 2178-2189.

[21] T.R. Garrett, M. Bhakoo, Z. Zhang, Bacterial adhesion and biofilms on surfaces, Progress in Natural Science, 18 (2008) 1049-1056.
[22] C. de la Fuente-Núñez, F. Reffuveille, L. Fernández, R.E. Hancock, Bacterial biofilm development as a multicellular adaptation: antibiotic resistance and new therapeutic strategies, Current opinion in microbiology, 16 (2013) 580-589.
[23] A. Daerr, A. Mogne, Pendent_Drop: An ImageJ Plugin to Measure the Surface Tension from an Image of a Pendent Drop, Journal of Open Research Software, 4 (2016).
[24] G. Wolfaardt, J. Lawrence, R. Robarts, S. Caldwell, D. Caldwell, Multicellular organization in a degradative biofilm community, Applied and Environmental Microbiology, 60 (1994) 434-446.
[25] B.B. Christensen, C. Sternberg, J.B. Andersen, R.J. Palmer, A.T. Nielsen, M. Givskov, S. Molin, [2] Molecular tools for study of biofilm physiology, Methods in enzymology, 310 (1999) 20-42.
[26] J.M. Allen, S.K. Allen, S.W. Baertschi, 2-Nitrobenzaldehyde: a convenient UV-A and UV-B chemical actinometer for drug photostability testing, Journal of pharmaceutical and biomedical analysis, 24 (2000) 167-178.
[27] M. Fletcher, The effects of proteins on bacterial attachment to polystyrene, J. Gen. Microbiol, 94 (1976) 404.
[28] G.A. O'Toole, Microtiter dish biofilm formation assay, JoVE (Journal of Visualized Experiments), (2011) e2437-e2437.
[29] Á.G. Marín, I.G. Loscertales, A. Barrero, Surface tension effects on submerged electrosprays, Biomicrofluidics, 6 (2012) 044104.
[30] G. Taylor, Disintegration of water drops in an electric field, Proceedings of the Royal Society of London A: Mathematical, Physical and Engineering Sciences, The Royal Society, 1964, pp. 383-397.
[31] J.F. De La Mora, I.G. Loscertales, The current emitted by highly conducting Taylor cones, Journal of Fluid Mechanics, 260 (1994) 155-184.
[32] V. Gundabala, N. Vilanova, A. Fernández-Nieves, Current-voltage characteristic of electrospray processes in microfluidics, Physical review letters, 105 (2010) 154503.
[33] J.A. Tapia-Hernández, P.I. Torres-Chávez, B. Ramírez-Wong, A. Rascón-Chu, M. Plascencia-Jatomea, C.G. Barreras-Urbina, N.A. Rangel-Vázquez, F. Rodríguez-Félix, Micro-and nanoparticles by electrospray: advances and applications in foods, Journal of agricultural and food chemistry, 63 (2015) 4699-4707.
[34] N. Stevens, C. Priest, R. Sedev, J. Ralston, Wettability of photoresponsive titanium dioxide surfaces, Langmuir, 19 (2003) 3272-3275.
[35] M. Miyauchi, N. Kieda, S. Hishita, T. Mitsuhashi, A. Nakajima, T. Watanabe, K. Hashimoto, Reversible wettability control of TiO 2 surface by light irradiation, Surface Science, 511 (2002) 401-407.
[36] R.-D. Sun, A. Nakajima, A. Fujishima, T. Watanabe, K. Hashimoto, Photoinduced surface wettability conversion of ZnO and TiO_2 thin films, The Journal of Physical Chemistry B, 105 (2001) 1984-1990.
[37] K. Hashimoto, H. Irie, A. Fujishima, TiO_2 photocatalysis: a historical overview and future prospects, Japanese journal of applied physics, 44 (2005) 8269.
[38] E. Scholten, H. Dhamankar, L. Bromberg, G.C. Rutledge, T.A. Hatton, Electrospray as a tool for drug micro-and nanoparticle patterning, Langmuir, 27 (2011) 6683-6688.

[39] K. Songsurang, N. Praphairaksit, K. Siraleartmukul, N. Muangsin, Electrospray fabrication of doxorubicin-chitosan-tripolyphosphate nanoparticles for delivery of doxorubicin, Archives of pharmacal research, 34 (2011) 583-592.
[40] L. Boulos, M. Prevost, B. Barbeau, J. Coallier, R. Desjardins, LIVE/DEAD® BacLight™: application of a new rapid staining method for direct enumeration of viable and total bacteria in drinking water, Journal of microbiological Methods, 37 (1999) 77-86.
[41] P. Dunlop, C. Sheeran, J. Byrne, M. McMahon, M. Boyle, K. McGuigan, Inactivation of clinically relevant pathogens by photocatalytic coatings, Journal of Photochemistry and Photobiology A: Chemistry, 216 (2010) 303-310.
[42] A. Kubacka, M. Ferrer, M. Fernández-García, Kinetics of photocatalytic disinfection in TiO 2-containing polymer thin films: UV and visible light performances, Applied Catalysis B: Environmental, 121 (2012) 230-238.
[43] J. Kiwi, V. Nadtochenko, Evidence for the mechanism of photocatalytic degradation of the bacterial wall membrane at the TiO_2 interface by ATR-FTIR and laser kinetic spectroscopy, Langmuir, 21 (2005) 4631-4641.
[44] H.A. Foster, I.B. Ditta, S. Varghese, A. Steele, Photocatalytic disinfection using titanium dioxide: spectrum and mechanism of antimicrobial activity, Applied microbiology and biotechnology, 90 (2011) 1847-1868.
[45] A. Kubacka, M.S. Diez, D. Rojo, R. Bargiela, S. Ciordia, I. Zapico, J.P. Albar, C. Barbas, V.A.M. dos Santos, M. Fernández-García, Understanding the antimicrobial mechanism of TiO_2-based nanocomposite films in a pathogenic bacterium, Scientific reports, 4 (2014) 4134.
[46] G. Pishchany, K.P. Haley, E.P. Skaar, *Staphylococcus aureus* growth using human hemoglobin as an iron source, JoVE (Journal of Visualized Experiments), (2013) e50072-e50072.
[47] B. Jalvo, J. Santiago-Morales, P. Romero, R.G. de Villoria, R. Rosal, Microbial colonisation of transparent glass-like carbon films triggered by a reversible radiation-induced hydrophobic to hydrophilic transition, Rsc Advances, 6 (2016) 50278-50287.
[48] M. Katsikogianni, Y. Missirlis, Concise review of mechanisms of bacterial adhesion to biomaterials and of techniques used in estimating bacteria-material interactions, Eur Cell Mater, 8 (2004).
[49] C. Van Oss, Hydrophobicity of biosurfaces—origin, quantitative determination and interaction energies, Colloids and Surfaces B: Biointerfaces, 5 (1995) 91-110.
[50] C.J. van Oss, Hydrophobicity and hydrophilicity of biosurfaces, Current opinion in colloid & interface science, 2 (1997) 503-512.
[51] K. Hori, S. Matsumoto, Bacterial adhesion: from mechanism to control, Biochemical Engineering Journal, 48 (2010) 424-434.
[52] E.J. Wolfrum, J. Huang, D.M. Blake, P.-C. Maness, Z. Huang, J. Fiest, W.A. Jacoby, Photocatalytic oxidation of bacteria, bacterial and fungal spores, and model biofilm components to carbon dioxide on titanium dioxide-coated surfaces, Environmental science & technology, 36 (2002) 3412-3419.
[53] Y. Cai, M. Strømme, Å. Melhus, H. Engqvist, K. Welch, Photocatalytic inactivation of biofilms on bioactive dental adhesives, Journal of Biomedical Materials Research Part B: Applied Biomaterials, 102 (2014) 62-67.
[54] C.N. Rao, T. Takashima, W.A. Bradley, T.Y. Lee, Near ultraviolet radiation at the earth's surface: measurements and model comparisons, Tellus B, 36 (1984) 286-293.

[55] P. Stiefel, U. Rosenberg, J. Schneider, S. Mauerhofer, K. Maniura-Weber, Q. Ren, Is biofilm removal properly assessed? Comparison of different quantification methods in a 96-well plate system, Applied microbiology and biotechnology, 100 (2016) 4135-4145.
[56] S.E. Finkel, R. Kolter, DNA as a nutrient: novel role for bacterial competence gene homologs, Journal of Bacteriology, 183 (2001) 6288-6293.
[57] I. Salem, N. Keller, V. Keller, Photocatalytic removal of monoterpenes in the gas phase. Activity and regeneration, Green Chemistry, 11 (2009) 966-973.
[58] M. Kete, E. Pavlica, F. Fresno, G. Bratina, U.L. Štangar, Highly active photocatalytic coatings prepared by a low-temperature method, Environmental Science and Pollution Research, 21 (2014) 11238-11249.

Chapter 4:

Antifouling membranes prepared by electrospinning

4 Antifouling membranes prepared by electrospinning

4.1

4.2 Part I: Superhydrophilic anti-fouling electrospun cellulose acetate membranes coated with chitin nanocrystals for water filtration

4.2.1 Introduction

Electrospinning is a century old process patented by Cooley and Morton in 1902 that is used for producing continuous fibers [1,2]. The first patent on industrial electrospinning appeared in 1934, where Formhals disclosed the equipment for commercial production of artificial threads/filaments of cellulose acetate [3]. Electrospinning is a very versatile technique for producing polymeric fibers in nano-to-micron scale from polymeric solutions and has been of great commercial and research interest. More recently, this technology has been investigated by researchers because of the continuing interest in applications in nanoscience and its potential to generate nanofibers [4-6].

Cellulose acetate based membranes are used extensively in industrial scale and have the advantage of being derived from an abundant natural polymer, viz. cellulose. Though cellulose acetate based membranes produced by phase inversion is a popular membrane material, electrospun cellulose acetate membranes materials have several advantages, specifically, the open and interconnected pore structure and the large specific surface area while having shown potential in air and water filtration [6,7]. However, membrane filtration and especially pressure-driven liquid filtration using electrospun membranes are challenging due to limitations related to mechanical strength and chemical and thermal stability [8]**.** Electrospun random membranes usually have poor mechanical strength due to the highly porous non-woven structure and with weak fiber-fiber connection via physical entanglements [9]. Process modifications to increase fiber–fiber interactions and reinforcing of electrospun fibers using nanoparticles are becoming a highly promising route to address this issue [10-14]. In addition, biofouling is a significant and constant problem with membrane filtration and specifically for hydrophobic cellulose acetate membranes [15,16]. Methods to address biofouling can include mechanical or chemical cleaning operations but another area of focus is the manipulation of the surface chemistry of the membranes to create a surface inhospitable for biofilm formation [17,18] .

In the quest for developing new advanced materials that utilize natural polymers, biobased nanoparticles from cellulose and chitin have been explored in the last two decades [19, 27]. We have successfully reinforced biopolymer fibers electrospun with low (>10 wt%) and high concentrations (50 wt%) of chitin and cellulose nanocrystals [22, 25, 26]. However, it was noticed that addition of nanoparticles to spinning solutions significantly affected the spinnability and process yield which are both significant challenges hindering the use of reinforced fibers in high volume applications such as water purification [26] .

Biofouling refers to the undesirable accumulation of a biotic deposit on a surface. This deposition may be due to both macroscopic and microscopic organisms. In contrast to abiotic kinds of fouling (scaling, organic and particle fouling), biofouling is a special case because the foulant, can grow at the expense of biodegradable substances from the water phase, turning them into metabolic products and biomass. “Biofilm” is an expression for a wide variety of manifestations of microbial aggregates [28]. Biofilms are understood to be mixtures of bacterial cells embedded in an extracellular polymeric matrix (EPS) made up of polysaccharides, proteins and nucleic acids [29]. Biofilm formation is a development process, which initially involves the adhesion of bacterial cells to a surface and production of EPS resulting in more firmly and irreversible bacterial attachment that cover and protect the cells from adverse conditions [30]. The abiotic fouling on the other hand, is the formation of ‘cake layer’ or ‘gel layer’ consisting of rejected materials and in membrane filtrations, NOMs are a major contributor for abiotic fouling.

In this current study, chitin nanocrystals are impregnated through electrospun cellulose acetate (CA) in a process to change the surface chemistry of the electrospun fibers. Chitin, poly(β-(1→4)-*N*-acetyl-D-glucosamine, acts as the structural polymer in the exoskeletons of arthropods, in the cell walls of fungi and yeast, and in other microorganisms [31].. Chitin nanocrystals, rod-like particles with typical dimensions of 400 nm in length and 30 nm in diameter, can be extracted through acid hydrolysis from the above mentioned sources [32, 33]. These nanocrystals have high surface area, good mechanical properties and possess antifungal and antibacterial properties. In a recent study, chitin nanocrystals were successfully incorporated in a PVDF membrane prepared through phase immersion to enhance the anti-fouling performance [34]. The current approach was aimed at combining the ease of producing CA electrospun membranes and its efficiency in membrane applications with unique surface characteristics of chitin nanocrystals to create a new generation of high flux, super-hydrophilic, anti-fouling composite membranes for

microfiltration water purification for food-processing industries. The fiber morphology, mechanical properties, contact angle, water flux and fouling were evaluated and discussed in this context.

4.2.2 Material and methods

4.2.2.1 Materials

Cellulose acetate (CA), M_n 50,000, was purchased from Sigma-Aldrich Chemistry, USA. Acetic acid (96%, EMSURE®), and acetone, analysis grade, were purchased from Merck KGaA (Germany). All chemicals were used as received without further purification.

Chitin nanocrystals (ChNC) were prepared via hydrochloric acid hydrolysis [27, 32, 33, 35]. Deproteinized and bleached chitin flakes (Sigma-Aldrich, Germany) underwent an acid hydrolysis reaction with 3 N hydrochloric acid at 80 °C for 90 min. When the reaction was complete, the resulting suspension was centrifuged to remove the excess acid and subsequently to collect the turbid supernatant containing the chitin nanocrystals. This collected fraction, the chitin nanocrystal suspension, was dialyzed against distilled water to achieve a suspension neutral pH and finally sonicated to ensure separation of the individual nanocrystals from one another prior to storage. The chitin nanocrystals suspension was briefly sonicated prior to impregnation on the electrospun cellulose acetate membranes. The concentration of the initial chitin nanocrystal suspension was 0.53 wt %.

4.2.2.2 Electrospinning

A schematic representation of the processing route used to prepare the membranes is given in Figure 4.1.1. Cellulose acetate, 5.0 g (M_n 50,000), was dissolved in a 45 g 1:1 mixture of concentrated acetic acid and acetone and stirred overnight (12 h) to ensure complete dissolution [22]. Electrospinning of the cellulose acetate solution (Figure 4.1.1, step i) was undertaken using the 150 mm Laboratory Electrospinning Platform (Electrospinz-ES1a, New Zealand) attached to a high voltage supplier, with the solution pumped through a 20 mL plastic syringe, (BD Plasti-Pak syringe, USA), using a single syringe pump (Aladdin-1000, World Precision Instrument, USA). The cellulose acetate fibers were successfully electrospun on aluminum foil on aluminum plates, with a supplied voltage of 10 kV, 150 mm tip to collector distance, and a flow rate of 10 mL h^{-1}. Electrospinning was performed at room temperature.

The chitin nanocrystals, with a diameter of 20 nm ± 10 nm and length of 300 nm ± 100 nm, were used to impregnate the CA electrospun membranes (Figure 4.1.1, step ii), as shown in Figure 4.1.1. Impregnated membranes (CA-ChNC) were prepared via Buchner funnel filtration apparatus with the cellulose acetate membrane on a 90 mm diameter glass frit. The chitin nanocrystal suspension of 0.2 g dry weight (see Figure 4.1.1), was drip fed through the electrospun cellulose acetate fibers. This was to allow for maximum exposure time for the chitin to accumulate on the cellulose acetate fibers. The chitin infused cellulose acetate membranes were air dried for 24 h and then heated to 100 °C for 10 minutes (Figure 4.1.1, step iii) to ensure binding between the chitin and the cellulose acetate fibers [36, 37]. Membranes were weighed on an analytical balance before and after impregnation to determine mass of chitin nanocrystals accumulated on the cellulose acetate membrane. 5% of the total mass of the CA-ChNC membrane is due to the ChNC.

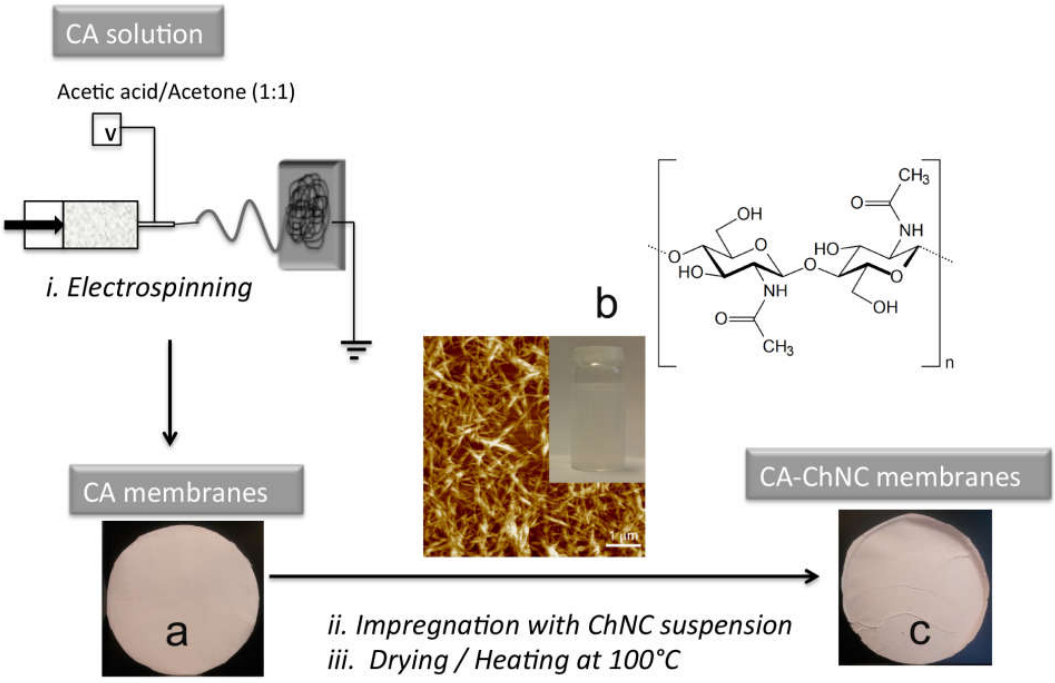

Figure 4.1.1. Scheme showing the methods and materials involved in membrane processing and functionalization. i) Electrospinning of CA membranes, ii) impregnation of CA membranes and iii) drying and heating of the impregnated membranes. electrospun cellulose acetate (CA) membrane (a), chitin nanocrystals (ChNC) used for impregnation (b, the images show ChNC suspension, AFM of nanocrystals and chemical structure of chitin) and CA-ChNC membrane after impregnation (c).

The viscosity of the cellulose acetate electrospinning solution was measured using the SV-10 VibroViscometer (A&D Company, Japan) with a glass sample holder. The solution was sampled every 5 seconds for 2 minutes at a vibration frequency of 30 Hz. The electrical conductivity of the cellulose acetate electrospinning solution was

determined using a SevenEasy™ conductivity meter (METTLER TOLEDO AG, Switzerland).

4.2.2.3 Membrane characterization

Porosity of the scaffolds was evaluated based on the weight and density of the scaffolds. The porosity was defined as the volume fraction of the voids (V_v) and was calculated using

$$v = 1 - \frac{\rho e}{\rho t} \quad (1)$$

Where ρ_e is the experimental density of the scaffold and ρ_t is the theoretical density of a non-porous scaffold. The densities of ChNC and cellulose acetate were taken as 1.46 and 1.3 g/cc, respectively. The experimental density, ρ_e, was determined based on the weight and volume of the samples cut into strips. All reported results are based on the average of three measurements. The Brunauer-Emmett-Teller (BET) surface area and pore volume of the CA and ChNC-CA membranes were determined by nitrogen adsorption-desorption isotherm measurements at 77 K.

The surface morphology of the electrospun fibers and the membrane were examined using MAGELLAN 400, SEM (FEI Company) or FEG-SEM (Zeiss, Merlin). The fiber samples were placed on conductive tape and sputter coated with tungsten. Images were taken operating at 3kV and a working distance of 10 mm for MAGELLAN 400, SEM (FEI Company) where as a 2.5 kV and 8 mm working distance was used in the case of FEG-SEM (Zeiss, Merlin). Post-filtration imaging to observe the continued presence of chitin nanocrystals on the surface of the electrospun CA membranes after 5 L distilled water at 0.5 bar pressure was performed with MAGELLAN 400, SEM (FEI Company). The membranes were sputter coated with gold and observed in the SEM at an acceleration voltage of 3 kV. The chitin nanocrystals as well as CA and CA-ChNC membranes surfaces were imaged using MultiMode 8 AFM (Bruker, Nanoscope controller, Santa Barbara, California, USA). A drop of diluted suspension of each sample was deposited onto freshly cleaved mica and left to dry at room temperature in the case of chitin nanocrystals. In the case of the electrospun membranes, a small piece of the membrane is mounted on the metal stub using double-sided tape. All the samples were imaged in tapping mode. Height, amplitude and phase images were recorded. The instrument was operated at a resonance frequency of 350 kHz and a spring constant of 10–200 nm^{-1}.

The tensile tests were performed on the CA and CA-ChNC membranes using a universal testing machine, Shimadzu Autograph AG-X (Shimadzu, Japan), with a load cell 500 N. The thickness of the membranes was determined using SEM imaging of the cross-section of cryo-fractured films, sputter coated with Au. Test specimens, conditioned at 45% relative humidity for 1 week, with dimensions of 50 mm x 5 mm were mounted on paper windows for ease of handling and mounting. A preload of 0.1 N was applied and a strain rate of 2mm/min and gauge length of 20 mm were used. The stress-strain curves were plotted from the measured load and sample extension (measured by video camera). The stress and strain are defined as:

$$\sigma = \frac{F}{A_0} \tag{2}$$

$$\varepsilon = \ln(L/L_o) \tag{3}$$

where F is the force at break, A_o is the area of cross-section of the tensile sample, and L_o is the initial sample length and L is the sample length at break. The elastic modulus was calculated from the initial part of the slope from the stress-strain curve. 4-6 test samples were tested for each material and the average values are reported.

Thermogravimetric analysis was performed using TGA (Q500 TGA, TA Instruments) with 5 mg sample heated to 800 °C at 10 °C min^{-1} under N_2 atmosphere. Onset of thermal degradation is the temperature at which 95% of the mass of the original sample remains.

Flux tests were performed by filtering distilled water through the membranes using a dead-end cell (HP 4750, Sterlitech, USA) with N_2 gas to maintain constant pressure at desired pressures. The time for 0.3 L of distilled water to pass through the membranes was recorded and used for the flux calculations. Flux, J, was calculated as follows:

$$J = \frac{Q_p}{A_m} \tag{4}$$

where Q_p is the filtrate volume through the membrane per time and A_m is the area of the membrane. A_m (14.6 cm^2) is a constant value provided by Sterlitech. Membranes were compacted at 0.5 bar for 5 minutes prior to flux experiments. Permeability was calculated from the linear regression slope from plotting the water flux at 0.4 – 1.2 bar pressure. Correlation factors for both were 0.99.

Anti-fouling capability of the CA and CA-ChNC membranes was determined by measuring the flux decline over time. Bovine serum albumin, fraction V (Merck Millipore, Germany) 2 g L^{-1} stock solution and humic acid (Alfa-Aesar, Germany) 0.5 g L^{-1} stock solution were prepared by dissolving the foulant in distilled water and used as prepared. Filtration of the foulant solutions through individual membranes in the dead end cell occurred at 0.13 bar pressure via a peristaltic pump (Model 323S, Watson-Marlow, United Kingdom) for 60 min. Every 15 min, the flux at 0.5 bar was measured using the dead-end cell with N_2 gas applied to maintain pressure. The flux was plotted against time to determine the effect of the chitin nanocrystals on the surface of the cellulose acetate fibers on fouling and cake formation of the CA and CA-ChNC membranes.

Surface wettability tests were carried out using an optical contact angle meter at room temperature, using the sessile drop technique. For this measurement, the samples were cut and placed on the test cell. Drops of purified water were gently deposited on the sample surface by the delivering syringe. Three water contact angle measurements on each membrane surface were taken at different positions on the sample.

Surface zeta potential was measured via electrophoretic light scattering (Zetasizer Nano ZS) using the Surface Zeta Potential Cell (ZEN 1020) from Malvern. Measurements were performed at 25ºC using 10 mM KCl, pH 7.0, aqueous solution with of 0.5% (w/w) poly(acrylic acid) (450 kDa), as tracer. pH was adjusted using 1M KOH and 1 M HCl.

4.2.2.4 Bacterial bioassays

Cells of *E. coli* (CECT 516) were grown overnight in nutrient medium (for 1 L solution in distilled water, beef extract 5 g, peptone 10 g, NaCl 5 g. pH adjusted to 7.2), while shaking at 37°C. Bacterial viability and biofilm assay were tested using different fluorescence techniques. For these tests, exponentially growing cultures on nutrient medium were diluted to an OD_{600} of 0.0138 (10^8 cells/ml). Diluted cultures (2 mL) were placed on the electrospun CA and CA-ChNC membranes inside the well of polystyrene 24-well plates. Membranes were incubated 18 and 24 h at 37°C without stirring. After the biofilm assay, membranes were carefully washed with distilled water after the liquid culture removal.

Fluorescein diacetate (FDA), a fluorogenic substrate that permits the detection of enzymatic activity, was used for a relative quantification of the biofilm formation. The fluorescence was measured in a fluorometer/luminometer Fluoroskan Ascent FL. 200 µL of the fluorescent stain were extended over the entire membrane surface. A concentration of 0.02% (w/w) in DMSO was used for FDA in all cases. For fluorescence reading, after 15 min of preincubation at 25 °C, FDA was excited at 485 nm, and emission recorded at 538 nm.

DAPI (4′,6-Diamidine-2′-phenylindole dihydrochloride; Roche) and Live/Dead BacLight Bacterial Viability Kit (Molecular Probes, Invitrogen Detection Technologies, Carlsbad, CA, USA) were used to evaluate bacterial viability on membranes. For membrane staining, the whole surface of each one was covered with 30 µL of DAPI/PI (2.5 µg/ml DAPI and 30µM PI in DMSO) or of Live/Dead stain (a 0.5:1 mixture of SYTO 9 and PI in DMSO). The incubation was performed in the dark for 15-30 min at room temperature. For blue fluorescence (DAPI) excitation was performed at 358 nm and emission was recorded at 461 nm. For green fluorescence (SYTO 9) excitation was performed at 488 nm and emission at 500-575nm. For red fluorescence (PI, dead cells), the excitation/emission wavelengths were 561 nm and 570-620 nm respectively.

For matrix visualization, biofilms were stained with 200 µl FilmTracer SYPRO Ruby (Molecular Probes, Invitrogen) per membrane, incubated in the dark for 30 min at room temperature, and rinsed with distilled water. The excitation/emission wavelengths were 450 nm and 610 nm respectively. After incubation, images were acquired at 18 and 24 h after inoculation in the microdevice using a Leica Microsystems Confocal SP5 fluorescence microscope (Leica Microsystems, Germany). A process of dehydration and drying with ethanol at different concentrations was carried out to analyze membranes in contact with microorganisms by SEM.

4.2.3 Results and discussion

4.2.3.1 Membrane morphology

Cellulose acetate fibers were successfully electrospun under the given conditions to form random membranes. The viscosity and conductivity of the cellulose acetate electrospinning solution were 1144 mPa·s and 8.67 mS cm^{-1}, respectively. Figure 4.1.2a shows the electrospun CA fibers where randomly aligned fibrous membranes are visible.

The electrospun fibers had diameters in the range of 0.5 – 3.3 μm, with the fiber distribution showing most were between 0.5 – 1.7 μm (Figure 4.2.2b). The individual fibers' surface morphology showed ridge-like surfaces (Figure 4.2.2c).

The chitin nanocrystals' dimensions are 20 nm ± 10 nm diameter and length of 300 nm ± 100 nm which agrees with out earlier reports [25, 35]. Impregnation of the ChNC on to the surface of the electrospun fibers was undertaken to ensure that the surface functionality of the chitin nanocrystals was utilized and readily accessible. The SEM morphology studies show the hierarchical network formation from the microscale (electrospun fiber networks, Figure 4.1.2 d-e) to the nanoscale (ChNC networks, Figure 4.2.2 f-g). Figure 4.2.2d shows the overall chitin nanocrystal impregnation network on the surface of the CA fiber random membranes, which is extensive even with a relatively low load level of 5% of the mass of the cellulose acetate membrane. The ChNC coatings on the CA fibers (Figure 4.2.2f) were highly homogeneous and were considered to be stabilized via H-bonding that was created during the drying step. Ma *et al* have used a similar approach to coat TEMPO cellulose nanowhiskers on to electrospun PAN scaffolds on a PET nonwoven substrate [36]. Figure 4.2.2g also shows the build-up and film formation tendency of the chitin nanocrystals in the junctions (crossover) of the electrospun fibers, which reduces the pore sizes after impregnation. This was shown by the decrease in the porosity of the CA-ChNC membranes when compared to CA membranes, from 88.1% to 85.6%. The average pore diameter decreased from 11.02 nm (CA) to 10.07 nm (CA-ChNC) based on BET measurements. The BET surface area was determined to be 2.73 m2/g for CA membranes and increased to 3.709 m2/g with the addition of the 5% ChNC. This increase may be attributed to the nanotexturing of the CA fibers with ChNC.

To further test the robustness of the chitin nanocrystal layer on the cellulose acetate fibers, 5 L of distilled water at 0.5 bars was passed through the membrane in the dead end cell. The Figure 4.2.3 a-b SEM images show that the chitin crystals' webbing between the fibers survives as well as the chitin crystals coating the individual fibers. The AFM images of a second CA-ChNC membrane that had 26 L distilled water pass through the membrane (Figure 4.2.3 c-d) show the chitin nanocrystals on the fiber surfaces also are retained.

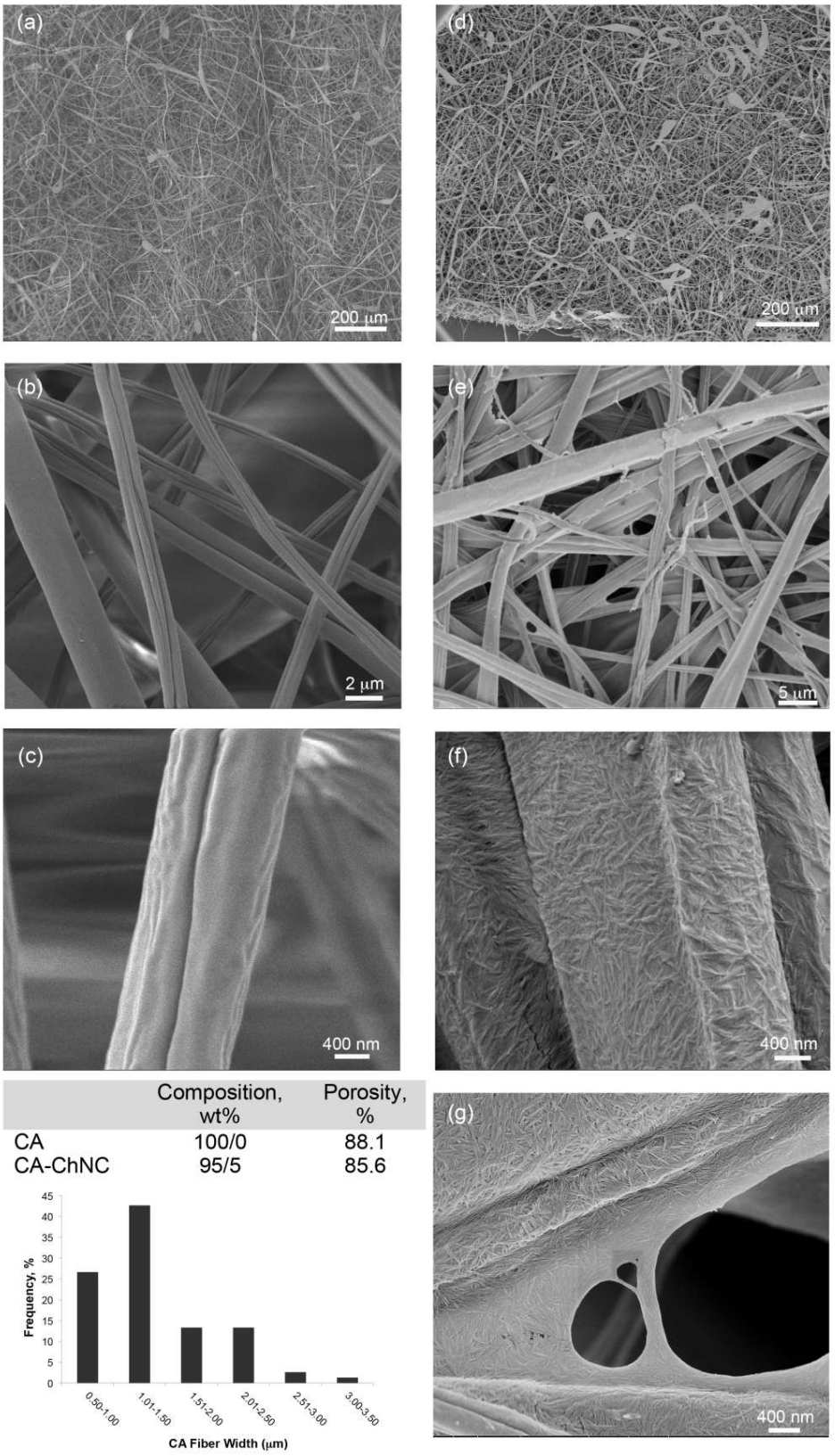

Figure 4.2.2. Electrospun cellulose acetate fibers were imaged with SEM to show fiber membrane formation (a), surface morphology (b,c) and to determine fiber size distribution (d). After filtration impregnation, the cellulose acetate membrane structure is retained (e, f) and the chitin nanocrystals were present both on the surface of the cellulose acetate fibers (g, h) and also formed web-like structures at fiber junctions (g).

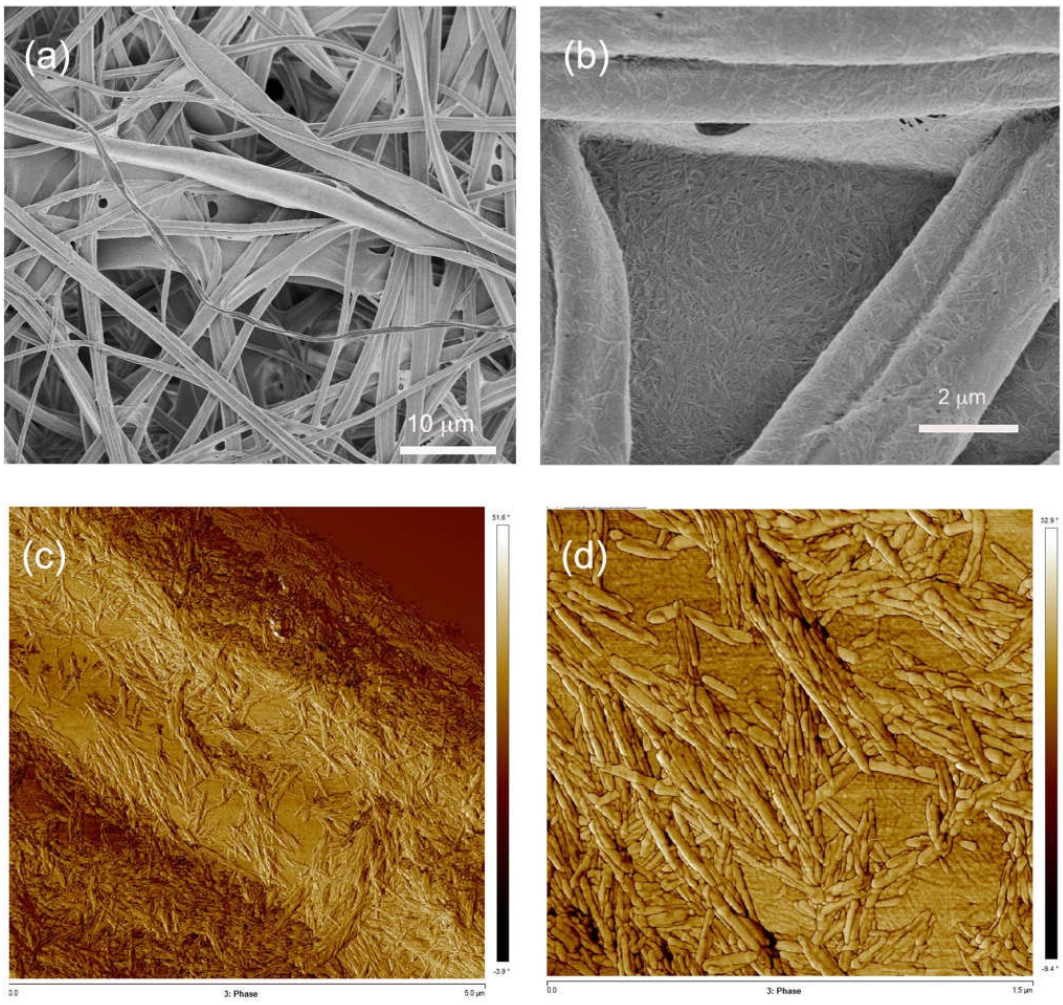

Figure 4.2.3. The robustness of the membrane shown by a) fiber structure and b-d) chitin crystals on the CA fibers after undergoing 5 L water filtration process. SEM images showing a) fiber structure and b) the coated surfaces and ChNC web formations. AFM images showing phase images of the chitin nanocrystal coating on the CA fiber at c) 5 X 5 µm d) 1.5 X 1. 5 µm.

4.2.3.2 Mechanical and thermal properties

The stress-strain curves and the tensile data of the electrospun membranes with and without chitin nanocrystal coating are given in Figure 4.2.4 and Table 4.1.1. The results show that the impregnation of electrospun cellulose acetate with ChNC has positively influenced the tensile strength and E-modulus of the membranes whereas the strain has decreased (Table 4.1.1). The tensile strength increased by 131%, from 1.43 MPa to 3.31 MPa, while the E-modulus by 340%, from 0.34 GPa to 1.16 GPa, with the infusion of 5% of ChNCs. The stress-stain behavior also changed significantly after impregnation with a low amount of ChNCs.

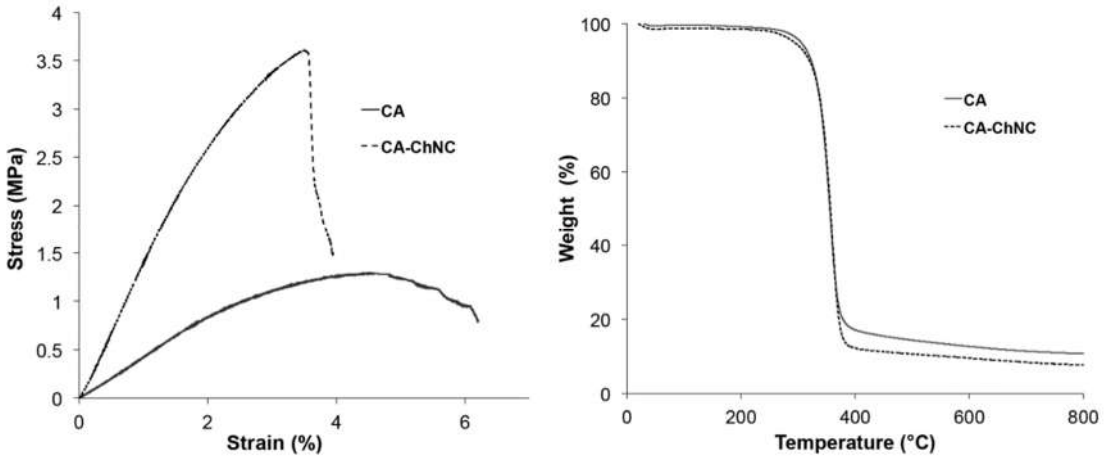

Figure 4.1.4. The effect of ChNC coating on the mechanical properties and the thermal stability of CA electrospun fibers a) stress-strain curves and b) TGA curves are shown.

This remarkable shift in mechanical performance can be attributed to the stiffening effect of the ChNCs coated on individual electrospun fibers as well as the membranes in general (as evidenced by previous SEM images in Figure 4.2.2 and 4.2.3). The web formation at the fiber junctions 'ties' the electrospun fibers together, positively impacting the mechanical stability of the network. The strain at break however decreased as expected, which is attributable to the restricted slippage of the electrospun fibers past each other due to the 'tied' junction points. This so called "welding" or "soldering" of electrospun fibers, which enhance the bonding at junction points have been reported by some researchers [38-40]. To achieve this fusion of fibers, approaches such as the heating of the electrospun membranes above the glass transition temperature but below the melting temperature of the polymer fibers [39, 40] or solvent treatment of the electrospun membranes are reported [38]. Huang et al increased the TS of electrospun membranes of polyacrylonitrile (PAN) by 500% (5 to 25 MPa) and polysulfone (PSu) 400 fold (0.8- 3.2 MPa) via solvent treatment [38]. In this work, the chitin nanocrystals dried on the electrospun membranes result in a similar 'welding' of the electrospun fibers with a relatively lower increase in mechanical TS (130%).

The thermal degradation behavior showed a slight decrease in onset of thermal degradation temperature with the addition of the chitin nanocrystals from 304 °C to 293 °C (Figure 4.1.4). This is attributable to the lower thermal stability of ChNCs compared to CA but will not compromise the use of the membranes in water purification [35].

Table 4.1.1. The effect of chitin nanocrystals on mechanical properties, thermal stability, and water flux of the membranes.

	Tensile Strength, MPa (±SD)	Strain, % (±SD)	Young's Modulus, GPa (±SD)	T_{onset} °C	Flux, L m^{-2} h^{-1} (±SD)	Permeability L m^{-2} h^{-1} bar^{-1}
CA	1.43 (0.21)	6.23 (1.21)	0.34 (0.02)	304	13400 (700)	13300
CA-ChNC	3.31 (0.45)	3.42 (0.49)	1.16 (0.05)	293	14000 (300)	14100

4.2.3.3 Water flux and permeability

The water flux measurements (Table 4.1.1) show that the water flux at 0.5 bar and the permeability was not changed by the addition of the chitin nanocrystals. This high flux post-impregnation could be attributed to the hydrophilic nature of the CA-ChNC membrane while the surface coating of the cellulose acetate fibers where the chitin nanocrystals align along the cellulose acetate fibers first and then form webs between the fibers can influence flux and permeability. The high flux for the CA and CA-ChNC membranes is one of the attributes of these membranes that show promise in microfiltration applications, such as ready-to-eat vegetable process water. In comparison, Ma et al have reported a flux of 5900 Lm-2h-1bar-1 for PAN nanofiber membranes impregnated with cellulose nanocrystals with a support layer [37] while our CA-ChNC membranes have a flux of 27900 Lm-2h-1bar-1. This could be a result of our membranes having larger pore sizes, not requiring a support layer and the hydrophilicity of the cellulose acetate membrane in comparison to the PAN nanofibres.

4.2.3.4 Fouling behavior

The flux of membranes was evaluated to confirm the anti-fouling potential of the CA-ChNC membranes and to determine what effect the chitin nanocrystals would have on the abiotic fouling of the membranes. The change in flux was determined over 60 minutes of dead end cell filtration. As can be seen in Figure 4.1.5, the flux of the CA membranes steadily decreased over time as either 2 g/L bovine serum albumin or 0.5 g/L humic acid solutions were continually passed over the membrane. In comparison, the flux of the CA-ChNC membranes remained constant over the 60-minute test period. While both membranes showed a decrease from the pure water flux upon initial contact with the membranes, after that initial contact the flux remained high and steady for the chitin nanocrystals coated membranes. These results indicate a promising potential for this type of membrane for future applications and further evaluation.

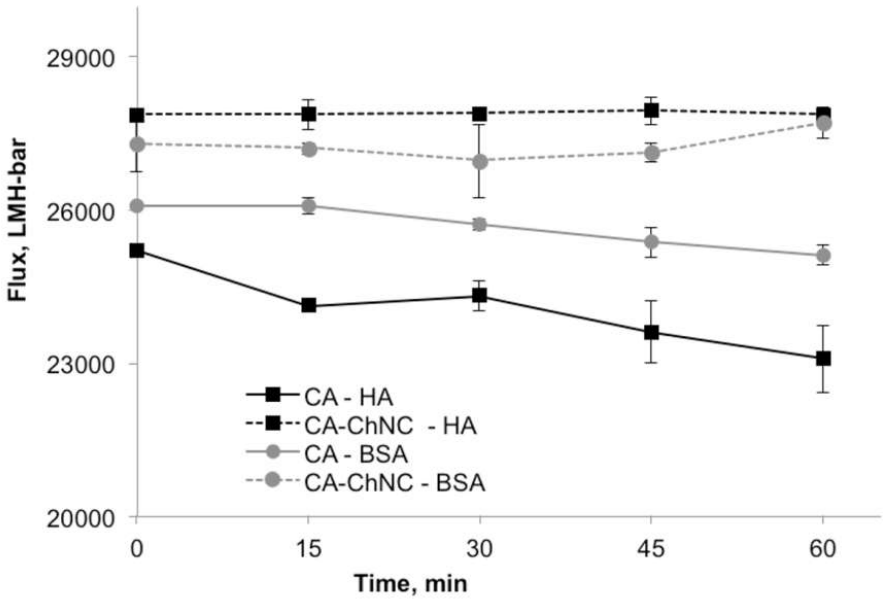

Figure 4.1.5. Flux variation as a function of time using cross-flow filtration through CA and CA-ChNC membranes using water contaminated with humic acid and bovine serum albumin.

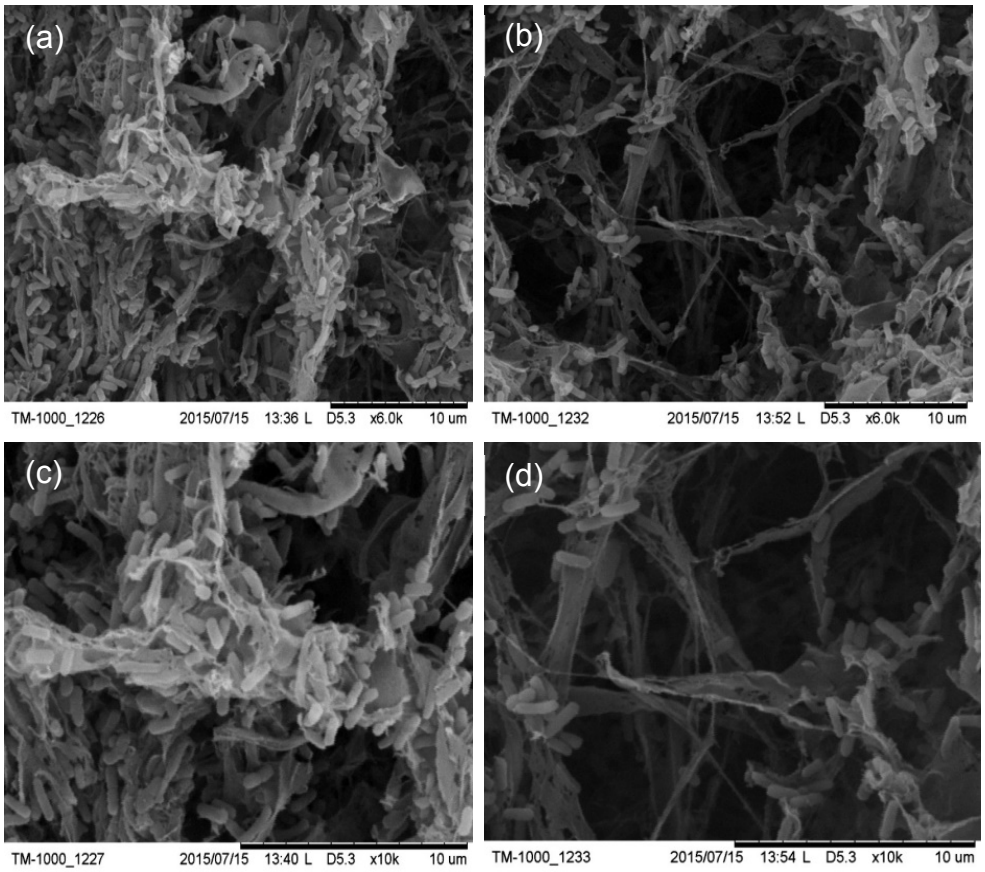

Figure 4.1.6. SEM micrographs of electrospun membranes of CA (a and c) and CA-ChNC (b and d) in contact (18 h) with cultures of *Escherichia coli* CECT 516.

As biofouling is always a consideration in membrane applications, the use of chitin nanocrystals as inhibitors of such biofouling on the surface structure of these cellulose acetate fiber membranes was considered. Biofilm formation was utilized to evaluate biofouling on chitin nanocrystals impregnated electrospun cellulose acetate. Figures 4.1.6 and 4.1.7 shows, respectively, SEM micrographs and Ruby FilmTracer confocal images of membranes kept in contact for 18 and 24 h with cultures of *E. coli* CECT 516. In all cases the cellulose acetate membrane infused with chitin nanocrystals demonstrated significant resistance to be colonized by *E. coli* (4.1.6b; 4.1.7b and f) in comparison to the electrospun cellulose acetate membranes (6a; 7a and e), with a 48 % decrease in biofilm formation after 18 h and with 87.7 % decrease after 24 h of incubation, according to the results obtained with FDA (Table 4.1.2).

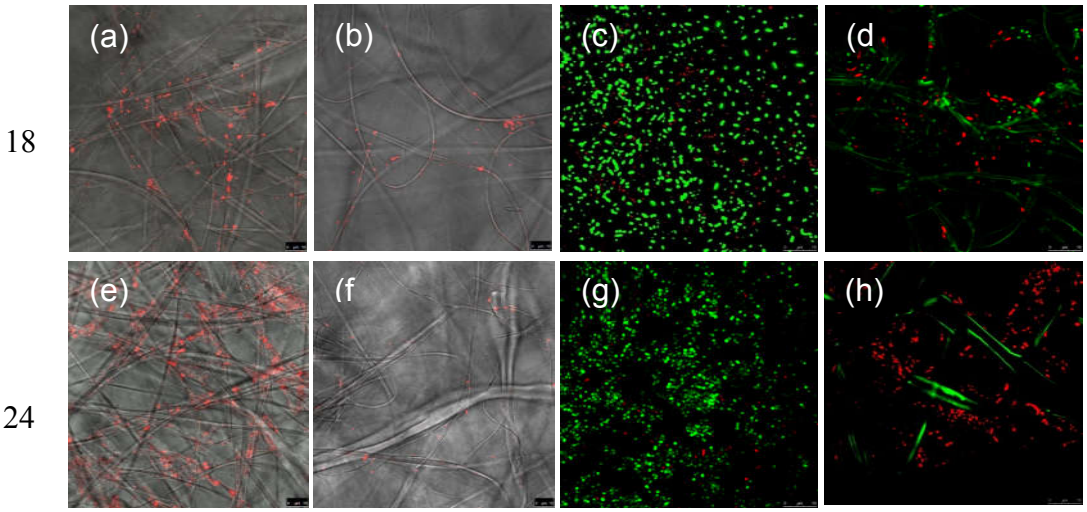

Figure 4.1.7. FilmTracer SYPRO Ruby biofilm matrix staining (a, b, e and f) and Live/Dead double staining (c, d, g and h) of *Escherichia coli* CECT 516 on membranes of CA (a, c, e and g) and CA-ChNC (b, d, f and h) after 18 h (a-d) and 24h (e-h) of biofilm incubation.

The results of FDA staining showed a much higher enzymatic activity of *E. coli* on raw CA membranes than on ChNC specimens. The higher number of PI-marked, non-viable cells on ChNC membranes is also apparent when comparing Figures 4.1.7c-7d and 7d-7h. After 24 in contact with membranes, the viability of bacterial cell became notably reduced with most cells damaged. The differential staining with Ruby FilmTracer revealed the protein network of extracellular substances providing the mechanical stability of biofilms. Furthermore, with increasing incubation time, we observed an increase of extracellular matrix formation which would indicate a biofilm proliferation

on CA membranes, while on CA-ChNC this formation was considerably lower, revealing a reduced biofouling (Figure 4.17). The results of DAPI/PI double staining is shown in Fig. 8. In this system, all cells exhibit blue (DAPI) fluorescence due to nucleus staining, whereas nonviable bacterial cells display red fluorescence (Propidium iodide, PI) with dye uptake depending on cell membrane integrity and physiological state of the bacterial cells. Again, the antibacterial activity of CA-ChNC is apparent in comparison with non-coated CA.

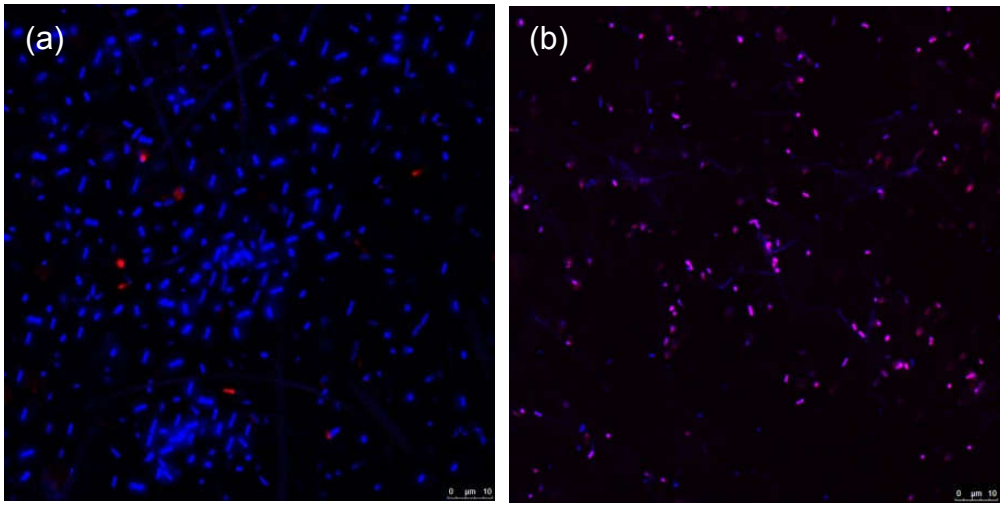

Figure 4.1.8. DAPI/PI double staining of *E. coli* CECT 516 on membranes of CA (a) and CA-ChNC (b) after 18 h of cultures in contact with membranes. Bacterial nucleus was visualized in blue by DAPI. Dead cells were stained in red by PI.

A possible explanation of this behavior is the antimicrobial activity of chitin. Chitin and derivatives as chitosan have been investigated as an antimicrobial material against a wide range of target organisms like algae, bacteria, yeasts and fungi. Several models have been proposed, the most acceptable being the interaction between positively charged chitin/chitosan molecules and negatively charged microbial cell membranes. In this model the interaction was mediated by the electrostatic forces between protonated $-NH_3^+$ groups and the negative residues, presumably by competing with Ca for electronegative sites on the membrane surface. This electrostatic interaction results in twofold interference: i) by promoting changes in the properties of membrane wall permeability, inducing internal osmotic imbalances and the inhibition of microbial growth and ii) by the hydrolysis of the peptidoglycans in the microorganism wall, leading to the leakage of intracellular electrolytes such as potassium ions and other low molecular weight proteinaceous constituents [41].

The formation of a biofilm includes several steps but a prerequisite is the adhesion of microbial cells to a solid surface. Studies of bacterial adhesive properties have indicated that a number of cell surface physico-chemical factors contribute to the process of adhesion. Such factors include cell surface hydrophobicity, the presence of extracellular polymers and cell surface charge. The latter determines the electrostatic interaction between the cell and the substratum [42].

The value of the contact angle gives the basic information on the hydrophobicity of surfaces. For CA and CA-ChNC membranes water contact angles are given in Table 4.1.2. The cellulose acetate membrane had a hydrophobic contact angle of 136.8° while the CA-ChNC membranes demonstrated extreme hydrophilicity with a measured contact angle of 0°, since all the water drop was absorbed by the membrane. The contact angles are dependent upon the chemical composition, porosity, and surface roughness and hydrophilicity increases with the presence of N, O, I, Cl, H, and F. The chemical structure of the chitin nanocrystals on the surface of cellulose acetate (Figure 4.1.1) is contributing to the dramatic reduction in the contact angle [26, 34] [26, 31]. As a general rule, hydrophobic bacteria adhere on hydrophobic surfaces, whereas hydrophilic microorganisms attach to hydrophilic surfaces. The interaction between two hydrophobic entities (*E. coli* cells and CA membranes in our case) is favored because they can enter into closer contact through the facilitated "squeezing of water" in between, but the bio-surface interactions are somewhat more complex due to cell appendages, such as pili and flagella that makes direct contact between surfaces quite difficult [43].

The ζ-potential of the membranes is shown in Table 4.1.2. All membranes were negatively charged. CA membranes reached a surface potential of -30.2 mV whereas the CA-ChNC membranes displayed a ζ-potential of - 4.7 mV at pH 7.5. As with contact angle, the chemical structure of the chitin nanocrystals on the surface of cellulose acetate (Figure 4.1.1) is changing the surface properties of the CA membrane, making it less negative. Electrostatic repulsion could be expected to play a role in bacterial adhesion, given the negative surface charge of bacterial outer membranes (the ζ-potential of *E. coli* is aprox. -30 mV) [44]. The data show, however, that the more negatively charged surfaces were more prone to suffer bacterial colonization as revealed by FDA (Table 4.1.2), FilmTracer and Live/Dead (Figure 4.1.6) staining and by SEM imaging (Figure 4.1.5). It has also been shown that some bacteria could interact with negatively charged

particles if they bind to cationic sites on the cell surface to form clusters favored by the repulsive interactions with negatively charged domains [45, 46].

Summarizing, besides the antimicrobial activity of chitin, the hydrophilic CA-ChNC membranes were much more resistant to bacterial colonization than unmodified CA membranes. The possibility to convert highly hydrophobic membrane surfaces into superhydrophilic surface via surface functionalization with ChNC is also expected to open up new possibilities in membrane technology. The membrane selectivity /rejection based on size exclusion and/or adsorption is of relevance in this context and will be reported in detail in future.

Table 4.1.2. The effect of chitin nanocrystals on the ζ-potential, biofilm formation and contact angle of the electrospun membranes.

	ζ-potential (pH 7.5, mV) (± SD)	FDA relative Biofilm Formation (18h) (± SD)	FDA relative Biofilm Formation (24h) (± SD)	Contact Angle, ° (± SD)	
CA	-30.2 (1.8)	1 (0.04)	1.38 (0.07)	136.8 (3.6)	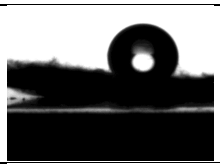
CA-ChNC	-4.7 (2.5)	0.52 (0.03)	0.17 (0.09)	0.0 (0.0)	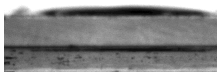

4.2.4 Conclusions

Chitin nanocrystals were successfully infused on to the electrospun cellulose acetate fiber networks resulting in a novel and highly efficient surface treatment approach for low-fouling membrane processing. The hierarchical morphology is shown by the membranes where micron scaled electrospun fiber network is surface coated with ChNC networks in nanoscale with pore sizes in the range on 10 nm. The ChNC coating on individual CA fibers that are 'tied' together at junction points by chitin nanocrystals webs increased the mechanical strength and modulus of the membranes. Addition of the chitin nanocrystals on the CA membrane surfaces resulted in decreased biofilm formation and abiotic fouling tendency accompanied with a transition from highly hydrophobic to super-hydrophilic surfaces. This is attributable to surface chemistry chitin nanocrystals and surface

interactions of cellulose acetate membrane and *E. coli* cells. Chitin nanocrystals on cellulose acetate membranes thus resulted in high flux membranes which shows potential in future water purification of process wash water from food industry containing biological and organic contaminants.

4.2.5 References

[1] J. Cooley. Apparatus for Electrically Dispersing Fluids US Patent Specification, 692631. (1902).
[2] W.J. Morton. Method of dispersing fluids., (1902).
[3] F. Anton. Process and apparatus for preparing artificial threads, (1934).
[4] D. Li, Y. Xia. Electrospinning of nanofibers: reinventing the wheel? Adv Mater, 16 (2004) 1151.
[5] W. Teo, S. Ramakrishna. A review on electrospinning design and nanofibre assemblies. Nanotechnology, 17 (2006) R89.
[6] Z. Huang, Y. Zhang, M. Kotaki, and S. Ramakrishna. A review on polymer nanofibers by electrospinning and their applications in nanocomposites. Composites Sci.Technol., 63 (2003) 2223.
[7] Z. Ma, M. Kotaki, and S. Ramakrishna. Electrospun cellulose nanofiber as affinity membrane. J.Membr.Sci., 265 (2005) 115.
[8] H.Y. Chung, J.R. Hall, M.A. Gogins, D.G. Crofoot, and T.M. Weik. Polymer, polymer microfiber, polymer nanofiber and applications including filter structures, (2004).
[9] H. Hou, J.J. Ge, J. Zeng, Q. Li, D.H. Reneker, A. Greiner, *et al*. Electrospun polyacrylonitrile nanofibers containing a high concentration of well-aligned multiwall carbon nanotubes. Chemistry of Materials, 17 (2005) 967.
[10] X. Wang, K. Zhang, M. Zhu, B.S. Hsiao, and B. Chu. Enhanced mechanical performance of self-bundled electrospun fiber yarns via post-treatments. Macromolecular Rapid Communications, 29 (2008) 826.
[11] R. Sen, B. Zhao, D. Perea, M.E. Itkis, H. Hu, J. Love, *et al*. Preparation of single-walled carbon nanotube reinforced polystyrene and polyurethane nanofibers and membranes by electrospinning. Nano letters, 4 (2004) 459.
[12] W. Park, M. Kang, H. Kim, and H. Jin, Electrospinning of poly (ethylene oxide) with bacterial cellulose whiskers, 249 (2007) 289.
[13] O.J. Rojas, G.A. Montero, and Y. Habibi. Electrospun nanocomposites from polystyrene loaded with cellulose nanowhiskers. J Appl Polym Sci, 113 (2009) 927.
[14] C. Xiang, Y.L. Joo, and M.W. Frey. Nanocomposite fibers electrospun from poly (lactic acid)/cellulose nanocrystals. Journal of Biobased Materials and Bioenergy, 3 (2009) 147.
[15] J. Baker, L. Dudley. Biofouling in membrane systems—a review. Desalination, 118 (1998) 81.
[16] H. Flemming, G. Schaule, T. Griebe, J. Schmitt, and A. Tamachkiarowa. Biofouling—the Achilles heel of membrane processes. Desalination, 113 (1997) 215.
[17] K.J. Howe, M.M. Clark. Fouling of microfiltration and ultrafiltration membranes by natural waters. Environ.Sci.Technol., 36 (2002) 3571.
[18] D. Rana, T. Matsuura. Surface modifications for antifouling membranes. Chem.Rev., 110 (2010) 2448.

[19] D. Klemm, F. Kramer, S. Moritz, T. Lindström, M. Ankerfors, D. Gray, *et al.* Nanocelluloses: a new family of nature-based materials. Angewandte Chemie International Edition, 50 (2011) 5438.
[20] R.J. Moon, A. Martini, J. Nairn, J. Simonsen, and J. Youngblood. Cellulose nanomaterials review: structure, properties and nanocomposites. Chem.Soc.Rev., 40 (2011) 3941.
[21] S.J. Eichhorn. Cellulose nanowhiskers: promising materials for advanced applications. Soft Matter, 7 (2011) 303.
[22] N. Herrera, A.P. Mathew, L. Wang, and K. Oksman. Randomly oriented and aligned cellulose fibres reinforced with cellulose nanowhiskers, prepared by electrospinning. Plastics, Rubber and Composites, 40 (2011) 57.
[23] Z. Karim, A.P. Mathew, M. Grahn, J. Mouzon, and K. Oksman. Nanoporous membranes with cellulose nanocrystals as functional entity in chitosan: Removal of dyes from water. Carbohydr.Polym., 112 (2014) 668.
[24] A. Dufresne. Polysaccharide nano crystal reinforced nanocomposites. Canadian Journal of Chemistry, 86 (2008) 484.
[25] N. Naseri, C. Algan, V. Jacobs, M. John, K. Oksman, and A.P. Mathew. Electrospun chitosan-based nanocomposite mats reinforced with chitin nanocrystals for wound dressing. Carbohydr.Polym., 109 (2014) 7.
[26] N. Naseri, A.P. Mathew, L. Girandon, M. Fröhlich, and K. Oksman. Porous electrospun nanocomposite mats based on chitosan–cellulose nanocrystals for wound dressing: Effect of surface characteristics of nanocrystals. Cellulose, 22 (2015) 521.
[27] A.P. Mathew, M.G. Laborie, and K. Oksman. Cross-linked chitosan/chitin crystal nanocomposites with improved permeation selectivity and pH stability. Biomacromolecules, 10 (2009) 1627.
[28] H. Flemming, Microbial biofouling: Unsolved problems, insufficient approaches, and possible solutions, in Biofilm highlights, Springer, 2011, pp. 81-109.
[29] T.R. Garrett, M. Bhakoo, and Z. Zhang. Bacterial adhesion and biofilms on surfaces. Progress in Natural Science, 18 (2008) 1049.
[30] M.E. Davey, G.A. O'toole. Microbial biofilms: from ecology to molecular genetics. Microbiol.Mol.Biol.Rev., 64 (2000) 847.
[31] M. Rinaudo. Chitin and chitosan: Properties and applications. Progress in Polymer Science, 31 (2006) 603.
[32] K. Gopalan Nair, A. Dufresne. Crab shell chitin whisker reinforced natural rubber nanocomposites. 1. Processing and swelling behavior. Biomacromolecules, 4 (2003) 657.
[33] R. Marchessault, F. Morehead, and N. Walter. Liquid crystal systems from fibrillar polysaccharides. (1959).
[34] A. Qin, X. Li, X. Zhao, D. Liu, and C. He. Preparation and characterization of nano-chitin whisker reinforced PVDF membrane with excellent antifouling property. J.Membr.Sci., 480 (2015) 1.
[35] P. Liu, H. Sehaqui, P. Tingaut, A. Wichser, K. Oksman, and A.P. Mathew. Cellulose and chitin nanomaterials for capturing silver ions (Ag) from water via surface adsorption. Cellulose, 21 (2014) 449.
[36] H. Ma, B.S. Hsiao, and B. Chu. Ultrafine cellulose nanofibers as efficient adsorbents for removal of UO22 in water. ACS Macro Letters, 1 (2011) 213.
[37] H. Ma, C. Burger, B.S. Hsiao, and B. Chu. Nanofibrous microfiltration membrane based on cellulose nanowhiskers. Biomacromolecules, 13 (2011) 180.

[38] L. Huang, S.S. Manickam, and J.R. McCutcheon. Increasing strength of electrospun nanofiber membranes for water filtration using solvent vapor. J. Membr.Sci., 436 (2013) 213.
[39] S. Kaur, Z. Ma, R. Gopal, G. Singh, S. Ramakrishna, and T. Matsuura. Plasma-induced graft copolymerization of poly (methacrylic acid) on electrospun poly (vinylidene fluoride) nanofiber membrane. Langmuir, 23 (2007) 13085.
[40] R. Gopal, S. Kaur, Z. Ma, C. Chan, S. Ramakrishna, and T. Matsuura. Electrospun nanofibrous filtration membrane. J.Membr.Sci., 281 (2006) 581.
[41] R.C. Goy, D.d. Britto, and O.B. Assis. A review of the antimicrobial activity of chitosan. Polímeros, 19 (2009) 241.
[42] J. Azeredo, R. Oliveira. The role of hydrophobicity and exopolymers in initial adhesion and biofilm formation. in: Piet Lens, Anthony P. Moran, Therese Mahony, Paul Stoodley and Vincent O'Flaherty (eds.) Biofilms in Medicine, Industry and Environmental Biotechnology, IWA Publishing, London, 2003. pp. 16-31.
[43] K. Hori, S. Matsumoto, Bacterial adhesion: From mechanism to control. Biochem. Eng. J., 48, 424–434 (2010).
[44] Y.L.Ong, A Razatos, G. Georgiou, M. M. Sharma,. Adhesion forces between *E. coli* bacteria and biomaterial surfaces. Langmuir, 15, 2719-2725 (1999).
[45] A. Dasari, J. Quirós, B. Herrero, K. Boltes, E. García-Calvo, R. Rosal Antifouling membranes prepared by electrospinning polylactic acid containing biocidal nanoparticles Journal of Membrane Science 405–406 (2012) 134–140
[46] C. Wilhelm, C. Billotey, J. Roger, J.N. Pons, J.C. Bacri, F. Gazeau, Intracellular uptake of anionic superparamagnetic nanoparticles as a function of their surface coating, Biomaterials 24, 1001–1011 (2003).

4.3 Part II: Coaxial poly (lactic acid) electrospun composites incorporating cellulose and chitin nanocrystals

4.3.1 Introduction

Electrospinning is a versatile procedure for producing polymeric fibers below the micron scale [1]. The technique has been recently investigated in view of its potential to generate high surface-to-volume ratio materials functionalized in the nanoscale [2,3]. By controlling operating conditions and solution parameters, electrospinning can be used to produce a variety of non-woven porous or smooth nanofibrous structures suitable for their use as filtration media [4]. Opposite to conventional membrane preparation technologies, such as phase inversion, the high pore interconnectivity and porosity of electrospun membranes make them promising materials for filtration processes [5]. However, filtration using electrospun fibrous membranes must overcome the hurdle of their lower mechanical strength compared to polymeric films, which is particularly critical in pressure-driven filtration for water treatment applications [6]. The reason is the low degree of molecular orientation in electrospun polymers, which is a consequence of the competition between flow-induced chain orientation and chain relaxation before fiber solidification [7]. The mechanical properties of electrospun fibers can be improved using post-treatments, such as stretching and annealing, that increase molecular orientation and crystallinity [8]. Alternatively, the co-electrospinning of polymers and fillers can produce composite fibers with enhanced mechanical properties [9,10].

Biofouling, is one of the main factors determining membrane performance in many practical applications [11]. It refers to the growth of microorganisms on membrane surface, and results in loss of permeability, increased transmembrane pressure, reduced membrane life and risk of pathogen dissemination [12]. Two approaches can be followed to minimize biofouling: Proper surface design to prevent primary adhesion, or the use of cleaning strategies including the use of biocides [13]. The manipulation of the physicochemical properties of membranes allow creating surfaces hostile for microbial attachment targeting the initial stage of microbial colonization, before biofilm formation [14]. Biofilms are complex communities of cells embedded in an extracellular polymeric matrix formed by polysaccharides, proteins, and nucleic acids, which protect cells from adverse conditions [15]. Once formed, biofilms are very difficult to remove. In fact, biofilm formation constitutes an advantageous strategy for survival and growth in hostile environments and represents a degree of complexity in structure and metabolism similar

to the tissues of higher organisms [16]. The high tunability of electrospun membranes offers new ways of creating antimicrobial environments. The incorporation of functional agents with antibiotic properties [17], the use of polymers with intrinsic antibacterial properties such as chitosan [18] and different treatments for surface modification [19] have been explored to create biofouling resistant electrospun fibers.

Poly(lactic acid), PLA, is a biodegradable thermoplastic aliphatic polyester derived from renewable resources, which, despite being hydrophobic, displays higher natural hydrophilicity than conventional hydrophobic thermoplastic polymers due to the better access of water molecules to the polar oxygen linkages of its backbone. Higher water fluxes and reduced biofouling tendency of PLA-based membranes offer a good option to replace conventional membranes made of petrochemical polymers [20]. However, electrospun PLA in membrane applications presents some limitations due to the poor mechanical properties of pure PLA fibers [5].

Cellulose and chitin fibrils in the nanometer range are biobased nanoparticles that expanded the possibilities of natural polymers in the field of engineered sustainable nanocomposites [21]. The dimensions of cellulose and chitin nanocrystals and nanofibers offer a high surface area filler and the possibility of creating functional materials with exceptional physical, chemical and mechanical properties [22]. Cellulose nanocrystals from microcrystalline cellulose were previously reported to substantially improve the mechanical properties of electrospun nanocomposites prepared from PLA [23], polyethylene oxide [24], and polyacrylamide [25].

Chitin, poly-β-(1-4)-N-acetyl-D-glucosamine, is a natural, renewable and biodegradable polymer, the second most abundant natural polymer after cellulose. Substantial amounts of this structural material can be found in animals, as part of exoskeletons, backbones and the cell walls of fungi and yeasts. Despite its easy accessibility, chitin is an underutilized resource because of its insolubility in water and common organic solvents [26]. However, in recent times the use of chitin has generated great interest due to its excellent mechanical and certain antibacterial properties. The incorporation of chitin derived nanocrystals to different polymeric membranes has been recently addressed with the purpose of enhancing their mechanical properties and antifouling performance [27,28].

In this work, structured electrospun PLA fibers reinforced with chitin and cellulose nanocrystals were prepared by means of coaxial electrospinning. The approach used

aimed at combining the environmentally desirable properties of PLA with the unique characteristics of cellulose/chitin nanocrystals to create high flux and low biofouling membranes with enhanced mechanical resistance. Placing cellulose and chitin nanomaterials on fiber shell aimed at modifying surface fiber properties to enhance water permeability and resistance to microbial attachment.

4.3.2 Material and methods

4.3.2.1 Materials

Transparent PLA (marketed under trade name PLA Polymer 2002D) was acquired in pellets from NatureWorks LLC, UK, with melt index (MFR) of 5–7 g/10 min (at 210 °C/2.16 kg), molecular weight 121400 g/mol, melting temperature 160 °C and 4% D-content (96% L-lactide). Polyacrylonitrile (PAN), molecular weight 150000, was obtained from Sigma-Aldrich. *N, N*-dimethylformamide (DMF, synthesis grade) and chloroform (synthesis grade) were purchased from Scharlab (Spain). Culture media components were biological grade reagents acquired from Conda-Pronadisa (Spain). Fluorescein diacetate (FDA), Live/Dead Bac-Light Bacterial Viability Kit and FilmTracer SYPRO Ruby were acquired from Invitrogen (Thermo Fisher, Waltham, USA).

The first type of cellulose nanocrystals, $CNC_{H_2SO_4}$, was prepared via sulfuric acid hydrolysis. Briefly, microcrystalline cellulose was mixed with sulfuric acid (63.5 wt %) under stirring in an ice bath. The suspension was heated up to 44 °C for 130 min under stirring. Then, the suspension was centrifuged for 10 min at 12000 rpm until the supernatant became turbid. The nanocrystal suspension was neutralized against deionized water through dialysis. Thereafter, the suspension was sonicated in an ice bath to separate the nanocrystals [29].

The second kind of cellulose nanocrystals, CNC_{BE}, was obtained following the bioethanol processing route [30,31]. Unbarked wood was hydrolyzed using dilute acid in a bioethanol pilot plant at SP Processum, Örnsköldsvik, Sweden, and refined to obtain pure cellulose. The refining was done by Soxhlet extraction for 6 h at 150 °C using toluene/acetone mixture (2:1 ratio). This material was then bleached, washed with deionized water and concentrated by centrifugation to 17 wt%. The purified cellulose from bioethanol process was led to 2 wt% suspensions, mixed by shear mixture and

passed through the homogenizer, 10 times to obtain a thick gel of cellulose nanocrystals (CNC_{BE}) as reported elsewhere [31].

Chitin nanocrystals (ChNC) were isolated from crab shells using hydrochloric acid hydrolysis. The raw material was boiled in 5 wt % KOH solution for 6 h under stirring to remove proteins. Afterwards, the suspension was washed with distilled water and then bleached with chlorite at 80 °C for 6 h. Thereafter, the bleached suspension was washed followed by bleaching during overnight treatment using 5 wt% KOH and then concentrated using centrifuge. After that, the purified chitin was hydrolyzed using HCl 3 N for 90 min at 80 °C under stirring. After hydrolysis, the excess acid was removed by centrifugation until the turbid supernatant was achieved. The isolation process was completed by neutralization against deionized water. Then, the suspension was sonicated to individualize the nanocrystals [32,33]. In what follows, $CNC_{H_2SO_4}$ and CNC_{BE} will be jointly referred to as cellulose nanocrystals, CNC, while the term nanocrystals, NC, will include also chitin nanocrystals, ChNC. Water dispersed NC were solvent exchanged into DMF by distillation-assisted evaporation to facilitate the electrospinning process.

4.3.2.2 Coaxial electrospinning

Figure 4.2.1 presents a schematic illustration of the experimental setup used for coaxial electrospinning. The spinneret consists of a double capillary tube where a smaller one is concentrically inserted. The inner fluid produced the core of the fiber, while the outer one formed the shell of core-shell or coaxial fibers. 7 wt% PLA in chloroform/DMF (3:2 v/v) was used for the core and 10 wt% of PAN in DMF with 5, 10, 15 or 20 wt% of NC (in solvent-free basis) was used to produce the PAN/NC fiber shell. The shell mixture was sonicated using an ultrasonic probe VC505 (500W, Sonics and Materials Inc.) for 5 min carried out in short intervals at 20% amplitude followed by 15 min of magnetic stirring at 80 °C. The flow rate of both solutions was maintained at a constant rate of 0.8 mL/h driven by a syringe pump (Harvard PHD 22/2000) and the voltage applied was 20 kV supplied by a high voltage power supply (Heinzinger LNC 30000). Electrospun nanofibers were deposited on a flat collector plate (16 cm x 16 cm) covered with aluminum foil and at 20 cm distance from the coaxial needle tip (Yflow SD, Spain). Each sample was collected for 6 h. All the coaxial membranes prepared in this work have the same polymeric shell@core structure, PAN/NC@PLA. The changes in fiber composition

are given by the type of nanocrystal and its concentration. The nomenclature used for the prepared membranes is shown in Table 4.2.1.

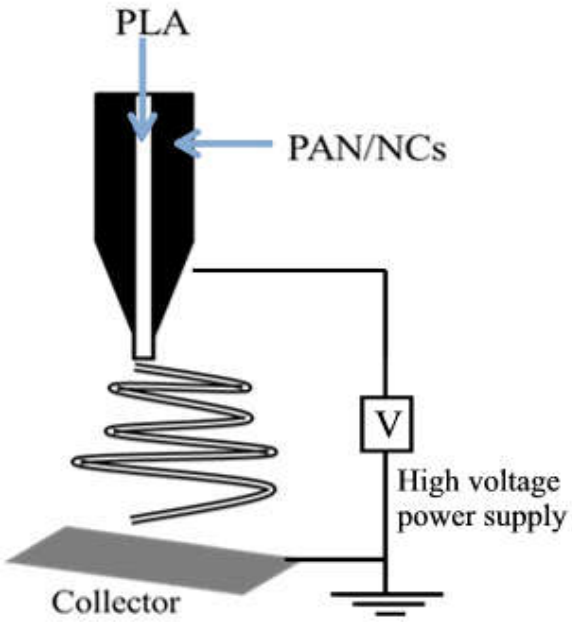

Figure 4.2.1. Schematic illustration of the coaxial electrospinning setup for core-shell fibers. Core: PLA; shell: PAN/NC.

Table 4.2.1. Composition and nomenclature of electrospun membranes[a].

Fibre type	Membrane identifier	Shell nanocrystal	Nanocrystal wt% [b]
	PLA	-	–
PAN@PLA	PAN@PLA	-	–
PAN/NC@PLA	PAN/$CNC_{H_2SO_4}$-5@PLA	Cellulose H_2SO_4	5
	PAN/$CNC_{H_2SO_4}$-10@PLA	Cellulose H_2SO_4	10
	PAN/$CNC_{H_2SO_4}$-15@PLA	Cellulose H_2SO_4	15
	PAN/$CNC_{H_2SO_4}$-20@PLA	Cellulose H_2SO_4	20
	PAN/CNC_{BE}-5@PLA	Cellulose BE	5
	PAN/CNC_{BE}-10@PLA	Cellulose BE	10
	PAN/CNC_{BE}-15@PLA	Cellulose BE	15
	PAN/CNC_{BE}-20@PLA	Cellulose BE	20
	PAN/ChNC-5@PLA	Chitin	5
	PAN/ChNC-10@PLA	Chitin	10
	PAN/ChNC-15@PLA	Chitin	15
	PAN/ChNC-20@PLA	Chitin	20

[a] In all cases, PLA concentration was 7 wt% (core polymer) and PAN oncentration was 10 wt% (shell polymer). Accordingly, the ratio PLA/PAN in the final fibres was 7/10 in weight.
[b] In solvent-free basis.

4.3.2.3 Membrane characterization

The morphology of electrospun fibers was observed by scanning electron microscopy (SEM) using a Carl Zeiss DSM 950 instrument operating at 25 kV. The membranes were sputter coated with gold before SEM observations. Transmission electron microscopy (TEM) images of coaxial structures were obtained using a transmission electron microscope (Zeiss M10, Germany) at an accelerating voltage of 50 kV. AFM images were obtained using a Multimode Nanoscope V Atomic force microscope (AFM) from Bruker. Fiber diameters were calculated from the analysis of SEM images using ImageJ software from at least 50 nanofibers randomly selected from each image.

The wettability of membrane surfaces was tested using an optical contact angle meter (Krüss DSA25 Drop Shape Analysis System) using the sessile drop method. Samples were placed on the test cell and drops of distilled water were deposited on the surfaces by the delivering syringe. Contact angle measurements for each surface were taken at room temperature on at least three different positions on each sample.

Surface zeta potential (ζ-potential) was measured via electrophoretic light scattering (Zetasizer Nano ZS) using the Surface Zeta Potential Cell (ZEN 1020) from Malvern. Measurements were performed at 25 °C using 10 mM KCl, aqueous solution pH 7.5, with of 0.5 wt% poly(acrylic acid) (450 kDa), for negatively charged membranes, and 0.5 wt% polyethylenimine (600 Da), for positively charged membranes, used as tracers. pH was adjusted using 1M KOH or 1 M HCl.

Bubble point test for maximum pore size was performed following the F316 Test Method described in American Society for Testing and Materials Standard (ASTM). Membranes, preconditioned by immersion in distilled water, were placed in a filter holder connected to a source of regulated gas pressure flowing upwards. The pressure of gas at the onset of bubble formation was recorded as bubble point and used to calculate the diameter of the larger membrane pores as follows:

$$d = \frac{4\,\gamma \cos \theta}{P} \qquad (1)$$

where P is the bubble-point pressure, γ the surface tension of the liquid, θ the liquid-solid contact angle and d the maximum pore average diameter. Filtration experiments were carried out using a 47 mm stainless steel pressure filter holder (Millipore) with an

effective membrane area of 11.3 cm^2 operating at a constant nitrogen transmembrane pressure of 0.2 bar. To open any possibly closed pores before the water flux test, freshly prepared membranes were pre-wetted and compacted at 0.5 bars for 5 min. Then, water flux was evaluated and membrane permeability was determined from the pure water flux per unit transmembrane pressure.

Membrane tensile strength and elongation at break were measured using a universal testing machine, Shimadzu Autograph AG-X with a load cell 500 N. Before taking measurements, test samples were preconditioned at 45% relative humidity for one week. Their thickness was measured using a digital thickness gauge. Samples of 50 mm length, 5 mm width and approximately 150 μm thickness were placed on paper windows with a preload of 0.1 N according to prescriptions. The speed of the strain testing was 2 mm/min and the tensile gauge length was 20 mm. At least 5 specimens were tested for each material. Ultimate tensile stress, σ_{max}, was calculated by dividing the maximum load of force at failure, F, by the initial cross-sectional area of the membrane specimen, A_o:

$$\sigma_{max} = \frac{F}{A_o} \quad (2)$$

Fracture strain, ε, was calculated as elongation at break based on the initial sample length, L_0, and the sample length at break point, L:

$$\varepsilon = \ln\left(\frac{L}{L_o}\right) \quad (3)$$

Young's modulus was calculated through a linear regression analysis of the initial linear portion of the stress-strain curves.

4.3.2.4 Bacterial bioassays

The bacterial strain used for bioassays was *Escherichia coli* CECT 516 (equivalent to ATCC 8739). Cell cultures grew overnight in Nutrient Bacterial medium (NB: for 1 L solution in distilled water, beef extract 5 g, peptone 10 g, NaCl 5 g, pH was adjusted to 7.2) while shaking at 37 °C. Reactivation was tracked by measuring optical density at 600 nm. For spore removal assays, spores of the fungi *Aspergillus niger* (ATCC 6275) were used after being resuspended in a saline solution (NaCl 0.9 wt.% w/v) to avoid their growth and the formation of mycelia.

To evaluate the removal of microorganisms during filtration, liquid cultures of *E. coli* and *A. niger* spores (10^7-10^8 cells/mL) were filtered through the membranes for 60 min and the optical density at 600 nm of the filtrate was measured every 15 min. The reduction in pathogen concentration was calculated using log-reduction values (LRV):

$$\text{LRV} = log_{10}\left(\frac{C_o}{C}\right) \quad (4)$$

Where C_o is influent pathogen concentration, and C the effluent pathogen concentration. Hence, a LRV of 1 is equivalent to 90% removal of a target pathogen, an LRV of 2 is equivalent to 99% removal and so on [34].

Biofilm formation was assessed for PLA and PAN/NC@PLA composites after placing membrane specimens on polystyrene 24-well plates. Exponentially growing cultures of *E. coli* on NB were diluted to an OD_{600} of 0.0138 (10^8 cells/mL). 2 mL of diluted cultures were placed on the surface of the electrospun membranes, which were subsequently incubated for 18 h at 37 °C without stirring. After the biofilm assay, the liquid culture was removed and membranes were carefully washed with distilled water to remove planktonic cells. For the quantification of biofilms, fluorescein diacetate (FDA) was used, following the manufacturer's instructions. The fluorescence was measured in a fluorometer/luminometer Fluoroskan Ascent FL as follows. 200 µL of the fluorescent stain were extended over the entire surface. After 15 min of incubation at 25 °C, FDA was excited at 485 nm, and emission recorded at 538 nm.

The visualization of cells and biofilms was performed by confocal microscopy 18 h after inoculation using a Leica Microsystems Confocal SP5 fluorescence microscope (Leica Microsystems, Germany). Viable and non-viable bacteria were tracked using Live/Dead BacLight Bacterial Viability Kit. For membrane staining, the surface of each specimen was covered with 30 µL of stain (a 0.5:1 mixture of SYTO 9 and PI in DMSO). The incubation was performed in the dark for 15-30 min at room temperature. For matrix visualization, the biofilms were stained with 200 µL FilmTracer SYPRO Ruby per film, incubated in the dark for 30 min at room temperature, and rinsed with distilled water. For green fluorescence (SYTO 9, intact cells) excitation was performed at 488 nm and emission at 500-575 nm. For red fluorescence (PI, dead cells), the excitation/emission wavelengths were 561 nm and 570-620 nm respectively. For FilmTracer SYPRO Ruby staining the excitation/emission wavelengths were 450 nm and 610 nm respectively.

Biofilm formation was also visualized by SEM. A process of dehydration and drying with ethanol at different concentrations was carried out to analyze samples in contact with microorganisms by SEM.

4.3.3 Results and discussion

4.3.3.1 Electrospinning solutions

Several parameters influence the transformation of polymer solutions into nanofibers by electrospinning, which include, among others, viscosity, electrical conductivity, and the surface tension of the electrospinning solution [35]. The values of the viscosity and conductivity of the nanocrystals and electrospinning suspensions are shown in Table S4.2.1 (Supporting Information). The viscosity obtained for the solution containing PLA (core polymer) was 310.8 mPa s and that of PAN solution (shell polymer) 924.6 mPa s. The results showed that the addition of $CNC_{H_2SO_4}$ and ChNC, induced a viscosity decrease in comparison with PAN solution, the lower viscosity corresponding to the more concentrated suspensions (20 wt%). A similar behavior was reported elsewhere [36-38]. After the addition of CNC_{BE}, however, viscosity increased due to the gel consistency of this nanocrystal solution. Compared with neat PLA core solution, the viscosity of the shell suspensions (PAN/NC) increased substantially.

The electrical conductivity of CNC ($CNC_{H_2SO_4}$ and CNC_{BE}) was higher than that of ChNC as a consequence of their negatively charged surface groups like sulphate ester groups (resulting from sulfuric acid hydrolysis) and carboxyl groups [31]. The conductivity of ChNC suspensions was most probably explained by the protonation of the N-H groups on chitin structure [33, 39]. Increasing NC concentration there was a slight increase in electrical conductivity of the electrospinning suspensions.

4.3.3.2 Morphology of core/shell composite nanofibers

The stability of the core/shell structure of composite nanofibers is a consequence of the stability of the compound jet of two liquids, which in turn depends on their physical properties, feed rates and applied voltage [40, 41]. In this work, the effect of interface tension was reduced using a similar solvent system to dissolve core and shell components, namely chloroform/DMF for the core and DMF for the shell. SEM micrographs of electrospun neat PLA and coaxial PAN/NC@PLA membranes are shown in Figure 4.2.2 (A to D) for the higher NC loadings. Electrospun membranes were homogenous,

exhibiting well defined, bead-free non-porous fibers. Figure 4.2.2 (E to H) also shows TEM images of PAN@PLA (E) and PAN/NC@PLA (F-H) core-shell composites for different NC loadings. The presence of nanocrystals on fiber surface is apparent. Further insight into fiber topography is shown in AFM images from Figure S4.2.1. Accurate determination of NC on fiber surface was not possible from TEM images, but their dimensions were reported earlier. Nanocrystals had diameters in the range of 5-20 nm and length in the range of 100-300 nm, which agrees with the nanometer scale of the details observed in TEM images [28, 31, 33].

The average fiber diameters were 199 ± 52 nm for neat PLA, 339 ± 40 nm for PAN/$CNC_{H_2SO_4}$-20@PLA, 338 ± 35 nm for PAN/CNC_{BE}-20@PLA and 399 ± 37 nm for PAN/ChNC-20@PLA nanofibers. (The diameters for the rest of membranes are listed in Table S4.2.2). Fiber diameters and confidence intervals were obtained from at least 50 measurements in SEM micrographs. The diameter of coaxial PAN/NC@PLA fibers results from the structural organization of the composite fiber consisting of an inner core of PLA and an outer layer of PAN/NC. The diameter of coaxial fibers was higher for lower NC loadings, which can be explained in terms of the lower viscosity and higher conductivity of suspensions with higher NC contents [38, 42]. The differences found in this work, however, were small and scarcely significant.

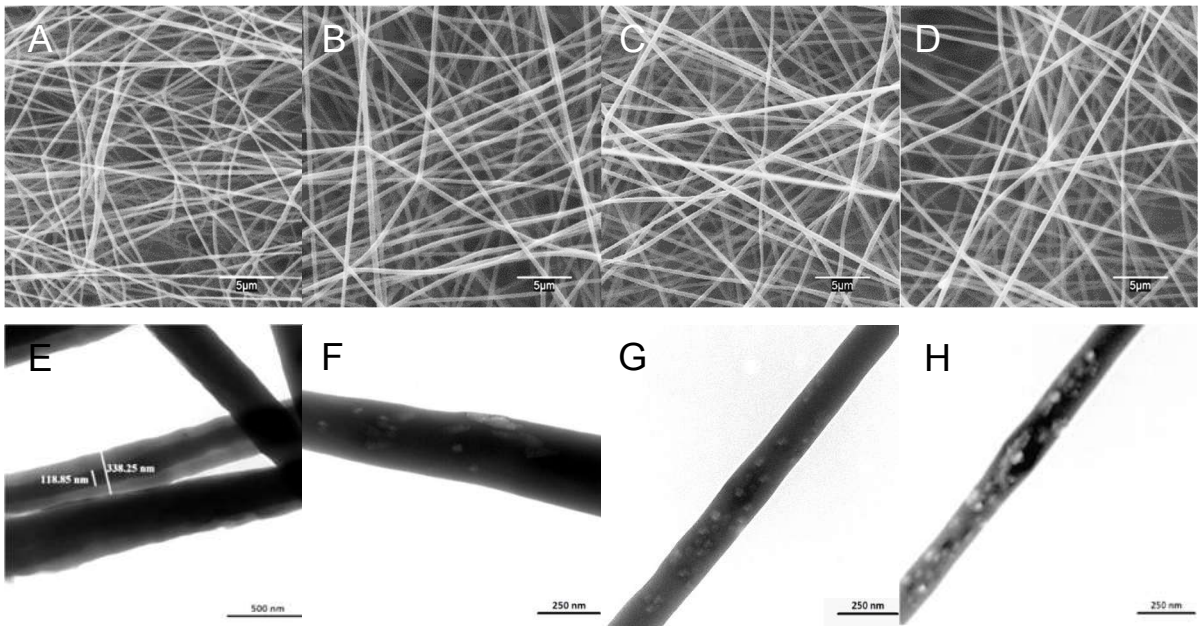

Figure 4.2.2. SEM micrographs of (A) neat PLA, (B) PAN/$CNC_{H_2SO_4}$- 20@PLA, (C) PAN/CNC_{BE}- 20@PLA, and (D) PAN/ChNC-20@PLA electrospun membranes. TEM images of (E) PAN@PLA core-shell, (F), PAN/$CNC_{H_2SO_4}$-5@PLA, (G) PAN/CNC_{BE}-15@PLA, and (H) PAN/ChNC-20@PLA coaxial membranes with NC on fiber surface.

Electrospinning produces highly porous nanofiber network structures with interconnected flow-through pores (Figure 4.2.2). Bubble point test was performed to evaluate the opening size of the largest membrane pores. For pure PLA membranes, the largest mean pore size was 0.8 ± 0.1 μm, which increased for coaxial PAN@PLA membranes without nanocrystals to 1.2 ± 0.1 μm. Coaxial PAN/NC@PLA membranes displayed higher pore sizes, the largest values corresponding to membranes with higher NC loadings (Table S4.2.2). There were no significant differences for membranes with different types of NC at similar loadings.

4.3.3.3 Mechanical properties

Tensile properties indicate how materials react to forces being applied in tension. The primary product of tensile tests is a load-elongation curve, which is then converted into a stress-strain plot according to Eq. 2 and 3. Figures 4.2.3 to 4.2.5 show the stress-strain curves of neat PLA and coaxial PAN/NC@PLA nanocomposite membranes. Table S4.2.2 gives the maximum tensile strength, σ_{max}, Young's modulus, E, and ultimate strain, ε, of all the membranes tested. Figure 4.2.3 shows the curves for representative samples prepared with $CNC_{H_2SO_4}$ and the corresponding matrices, PLA and PAN@PLA, while the average tensile data are shown in Table S4.2.2. For PLA membranes, the mean σ_{max} and E were 2.3 MPa and 0.51 GPa respectively in agreement with previously reported results [5, 20, 23, 43]. Coaxial membranes with $CNC_{H_2SO_4}$ showed significant improvement in tensile strength at low NC content (5 wt%), which increased by 169 % compared to the neat PLA membranes and by 260 % compared to the coaxial membrane without NC, PAN@PLA. At 20 wt% $CNC_{H_2SO_4}$, the tensile properties of the coaxial nanocomposite membranes slightly decreased compared to neat PLA membranes, which could be attributed to the aggregation of NC at their high concentration levels on the fiber surface [44]. A similar trend was observed for Young's modules, PAN/$CNC_{H_2SO_4}$-5@PLA being the stiffest material with a 172 % increase respect to PLA and 146 % respect to the coaxial membranes without NC.

Figure 4.2.4 shows the stress-strain curves for PLA and PAN/CNC_{BE}@PLA coaxial membranes, the main parameters being presented in Table S4.2.2. Similar to $CNC_{H_2SO_4}$ loaded membranes, coaxial membranes with 5 wt% CNC_{BE} were the strongest with an improvement in tensile strength of 188 % form neat PLA. Membranes loaded with 10 % and 15 % CNC_{BE} showed a slight decrease in $\sigma_{max,}$ which could be attributed to the

irregular aligning and poor adhesion between fibers [45]. However, Young's modulus increased with higher NC content, being the 20 % CNC_{BE} composition the stiffest, 176 % over neat PLA membranes.

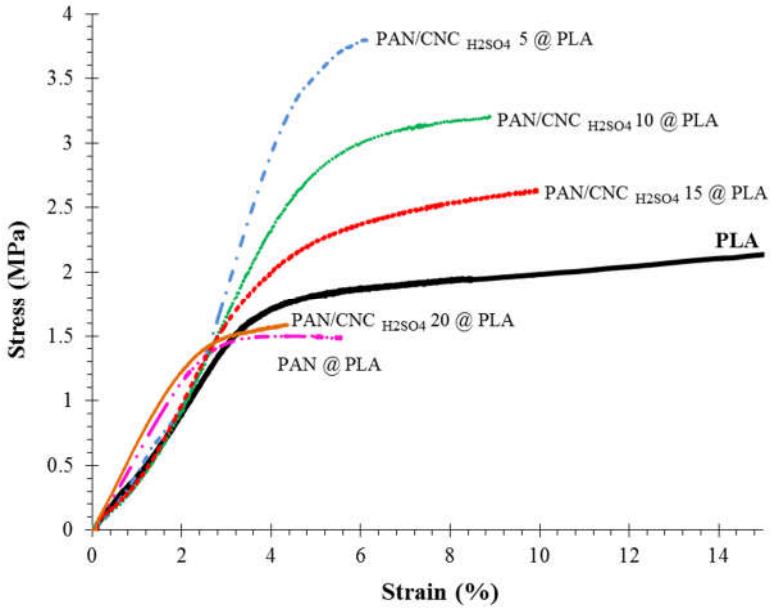

Figure 4.2.3. Stress-strain curves of PLA and PAN/$CNC_{H_2SO_4}$@PLA coaxial membranes.

Figure 4.2.5 and Table S4.2.2 show the mechanical properties of PAN/ChNC@PLA coaxial membranes. Overall, ChNC improved the mechanical properties of the coaxial membranes. All composite materials performed better than pure PLA and the coaxial PAN@PLA membranes, with best results for 15 wt% ChNC loading. For PAN/ChNC-15@PLA σ_{max} increased by 227% and E by 529% compared to neat PLA membranes, making this composite the strongest and the stiffest among all tested materials. Previous studies have shown also that chitin was able to improve the mechanical properties of electrospun cellulose acetate membranes by impregnation with ChNC [28].

Non-woven electrospun membranes are made of randomly oriented fibers and their mechanical properties depend on their direction and the interaction between fibers. A poor adhesion between fibers and a broad distribution in fiber diameter favor failures at the fiber-fiber interface brings about lower fiber strength [24]. The improvement in mechanical properties of coaxial nanocomposites of poly(ethylene oxide) electrospun fibers containing CNC has been attributed to the better stress transfer favored by nanocrystal alignment [24]. The enhancement of mechanical properties due to the incorporation of relatively low amounts of CNC fillers has been rationalized in terms of

the mechanical percolation effect, due to the formation of a rigid interconnected structure of CNC [46]. The higher crystallinity induced by CNC has been also shown to result in harder and more thermally stable fibers [47]. The higher crystallinity of mixed PLA/CNC electrospun fibers arises from CNC acting as nucleation sites during the electrospinning of composite fibers [44].

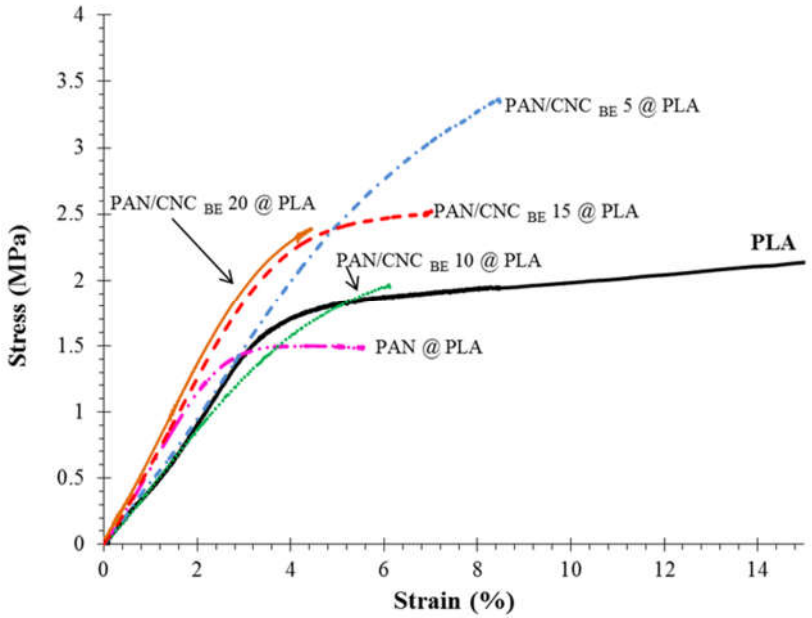

Figure 4.2.4. Stress-strain curves of PLA and PAN/CNC$_{BE}$@PLA coaxial membranes.

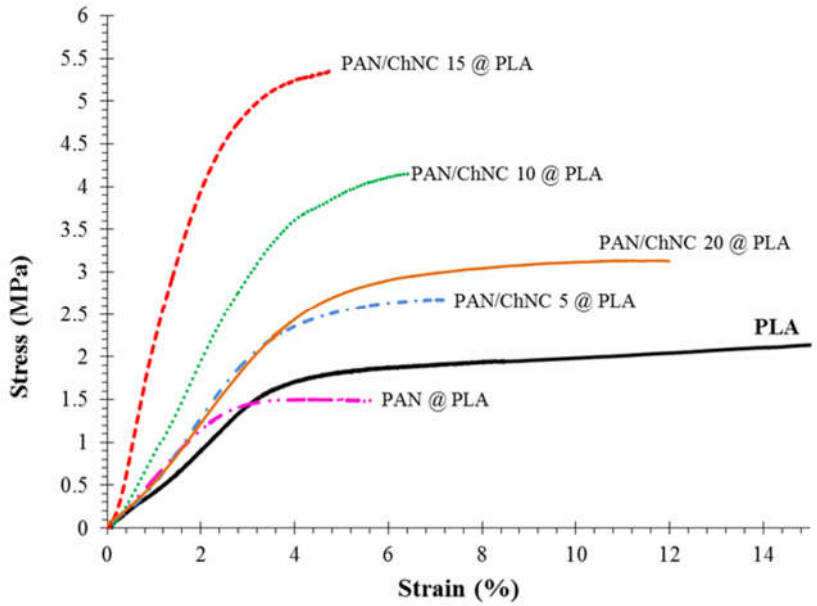

Figure 4.2.5. Stress-strain curves of PLA and PAN/ChNC@PLA coaxial membranes.

The increase in Young's modulus of composite PLA membranes containing CNC was attributed to the smaller fiber diameter of composite materials as a consequence of the higher viscosity and electrical conductivity of PLA/CNC suspensions compared to neat PLA solutions [23]. For the coaxial composites prepared in this work the lower fiber diameter observed for membranes with higher NC loadings was not important enough to influence the mechanical properties of composite membranes. The improvement of Young's modulus of heterogeneous mats has also been related to the formation of secondary ultrafine nanofibers interacting with primary nanofibers through bonding points [24]. We also found the formation of secondary ultrafine nanofibers during the electrospinning of composite materials as shown in Figure S4.2.2, but their formation is not probably extensive enough to significantly influence Young's modulus.

Core-shell fibers have also been prepared using emulsion electrospinning with CNC forming the core and PLA the shell that showed strong structural reinforcing effect due to the formation of a rigid percolating network of CNC [48]. The membranes prepared in this work, with NC in the outer part of the fiber, displayed significantly enhanced mechanical properties due to the same reasons. For the three types of coaxial nanocomposites, the ultimate strain decreased compared to pure PLA membranes meaning that the coaxial structure and the presence of the nanocrystals reduced fiber ductility making membranes more resistant to deformation [49]. The decrease of the elongation of electrospun non-woven PLA fibers containing CNC was also reported for PLA/CNC non-coaxial nanocomposites as a consequence of the reinforcing effect [44].

4.3.3.4 Water flux and permeability

The permeability of electrospun PLA and PAN/NC@PLA coaxial membranes is shown in Figure 4.2.6 and Table S4.2.2 for a transmembrane pressure of 0.2 bar. In all cases, the water flux was higher for the composite coaxial membranes than for neat PLA membranes (504 L m^{-2} h^{-1}) and for PAN@PLA coaxial membranes (777 L m^{-2} h^{-1}). PAN/$CNC_{H_2SO_4}$@PLA coaxial membranes displayed water fluxes increasing with CNC content from 1106 L m^{-2} h^{-1} (5 wt%) to 2140 L m^{-2} h^{-1} (20 wt%). Water flux for coaxial membranes coated with CNC_{BE} ranged from 1357 L m^{-2} h^{-1} (5 wt%) to 1700 L m^{-2} h^{-1} (20 wt%), while membranes with ChNC, which showed the highest flux values, ranged from 1403 L m^{-2} h^{-1} (5 wt%) to 2646 L m^{-2} h^{-1} (20 wt%). The incorporation of NC to the fiber surface increased pore size (Table S4.2.2) and significantly improved their wettability

making them more hydrophilic (Table 4.2.2). Both factors explain the increased water flux and permeability observed in agreement with results published elsewhere on the effect of nanocellulose addition to polymeric membranes [50,51].

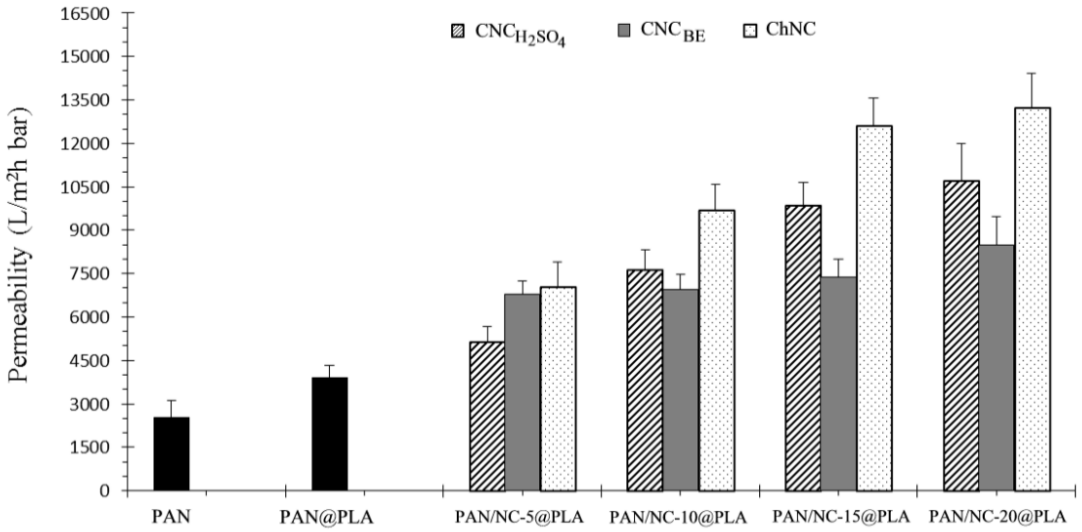

Figure 4.2.6. Water permeability of neat PLA and coaxial membranes.

Table 4.2.2. Effect of the nanocrystals on water contact angle, surface ζ-potential and biofilm formation[a].

Membranes	Water contact angle (WCA)	Surface ζ-potential (pH 7.5, mV)	FDA relative biofilm formation (18 h)
PLA	121.6 ± 2.4	-31.3 ± 3.9	1.00 ± 0.06
PAN@PLA	6.5 ± 3.2	-10.5 ± 1.3	2.94 ± 0.03
PAN/CNC$_{H_2SO_4}$-5@PLA	72.2 ± 3.6	-13.1 ± 4.0	3.68 ± 0.09
PAN/CNC$_{H_2SO_4}$-10@PLA	68.9 ± 2.5	-11.6 ± 2.1	5.19 ± 0.04
PAN/CNC$_{H_2SO_4}$-15@PLA	66 ± 1.8	-21.3 ± 1.7	5.87 ± 0.10
PAN/CNC$_{H_2SO_4}$-20@PLA	57.1 ± 4.1	-23.2 ± 3.0	7.67 ± 0.08
PAN/CNC$_{BE}$-5@PLA	80.8 ± 1.3	-13.8 ± 3.2	2.6 ± 0.2
PAN/CNC$_{BE}$-10@PLA	71.6 ± 2.1	-16.2 ± 2.9	4.2 ± 0.1
PAN/CNC$_{BE}$-15@PLA	64.9 ± 1.5	-23.6 ± 2.5	5.33 ± 0.07
PAN/CNC$_{BE}$-20@PLA	62 ± 2.3	-27.2 ± 3.3	6.68 ± 0.02
PAN/ChNC-5@PLA	0 [b]	-7.0 ± 1.8	0.31 ± 0.05
PAN/ChNC-10@PLA	0 [b]	-1.8 ± 2.4	0.21 ± 0.04
PAN/ChNC-15@PLA	0 [b]	0.7 ± 1.1	0.06 ± 0.15
PAN/ChNC-20@PLA	0 [b]	1.1 ± 2.1	0.02 ± 0.12

[a] ζ-potential measurements were performed at 25 °C using 10 mM KCl, pH 7.5, aqueous solution with 0.5 wt% poly(acrylic acid), for membranes negatively charged, and 0.5 wt% polyethylenimine, for membranes positively charged, as tracers.
[b] Too low to be measured.

4.3.3.5 Pathogen removal and biofilm formation

Cultures of *E. coli* cells and *A. niger* spores, as representative waterborne and airborne microorganisms respectively, were filtered using neat PLA and composite coaxial membranes (PAN/NC@PLA). LRV was used to quantify the ability of membranes to remove pathogenic microorganisms as indicated in Eq. 4. *A. niger* spores range in size from 2 to 5 μm, significantly larger than the pore size of a microfiltration membrane. Accordingly, the removal of the spores reached 99-99.99%. As expected, all tested membranes could be used for the removal of particles larger than their bubble point (corresponding to the largest pore size). Figure 4.2.7 shows that the efficiency of membranes for the removal of bacteria improved in coaxial membranes with nanocrystals with respect to the pure polymeric membranes (PLA and PAN@PLA). The retention of bacteria increased from 69.5 % (LRV 0.52; neat PLA membrane) and 65.2 % (LRV 0.46; PAN@PLA membrane) to values between 81.9 % (LRV 0.74) and 97.3 % (LRV 1.57). Due to the pore size of the microfiltration membranes used and the size of the coliform bacteria (0.5 μm width by 2 μm in length approx.), size exclusion is the expected mechanism for the removal of *E. coli* cells. Significantly, the coaxial membranes loaded with 20 wt% nanocrystals were more efficient that the rest for the removal of bacterial cells, particularly those prepared with ChNC, despite having the largest pore sizes (Table S4.2.2).

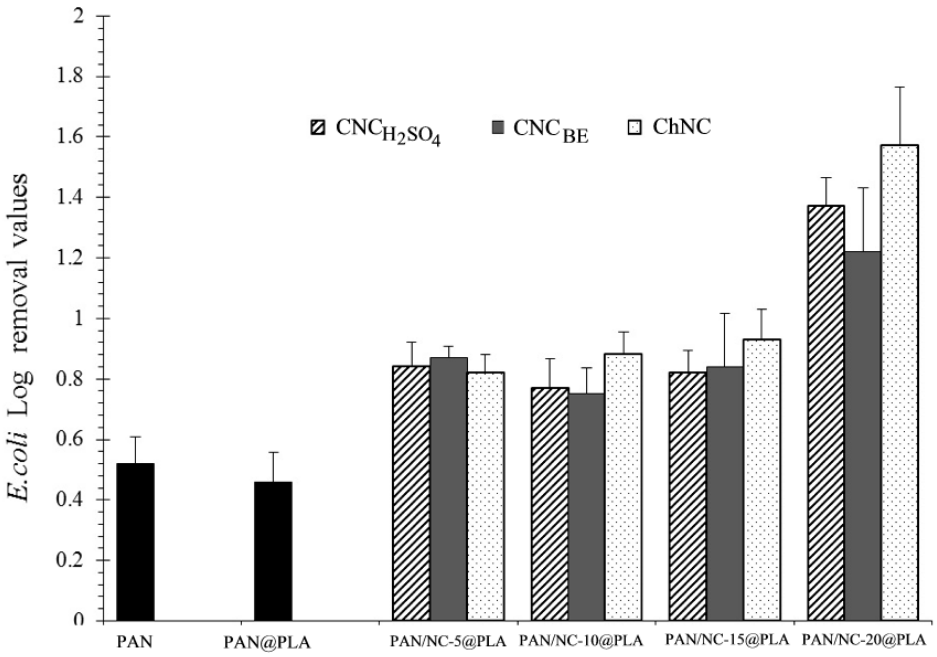

Figure 4.2.7. Log removal values (LRV) from cultures of *E. coli* cells by neat PLA and coaxial composite membranes after 60 min of filtration.

Surface topography greatly influences the ability of bacteria to adhere to a surface. During the initial steps of colonization, surface roughness at nanoscale and microscale levels promotes the adhesion of bacteria by providing more surface area for cell attachment. Other factors such as surface charge and hydrophobicity have been shown to influence microbial attachment [15]. The wettability of the surfaces is given by the water contact angle (WCA) and the surface charge measured by surface ζ-potential. Table 4.2.2 shows the WCA and surface ζ-potential of the studied membranes. Neat PLA membranes were hydrophobic with WCA > 120°, while coaxial PAN@PLA membranes were highly hydrophilic, with WCA < 10°. Coaxial membranes with $CNC_{H_2SO_4}$ on the outer shell displayed WCA in the 57.1-72.2° range, similarly to those obtained with CNC_{BE}. In both cases, WCA decreased with increasing NC loadings and the more hydrophilic membranes corresponded to those loaded with 20% NC. Coaxial membranes prepared with ChNC showed superhydrophilicity with complete spreading of the water drop immediately after being deposited on the membrane. This is consistent with previous results reported for coatings with chitin nanocrystals on the surface of cellulose acetate electrospun fibers [28].

Concerning surface charge, neat PLA membranes were negatively charged with ζ-potential of -31.3 ± 3.9 mV (pH 7.5), whereas coaxial PAN@PLA membranes displayed a surface ζ-potential of -10.5 ± 1.3 mV at the same pH. All coaxial membranes loaded with CNC ($CNC_{H_2SO_4}$ and CNC_{BE}) were also negatively charged with surface ζ-potential ranging from -11.6 to -27.2 mV. Surface ζ-potential values were more negative for increased NC contents and slightly more negative in the case of CNC_{BE}. PAN/ChNC@PLA membranes were negatively charged for low NC loadings turning neutral or positive for the higher ChNC contents. The chemical structure of the nanocrystals on the surface of the polymeric coaxial fibers influenced membrane surface properties making them more hydrophilic and less negatively charged. The carboxyl groups in CNC_{BE} and $CNC_{H_2SO_4}$, more abundant in the former, explain the negative charge of membranes [31]. Chitin nanocrystals possess amino groups due to acid hydrolysis-induced deacetylation, the protonation of which makes the surface overall less negative or even positively charged surface charge [33, 52].

Figure 4.2.8 shows the confocal images for Live/Dead bacterial viability (A, C, E and G) and Ruby FilmTracer staining (B, D, F and H). Regarding bacterial viability, PLA and

CNC did not significantly impair bacterial cells, as noted by the absence of red-marked (cell membrane-damaged) bacteria in Figures 4.2.8-A, C and E. Conversely, chitin nanocrystals remarkably reduced the viability of the cells on membrane surface as shown by the high number of PI-marked non-viable cells on PAN/ChNC@PLA membranes (Figure 4.2.8-G). The antibacterial effect of natural chitin is believed to arise from a small portion of deacetylated structural units in their chitin structure [53]. The acid hydrolysis produced during the extraction of nanocrystals enlarges the proportion of deacetylated groups with the outcome of a high antibacterial activity [54,55]. The hydrolytic treatment leads to the formation of NH_3^+ groups, which can interact with the negatively charged residues of carbohydrates, lipids and proteins located on the cell surface of bacteria, so explaining their role in bacterial impairment [52, 56].

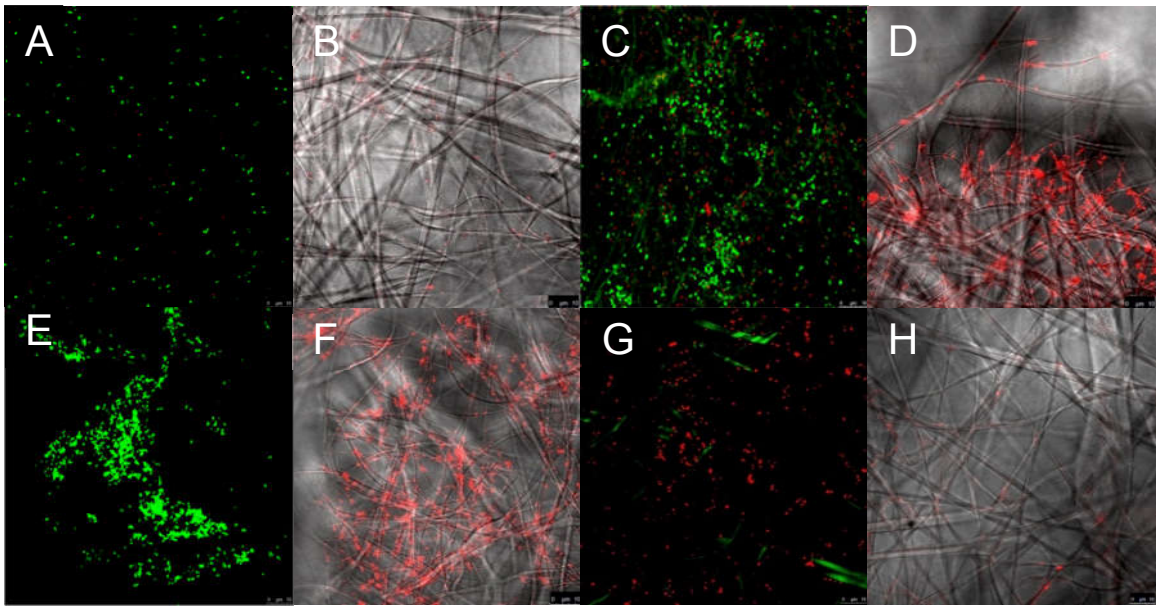

Figure 4.2.8. Live/Dead double staining (A, C, E and G) and FilmTracer SYPRO Ruby biofilm matrix staining (B, D, F and H) of *E. coli* on membranes of PLA (A and B), PAN/$CNC_{H_2SO_4}$-20@PLA (C and D), PAN/CNC_{BE}-20@PLA (E and F) and PAN/ChNC-20@PLA (G and H) after 18 h of biofilm incubation. Live cells were green stained by SYTO 9 and dead cells were red stained by PI (A, C, E and G).

Figure 4.2.9 shows SEM micrographs of membranes kept in contact with *E. coli* cultures for 18 h. PLA membranes displayed moderated resistance to be colonized by *E. coli* (Figure 4.2.9 A) with very reduced poor protein network of extracellular matrix indicating low biofilm formation (Figure 4.2.8 B). These observations agree with the enzymatic activity collected from FDA staining (Table 4.2.2). The coaxial membranes loaded with CNC, however, presented an important development of the extracellular matrix and

biofilm formation upon contact with *E. coli* cultures (Figure 4.2.8 D and F and Figure 4.2.9 B and C). No significant differences in the susceptibility to *E. coli* colonization was observed between $CNC_{H_2SO_4}$ and CNC_{BE}, but higher NC loadings led to increased microbial colonization as shown in the FDA values of Table 4.2.2. However, coaxial membranes prepared with ChNC presented significant resistance to bacterial colonization and biofilm formation (Figures 4.2.8 G and H and Figure 4.2.9 D and Table 4.2.2).

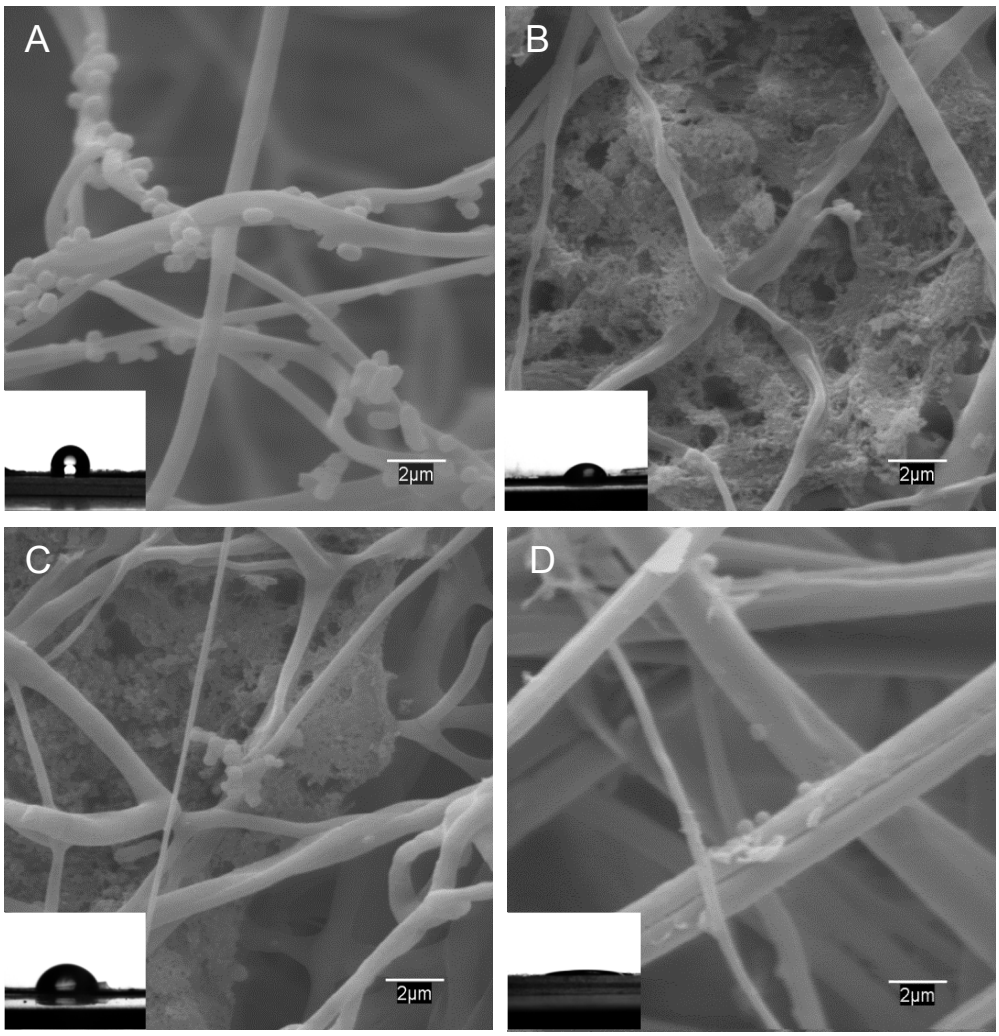

Figure 4.2.9. SEM images of *E. coli* colonization of PLA membranes (A), PAN/$CNC_{H_2SO_4}$-20@PLA (B), PAN/CNC_{BE}-20@PLA (C), and PAN/ChNC-20@PLA (D) after 18 h of biofilm incubation.

Several studies reported that microorganisms preferably attach to hydrophobic nonpolar surfaces such as Teflon and other plastics rather than to hydrophilic materials such as glass or metals [57-59]. Our study revealed that bacterial colonization took place preferentially on membranes with intermediate hydrophilicity values, whereas the more

hydrophobic (PLA) and the more hydrophilic (PAN@PLA) surfaces presented a lower affinity for bacteria as revealed by FDA enzymatic activity (Table 4.2.2). This result is consistent with previously reported data concerning the attachment of a hydrophilic *E. coli* strain to glass-like carbon films [60]. The rationalization of bacterial attachment to surfaces exclusively in terms of hydrophilic-hydrophobic interactions has low predictive value at least due to two reasons. First, cell binding is affected by the culture media used due to differences in surface tension or the absorption of organic and inorganic compounds, which modify the way microorganisms adhere [57]. Second, bacterial morphology makes cell-surface interactions a complex issue due to the existence of cell appendages and adhesion structures avoiding direct contact [61].

Other factor governing bacterial adhesion is surface charge. Given the negative surface charge of bacterial outer membranes (the ζ-potential of *E. coli* is about -30 mV) [58] and the negative surface charge of all membranes in this study except those loaded with ChNC, the electrostatic repulsion could be expected to avoid colonization. However, the data show that the more negatively charged surfaces presented higher biofilm formation, except for pure PLA membranes, which were also the most hydrophobic. It has been pointed out that cells bearing an overall negative charge, also possess positively charged domains, which could interact with negatively charged surfaces, so explaining results like those obtained in this work [62,63]. The neutral of more positively charged and superhydrophilic surfaces of PAN/ChNC@PLA composites were actually resistant to bacterial colonization. These results suggest that the high hydrophilicity of membranes with ChNC together with the presence of positively charged groups able to destabilize cell membranes would be the factors explaining the low bacterial colonization and biofilm formation of PAN/ChNC@PLA membranes.

Coaxial PAN/ChNC@PLA membranes combine improved mechanical properties, an increase in water flux and permeability and a noteworthy antimicrobial behavior. It is significant that the incorporation of CNC confers similar mechanical and filtration properties but a much poorer performance in terms of antibiofouling resistance. This would be a significant advantage for applications in which biofilm formation is undesirable. Conversely, enhanced formation of biofilms would favor applications in which the microbial communities in the biofilm are pursued. For example, for the design of biofilters.

4.3.4 Conclusions

Core-shell nanocomposite membranes were prepared by coaxial electrospinning. Cellulose or chitin nanocrystals were electrospun with PAN to create the outer layer of core-shell fibers, the inner part of which was PLA. The membranes were formed by well-defined fibers with external diameter mostly in the 350-400 nm range and inner core > 100 nm.

The mechanical properties of composite membranes significantly enhanced upon incorporation of 5-20 wt% of NC, reaching ultimate tensile strength similar to that of non-coaxial neat PLA fibers. Best results concerning tensile strength and Young's modulus were obtained for 5 wt% CNC and 15 wt% ChNC-loadings. The reinforcing effect was attributed to the percolating network of nanocrystals.

The incorporation of NC significantly enhanced water flux. Permeability increased by at least a factor of two for membranes with 20 wt% NC with respect to coaxial PAN@PLA without NC. Pore size was in the 1.2-2.6 μm range for all coaxial membranes, which demonstrated suitable properties for microfiltration applications. All membranes achieved a complete removal of *A. niger* spores and a reduction of *E. coli* cells of up to 1-log.

The incorporation of NC to the outer layer of coaxial fibers made membranes more hydrophilic and less negatively charged than neat PLA. In the case of ChNC composites the membranes displayed superhydrophilicity and neutral or slightly positive surface charge. The coaxial membranes containing ChNC were much less prone to microbial colonization and were essentially free of biofilm formation after exposure to *E. coli* cultures in conditions favoring microbial growth. The data show extensive cell impairment for bacteria in contact with membrane surface.

4.3.5 References

[1] N. Bhardwaj, S.C. Kundu, Electrospinning: A fascinating fiber fabrication technique, Biotechnology Advances, 28 (2010) 325-347.

[2] W.E. Teo, S. Ramakrishna, A review on electrospinning design and nanofibre assemblies, Nanotechnology, 17 (2006) R89.

[3] L. Persano, A. Camposeo, C. Tekmen, D. Pisignano, Industrial upscaling of electrospinning and applications of polymer nanofibers: a review, Macromolecular Materials and Engineering, 298 (2013) 504-520.

[4] F.E. Ahmed, B.S. Lalia, R. Hashaikeh, A review on electrospinning for membrane fabrication: Challenges and applications, Desalination, 356 (2015) 15-30.

[5] L. Li, R. Hashaikeh, H.A. Arafat, Development of eco-efficient micro-porous membranes via electrospinning and annealing of poly (lactic acid), Journal of Membrane Science, 436 (2013) 57-67.

[6] S. Kaur, S. Sundarrajan, D. Rana, R. Sridhar, R. Gopal, T. Matsuura, S. Ramakrishna, Review: the characterization of electrospun nanofibrous liquid filtration membranes, Journal of Materials Science, 49 (2014) 6143-6159.
[7] J. Yao, C. Bastiaansen, T. Peijs, High strength and high modulus electrospun nanofibers, Fibers, 2 (2014) 158.
[8] X. Wang, K. Zhang, M. Zhu, B.S. Hsiao, B. Chu, Enhanced Mechanical Performance of Self-Bundled Electrospun Fiber Yarns via Post-Treatments, Macromolecular Rapid Communications, 29 (2008) 826-831.
[9] J.S. Jeong, J.S. Moon, S.Y. Jeon, J.H. Park, P.S. Alegaonkar, J.B. Yoo, Mechanical properties of electrospun PVA/MWNTs composite nanofibers, Thin Solid Films, 515 (2007) 5136-5141.
[10] A. Doustgani, E. Vasheghani-Farahani, M. Soleimani, S. Hashemi-Najafabadi, Optimizing the mechanical properties of electrospun polycaprolactone and nanohydroxyapatite composite nanofibers, Composites Part B: Engineering, 43 (2012) 1830-1836.
[11] V. Kochkodan, N. Hilal, A comprehensive review on surface modified polymer membranes for biofouling mitigation, Desalination, 356 (2015) 187-207.
[12] P. Zhang, L. Lin, D. Zang, X. Guo, M. Liu, Designing bioinspired anti-biofouling surfaces based on a superwettability strategy, Small, (2016) n/a-n/a.
[13] H.C. Flemming, Biofouling in water systems – cases, causes and countermeasures, Applied Microbiology and Biotechnology, 59 (2002) 629-640.
[14] D. Rana, T. Matsuura, Surface modifications for antifouling membranes, Chemical Reviews, 110 (2010) 2448-2471.
[15] T.R. Garrett, M. Bhakoo, Z. Zhang, Bacterial adhesion and biofilms on surfaces, Progress in Natural Science, 18 (2008) 1049-1056.
[16] C.D. Nadell, K. Drescher, K.R. Foster, Spatial structure, cooperation and competition in biofilms, Nature Reviews Microbiology, 14 (2016) 589-600.
[17] J. Quirós, K. Boltes, S. Aguado, R. Guzman de Villoria, J.J. Vilatela, R. Rosal, Antimicrobial metal-organic frameworks incorporated into electrospun fibers, Chemical Engineering Journal, 262 (2015) 189-197.
[18] S. Torres-Giner, M.J. Ocio, J.M. Lagarón, Novel antimicrobial ultrathin structures of zein/chitosan blends obtained by electrospinning, Carbohydrate Polymers, 77 (2009) 261-266.
[19] C. Yao, X.S. Li, K.G. Neoh, Z.L. Shi, E.T. Kang, Surface modification and antibacterial activity of electrospun polyurethane fibrous membranes with quaternary ammonium moieties, Journal of Membrane Science, 320 (2008) 259-267.
[20] A. Moriya, T. Maruyama, Y. Ohmukai, T. Sotani, H. Matsuyama, Preparation of poly(lactic acid) hollow fiber membranes via phase separation methods, Journal of Membrane Science, 342 (2009) 307-312.
[21] D. Klemm, F. Kramer, S. Moritz, T. Lindstrom, M. Ankerfors, D. Gray, A. Dorris, Nanocelluloses: A new family of nature-based materials, Angewandte Chemie-International Edition, 50 (2011) 5438-5466.
[22] R.J. Moon, A. Martini, J. Nairn, J. Simonsen, J. Youngblood, Cellulose nanomaterials review: structure, properties and nanocomposites, Chemical Society Reviews, 40 (2011) 3941-3994.

[23] Q.F. Shi, C.J. Zhou, Y.Y. Yue, W.H. Guo, Y.Q. Wu, Q.L. Wu, Mechanical properties and in vitro degradation of electrospun bio-nanocomposite mats from PLA and cellulose nanocrystals, Carbohydrate Polymers, 90 (2012) 301-308.
[24] C.J. Zhou, R. Chu, R. Wu, Q.L. Wu, Electrospun polyethylene oxide/cellulose nanocrystal composite nanofibrous mats with homogeneous and heterogeneous microstructures, Biomacromolecules, 12 (2011) 2617-2625.
[25] C.J. Zhou, Q.L. Wu, Y.Y. Yue, Q.G. Zhang, Application of rod-shaped cellulose nanocrystals in polyacrylamide hydrogels, Journal of Colloid and Interface Science, 353 (2011) 116-123.
[26] M. Mincea, A. Negrulescu, V. Ostafe, Preparation, modification and applications of chitin nanowhiskers: A review, Reviews on Advanced Materials Science, 30 (2012) 225-242.
[27] A.W. Qin, X. Li, X.Z. Zhao, D.P. Liu, C.J. He, Preparation and characterization of nano-chitin whisker reinforced PVDF membrane with excellent antifouling property, Journal of Membrane Science, 480 (2015) 1-10.
[28] L.A. Goetz, B. Jalvo, R. Rosal, A.P. Mathew, Superhydrophilic anti-fouling electrospun cellulose acetate membranes coated with chitin nanocrystals for water filtration, Journal of Membrane Science, 510 (2016) 238-248.
[29] D. Bondeson, A. Mathew, K. Oksman, Optimization of the isolation of nanocrystals from microcrystalline cellulose by acid hydrolysis, Cellulose, 13 (2006) 171-180.
[30] K. Oksman, J.A. Etang, A.P. Mathew, M. Jonoobi, Cellulose nanowhiskers separated from a bio-residue from wood bioethanol production, Biomass & Bioenergy, 35 (2011) 146-152.
[31] A.P. Mathew, K. Oksman, Z. Karim, P. Liu, S.A. Khan, N. Naseri, Process scale up and characterization of wood cellulose nanocrystals hydrolysed using bioethanol pilot plant, Industrial Crops and Products, 58 (2014) 212-219.
[32] K.G. Nair, A. Dufresne, Crab shell chitin whisker reinforced natural rubber nanocomposites. 1. Processing and swelling behavior, Biomacromolecules, 4 (2003) 657-665.
[33] A.P. Mathew, M.P.G. Laborie, K. Oksman, Cross-linked chitosan/chitin crystal nanocomposites with improved permeation selectivity and pH stability, Biomacromolecules, 10 (2009) 1627-1632.
[34] S.D. Faust, O.M. Aly, Chemistry of water treatment, CRC Press1998.
[35] J. Doshi, D.H. Reneker, Electrospinning process and applications of electrospun fibers, Journal of Electrostatics, 35 (1995) 151-160.
[36] N. Naseri, C. Algan, V. Jacobs, M. John, K. Oksman, A.P. Mathew, Electrospun chitosan-based nanocomposite mats reinforced with chitin nanocrystals for wound dressing, Carbohydrate Polymers, 109 (2014) 7-15.
[37] N. Naseri, A.P. Mathew, L. Girandon, M. Frohlich, K. Oksman, Porous electrospun nanocomposite mats based on chitosan-cellulose nanocrystals for wound dressing: effect of surface characteristics of nanocrystals, Cellulose, 22 (2015) 521-534.
[38] N. Naseri, A.P. Mathew, K. Oksman, Electrospinnability of bionanocomposites with high nanocrystal loadings: The effect of nanocrystal surface characteristics, Carbohydrate Polymers, 147 (2016) 464-472.
[39] P.M. Shyly, S.D.D. Roy, P. Thiravetyan, S. Thanikaikarasan, P.J. Sebastian, D. Eapen, X.S. Shajan, Investigations on the effect of chitin nanofiber in PMMA based solid polymer electrolyte systems, Journal of New Materials for Electrochemical Systems, 17 (2014) 147-152.

[40] I.G. Loscertales, A. Barrero, I. Guerrero, R. Cortijo, M. Marquez, A.M. Ganan-Calvo, Micro/nano encapsutation via electrified coaxial liquid jets, Science, 295 (2002) 1695-1698.
[41] J.E. Díaz, A. Barrero, M. Márquez, I.G. Loscertales, Controlled encapsulation of hydrophobic liquids in hydrophilic polymer nanofibers by co-electrospinning, Advanced Functional Materials, 16 (2006) 2110-2116.
[42] X.H. Zong, K. Kim, D.F. Fang, S.F. Ran, B.S. Hsiao, B. Chu, Structure and process relationship of electrospun bioabsorbable nanofiber membranes, Polymer, 43 (2002) 4403-4412.
[43] R.A. Auras, L.T. Lim, S.E.M. Selke, H. Tsuji, Poly(lactic acid): synthesis, structures, properties, processing, and applications, John Wiley & Sons2011.
[44] C. Xiang, Y.L. Joo, M.W. Frey, Nanocomposite fibers electrospun from poly (lactic acid)/cellulose nanocrystals, Journal of Biobased Materials and Bioenergy, 3 (2009) 147-155.
[45] M.S. Huda, L.T. Drzal, A.K. Mohanty, M. Misra, Effect of fiber surface-treatments on the properties of laminated biocomposites from poly (lactic acid)(PLA) and kenaf fibers, Composites Science and Technology, 68 (2008) 424-432.
[46] S. Huan, L. Bai, G. Liu, W. Cheng, G. Han, Electrospun nanofibrous composites of polystyrene and cellulose nanocrystals: manufacture and characterization, RSC Advances, 5 (2015) 50756-50766.
[47] A. El-Hadi, R. Schnabel, E. Straube, G. Müller, S. Henning, Correlation between degree of crystallinity, morphology, glass temperature, mechanical properties and biodegradation of poly (3-hydroxyalkanoate) PHAs and their blends, Polymer Testing, 21 (2002) 665-674.
[48] Y. Li, F.K. Ko, W.Y. Hamad, Effects of emulsion droplet size on the structure of electrospun ultrafine biocomposite fibers with cellulose nanocrystals, Biomacromolecules, 14 (2013) 3801-3807.
[49] J. Lee, G. Tae, Y.H. Kim, I.S. Park, S.H. Kim, S.H. Kim, The effect of gelatin incorporation into electrospun poly (l-lactide-co-ε-caprolactone) fibers on mechanical properties and cytocompatibility, Biomaterials, 29 (2008) 1872-1879.
[50] H. Ma, C. Burger, B.S. Hsiao, B. Chu, Nanofibrous microfiltration membrane based on cellulose nanowhiskers, Biomacromolecules, 13 (2011) 180-186.
[51] P. Qu, H. Tang, Y. Gao, L. Zhang, S. Wang, Polyethersulfone composite membrane blended with cellulose fibrils, BioResources, 5 (2010) 2323-2336.
[52] A. Mera, J. Araki, T. Ohtsuki, M. Shimosaka, N. Yoshida, Chitin nanowhiskers mediate transformation of *Escherichia coli* by exogenous plasmid DNA, Journal of Biotechnology and Biomaterials, 1 (2011).
[53] C. Peniche, W. Argüelles-Monal, F. Goycoolea, Chitin and chitosan: major sources, properties and applications, Monomers, polymers and composites from renewable resources, 1 (2008) 517-542.
[54] M.S. Benhabiles, R. Salah, H. Lounici, N. Drouiche, M.F.A. Goosen, N. Mameri, Antibacterial activity of chitin, chitosan and its oligomers prepared from shrimp shell waste, Food Hydrocolloids, 29 (2012) 48-56.
[55] W. Tachaboonyakiat, E. Sukpaiboon, O. Pinyakong, Development of an antibacterial chitin betainate wound dressing, Polymer Journal, 46 (2014) 505-510.
[56] Y. Andres, L. Giraud, C. Gerente, P. Le Cloirec, Antibacterial effects of chitosan powder: mechanisms of action, Environmental Technology, 28 (2007) 1357-1363.

[57] C.J. van Oss, Hydrophobicity and hydrophilicity of biosurfaces, Current Opinion in Colloid & Interface Science, 2 (1997) 503-512.
[58] Y.L. Ong, A. Razatos, G. Georgiou, M.M. Sharma, Adhesion Forces between *E. coli* bacteria and biomaterial surfaces, Langmuir, 15 (1999) 2719-2725.
[59] B. Prakash, B. Veeregowda, G. Krishnappa, Biofilms: a survival strategy of bacteria, Current Science, 85 (2003) 1299-1307.
[60] B. Jalvo, J. Santiago-Morales, P. Romero, R. Guzman de Villoria, R. Rosal, Microbial colonisation of transparent glass-like carbon films triggered by a reversible radiation-induced hydrophobic to hydrophilic transition, RSC Advances, 6 (2016) 50278-50287.
[61] K. Hori, S. Matsumoto, Bacterial adhesion: from mechanism to control, Biochemical Engineering Journal, 48 (2010) 424-434.
[62] A. Dasari, J. Quirós, B. Herrero, K. Boltes, E. García-Calvo, R. Rosal, Antifouling membranes prepared by electrospinning polylactic acid containing biocidal nanoparticles, Journal of Membrane Science, 405 (2012) 134-140.
[63] C. Wilhelm, C. Billotey, J. Roger, J. Pons, J.-C. Bacri, F. Gazeau, Intracellular uptake of anionic superparamagnetic nanoparticles as a function of their surface coating, Biomaterials, 24 (2003) 1001-1011.

Chapter 5:

GENERAL DISCUSSION

5 General discussion

The aim of the present thesis was to study the features of microbial colonization and biofilm formation using different bacterial strains on different engineered substrates, including materials with tunable hydrophilicity and self-cleaning photocatalytic properties. The goal pursued was to determine the conditions required to avoid biofilm attachment by modifying certain surface properties, such as topography and surface chemistry.

Escherichia coli CECT 516, *Pseudomonas putida* CECT 4584 and *Staphylococcus aureus* CECT 240 were the microorganisms used in this work to carry out the microbiological assays. Spores of the fungi *Aspergillus niger* ATCC 6275 were also used to evaluate the removal of microorganisms during filtration using nanoengineered membranes, prepared in our laboratory, as part of the objectives of this thesis. *Escherichia coli* is a gram-negative rod shaped and flagellated bacterium that is a normal inhabitant of the intestines of most animals, including humans [1]. The strain used in the studies carried out in this thesis is non-pathogenic but, some *E. coli* strains can cause a wide variety of intestinal and extra-intestinal diseases, such as diarrhea, urinary tract infections, septicemia, and neonatal meningitis [1]. *Pseudomonas putida* is a non-pathogenic, rod-

shaped, flagellated, gram-negative bacterium that is found in most soil and water habitats where there is oxygen [2] . This strain was chosen due to its high colonization capacity [2] and because it has high level of genome conservation with pathogenic Pseudomonas, such as *Pseudomonas aeruginosa* with which 85% of the predicted coding regions are shared, but without their key virulence systems [3]. As a result, *P. putida* constitutes a safe strain that allow extrapolating results to the virulent strains. *Staphylococcus aureus* is a spherical gram-positive bacterium, immobile and forming grape-like clusters. It is considered one of the most important pathogens in humans and animals. The pathogenesis of *S. aureus* is attributed to the combined effect of extracellular factors and toxins, together with the invasive properties of the strain such as adherence, biofilm formation, and resistance to phagocytosis [4].

Biofilm formation is, in general, a two-step process that requires the primary adhesion of bacteria to a substrate surface followed by the formation of multiple cell layers [5]. Despite general agreement that biofilms are the basis for persistent or chronic bacterial infections [4], the mechanisms responsible for initial adhesion to a abiotic surfaces like plastic or glass are not yet well understood. Bacterial adhesion is influenced by the physicochemical properties of both the material and the bacterial cell surface [6], and the understanding of the molecular mechanisms implicated in the biofilm formation process, as well as the material properties involved in favoring, reducing or avoiding such formation, have been widely studied. For instance, in *S. epidermidis*, the cell wall lytic enzyme AtlE, which affects the hydrophobicity of the cell surface, has been associated to the initial adhesion to plastic and glass surfaces [7, 8]. Gross *et al.* [6] showed for the first time that the charge of teichoic acids plays a pivotal role in the initial step of biofilm formation [6]. The cell surface of *S. aureus*, as in most bacteria, has a moderately negative net charge at neutral pH [9], which is generally attributed to the fact that the teichoic acids contain fewer positively charged D-alanine residues than negatively charged phosphate groups [6]. The direct interaction of bacteria and surfaces is dependent on van der Waals forces, which are attractive, and interionic forces, which can be either attractive or repulsive [10]. Even if bacteria and surfaces are charged alike, van der Waals forces can overcome repulsion and lead to adhesion [11, 12].

It was demonstrated throughout the assays carried out in this work that bacterial colonization was favored in surfaces with intermediate hydrophilicity (dry-irradiated carbon films, chapter 2, PLA electrospun membranes functionalized with CNC, chapter

3), whereas hydrophobic (PLA electrospun membranes, chapter 4.2), extremely hydrophilic (carbon films irradiated in wet air, chapter 2) or super-hydrophilic surfaces (electrospun membranes functionalized with ChCN, chapter 4) were less prone to bacterial adhesion, irrespective of their surface charge. However, bacterial adhesion to hydrophobic cellulose acetate electrospun membranes and to hydrophobic TiO_2-covered glass slides was also observed. As it has been previously discussed throughout the chapters of this thesis, there are several surface properties involved in the initial steps of bacterial colonization [13, 14]. Thus, this process can neither be referred to, nor explained by, a single one. Together with hydrophobicity, the topography and roughness of the surface play a determinant role in biofilm formation [15, 16]. This fact was also reflected in the results obtained in this work. Surface irregularities are a key factor in promoting (or avoiding) bacterial adhesion and biofilm development. Smooth surfaces do not favor bacterial adhesion, which may explain why in this work the more hydrophobic TiO_2-covered glass slides displayed more extensive biofilm formation. In fact, TiO_2 coatings modified the topography of the surface (glass slides, glass fiber filters and glass coverslips), offering more adhesion points for bacterial anchoring structures.

Similarly, PLA coaxial electrospun membranes functionalized with CNCs also altered both their surface free energy and topography and roughness, thus favoring bacterial adhesion. Enhanced biofilm formation would favor applications in which the microbial communities in the biofilm are pursued. For example, they can be used for the design of biofilters in bioremediation processes [17-19]. In the case of electrospun membranes functionalized with ChNCs, the effect observed was the opposite. Not only there was less adhesion, but also, these coatings proved to be harmful to the bacteria colonizing on the fibers. ChNCs remarkably reduced the viability of the cells on membrane surface, irrespective of the functionalization technique (impregnation or incorporation of chitin nanocrystals by electrospinning). Chitin and other derivatives of chitosan have been investigated as antimicrobial materials against a wide range of target organisms like algae, bacteria, yeasts and fungi. The widely accepted explanation of their antimicrobial character is the interaction between the positively charged chitin/chitosan moieties and the negatively charged microbial cell membranes [20] . The antibacterial effect of natural chitin is believed to arise from a small portion of deacetylated structural units in their chitin structure [21]. The acid hydrolysis produced during the extraction of chitin nanocrystals enlarges the proportion of deacetylated groups with the outcome of a higher

antibacterial activity than CNCs [22, 23]. The hydrolytic treatment leads to the formation of NH_3^+ groups, which can interact with the negatively charged residues of carbohydrates, lipids and proteins located on the cell surface of bacteria [24, 25]. Previous studies showed that this electrostatic interaction results in twofold interference: (1) by promoting changes in the properties of membrane wall permeability, inducing internal osmotic imbalances and the inhibition of microbial growth and (2) by the hydrolysis of the peptidoglycans in the microorganism wall, leading to the leakage of intracellular electrolytes such as potassium ions and other low molecular weight proteinaceous constituents, so explaining their role in bacterial impairment [20].

Photocatalytic TiO_2 coatings also performed antibacterial activity when samples were illuminated with a source containing UV radiation. Many researches revealed that the cause for visible light damage in bacterial cells exposed to photocatalytic irradiated material was the production of ROS as intermediates of oxygen-dependent photosensitized reactions [26-30]. The production of ROS has been linked to membrane integrity destabilization, which leads to a reduction of the bacterial cell ability to control the traffic of certain substances, such as nutrients and ions thereby causing homeostatic imbalance, cellular metabolic disturbance and death [31]. Besides this effect, it is known that photocatalytic TiO_2 activity has a negative effect in appendage biosynthesis and protein insertion as well as in cell signaling and cell to cell communication, which have been shown to play a role in diverse functions such as pathogenesis, biofilm development, and stress resistance [27]. The reduction of biofilm forming bacteria on photocatalytic surfaces containing TiO_2 nanoparticles has been described elsewhere. However, the vast majority of studies have focused on the effect of photocatalysis in the early stages of biofilm formation, when it is still reversible [32-34]. Chapter 3 focused precisely on the possibility of removal of mature biofilms through TiO_2 photocatalytic coatings. Although all the cells were clearly damaged by ROS, the results reported here showed that the irradiation had no effect on the amount of biofilm remaining after exposure-treatment cycles with TiO_2-functionalized surfaces, if a biofilm was allowed to grow in the dark to a certain extent (chapter 3.1). In environmentally realistic conditions the population densities are quite variable. Some studies concluded that the resistance of bacterial populations towards antibacterial engineered nanomaterials depends on the initial cell density, dense cultures being more resistant than the less ones [35]. The reason is that the population growth rate is immediately reduced when interacting with less dense

populations due to, among other, a decrease in bacterial chemical communication, also stopping biofilm formation. In high density populations, the toxic effect is delayed offering them the possibility to recover [35].

To obtain a better understanding of the complexity of biofilm development, the efficiency of TiO_2 photocatalytic activity was studied using different dark-light cycles, as well as different biofilm maturation times. The results showed that, besides the complete cell impairment achieved photocatalytic TiO_2 electrosprayed with a minimum surface density led to the complete removal of *S. aureus* cells without subsequent colonization (chapter 3.2). In these experiments, the outcome was favored by the flow conditions used for the contact between surfaces and colonizing cells. The TiO_2 nanoparticles dispersed using electrospray and irradiated by simulated sunlight provide well-dispersed antimicrobial coatings and an efficient method for avoiding biofilm formation. Electrospray allowed producing homogeneous photocatalytic surfaces with the precise surface coverage required to cope with the bacterial growth that could take place during dark periods under environmental light-dark exposure.

It should be noted that the work conducted during this thesis have not only focused on the search and obtaining of materials with antimicrobial activity, but also have sought to improve properties of such materials such as mechanical properties or better water flow and permeability in electrospun membranes for water filtration systems. In this sense, cellulose acetate and PLA membranes were functionalized with cellulose and chitin nanocrystals. The results showed that the impregnation of electrospun cellulose acetate with ChNC has positively influenced the tensile strength and Young's of the membranes whereas the strain at break decreased. This remarkable shift in mechanical performance was attributed to the stiffening effect of the nanocrystals coating the electrospun fibers. The accumulation of nanocrystals at the fiber junctions positively impacted the mechanical stability of the membranes. The strain at break however decreased, which was attributed to the restricted slippage of the electrospun fibers past each other due to the merging at junction points. Nanochitin composite membranes also performed high water flux and improved abiotic antifouling capacity.

The batch of coaxial membranes prepared in this work, with nanocrystals in the outer part of the fiber, displayed significantly enhanced mechanical properties due to the formation of a rigid network of cellulose on chitin nanocrystals, depending on the case [36]. For the

three types of coaxial nanocomposites prepared, the ultimate strain decreased compared to pure PLA membranes meaning that the coaxial structure and the presence of the nanocrystals reduced fiber ductility and made membranes more resistant to deformation [36, 37]. The decrease of the elongation of electrospun non-woven PLA fibers containing CNC was previously reported for PLA/CNC non-coaxial nanocomposites as a consequence of the same reinforcing effect [38]. Referring to water flux and permeability, the incorporation of nanocrystals on the surface of the polymeric electrospun membranes increased their pore size and wettability, making them more hydrophilic. Both factors explain the increased water flux and permeability observed in agreement with results published elsewhere on the effect of nanocellulose addition to polymeric membranes [39, 40].

In summary, the general rule is that bacteria will preferentially colonize surfaces that are hydrophobic, have surface roughness on the nano- and microscale, and are exposed to a conditioning layer in contrast to smooth, hydrophilic surfaces. This trend is not absolute for all bacteria; however, it provides a general design principle for developing bacteria-resistant surfaces. The recent advancements in material design and surface engineering have provided a plethora of opportunities for creating new materials, coatings and surface modifications in order to avoid and/or reduce bacterial attachment and biofilm formation. Nevertheless, compared with the effects of surface charge, hydrophobicity, and chemistry, how surface stiffness and topography (except for roughness) affect bacterial adhesion and biofilm development is still poorly understood. Bacteria adapt to environmental changes using extracellular appendages that improve their chances of survival. Further investigations and evaluations are needed using in vitro conditions that better mimic the complex interface environments between bacteria and surfaces. This research field will also benefit from a better understanding of the bacterial systems involved in surface sensing, especially at the molecular level and cell-to-cell communications. Integration of these knowledge and technologies is necessary to guide rational design of smart self-cleaning materials to reduce fouling in general and biofouling in particular.

References

[1] F. Ørskov, I. Ørskov, *Escherichia coli* serotyping and disease in man and animals, Canadian journal of microbiology, 38 (1992) 699-704.

[2] L. Molina, C. Ramos, E. Duque, M.C. Ronchel, J.M. García, L. Wyke, J.L. Ramos, Survival of *Pseudomonas putid*a KT2440 in soil and in the rhizosphere of plants under greenhouse and environmental conditions, Soil Biology and Biochemistry, 32 (2000) 315-321.
[3] K. Nelson, C. Weinel, I. Paulsen, R. Dodson, H. Hilbert, V. Martins dos Santos, D. Fouts, S. Gill, M. Pop, M. Holmes, Complete genome sequence and comparative analysis of the metabolically versatile *Pseudomonas putida* KT2440, Environmental microbiology, 4 (2002) 799-808.
[4] J.W. Costerton, P.S. Stewart, E.P. Greenberg, Bacterial biofilms: a common cause of persistent infections, Science, 284 (1999) 1318-1322.
[5] M.E. Davey, G.A. O'toole, Microbial biofilms: from ecology to molecular genetics, Microbiology and molecular biology reviews, 64 (2000) 847-867.
[6] M. Gross, S.E. Cramton, F. Götz, A. Peschel, Key role of teichoic acid net charge in *Staphylococcus aureus* colonization of artificial surfaces, Infection and immunity, 69 (2001) 3423-3426.
[7] C. Heilmann, C. Gerke, F. Perdreau-Remington, F. Götz, Characterization of Tn917 insertion mutants of Staphylococcus epidermidis affected in biofilm formation, Infection and Immunity, 64 (1996) 277-282.
[8] C. Heilmann, M. Hussain, G. Peters, F. Götz, Evidence for autolysin-mediated primary attachment of Staphylococcus epidermidis to a polystyrene surface, Molecular microbiology, 24 (1997) 1013-1024.
[9] R. Sonohara, N. Muramatsu, H. Ohshima, T. Kondo, Difference in surface properties between *Escherichia coli* and *Staphylococcus aureus* as revealed by electrophoretic mobility measurements, Biophysical chemistry, 55 (1995) 273-277.
[10] H.H.M.N. Rijnaarts, WillemBouwer, Edward J.Lyklema, JohannesZehnder, Alexander J.B., Reversibility and mechanism of bacterial adhesion, Colloids and Surfaces B: Biointerfaces, 4 (1995) 17.
[11] M. Van Loosdrecht, J. Lyklema, W. Norde, G. Schraa, A. Zehnder, Electrophoretic mobility and hydrophobicity as a measured to predict the initial steps of bacterial adhesion, Applied and Environmental Microbiology, 53 (1987) 1898-1901.
[12] M. Van Loosdrecht, J. Lyklema, W. Norde, G. Schraa, A. Zehnder, The role of bacterial cell wall hydrophobicity in adhesion, Applied and environmental microbiology, 53 (1987) 1893-1897.
[13] F. Song, H. Koo, D. Ren, Effects of material properties on bacterial adhesion and biofilm formation, Journal of dental research, 94 (2015) 1027-1034.
[14] L.D. Renner, D.B. Weibel, Physicochemical regulation of biofilm formation, MRS bulletin, 36 (2011) 347-355.
[15] K.A. Whitehead, J. Verran, The effect of surface topography on the retention of microorganisms, Food and bioproducts processing, 84 (2006) 253-259.
[16] J.F. Schumacher, M.L. Carman, T.G. Estes, A.W. Feinberg, L.H. Wilson, M.E. Callow, J.A. Callow, J.A. Finlay, A.B. Brennan, Engineered antifouling microtopographies–effect of feature size, geometry, and roughness on settlement of zoospores of the green alga Ulva, Biofouling, 23 (2007) 55-62.
[17] C. Lauderdale, P. Chadik, M.J. Kirisits, J. Brown, Engineered biofiltration: Enhanced biofilter performance through nutrient and peroxide addition, Journal: American Water Works Association, 104 (2012).
[18] M.E. Acuña, F. Perez, R. Auria, S. Revah, Microbiological and kinetic aspects of a biofilter for the removal of toluene from waste gases, Biotechnology and bioengineering, 63 (1999) 175-184.

[19] R. Singh, D. Paul, R.K. Jain, Biofilms: implications in bioremediation, Trends in microbiology, 14 (2006) 389-397.
[20] R.C. Goy, D.d. Britto, O.B. Assis, A review of the antimicrobial activity of chitosan, Polímeros, 19 (2009) 241-247.
[21] C. Peniche, W. Argüelles-Monal, F. Goycoolea, Chitin and chitosan: major sources, properties and applications, Monomers, polymers and composites from renewable resources, 1 (2008) 517-542.
[22] M. Benhabiles, R. Salah, H. Lounici, N. Drouiche, M. Goosen, N. Mameri, Antibacterial activity of chitin, chitosan and its oligomers prepared from shrimp shell waste, Food hydrocolloids, 29 (2012) 48-56.
[23] W. Tachaboonyakiat, E. Sukpaiboon, O. Pinyakong, Development of an antibacterial chitin betainate wound dressing, Polymer journal, 46 (2014) 505-510.
[24] A.J. Mera A, Ohtsuki T, Shimosaka M, Yoshida N, Chitin Nanowhiskers Mediate Transformation of *Escherichia coli* by Exogenous Plasmid DNA, J Biotechnol Biomaterial, 1 (2011).
[25] Y. Andres, L. Giraud, C. Gerente, P. Le Cloirec, Antibacterial effects of chitosan powder: mechanisms of action, Environmental technology, 28 (2007) 1357-1363.
[26] P. Dunlop, C. Sheeran, J. Byrne, M. McMahon, M. Boyle, K. McGuigan, Inactivation of clinically relevant pathogens by photocatalytic coatings, Journal of Photochemistry and Photobiology A: Chemistry, 216 (2010) 303-310.
[27] A. Kubacka, M.S. Diez, D. Rojo, R. Bargiela, S. Ciordia, I. Zapico, J.P. Albar, C. Barbas, V.A.M. dos Santos, M. Fernández-García, Understanding the antimicrobial mechanism of TiO_2-based nanocomposite films in a pathogenic bacterium, Scientific reports, 4 (2014) 4134.
[28] J. Kiwi, V. Nadtochenko, Evidence for the mechanism of photocatalytic degradation of the bacterial wall membrane at the TiO_2 interface by ATR-FTIR and laser kinetic spectroscopy, Langmuir, 21 (2005) 4631-4641.
[29] H.A. Foster, I.B. Ditta, S. Varghese, A. Steele, Photocatalytic disinfection using titanium dioxide: spectrum and mechanism of antimicrobial activity, Applied microbiology and biotechnology, 90 (2011) 1847-1868.
[30] A. Kubacka, M. Ferrer, M. Fernández-García, Kinetics of photocatalytic disinfection in TiO 2-containing polymer thin films: UV and visible light performances, Applied Catalysis B: Environmental, 121 (2012) 230-238.
[31] X. Lin, J. Li, S. Ma, G. Liu, K. Yang, M. Tong, D. Lin, Toxicity of TiO 2 nanoparticles to *Escherichia coli*: effects of particle size, crystal phase and water chemistry, PloS one, 9 (2014) e110247.
[32] E.J. Wolfrum, J. Huang, D.M. Blake, P.-C. Maness, Z. Huang, J. Fiest, W.A. Jacoby, Photocatalytic oxidation of bacteria, bacterial and fungal spores, and model biofilm components to carbon dioxide on titanium dioxide-coated surfaces, Environmental science & technology, 36 (2002) 3412-3419.
[33] Y. Cai, M. Strømme, Å. Melhus, H. Engqvist, K. Welch, Photocatalytic inactivation of biofilms on bioactive dental adhesives, Journal of Biomedical Materials Research Part B: Applied Biomaterials, 102 (2014) 62-67.
[34] C.N. Rao, T. Takashima, W.A. Bradley, T.Y. Lee, Near ultraviolet radiation at the earth's surface: measurements and model comparisons, Tellus B, 36 (1984) 286-293.
[35] N. Musee, M. Thwala, N. Nota, The antibacterial effects of engineered nanomaterials: implications for wastewater treatment plants, Journal of Environmental Monitoring, 13 (2011) 1164-1183.

[36] L. Li, R. Hashaikeh, H.A. Arafat, Development of eco-efficient micro-porous membranes via electrospinning and annealing of poly (lactic acid), Journal of Membrane Science, 436 (2013) 57-67.
[37] J. Lee, G. Tae, Y.H. Kim, I.S. Park, S.-H. Kim, S.H. Kim, The effect of gelatin incorporation into electrospun poly (l-lactide-co-ε-caprolactone) fibers on mechanical properties and cytocompatibility, Biomaterials, 29 (2008) 1872-1879.
[38] C. Xiang, Y.L. Joo, M.W. Frey, Nanocomposite fibers electrospun from poly (lactic acid)/cellulose nanocrystals, Journal of Biobased Materials and Bioenergy, 3 (2009) 147-155.
[39] H. Ma, C. Burger, B.S. Hsiao, B. Chu, Nanofibrous microfiltration membrane based on cellulose nanowhiskers, Biomacromolecules, 13 (2011) 180-186.
[40] P. Qu, H. Tang, Y. Gao, L. Zhang, S. Wang, Polyethersulfone composite membrane blended with cellulose fibrils, BioResources, 5 (2010) 2323-2336.

CONCLUSIONES/CONCLUSIONS

6 Conclusiones

Nuevos materiales compuestos fueron preparados con éxito mediante diferentes revestimientos y técnicas electrohidrodinámicas. Los revestimientos elaborados fueron, en general, capas homogéneas de agregados de partículas con superficies planas y completamente funcionales. Las membranas electrohiladas presentaron fibras lisas, no tejidas y bien definidas, sin imperfecciones y con diámetros de unos pocos cientos de nanómetros.

Las membranas electrohiladas funcionalizadas con CNC o ChNCs resultaron hidrófilas o superhidrófilas, respectivamente, mostraron un incremento en la permeabilidad, mejoraron sus propiedades mecánicas y, en el caso de las membranas de ChNCs, cargadas positivamente, inhibieron fuertemente la formación de *biofilms*.

Los tratamientos de irradiación aplicados a diferentes superficies funcionalizadas desencadenaron la transición de una superficie hidrófoba a una superficie hidrófila. Tales modificaciones desempeñaron un papel determinante en la fijación inicial de las células bacterianas a las superficies manipuladas. Los estados hidrófilos transitorios, aun siendo rápidamente revertidos, podrían estar asociados a una mayor adhesión bacteriana.

La colonización bacteriana fue favorecida en superficies con hidrofilicidad intermedia mientras que las superficies hidrofóbicas o superhidrófilas fueron menos propensas a la adhesión bacteriana, independientemente de su carga superficial. La colonización bacteriana también fue favorecida en superficies rugosas en lugar de en superficies lisas, destacando la importancia de la topografía y la rugosidad en las etapas iniciales de adhesión bacteriana.

La simulación de la radiación solar en las superficies funcionalizadas con nanopartículas fotocatalíticas resultó en una fuerte actividad biocida, impidiendo la acumulación de biopelículas en condiciones de flujo y manteniendo la superficie libre de células y de la matriz polimérica extracelular bacteriana tras su acumulación durante los ciclos de oscuridad. Sin embargo, existe una cobertura superficial mínima de material fotocatalítico por debajo de la cual no es posible eliminar la matriz extracelular formada durante el período oscuro del ciclo.

7 Conclusions

New composite materials were successfully prepared by different coatings and electrohydrodynamic techniques. The coatings elaborated were, in general, homogeneous layers of tight aggregates of particles displaying planar and fully functional surfaces. The membranes created presented smooth, non-woven and well defined fibers without beading and with diameters of a few hundreds of nanometers.

Electrospun membranes functionalized with CNC and ChNC were hydrophilic or superhydrophilic respectively, displayed increased permeability, improved their mechanical properties and, in the case of the positively charged ChNC strongly inhibited biofilm formation.

The irradiation treatments applied to different functionalized surfaces triggered the transition from a hydrophobic to hydrophilic surface. Such modifications played a determinant role on the initial attachment of bacterial cells to the engineered surfaces. Transient hydrophilic states, even rapidly reverted, could be associated to higher bacterial attachment.

Bacterial colonization was favored in surfaces with intermediate hydrophilicity whereas hydrophobic or super-hydrophilic surfaces were less prone to bacterial adhesion, irrespective of their surface charge. Bacterial colonization was also favored on rough surfaces rather than on smooth ones, highlighting the importance of topography and roughness in the initial stages of bacterial adhesion.

The simulation of the solar radiation on the surfaces functionalized with photocatalytic nanoparticles displayed strong biocidal activity, avoiding biofilm accumulation in flow conditions and keeping the surface free of cells and bacterial exopolymeric matrix after dark-light cycles. However, there is a minimum surface coverage of photocatalytic material below which the exopolymeric material accumulated during the dark period of the cycle cannot be removed.

8 SUPPLEMENTARY INFORMATION

8.1 Microbial colonization of transparent glass-like carbon films triggered by a reversible radiation-induced hydrophobic to hydrophilic transition

1. Atomic force microscopy measurements. Description of the experimental procedure and main results.

2. Figure S2.1. AFM analysis of the surface of carbon film/PMMA composites before UV treatments (a, c, e, g) and after UV dry treatment (b, f) and UV wet treatment (d, h). Vertical and horizontal lines are typical AFM artifacts (a-d: 10 x 10 μm, d-h: 1 x 1 μm).

3. Figure S2.2. FilmTracer SYPRO Ruby staining revealing biofilm matrix for *E. coli* cultured on (a) glass-like carbon film as produced, (b) vacuum preconditioned film, (c) chamber-irradiated films in dry air, (d) chamber-irradiated films in wet air, (e) lamp-irradiated films in dry air and (f) lamp-irradiated films in wet air.

Atomic force microscopy measurements. Surface topography of the carbon film was analyzed by atomic force microscopy (AFM) using a Park XE150 apparatus. The images were acquired in non-contact mode using a non-contact cantilever (PPP-NCHR, Park System) with a tip set point of about ~30-40 nm and amplitudes between ~25-45 nm and a scan rate of 0.50Hz. The images (512 x 512 pixels and areas of 10 μm2 and 2 μm2) were processed and analyzed using XEI software (version 1.7.1). A comparison of AFM scans before treatment (Figures S1 a, c, e and g) and UV treated samples in the same areas showed globular and vermicular features appearing after both dry (Figures S1 b and f) and wet (Figures S1 d and h) irradiation. Some of the cavities of non-irradiated samples almost disappeared. A deeper analysis showed that the globular and vermicular features detected after UV treatments derived from surface features presented in the carbon film/PMMA composite PMMA transfer (Figures S1e and f). These features seemed to swell and smooth their edges because of the irradiation. UV treatment in wet air seems to show smoother and more swollen features than those irradiated in dry air. We analyzed the surface features of the copper foil treated with the same synthesis conditions (850 °C) but without ethylene, to avoid carbon film synthesis. The results showed that copper foil developed roughness in the form of small domes of about 300 nm, which were transferred

to the carbon film/PMMA composite as cavities of approximately the same size (Figures S2.1 g and h).

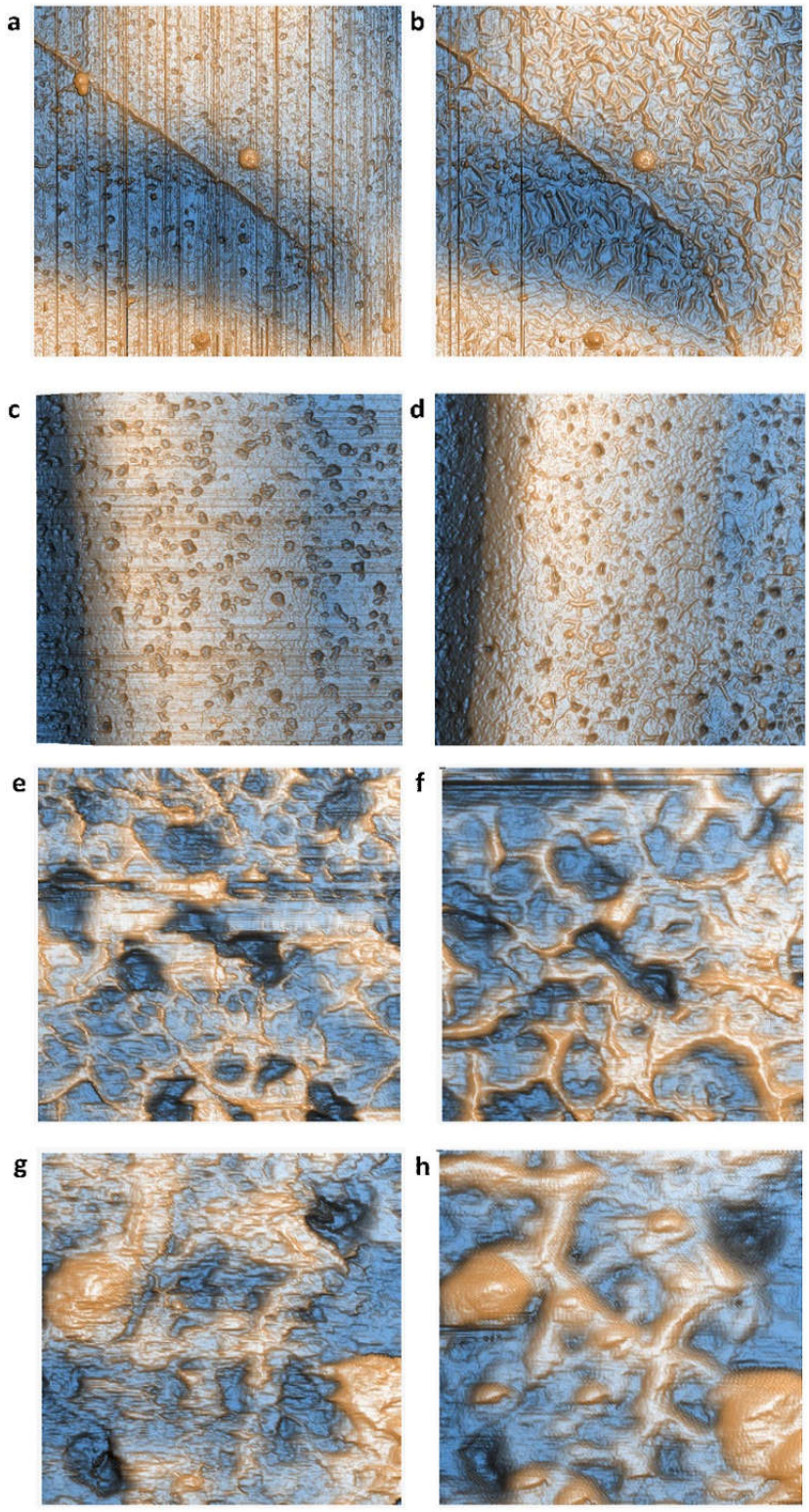

Figure S2.1. AFM analysis of the surface of carbon film/PMMA composites before UV treatments (a, c, e, g) and after UV dry treatment (b, f) and UV wet treatment (d, h). Vertical and horizontal lines are typical AFM artifacts (a-d: 10 x 10 µm, d-h: 1 x 1 µm).

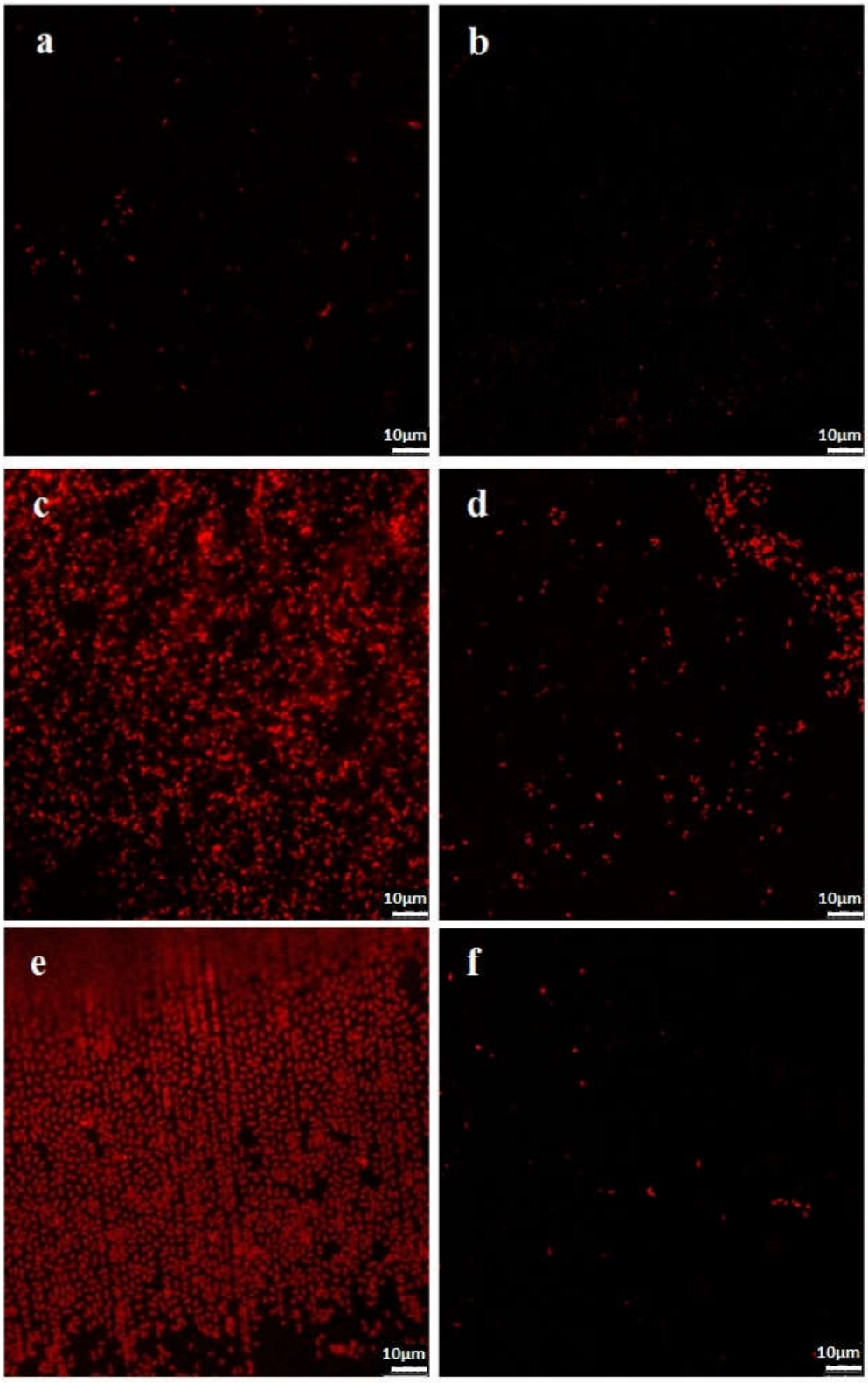

Figure S2.2. FilmTracer SYPRO Ruby staining revealing biofilm matrix for *E. coli* cultured on (a) glass-like carbon film as produced, (b) vacuum preconditioned film, (c) chamber-irradiated films in dry air, (d) chamber-irradiated films in wet air, (e) lamp-irradiated films in dry air and (f) lamp-irradiated films in wet air.

8.2 Biofilm formation on self-cleaning surfaces functionalized by photocatalytic nanoparticles

Experimental. Surface hydrophobicity derived from contact angle measurements.

Figure S3.1.1. X-ray diffractogram of prepared TiO_2 xerogel.

Figure S3.1.2. Evolution of MB with irradiation time on TiO_2-coated filters and slides. (B refers to blank runs and 1 and 2 to replicates.)

Figure S3.1.3. FilmTracer SYPRO Ruby biofilm matrix staining of samples with and without TiO_2, C(+) and C(-) respectively and with and without irradiation, L(+) and L(-) respectively for filters and slides kept in contact with *P. putida* and *S. aureus* for 48 h in the dark at 37 °C.

Figure S3.1.4. SEM images of *P. putida* (A, B, E and F) and *S. aureus* (C, D, G and H) biofilms on TiO_2 glass slides (A, B, C and D) and TiO_2 fiber filters (E, F, G and H) after 48 h incubation and before irradiation (A, C, E and G) and after 2 h irradiation (B, D, F and H).

Experimental. Surface hydrophobicity derived from contact angle measurements. The Lifshitz–van der Waals (LW), electron donor (−) and electron acceptor (+) components of the surface tension were estimated from CA values for water, glycerol and diiodomethane according to the following expression in which θ are the pure liquid contact angles [1]:

$$\left(1+\cos\theta\right)\gamma_L = 2\left(\sqrt{\gamma_S^{LW}\gamma_L^{LW}} + \sqrt{\gamma_S^{+}\gamma_L^{-}} + \sqrt{\gamma_S^{-}\gamma_L^{+}}\right) \quad (1)$$

In this approach, the total surface free energy (γ_S) is the sum of the non-polar London-van der Waals component (γ_S^{LW}) and the acid-base component (γ_S^{AB}), which in turn comprises two non-additive parameters: the electron-acceptor (γ_S^{+}) and the electron-donor (γ_S^{-}) surface tension parameters:

$$\gamma_S = \gamma_S^{LW} + \gamma_S^{AB} = \gamma_S^{LW} + 2\sqrt{\gamma_S^{+}\gamma_S^{-}} \quad (2)$$

The three components of the solid free surface energy, γ_S^{LW}, γ_S^+ and γ_S^- are unknowns that can be solved by measuring the CA with three liquids taking into account that the components of the liquid free surface energy, γ_L^{LW}, γ_L^+ and γ_L^- for the probe liquids are available in the literature for a number of pure substances [2]. According to Van Oss, the total interfacial tension between the solid film and water, γ_S, can be expressed as [3]:

$$\gamma_{SL} = \left(\sqrt{\gamma_S^{LW}} - \sqrt{\gamma_L^{LW}}\right)^2 + 2\left(\sqrt{\gamma_S^+\gamma_S^-} + \sqrt{\gamma_L^+\gamma_L^-} - \sqrt{\gamma_S^+\gamma_L^-} - \sqrt{\gamma_L^+\gamma_S^-}\right) \quad (3)$$

The free energy of interaction between two identical condensed phases immersed gives a direct measure of their hydrophobicity and can be derived from γ_{SL}:

$$\Delta G_{SLS} = -2\gamma_{SL} \quad (4)$$

ΔG_{SLS} gives a measure of the hydrophobicity or hydrophilicity of the surface. If $\Delta G_{SLS} > 0$, the surface is hydrophilic, and if $\Delta G_{SLS} < 0$, it is hydrophobic.

[1] C.J. Van Oss, M.K. Chaudhury, R.J. Good, Interfacial Lifshitz-van der Waals and polar interactions in macroscopic systems, Chem. Rev., 88 (1988) 927-941.

[2] A. Holländer, On the selection of test liquids for the evaluation of acid-base properties of solid surfaces by contact angle goniometry. J. Colloid Interface Sci., 169 (1995) 493-496.

[3] C.J. van Oss, Development and applications of the interfacial tension between water and organic or biological surfaces, Colloids Surf B: Biointerfaces, 54 (2007) 2-9.

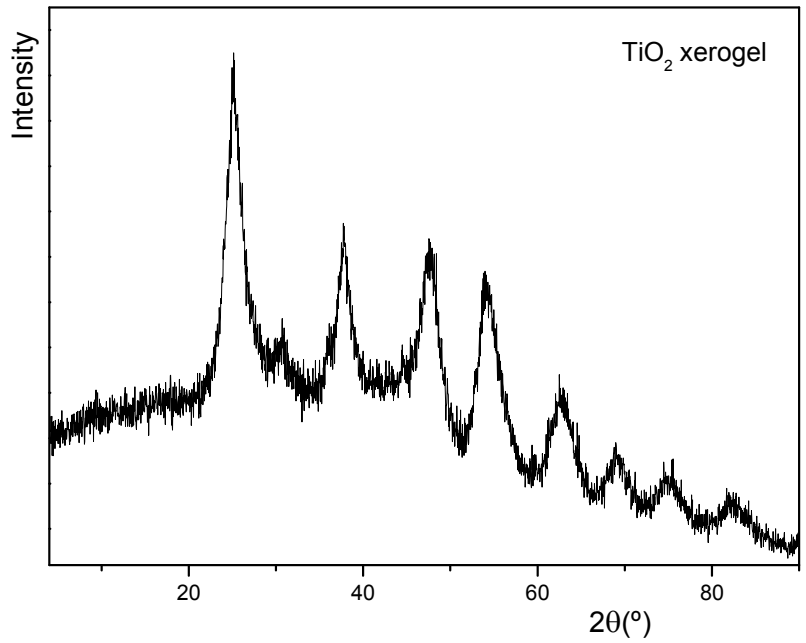

Figure S3.1.1. X-ray diffractogram of prepared TiO_2 xerogel.

	Filters			Slides		
t (min)	B	1	2	B	1	2
0	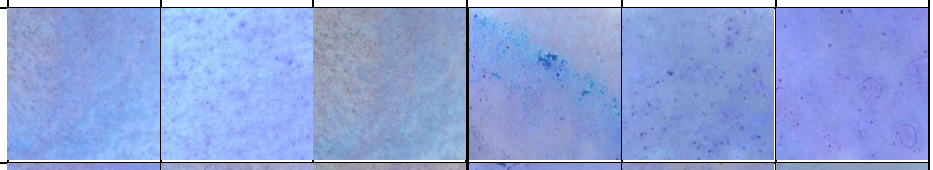					
15	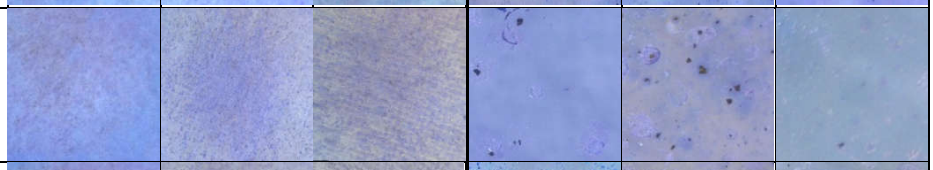					
30	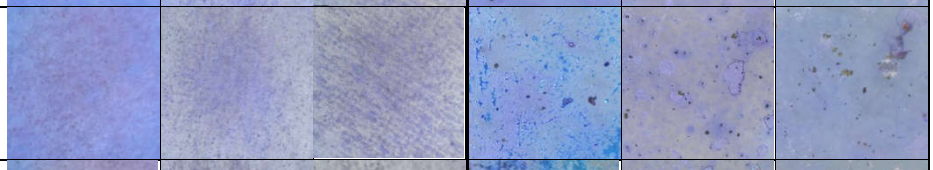					
90	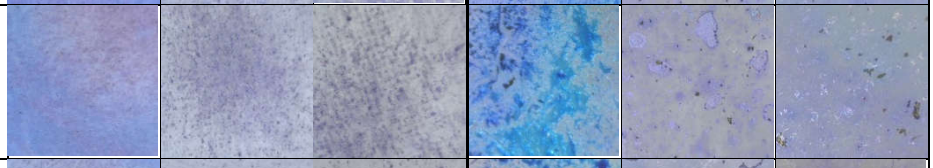					
180	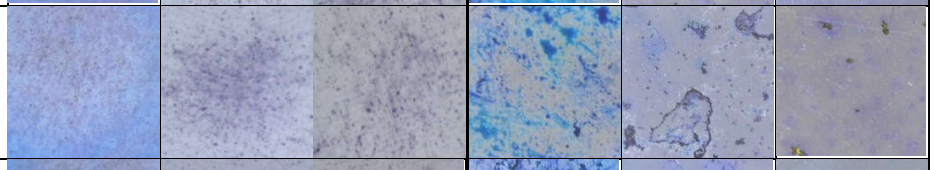					
240	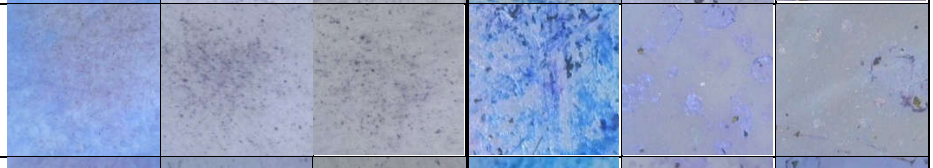					
300	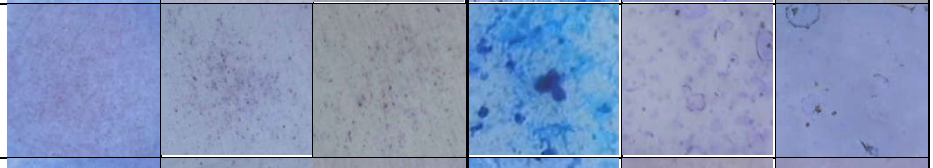					
390	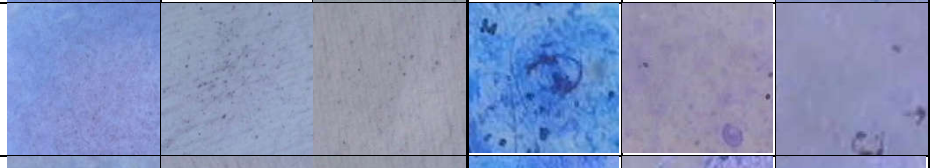					
480	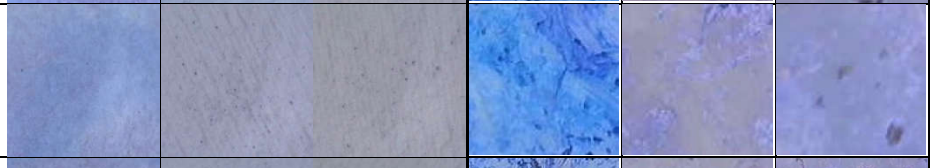					
630	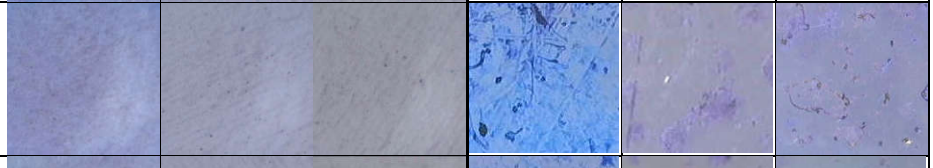					
750	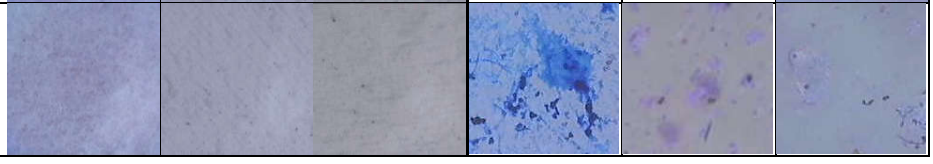					

Figure S3.1.2. Evolution of MB with irradiation time on TiO_2-coated filters and slides. (B refers to blank runs and 1 and 2 to replicates).

P. putida ***S. aureus***

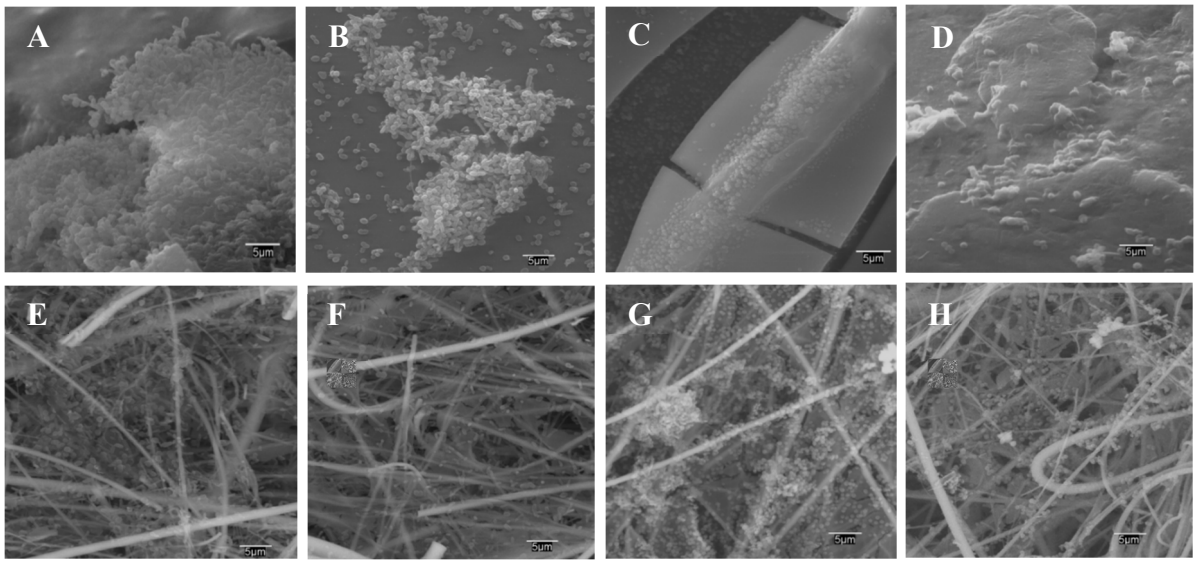

Figure S3.1.3. SEM images of *P. putida* (A, B, E and F) and *S. aureus* (C, D, G and H) biofilms on TiO_2 glass slides (A, B, C and D) and TiO_2 fiber filters (E, F, G and H) after 48 h incubation and before irradiation (A, C, E and G) and after 2 h irradiation (B, D, F and H).

***P. putida*:**

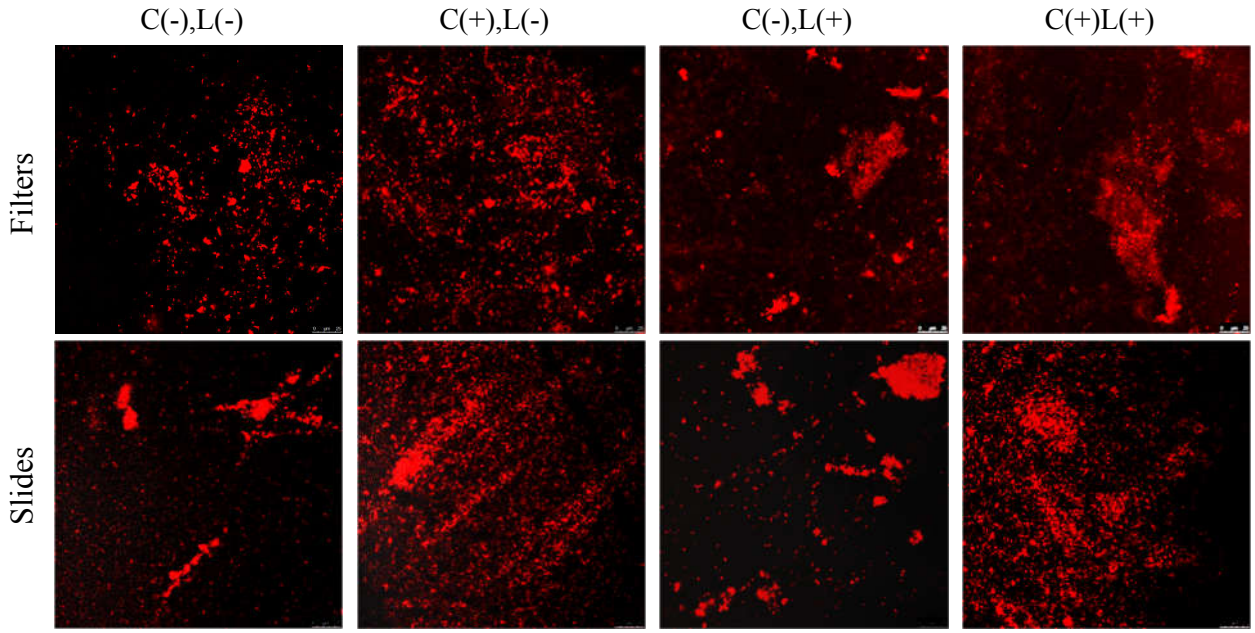

S. aureus:

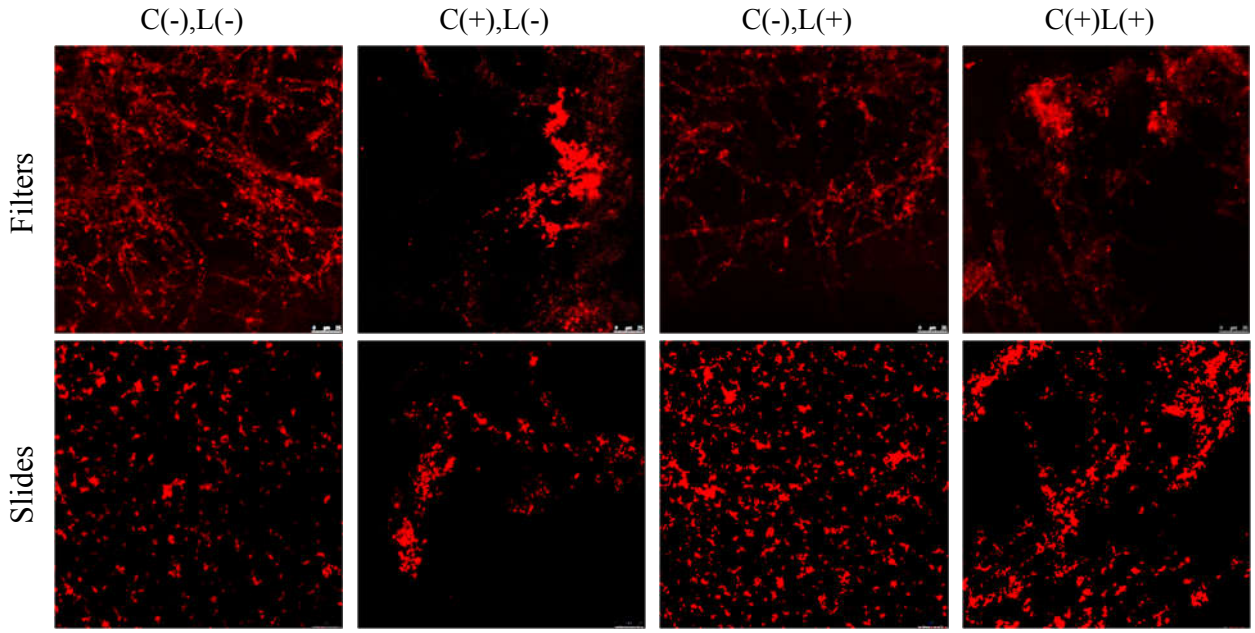

Figure S3.1.4. FilmTracer SYPRO Ruby biofilm matrix staining of samples with and without TiO_2, C(+) and C(-) respectively and with and without irradiation, L(+) and L(-) respectively for filters and slides kept in contact with *P. putida* and *S. aureus* for 48 h in the dark at 37 °C.

8.3 Coaxial poly (lactic acid) electrospun composites incorporating cellulose and chitin nanocrystals

Table S4.2.1. Viscosity and electrical conductivity of raw nanocrystal and electrospinning suspensions.

Figure S4.2.1. AFM images showing height (a) and phase images (b, c) of PAN/CNC_{AC}-20@PLA fibers at 2 x 2 μm (a, b) and 1 x 1 μm (c) magnifications.

Table S4.2.2. Fiber diameter, maximum pore size, mechanical properties, water flux and permeability of membranes.

Figure S4.2.2. SEM micrographs of PAN/ChNC-15@PAN composite nanofibers (arrows pointing to secondary nanofibers).

Table S4.2.1. Viscosity and electrical conductivity of raw nanocrystal and electrospinning suspensions.

	Viscosity (mPa s)	Electrical conductivity ($\mu S\ cm^{-1}$)
CNC_{H2SO4} (1.3 wt%)	1.06	1764
CNC_{BE} (1.5 wt%)	1112	1895
ChNC (0.5 wt%)	0.95	721.1
PLA (7 wt% in $CHCl_3$/DMF, 3:2 vol.)	310.8	1.4
PAN (10 wt% DMF)	924.6	55.0
PAN/CNC_{H2SO4} 5%	834.4	67.5
PAN/CNC_{H2SO4} 10%	716.1	62.9
PAN/CNC_{H2SO4} 15%	628.9	71.3
PAN/CNC_{H2SO4} 20%	597.8	77.4
PAN/CNC_{BE} 5%	1037	70.0
PAN/CNC_{BE} 10%	1221	70.1
PAN/CNC_{BE} 15%	1374	75.7
PAN/CNC_{BE} 20%	1450	83.2
PAN/ChNC 5%	851.0	59.6
PAN/ChNC 10%	764.1	56.8
PAN/ChNC 15%	622.4	62.9
PAN/ChNC 20%	598.2	65.5

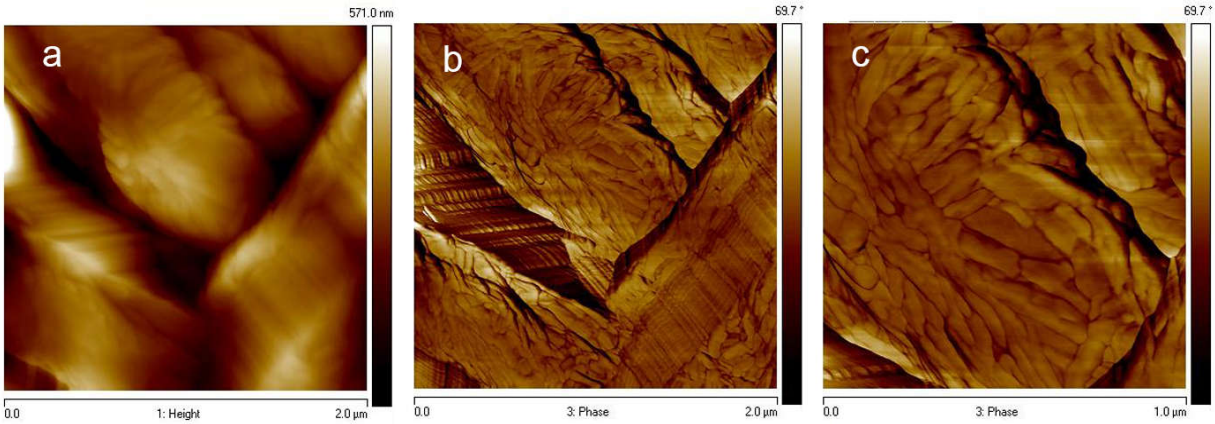

Figure S4.2.1. AFM images showing height (a) and phase images (b, c) of PAN/CNC_{AC}-20@PLA fibers at 2 x 2 µm (a, b) and 1 x 1 µm (c) magnifications.

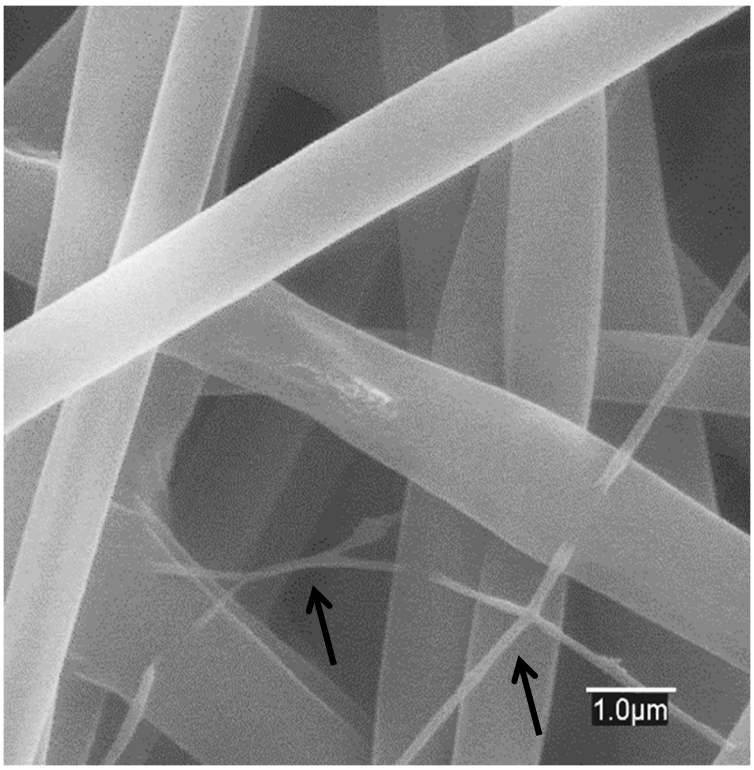

Figure S4.2.2. SEM micrographs of PAN/ChNC-15@PAN composite nanofibers (arrows pointing to secondary nanofibers).

Table S4.2.2. Fiber diameter, maximum pore size, mechanical properties, water flux and permeability of membranes.

	PLA	PAN@PLA	PAN/CNC_{AH}-5@PLA	PAN/CNC_{AH}10@PLA	PAN/CNC_{AH}-15@PLA	PAN/CNC_{AH}-20@PLA
Fiber diameter, nm	199 ± 52	458 ± 31	360 ± 25	356 ± 18	349 ± 29	339 ± 40
Max. pore size, µm	0.8 ± 0.1	1.2 ± 0.1	1.3 ± 0.1	1.5 ± 0.1	2.1 ± 0.1	2.5 ± 0.1
Tensile strength, MPa	2.4 ± 0.5	1.5 ± 0.3	3.9 ± 1.1	3.2 ± 0.9	2.9 ± 0.4	2.0 ± 0.3
Strain, %	17.9 ± 1.7	5.5 ± 1.0	6.2 ± 0.7	8.9 ± 1.5	9.9 ± 1.2	4.4 ± 0.9
Young's modulus, GPa	0.5 ± 0.1	0.6 ± 0.1	0.9 ± 0.1	0.7 ± 0.1	0.7 ± 0.1	0.7 ± 0.1
Flux, L m^{-2} h^{-1}	504 ± 32	777 ± 37	1106 ± 50	1472 ± 40	1875 ± 33	2140 ± 12
Permeability, L m^{-2} h^{-1} bar^{-1}	2024 ± 55	3888 ± 86	5531 ± 150	7634 ± 178	9375 ± 166	10701 ± 60

	PAN/CNC_{BE}-5@PLA	PAN/CNC_{BE}-10@PLA	PAN/CNC_{BE}-15@PLA	PAN/CNC_{BE}-20@PLA
Fiber diameter, nm	356 ± 34	351 ± 17	342 ± 23	338 ± 35
Max. pore size, µm	1.2 ± 0.1	1.5 ± 0.1	2.2 ± 0.12	2.6 ± 0.1
Tensile strength, MPa	4.4 ± 1.4	1.8 ± 0.5	1.5 ± 1.3	2.4 ± 0.1
Strain, %	16.9 ± 1.9	5.1 ± 1.1	5.7 ± 1.0	4.4 ± 0.9
Young's modulus, GPa	0.5 ± 0.1	0.5 ± 0.1	0.9 ± 0.1	0.9 ± 0.1
Flux, L m^{-2} h^{-1}	1357 ± 74	1390 ± 23	1472 ± 29	1700 ± 53
Permeability, L m^{-2} h^{-1} bar^{-1}	6788 ± 171	6952 ± 114	7365 ± 147	8503 ± 167

	PAN/ChNC-5@PLA	PAN/ChNC-10@PLA	PAN/ChNC-15@PLA	PAN/ChNC-20@PLA
Fiber diameter, nm	422 ± 26	415 ± 13	409 ± 21	399 ± 37
Max. pore size, µm	1.3 ± 0.1	1.6 ± 0.1	2.1 ± 0.1	2.5 ± 0.1
Tensile strength, MPa	2.7 ± 0.6	4.1 ± 0.7	5.4 ± 0.2	2.9 ± 1.0
Strain, %	7.3 ± 0.3	6.4 ± 0.3	4.8 ± 0.6	3.6 ± 1.0
Young's modulus, GPa	0.8 ± 0.1	1.1 ± 0.1	2.7 ± 0.2	1.1 ± 0.2
Flux, L m^{-2} h^{-1}	1403 ± 15	1934 ± 46	2522 ± 53	2646 ± 35
Permeability, L m^{-2} h^{-1} bar^{-1}	7019 ± 75	9672 ± 127	12613 ± 166	13234 ± 174